CORA Cork Open Research Archive
Cartlann Taighde Oscailte Chorcaí

Title	Multiscale simulation of electronic & optical properties of (Al,Ga)N-based light emitting devices
Authors	Finn, Robert
Publication date	2026-02-25
Original Citation	Finn, R. 2026. Multiscale simulation of electronic & optical properties of (Al,Ga)N-based light emitting devices. PhD Thesis, University College Cork.
Type of publication	Doctoral thesis
Rights	© 2026, Robert Finn. - https://creativecommons.org/licenses/by-nc-nd/4.0/
Download date	2026-11-06 01:57:12
Item downloaded from	https://hdl.handle.net/10468/18797

UCC
University College Cork, Ireland
Coláiste na hOllscoile Corcaigh

Multiscale simulation of electronic & optical properties of (Al,Ga)N-based light emitting devices

Robert Finn
B.S.C.
116494634



NATIONAL UNIVERSITY OF IRELAND, CORK

Thesis submitted for the degree of Doctor of Philosophy

25 February 2026

Head of Department: Dr. Fatima Gunning

Supervisors: Dr Stefan Schulz
Prof. Peter Parbrook

Research supported by Research Ireland Taighde Éireann

Contents

List of Figures . . . iii
List of Tables . . . x
Publication List . . . xii
Abstract . . . xvii
Acknowledgements . . . xix

1 Prologue **1**
1.1 III-Nitrides . . . 1
1.2 UV LEDs & modelling challenges . . . 3
1.3 Thesis Overview . . . 7

2 Introduction **9**
2.1 Wurtzite crystal structure . . . 9
2.2 Electronic band structure . . . 14
2.2.1 Degree of optical polarisation . . . 18
2.3 Heterostructures . . . 19
2.4 Light Emitting Diodes . . . 27
2.5 LED Efficiency & ABC model . . . 31
2.6 Alloy disorder . . . 36

3 Theory **39**
3.1 Density Functional Theory . . . 40
3.2 Semi-Empirical . . . 42
3.2.1 $\mathbf{k} \cdot \mathbf{p}$ method . . . 42
3.2.2 Modified continuum-based approaches . . . 49
3.2.2.1 Localisation Landscape Theory . . . 50
3.2.3 Tight-binding model . . . 54
3.2.3.1 Strain & Valence Force Field Model . . . 59
3.2.3.2 Polarisation . . . 63
3.3 Drift-Diffusion . . . 67
3.3.1 Drift-Diffusion Model . . . 68
3.3.2 Energy Landscape for drift-diffusion . . . 73

4 Electronic properties of (Al,Ga)N/AlN QWs **78**
4.1 Introduction . . . 78
4.2 Model quantum well system . . . 79
4.3 Results . . . 83
4.3.1 General considerations . . . 83

4.3.2 Single-particle energies and states 84
4.4 Conclusion 92

5 Carrier density dependant polarisation screening in (Al,Ga)N/(Al,Ga)N QWs 94
5.1 Introduction 94
5.2 Theoretical background 95
5.2.1 Valence Band Structure of AlN and GaN 96
5.2.2 Model Quantum Well System, Density of States and Degree of Optical Polarisation 100
5.3 Results 104
5.3.1 $Al_{0.48}Ga_{0.52}N/Al_{0.63}Ga_{0.37}N$ Quantum Well Systems . . . 104
5.3.1.1 Urbach Tails 104
5.3.1.2 Degree of Optical Polarisation 108
5.3.2 $Al_{0.75}Ga_{0.25}N/Al_{0.90}Ga_{0.10}N$ Quantum Well System 110
5.3.2.1 Urbach Tails 110
5.3.2.2 Degree of Optical Polarisation 115
5.4 Conclusion 118

6 Carrier transport and recombination in (Al,Ga)N-based UV light emitters 120
6.1 Introduction 120
6.2 Single (Al,Ga)N QW 122
6.2.1 Results 123
6.3 (Al,Ga)N-based MQW DUV LED 131
6.3.1 Theoretical framework 134
6.4 Results 136
6.4.1 Doping and activation energy 137
6.4.2 Impact of alloy disorder 140
6.5 Conclusion 149

7 Conclusion and outlook 151
7.1 Conclusion 151
7.2 Outlook 154

A Material parameters used for AlN and GaN 157

B Multi-QW deep UV LED device parameters 160

C Multi-QW deep UV LED band edge profiles 161

List of Figures

1.1 Band gap evolution of AlN, GaN and InN as a function of the in-plane lattice constants, a. The lattice constants and band gap energies of the binary materials, along with their band gap bowing parameters, are taken from Ref. [14], and the alloy band gaps are calculated using linear interpolation with bowing. 2

1.2 External quantum efficiency versus the emission wavelength of fabricated UV LEDs in the spectral range of 200 - 400 nm. Figure taken from https://www.tu.berlin/en/originagkneissl/research accessed 12/7/2025 3

2.1 Hexagonal cell of the wurtzite crystal structure. The cations are in red and the anions are in blue. The lattice constant a (in-plane) and c (out-of-plane) are shown. The green plane highlights the hexagonal close-packed structure with the four basis atoms labelled $\mathbf{\Delta}_1$, $\mathbf{\Delta}_2$, $\mathbf{\Delta}_3$ and $\mathbf{\Delta}_4$. The faded atoms represent periodic replicas of the unit cell ions. 12

2.2 Schematic of the first Brillouin zone for a hexagonal lattice. Highlighted in red are points of high symmetry with the Γ-point indicating $\mathbf{k} = \mathbf{0}$. 13

2.3 Schematic of light emission in a direct (left) and indirect (right) band gap material. In direct band gaps, a vertical transition from the conduction band (CB) and valence band (VB) emits a photon. In indirect band gaps, a phonon assists the transition to conserve momentum (k). 17

2.4 Schematic illustration of the band edges at the Γ point for GaN and AlN. The A, B and C bands denote the p_x-, p_y- and p_z-orbitals, respectively. The grey lines indicate that at a certain Al composition x in an $Al_xGa_{1-x}N$ alloy there will be a crossing of the bands. 19

2.5 Schematic of a double heterostructure with a (a) type I band alignment where the carriers are confined in both the conduction and valence band in material **B**, and (b) a type II band offset where only one band confines carriers in the region of material **C** (in this example, the conduction band). 20

2.6 Schematic of a quantum well (QW) bandstructure. The inclusion of a QW confines the electron (green) and hole (red) wave functions within the region of lower band gap energy. This increases the wave function overlap and allows efficient photon emission (hv) of a lower energy than the barrier material. Without the QW there would be poor wave function overlap and thus inefficient recombination. . 21

2.7 a) Quantum well (QW) (material **B**) embedded between two barriers (material **A**) inducing bound charges at the QW interfaces due to differences in the polarisation fields of material **A** and **B**. The left (right) interface has a negative (positive) sheet charge density generating a capacitor like setup. b) The potential, φ_{pol}, exhibits a capacitor-like profile which is constant outside the well and increases linearly within the well along the c-axis. 25

2.8 Conduction and valence band energies as a function along the c-axis (growth direction) of a quantum well. a) shows a QW with no polarisation and thus good wave function overlap of the electrons and holes leading to efficient recombination. b) shows a QW with a polarisation field and thus the built-in field shifts the electron and hole wave function to either side of the QW and reduces the band gap energy. This causes the recombination rate to reduce and the photon (hv) emitted to be redshifted. 26

2.9 Schematic illustration of a band diagram for a n-doped, p-doped and undoped (intrinsic) material at zero temperature. The conduction and valence band energy of a semiconductor with their respective donor (green) and acceptor (red) energy levels. These energy levels sit within the band gap and ideally have a small energy level separation, E_D and E_A, between their respective bands so that it requires little energy to excite the carriers. The doping for the n-doped (p-doped) material has shifted the Fermi energy level, E_f, closer to the conduction (valence) band edge. The Fermi energy level of an intrinsic material remains in the centre of the band gap. 28

2.10 Schematic illustration of the conduction and valence band energies for a p-n junction where the built-in potential, $q\varphi$, is keeping the Fermi energy level (E_f) constant. The region where the n-doped and p-doped materials meet form the depletion layer which has a low free carrier density and the presence of an internal electric field, E. The donor impurity energies for the electrons (holes) are shown as a dashed green (red) line. 30

2.11 Shown are the conduction, E_c, and valence, E_v, band energy with the three recombination mechanisms of the ABC model. A) shows the Shockley-Read-Hall non-radiative recombination at a defect (trap) site. B) Radiative Recombination where the electron hole pair recombine emitting a photon. C) Auger-Meitner recombination which involves a three particle process. An electron hole pair recombine and interact with either an electron (eeh) or a hole (hhe) exciting it to higher energies. 34

2.12 Diagram of the density of states (DOS) versus energy. In blue is the ideal step function that describes the DOS for a QW that has two degrees of freedom. The red exponential DOS describes the localised carriers generating this 'tail state'. 37

3.1 Schematic of a local tetrahedron of the cation (red) atomic site at position $\mathbf{r}_0$ bonded (dashed lines) to four nearest neighbour anions (blue). Each anion is located at vectors $\mathbf{r}_{ij}$ from atom 0. Only the vector to atom 1, $\mathbf{r}_{01}$, is shown. The local tetrahedrons edges, $\mathbf{R}_{ij}$, are shown as solid lines. 63

4.1 Schematic illustration of the supercell underlying the atomistic tight-binding calculations of the electronic properties of c-plane $Al_xGa_{1-x}N$/AlN quantum wells. In the region indicated by 'AlGaN', we assume a random distribution of Al (red) and Ga (green) atoms. 80

4.2 Strain tensor components ϵ_{xx}, ϵ_{yy} and ϵ_{zz} for a linescan along the z-axis (c-axis) of the simulation cell containing an $Al_{0.5}Ga_{0.5}N$/AlN quantum well. Data averaged over the simulation cell is shown in (a) while (b) shows an individual linescan. 81

4.3 Contour plot of the polarisation potential ϕ_p arising from spontaneous and piezoelectric polarisation for an arbitrarily chosen x-z-plane in a c-plane $Al_{0.5}Ga_{0.5}N$/AlN quantum well. 82

4.4 Relative ground state transition energy $\Delta E_g(n) = E_g(n) - E_g^{\text{avg}}$ in c-plane $Al_xGa_{1-x}N$/AlN QWs for different microscopic alloy configurations n; more details are given in the main text. The data are shown for Al contents of 10%, 25%, 50% and 75% in the well. The inset shows the standard deviation, σ, as a function of the Al content in the well. 85

4.5 Relative *electron* ground state energy $\Delta E^e_{\text{GS}}(n) = E^e_{\text{GS}}(n) - E^{\text{e,avg}}_{\text{GS}}$ in c-plane $Al_xGa_{1-x}N$/AlN QWs for different microscopic configurations n; more details are given in the main text. The data are shown for Al contents of 10%, 25%, 50% and 75% in the well. The inset shows the standard deviation, σ, as a function of the Al content in the well. 87

4.6 Relative *hole* ground state energy $\Delta E^h_{\rm GS}(n) = E^h_{\rm GS}(n) - E^{h,\rm avg}_{\rm GS}$ in c-plane $Al_xGa_{1-x}N$/AlN QWs for different microscopic configurations n; more details are given in the main text. The data are shown for Al contents of 10%, 25%, 50% and 75% in the well. The inset shows the standard deviation, σ, as a function of the Al content in the well. 88

4.7 Isosurface plots of the electron (red) and hole (blue) ground state charge densities for c-plane (Al,Ga)N/AlN QWs with (a) 10%, (b) 25%, (c) 50% and (d) 75% Al content. The light and dark surfaces correspond to 10% and 50% of the maximum values, respectively. The charge densities are shown for a top-view (down the c-axis). 89

4.8 Isosurface plots of the electron (red) and hole (blue) ground state charge densities for Config. 18 of the c-plane $Al_{0.75}Ga_{0.25}N$ QW. The light and dark surfaces correspond to 10% and 50% of the maximum values, respectively. The charge densities are shown for a top-view (down the c-axis). The dashed lines are used to indicate the supercell boundaries. 90

4.9 Isosurface plots of the charge densities of the five energetically lowest hole states (ψ^h_0 to ψ^h_4) in a c-plane (Al,Ga)N/AlN quantum well with 50% Al content. The same alloy configuration as in Fig. 4.7 (c) is chosen here. The light and dark isosurfaces correspond to 10% and 50% of the respective maximum charge density values. 92

5.1 Schematic illustration of the valence band order for high aluminium content containing (Al,Ga)N systems when (a) unstrained, (b) under biaxial compressive strain, (c) in the presence of quantum confinement and (d) intrinsic built-in fields. The heavy hole, light hole and crystal field split-off bands are denoted as the A-, B- and C-bands, respectively. Note that our schematic is to highlight general trends. Quantum confinement will break the translation invariance e.g. along the wurtzite c-axis and a band structure cannot be defined along this direction. The above should however indicate how quantised energy levels that are constructed from e.g. $|p_z\rangle$-like basis states are affected by confinement effects. 99

5.2 Derivative of hole density of states (d-h-DOS) calculated for the 3.3 nm $Al_{0.48}Ga_{0.52}N/Al_{0.63}Ga_{0.37}N$ quantum well at low carrier densities, i.e. in the absence of built-in field screening effects. Tight-binding (TB) data (black circles) and exponential fit to the Urbach tail (red line) are given. The inset shows the natural logarithm of the TB d-h-DOS data fitted with a linear function. . . 103

5.3 Urbach tail energy E_u for $Al_{0.48}Ga_{0.52}N/Al_{0.63}Ga_{0.37}N$ quantum wells of width $L_w = 1.3$ nm (red), $L_w = 2.3$ nm (blue) and $L_w = 3.3$ nm (black) at carrier densities of $n = 1 \times 10^{18}$ cm^{-3}, $n = 1 \times 10^{19}$ cm^{-3} and $n = 1 \times 10^{20}$ cm^{-3}. 105

5.4 Planar integrated probability densities of holes, $P_m(k)$, for an arbitrarily chosen alloy configuration of an $Al_{0.48}Ga_{0.52}N/Al_{0.63}Ga_{0.37}N$ quantum well of width $L_w = 1.3$ nm, $L_w = 2.3$ nm and $L_w = 3.3$ nm. The data are displayed at carrier densities of $n = 1 \times 10^{18}$ cm^{-3}, (a)-(c), and $n = 1 \times 10^{20}$ cm^{-3}, (d)-(f), for 60 hole states. Index m refers to the single-particle hole state number, with $m = 1$ being the ground state, while k refers to the layer in the supercell along the wurtzite c-axis. The quantum well boundaries are indicated by the light blue dashed lines. The colourbar is kept the same between the different figures and is determined by the maximum $P_m(k)$ value found in the $L_w = 3.3$ nm $Al_{0.75}Ga_{0.25}N/Al_{0.90}Ga_{0.10}N$ quantum well system at a carrier density of $n = 1 \times 10^{18}$ cm^{-3} discussed in Sec. 5.3.2. 106

5.5 Averaged degree of optical polarisation, DOP ρ, over 150 configurations at a temperature of 300 K for $Al_{0.48}Ga_{0.52}N/Al_{0.63}Ga_{0.37}N$ quantum wells of width $L_w = 1.3$ nm (red), $L_w = 2.3$ nm (blue) and $L_w = 3.3$ nm (black) as a function of the carrier density n. . 109

5.6 Urbach tail energies, E_u, for $Al_{0.75}Ga_{0.25}N/Al_{0.90}Ga_{0.10}N$ quantum wells of width $L_w = 1.3$ nm (red), $L_w = 2.3$ nm (blue) and $L_w = 3.3$ nm (black) at carrier densities of $n = 1 \times 10^{18}$ cm^{-3}, $n = 1 \times 10^{19}$ cm^{-3} and $n = 1 \times 10^{20}$ cm^{-3}. 111

5.7 Planar integrated probability densities of holes, $P_m(k)$, for an arbitrarily chosen configuration of an $Al_{0.75}Ga_{0.25}N/Al_{0.90}Ga_{0.10}N$ quantum well of width $L_w = 1.3$ nm, $L_w = 2.3$ nm and $L_w = 3.3$ nm. The data are displayed at carrier densities of $n = 1 \times 10^{18}$ cm^{-3}, (a)-(c), and $n = 1 \times 10^{20}$ cm^{-3}, (d)-(f), for 60 states. Index m refers to the single-particle hole state number, with $m = 1$ being the ground state, while k refers to the layer in the supercell along the wurtzite c-axis. The quantum well boundaries are indicated by the light blue dashed lines. $P_m(k)$ has been plotted to the maximum $P_m(k)$ value found in the $L_w = 3.3$ nm $Al_{0.75}Ga_{0.25}N/Al_{0.90}Ga_{0.10}N$ QW system at a carrier density of $n = 1 \times 10^{18}$ cm^3. 112

5.8 Average probability of hole charge density, $|\Psi_h^{\mathrm{avg}}|^2$, confined inside the (Al,Ga)N quantum wells as a function of energy. The data are averaged over the 150 configurations. The average state energy is plotted with respect to the averaged ground state energy of each quantum well system. The $Al_{0.48}Ga_{0.52}N/Al_{0.63}Ga_{0.37}N$ wells are shown for (a) $L_w = 1.3$ nm, (b) $L_w = 2.3$ nm, and (c) $L_w = 3.3$ nm; the data for $Al_{0.75}Ga_{0.25}N/Al_{0.90}Ga_{0.10}N$ wells is displayed in (d)-(f). For each QW system $|\Psi_h^{avg}|^2$ is plotted for two carrier densities: $n = 1 \times 10^{18}$ cm^{-3} (circles) and $n = 1 \times 10^{20}$ cm^{-3} (crosses). The colour coding gives the averaged orbital contribution of each energy level (red: p_z; blue: $p_x + p_y$). 114

5.9 Averaged degree of optical polarisation, DOP ρ, over 150 configurations at a temperature of 300 K for $Al_{0.75}Ga_{0.25}N/Al_{0.90}Ga_{0.10}N$ quantum wells of width $L_w = 1.3$ nm (red), $L_w = 2.3$ nm (blue) and $L_w = 3.3$ nm (black) as a function of carrier density n. . . . 116

6.1 Schematic illustration of the (Al,Ga)N-based *p-i-n* system underlying the single quantum well simulations. The intrinsic barriers plus quantum well region is denoted as the "atomistic" mesh in the main text, while the *n*- and *p*-regions are described by a sparser device mesh. 122

6.2 Current-voltage curves, on a log-scale, for an $Al_{0.7}Ga_{0.3}N/Al_{0.8}Ga_{0.2}N$ quantum well embedded in a *p-n* junction. The data are shown for simulations that (i) account for random alloy (RA) fluctuations in the well and barriers (blue), (ii) account for RA fluctuations in the well but treat the barrier in a virtual crystal approximation (VCA) (red), and (iii) use a VCA in the entire *p-i-n* structure (pink). The inset shows the I-V curves on a linear scale. 124

6.3 3D isosurface plot of the current density in the intrinsic (Al,Ga)N quantum well and barrier regions at a bias of 5.5 V, using the fully atomistic description, described in the main text. The current density for the holes (blue) and electrons (red) are plotted at 700 A cm^{-2}, reflecting locally high current densities due to alloy fluctuations; dashed black lines indicate well boundaries. 126

6.4 Electron (red) and hole (blue) density along the *c*-axis of a $Al_{0.7}Ga_{0.3}N/Al_{0.8}Ga_{0.2}N$ quantum well embedded in a *p-i-n* junction at a bias of 5.5 V; data are shown for the intrinsic regions of the device. (a) Averaged carrier distribution of the fully atomistic calculation over each *c*-plane along the *c*-axis (solid lines), and the carrier distribution for the virtual crystal approximation (dashed lines); (b) Scatter plot of the carrier distribution in the fully atomistic calculation. The vertical dashed black lines indicate well boundaries. Note (b) is an order of magnitude larger than (a) on the *y*-axis. 127

6.5 Radiative and Auger-Meitner non-radiative recombination rates along the *c*-axis of the $Al_{0.7}Ga_{0.3}N/Al_{0.8}Ga_{0.2}N$ *p-i-n* system at a bias of 5.5 V; the data are shown for the intrinsic regions of the device. Solid lines: results from the atomistic calculations taking alloy fluctuations into account (averaged over each *c*-plane). Dashed lines: data obtained from a virtual crystal approximation of the same system; vertical dashed black lines indicate well boundaries. 129

6.6 Schematic of the deep UV LED investigated. The VCA regions are composed of the n-doped $Al_{0.85}Ga_{0.15}N$ contact layer, p-doped GaN contact layer, the (p)-$Al_{0.85}Ga_{0.15}N$ and (p)-AlN electron blocking layer (EBL). Between the EBL and n-$Al_{0.85}Ga_{0.15}N$ contact layer is the active region that accounts for alloy disorder. The $Al_{0.75}Ga_{0.25}N$ QWs are shown in orange, the $Al_{0.85}Ga_{0.15}N$ barriers are in green, the EBL is in red and and the contact layers are in blue. The bracketed (p) layers indicate the regions of varied activation energy and doping densities. 132

6.7 Internal quantum efficiency (IQE) as a function of current density for the six systems with different doping profiles and activation energies as shown in Table 6.1. The activation energies E_A^α are given in meV, with α denoting the electron blocking layer (EBL) and hole injection layer (HIL). 138

6.8 (a) Current injection efficiency (CIE) and (b) radiative recombination efficiency (RRE) as a function of current density for the six systems with different doping profiles and activation energies as summarised in Table 6.1. The activation energies E_A^α are given in meV, with α denoting the electron blocking layer (EBL) and hole injection layer (HIL). 139

6.9 Internal quantum efficiency (IQE, blue), current injection efficiency (CIE, yellow) and radiative recombination efficiency (RRE, red) as a function of current density of the random alloy (RA, cross) and virtual crystal approximation (VCA, circle) for SYS 3 (E_A^{EBL} = 450 meV; E_A^{HIL} = 450 meV). 141

6.10 The conduction/valence band edge energies (CBE/VBE) and conduction/valence quasi-fermi levels (Ef_n/Ef_p) are shown in (a) and (b), respectively. The energies are plotted along the c-axis of the deep UV LED studied here [SYS 3 (E_A^{EBL} = 450 meV; E_A^{HIL} = 450 meV)] for both the random alloy (RA, green) and virtual crystal approximation (VCA, blue) at a current density of 135 A cm^{-2}. The RA data has also been averaged (Avg RA, red) over each plane along the wurtzite c-axis as described in Sec. 6.2.1 for Fig. 6.4. The electron and hole carrier densities (log scale) are shown in (c) and (d), respectively. All data are plotted from the end of the n-contact (0 nm) to 10 nm after the last QW (60 nm). 142

6.11 Hole density (log plot) along the c-axis of the deep UV LED [SYS 3 (E_A^{EBL} = 450 meV; E_A^{HIL} = 450 meV)]. The random alloy (RA, red) structure, the virtual crystal approximation (VCA, blue) and the random alloy structure with QWs described in VCA (VCA QWs, green) are plotted at a current density of 135 A cm^{-2}. The data is taken from the end of the n-contact (0 nm) to 10 nm after the last QW (60 nm). The random alloy and the random alloy structure with VCA QWs have been averaged over each plane along the c-axis 144

6.12 Electron leakage as a function of the current density for SYS 3 (E_A^{EBL} = 450 meV; E_A^{HIL} = 450 meV). Plotted is the random alloy (RA) results as a red line, the virtual crystal approximation (VCA) as a blue line, the RA with VCA QWs (VCA QWs) with green crosses and the RA structure with a VCA barrier before the EBL (VCA Barrier) as purple crosses. 145

6.13 Current-voltage curves, on a log-scale, for SYS 3 (E_A^{EBL} = 450 meV; E_A^{HIL} = 450 meV) of both the random alloy (RA, blue) and virtual crystal approximation (VCA, red). The inset shows the I-V curves on a linear scale confined to 400 A cm^{-2}. 146

C.1 Table of band edge energies for the deep UV LED SYS 3 (E_A^{EBL} = 450 meV; E_A^{HIL} = 450 meV) investigated in chapter 6 Sec. 6.4.2. The conduction (CBE) and valence band edge energies (VBE) are plotted for the random alloy (a,c) and virtual crystal approximation systems (b,d) at a current density of $\approx$ 135 A cm^{-2}. The conduction (valence) band is in blue and the electron (hole) Fermi level, Ef$_n$ (Ef$_p$), is in red. The black dashed lines define the boundaries for the random alloy in (a) and (c). 162

List of Tables

6.1 Investigated systems (SYS) with varying activation energies E_A for the electron blocking layer (EBL) (p-AlN) and hole injection layer (HIL) (p-Al$_{0.85}$Ga$_{0.15}$N). N/A denotes no p-doping in this region. 133

A.1 Material parameters used in this study for AlN and GaN calculations. a and c denote the in-plane and out-of plane lattice constants, respectively. Elastic constants and first-order piezoelectric constants are denoted as C_{ij} and e_{ij}. The spontaneous polarisation is given as P_{sp} and the dielectric constant is expressed ϵ_r. The effective electron mass parallel ($||$) and perpendicular ($\perp$) to the c-plane is given as m_e^x, while the Luttinger-like hole effective masses are shown as A_i. The conduction and valence band deformations are expressed as a_c and D_i, respectively. k_r, k_θ, $k_{r\theta}$ and k_{rr} are the force constants for bond stretching, bond bending, bond-angle and bond-bond terms, respectively. Finally the valence band offset for GaN/AlN is ΔE_{VB}. 157

A.2 Tight-binding parameters in eV for the nearest neighbours of wurtzite AlN and GaN. 159

B.1 Drift-diffusion parameters used for different regions in the simulation cell. † values are taken from Ref. [16] and the ⋄ parameters are from Ref. [69]. □ symbolises the radiative, B, and Auger-Meitner coefficients, C_{nnp} & C_{npp}, which are taken from Ref. [105]. 160

Publication List

Journal Publications

[1] "Impact of carrier-density screening on Urbach-tail energies and optical polarization in (Al,Ga)N quantum well systems", Robert Finn, Michael O'Donovan, Thomas Koprucki and Stefan Schulz, *Physical Review Applied* **24** 044084 (2025)

[2] "Developing a hybrid single band carrier transport model for (Al,Ga)N heterostructures", Michael O'Donovan, Robert Finn, Patricio Farrell, Timo Streckenbach, Julien Moatti, Stefan Schulz and Thomas Koprucki, *Journal of Computational Electronics* **24** 114 (2025)

[3] "Theoretical study of the temperature dependence of Auger-Meitner recombination in (Al,Ga)N quantum wells", Joshua M McMahon, Robert Finn and Stefan Schulz, *Journal of Physics: Condensed Matter* **37** 095501 (2024)

[4] "Theoretical study of the impact of alloy disorder on carrier transport and recombination processes in deep UV (Al,Ga)N light emitters", Robert Finn, Michael O'Donovan, Patricio Farrell, Julien Moatti, Timo Streckenbach, Thomas Koprucki and Stefan Schulz, *Applied Physics Letters* **122** 241104 (2023)

[5] "Atomistic study of Urbach tail energies in (Al,Ga)N quantum well systems", Michael O'Donovan, Robert Finn, Stefan Schulz and Thomas Koprucki, *2023 International Conference on Numerical Simulation of Optoelectronic Devices (NUSOD)*, Turin, Italy, pp 79-80. IEEE, (2023)

[6] "Theoretical investigation of carrier transport and recombination processes for deep (Al,Ga)N light emitters", Robert Finn, Michael O'Donovan, Patricio Farrell, Timo Streckenbach, Julien Moatti, Thomas Koprucki and Stefan Schulz, *2023 International Conference on Numerical Simulation of Optoelectronic Devices (NUSOD)*, Turin, Italy, pp 83-84. IEEE, (2023)

[7] "Impact of random alloy fluctuations on the electronic and optical properties of (Al,Ga)N quantum wells: Insights from tight-binding calculations", Robert Finn and Stefan Schulz, *The Journal of Chemical Physics* **157** 244705 (2022)

[8] "Impact of random alloy fluctuations on the electronic and optical properties of c-plane $Al_xGa_{1-x}N$ quantum wells", Robert Finn and Stefan Schulz, *2022 International Conference on Numerical Simulation of Optoelectronic Devices (NUSOD)*, Turin, Italy, pp 135-136. IEEE, (2022)

Conference talks

"Theoretical study of carrier density screening on Urbach tail energies in (Al,Ga)N quantum well systems", Robert Finn, Michael O'Donovan,

Thomas Koprucki and Stefan Schulz, at *UK Nitride Consortium*, Glasgow, Scotland, January 2024

"Theoretical study on carrier transport and recombination processes in deep-UV (Al,Ga)N light emitters", Robert Finn, Michael O'Donovan, Patricio Farrell, Julien Moatti, Timo Streckenbach, Thomas Koprucki and Stefan Schulz, at *International Conference on Nitride Semiconductors*, Fukuoka, Japan, November 2023

"Theoretical study of carrier transport & recombination in deep-UV (Al,Ga)N quantum wells", Robert Finn, Michael O'Donovan, Patricio Farrell, Julien Moatti, Timo Streckenbach, Thomas Koprucki and Stefan Schulz, at *Conference on Numerical Simulation of Optoelectronic devices*, Turin, Italy, September 2023

"Theoretical study of carrier transport in deep-UV (Al,Ga)N quantum wells", Robert Finn, Michael O'Donovan, Patricio Farrell, Julien Moatti, Timo Streckenbach, Thomas Koprucki and Stefan Schulz, at *UK Nitride Consortium*, Bristol, England, January 2023

"Impact of random alloy fluctuations on the electronic and optical properties of *c*-plane (Al,Ga)N/AlN quantum wells: Importance for UV light emitters", Robert Finn and Stefan Schulz, at *Conference on Numerical Simulation of Optoelectronic devices*, Online, September 2022

Conference Posters

"Degree of optical polarization and Urbach tails in (Al,Ga)N quantum wells: An atomistic tight-binding study", Robert Finn, Michael O'Donovan, Thomas Koprucki and Stefan Schulz, at *International Conference on Nitride Semiconductors*, Malmö, Sweden, July 2025

"Simulation of (Al,Ga)N-based UV-LEDs including effects from disorder", Michael O'Donovan, Robert Finn, Patricio Farrell, Julien Moatti, Timo Streckenbach, Thomas Koprucki and Stefan Schulz, at *International Conference on Nitride Semiconductors*, Malmö, Sweden, July 2025

"Theoretical investigation on carrier transport & recombination processes in deep UV (Al,Ga)N light emitters", Robert Finn, Michael O'Donovan, Patricio Farrell, Julien Moatti, Timo Streckenbach, Thomas Koprucki and Stefan Schulz, at *Photonics Ireland Conference*, Limerick, Ireland, September 2023

"Atomistic theoretical study on the impact of random alloy fluctuations on the electronic and optical properties of (Al,Ga)N/AlN quantum wells", Robert Finn and Stefan Schulz, at *International Workshop on Nitride Semiconductors*, Berlin, Germany, October 2022

"Impact of random alloy fluctuations on the electronic and optical properties of (Al,Ga)N/AlN quantum wells: Insights from atomistic calculations", Robert Finn and Stefan Schulz, at *UK Nitride Consortium*

Winter Meeting, Online, January 2022

Contributions to talks

"Multi-scale hybrid band simulation of (Al,Ga)N UV-C light emitting diodes", Robert Finn, Patricio Farrell, Julien Moatti, Timo Streckenbach, Thomas Koprucki, Stefan Schulz and Michael O'Donovan, at *International Conference on Numerical Simulation of Optoelectronic Devices (NUSOD)*, Łódź, Poland, September 2025 (*Upcoming*)

"Theoretical investigation of optical polarisation in alloy disordered (Al,Ga)N quantum well systems", Robert Finn, Michael O'Donovan, Thomas Koprucki and Stefan Schulz, at *International Conference on Numerical Simulation of Optoelectronic Devices (NUSOD)*, Łódź, Poland, September 2025 (*Upcoming*)

"Atomistic study of Urbach tail energies in (Al,Ga)N quantum well systems", Michael O'Donovan, Robert Finn, Stefan Schulz and Thomas Koprucki, *International Conference on Numerical Simulation of Optoelectronic Devices (NUSOD)*, Turin, Italy, September (2023)

"III-N materials for UV light emitters: from atomistic structure to optical properties", Robert Finn and Stefan Schulz, at *SPIE Photonics West 2023*, San Francisco, United States, January 2023

I, Robert Finn, certify that this thesis is my own work and I have not obtained a degree in this university or elsewhere on the basis of the work submitted in this thesis.

Robert Finn

"Chance would be a fine thing... a fine thing indeed."

— Mark Corrigan, Peep Show, Season 6 Episode 1

Abstract

Wurtzite III-Nitride semiconductor materials, such as AlN, GaN, InN and their alloys, all possess direct band gaps and can, in principle, emit light from the deep ultraviolet wavelength region up to the infrared part of the spectrum. However, experimental studies have shown that the efficiency of III-N devices in these extreme wavelength windows are very low. Although there has been extensive research done on these materials, (Al,Ga)N-based alloys used in ultraviolet-emitting devices remain mostly inefficient. In order to improve these device efficiencies, a strong theoretical guidance is required. However, experimental studies in the literature have revealed that a multitude of factors are at play, making the modelling of these devices extremely challenging.

This thesis aims to develop a multiscale simulation framework that captures the intrinsic features of (Al,Ga)N-based heterostructures and devices. To do so, in a first step an atomistic tight-binding model has been developed to understand the impact of alloy disorder and connected carrier localisation effects, a feature seen to be important in experimental studies, on the electronic and optical properties of quantum wells. In a second step this electronic structure model is connected with a carrier transport drift-diffusion framework that incorporates quantum corrections via the localisation landscape theory, while addressing the differences in the valence band ordering between AlN and GaN via a hybrid effective mass approach. In general this multiscale approach allows us to gain insight into fundamental electronic structure properties of (Al,Ga)N alloys and heterostructures, their optical properties and important information on carrier transport and recombination properties of deep UV LEDs.

Our results indicate that random alloy fluctuations are sufficient to induce carrier localisation across a range of (Al,Ga)N quantum wells, most noticeably for the holes, while electrons may also be localised at higher Al contents in the wells. Furthermore, we find that these localisation effects are stronger with increasing quantum well width, due to the corresponding increase in the built-in potential drop across the quantum well, as reflected by increasing Urbach tail energies. Under high carrier densities, this potential drop reduces due to carrier density screening, resulting in a noticeable decrease in observed carrier localisation effects, indicated by a decrease in Urbach tail energies. Additionally, we investigate the degree of optical polarisation in wells of transverse electric and transverse magnetic emission. There we find that carrier localisation can enhance the transverse electric component of emission, particularly for quantum

wells where the dominant emission is transverse magnetic.

Finally, we perform quantum corrected multiscale drift-diffusion calculations on deep UV (Al,Ga)N-based light emitting diodes. We find that alloy fluctuations result in percolative pathways that enhance carrier transport through the disordered alloy. Additionally, carrier localisation can significantly increase the carrier density locally inside the active region of the device, which in turn enhance both the radiative and non-radiative Auger-Meitner recombination rates. These effects lead to a more asymmetric distribution of the carriers across a multi-quantum well structure compared to a simulation that neglects alloy fluctuations, and a noticeable increase in electron leakage. Our results also show that effective carrier injection into the active region of a deep UV light emitting diode requires *p*-type doping of the electron blocking layer.

Overall, these findings indicate the importance of accounting for alloy fluctuations in wurtzite (Al,Ga)N in order to accurately simulate the electronic, optical and carrier transport properties of (Al,Ga)N-based devices.

Acknowledgements

In an ideal world I would of wrote a list of everybody's names that I wish to thank. However, the list would have been longer than the thesis.

First and foremost, I must thank my supervisor Stefan Schulz. Without his easygoing nature and steadfast dedication to his work and students, I believe it would be safe to say I never would of made it as far as I have.

Next I must thank the staff at Tyndall, who are all very supportive. Each of them work towards the best outcome for both the research and the researcher.

I must thank all the friends I have made in Tyndall, both the old guard and the new. Without them these last few years would have been impossible. With them, everyday going into work is just another funny little adventure. Special thanks must be paid to the Photonics Theory Group, the UV LED group and the ever expanding 12 pubs crew.

I have to thank all my friends outside of Tyndall. Each of whom are unique to themselves and lead incredible lives. If the saying "You're only as good as the company you keep" is true, then I look forward towards a bright future. I must also sincerely thank my friends Tim, Katie and Fogarty for their support these last few years, and the fun we had preparing for the Cork half.

Finally, I thank my family, to whom I dedicate this thesis to. To my siblings, Christopher, Stephen and Sarah, this work is as much theirs as it is mine. I would not be here without them. Lastly, I have to thank my mother, Helen. She used to say I could be a doctor. Although I am surprised I arrived at this point, I don't think she would have been.

Chapter 1

Prologue

1.1 III-Nitrides

III-nitride-based (AlN, GaN, InN) light emitting diodes (LEDs) have seen extensive research since fundamental breakthroughs in the 1980s. At the time, researchers overcame two major challenges: poor crystalline quality of GaN films due to the large lattice mismatch to available substrates, and the difficulty of reliable *p*-type doping of GaN materials [9, 10, 11]. This soon led to the development of GaN-based blue LEDs which, when combined with a yellow emitting phosphor [12], enabled white LEDs to be produced on an industrial scale [10]. These LEDs have since achieved efficiencies surpassing that of any conventional light source [10]. In recognition of this achievement, the Royal Swedish Academy of Sciences awarding the Nobel Prize for Physics to Isamu Akasaki, Hiroshi Amano, and Shuji Nakamura "for the invention of efficient blue light emitting diodes which has enabled bright and energy-saving white light sources" in 2014 [13].

The III-N materials all possess direct band gaps (6.16 eV for AlN, 3.44 eV for GaN, 0.64 eV for InN) [14] that enable, in principle, band gap engineering from the deep-ultraviolet (UV) range up to the infrared spectrum. This is illustrated in Fig. 1.1 which shows that ideally the (In,Ga)N alloy spans from the infrared and across the visible spectrum, and (Al,Ga)N covers from UV-A ($\approx$ 400 nm) to the deep UV-C ($\approx$ 200 nm) spectrum.

While (In,Ga)N alloys have been researched for visible light emitters for many years, (Al,Ga)N has only in the last few years received a more prominent research focus. (Al,Ga)N-based materials have the potential for widespread use

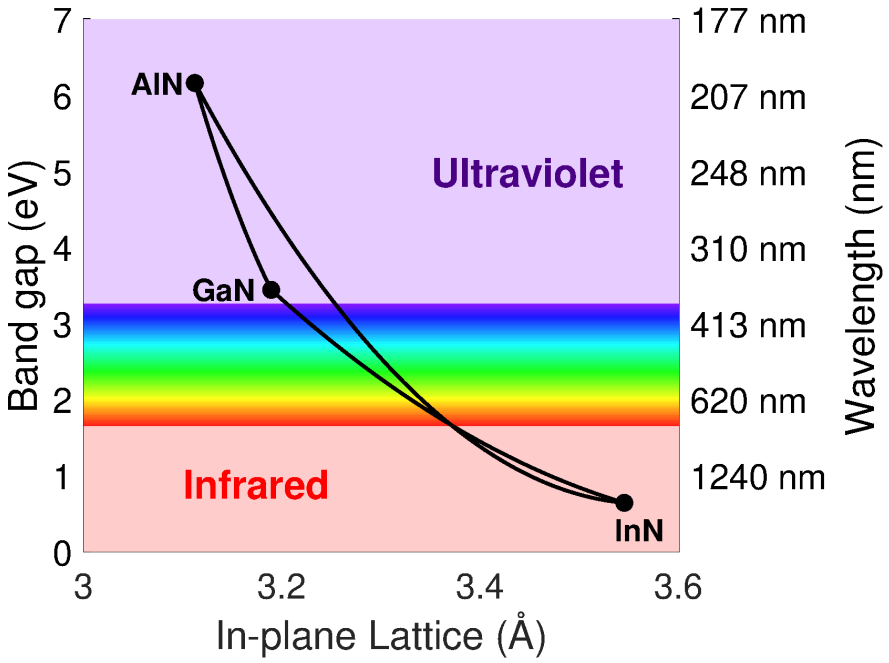


Figure 1.1: Band gap evolution of AlN, GaN and InN as a function of the in-plane lattice constants, a. The lattice constants and band gap energies of the binary materials, along with their band gap bowing parameters, are taken from Ref. [14], and the alloy band gaps are calculated using linear interpolation with bowing.

across the entire UV spectral range. A UV market analysis from YOLE in 2021 reported that the total UV light source market will have reached $\approx$ 3.5 billion USD with a compound annual growth rate of 17.8 % by 2026 with (Al,Ga)N-based UV LEDs accounting for more than half of the annual growth [15]. UV LEDs already serve a wide range of applications, and ongoing advancements in their efficiency are opening opportunities to enter new and specific markets across various industries. In the UV-A (315 nm - 400 nm) range there are applications such as UV curing, 3D printing, sensing, whitening agents and medical applications like blood gas analysis [10, 16, 17, 18]. For the UV-B (280 nm - 315 nm) range, applications such as plant lighting and phototherapy e.g. psoriasis and vitiligo are desired [16, 19, 20], while the UV-C (200 nm - 280 nm) range has attracted considerable attention for its applications of high volume water purification, waste water treatment, disinfection of medical equipment and sensing of gases (e.g. SO_2, NH_3) and biomolecules (e.g. NADH, DNA, RNA) [16, 21, 22, 23, 24, 25].

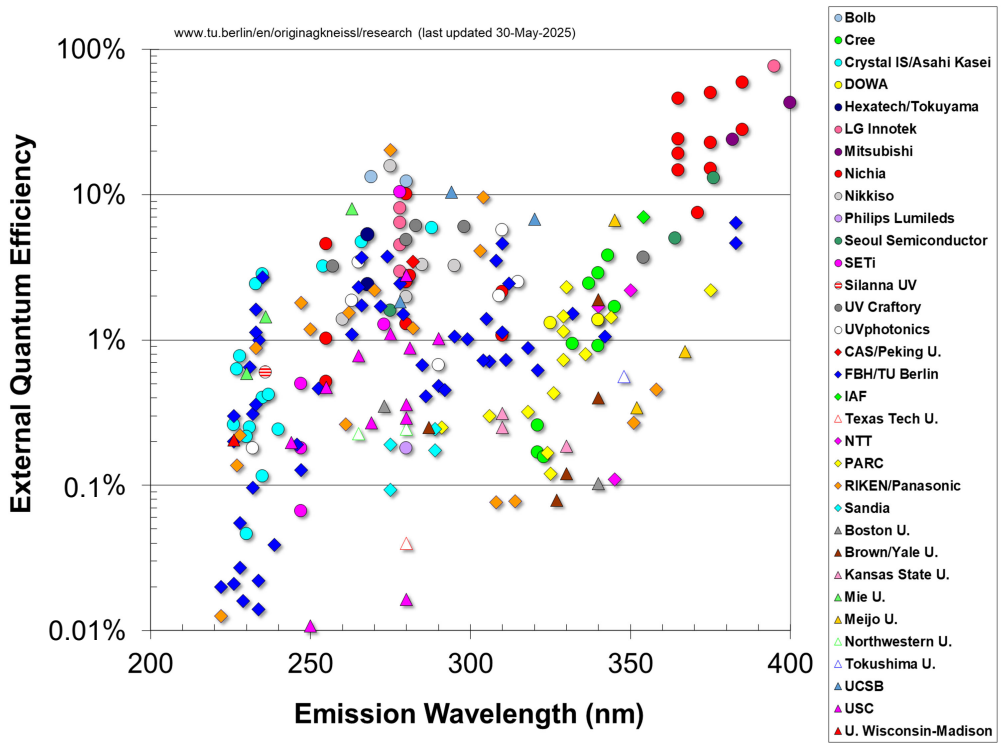


Figure 1.2: External quantum efficiency versus the emission wavelength of fabricated UV LEDs in the spectral range of 200 - 400 nm. Figure taken from https://www.tu.berlin/en/originagkneissl/research accessed 12/7/2025

1.2 UV LEDs & modelling challenges

In comparison to conventional UV light sources, such as low and medium pressure mercury lamps, UV LEDs offer significant advantages [16, 18]. LEDs are wavelength tunable and require no warm up time, allowing for rapid on/off switching, which is an important feature for sensing [16, 18]. They are electronically dimmable, exhibit no forward heat radiation and are highly temperature stable [16, 18]. In addition, UV LEDs exhibit very long operational lifetimes, are robust, compact and thus provide greater flexibility in device design and applications [16, 18]. Furthermore, they are also environmentally friendly since they do not contain any mercury and they have the potential to be significantly more efficient than mercury-based UV lamps [16, 18].

However, (Al,Ga)N-based UV LEDs still face significant limitations across the UV spectral range, with each wavelength region presenting unique challenges [16, 18]. In general, to ensure high crystalline quality, these devices are grown on either a GaN or AlN based template layer [16]. For UV-A LEDs

with emission wavelengths above 360 nm, device performance have reached excellent levels [16]. This is because the band gap of pure GaN lies in the middle of the UV-A range at ≈ 360 nm. Thus, device structures for wavelengths above 360 nm can be adapted from visible LED technology and grown on GaN templates. However, below 360 nm there is a reduction in the device efficiency, as shown in Fig. 1.2. When using GaN templates, the light extraction efficiency (LEE) is reduced due to reabsorption of the emitted photons from the (Al,Ga)N active region. While switching to an AlN template can mitigate this reabsorption due to the larger band gap, using an AlN template on a UV-A device which requires high GaN contents, has its own difficulties due to AlN's in-plane lattice mismatch of ≈ 2.4% to GaN. This gives rise to significant strain issues in the heterostructure [16]. Furthermore, in addition to problems with photon reabsorption and lattice strain, designing a low resistance ohmic *p*-type contact directly to (Al,Ga)N, especially with high Al content, is still very difficult [16].

Research efforts for the UV-B LEDs are much smaller than both the UV-A and UV-C range, most likely due to UV-B LEDs not having as many major industry driven applications in comparison to UV-A and, particularly, UV-C [16]. One of the key challenges for UV-B emitters is the high threading dislocation density (TDD) formed due to a lack of suitable substrates. The high TDD reduces the internal quantum efficiency of UV-B light emitters by introducing non-radiative recombination centres. In addition to this, UV-B devices suffer from the same limitations affecting UV LEDs more broadly, such as poor LEE and the difficulty of poor ohmic *p*-contact, further compounding the reduction in output power of these devices.

The large lattice mismatch found for UV-B (Al,Ga)N devices is, in general, not present in UV-C based devices which contain high Al contents and thus, in principle, can be grown on high quality AlN [16]. Hence, why there is an observable increase in the reported efficiencies when moving from UV-B into UV-C as shown in Fig. 1.2 at 280 nm. However, with increasing Al composition, and thus a shift to lower wavelengths, there is a noticeable steep decline in the efficiencies. Like the other UV ranges, this drop is due to a combination of material and device challenges. For example, carrier injection efficiency of these devices decreases due to an increase in electron overflow, which can be related to a reduced conduction band offset of the conventionally used AlN electron blocking layer. Furthermore, higher Al compositions have increasing difficulty with the activation of *p*-type dopants, leading to poor hole injection into the

active region [16]. In addition, in order to circumvent issues with ohmic contacts on AlN substrates, GaN layers are often introduced to serve as *p*-contact layers due to their ability to form low resistance ohmic contacts, unlike high Al containing (Al,Ga)N. While this improves the hole injection into the active region, the narrow band gap of GaN leads to high rates of UV absorption, which only becomes more severe at shorter wavelengths [10, 16]. A factor which significantly reduces LEE for UV-C LEDs. Moreover, fundamental differences in the valence band structure of AlN and GaN lead to a further reduction in the LEE by a change in the polarisation of the emitted light, from primarily out-of-plane emission at lower Al contents to predominantly in-plane emission at higher Al contents. Since UV LEDs are typically designed for top and bottom emission, this shift in polarisation results in increased internal reflection and reabsorption, further diminishing the LEE [26, 27, 28].

In order to help address these efficiency gaps, a theoretical guidance is a viable tool. However, providing such guidance is challenging as, similarly found in other III-nitride systems such as (In,Ga)N [29], alloy disorder generates strong potential fluctuations that can confine carriers within spatial regions of lower potential energy [30]. Experimental studies on (Al,Ga)N have reported carrier localisation effects [31, 32, 33]. These localisation effects have been linked to various phenomena in III-Ns, such as inhomogeneous broadening of the emission peaks and an unusual "S-shaped" temperature dependence of the photoluminescence peak energy [31, 32, 33].

In theoretical studies, the impact of alloy disorder is largely unexplored for (Al,Ga)N devices as it presents a significant challenge for several reasons. Firstly, to treat carrier localisation effects, atomistic calculations are in principle an ideal starting point. First principle approaches, such as density functional theory (DFT), can provide the required microscopic insight into the electronic structure of III-N materials and alloys, particularly for bulk systems. However, 'conventional' DFT implementations are in general limited to small supercells. For heterostructures, like quantum wells (QWs), large (in-plane and out-of-plane) supercells are required to capture random alloy disorder-induced carrier localisation effects in the growth plane, but also the barrier materials. This presents a significant, basically unfeasible, computational challenge [34, 35].

Secondly, standard and widely available one dimensional (1D) multi-band $\mathbf{k} \cdot \mathbf{p}$ simulations of (Al,Ga)N describe the alloy by averaged material parameters, thereby neglecting local fluctuations in the alloy content [36, 37]. Full device

simulations are typically limited to 1D, as capturing alloy disorder accurately requires computationally intensive three dimensional (3D) calculations. Modified continuum-based 1D models can incorporate alloy disorder effects through an inhomogeneous broadening parameter, this parameter is generally treated as a fitting variable, calibrated to experimental data [38, 39]. However, it will not reflect any spatial inhomogeneities in the potential energy landscape and can therefore miss important features such as percolation pathways, an effect shown to be important for carrier transport in (In,Ga)N and (Al,Ga)N systems [40, 41].

As a result, 1D models often tend to overestimate the turn-on voltage for these devices when the "standard" material parameters are used. To better fit experimental data, these 1D simulations usually reduce the intrinsic polarisation fields by 50% [30, 39], although, the justification for this significant reduction is not clear [30].

In contrast, theoretical work by Li *et al.* [42] for (In,Ga)N-based devices demonstrated that including alloy fluctuations on a 3D potential landscape in drift-diffusion simulations significantly improved agreement with experimental current-voltage curves. This modified continuum-based model has also been used to investigate the impact of alloy fluctuations on carrier diffusion, showing the compositional fluctuations reduce the lateral diffusion lengths and enhanced radiative recombination [43]. All this underscore the necessity of including alloy fluctuations when modelling these materials and related devices. This modified continuum-based approach which allows for local fluctuations in alloy content in a 3D simulation is treated on a single band model [42, 44, 45, 46]. While this is suitable for (In,Ga)N or (Al,Ga)N UV LEDs with high GaN content, it is not the case for high Al content devices where the valence band ordering changes. Significant differences in the GaN and AlN valence band ordering, which gives rise to the switching in the polarisation properties of the emitted light, as already briefly discussed above, requires the inclusion of multiple valence bands in electronic structure calculations.

In recent years, empirical tight-binding models have demonstrated that they can capture carrier localisation effects accurately on an atomistic level while at the same time allowing for the treatment of very large supercells [34]. In this thesis, we have developed an empirical tight-binding model to describe the electronic and optical properties for (Al,Ga)N-based materials. Furthermore, we extend this approach to build a multiscale simulation framework that provides insight

into fundamental properties that also extends to the carrier transport dynamics for (Al,Ga)N-based devices.

1.3 Thesis Overview

Chapter 1 introduces the fundamental background on the wurtzite crystal structure, key material properties of III-nitrides, and LED device design. In Chapter 2 an overview is given on the theoretical approaches used to model these materials, heterostructures and devices. We introduce both atomistic and continuum based models to describe their electronic structure. Building on this, we pay particular attention on generating an atomistic framework that includes the effect of strain and polarisation fields on a microscopic scale to gain insight into the electronic and optical properties of (Al,Ga)N systems with alloy disorder. Furthermore, a detailed description of how an energy landscape is extracted from tight-binding models and connected to a drift-diffusion model is presented, allowing for a quantum corrected multiscale simulation of carrier transport through the use of localisation landscape theory, while accounting for alloy fluctuations.

Chapter 3 employs the atomistic tight-binding model to investigate the influence alloy disorder has on the electronic structure of (Al,Ga)N QWs, with Al compositions spanning from the UV-A to deep UV-C range. We find that alloy disorder induces carrier localisation effects over the entire composition range, with significant hole localisation occurring and the potential for electron localisation to occur in high Al-containing QWs.

Chapter 4 utilises the tight-binding calculations on two UV-C (Al,Ga)N QWs, $Al_{0.48}Ga_{0.52}N/Al_{0.63}Ga_{0.37}N$ and $Al_{0.75}Ga_{0.25}N/Al_{0.90}Ga_{0.10}N$ systems, to gain insight into the degree of optical polarisation, capturing the effects of carrier localisation and the connected valence band mixing. In a first step, we examine how carrier density screening influences Urbach tail energies for (Al,Ga)N QWs, a phenomenon directly linked to carrier localisation. We then pay special attention to how carrier density screening effects the valence band ordering across QWs of varying widths. Overall, it was found that for the narrow QWs, the Urbach energies remain low and relatively insensitive to carrier density, indicating carrier localisation is influenced by the well width rather than screening effects. In contrast, the wider QWs exhibit higher Urbach tail energies at low carrier densities. These Urbach energies were found to decrease with

increasing carrier density to similar or lower Urbach energies of the narrow QWs. These trends were attributed to the stronger built-in field potential drop across a wider QW. Carrier density screening reduced this large potential drop and consequently the carrier localisation effects. In addition, the higher Urbach energies helped to delay the optical polarisation switch from out-of-plane emission (required for high LEE) to in-plane emission (detrimental LEE), with our results suggesting the wider wells are preferable for improving the degree of optical polarisation.

Chapter 5 focuses on the carrier transport and recombination processes in deep UV LEDs. First, a comparison of a single-(Al,Ga)N QW employing simulations that included and neglected alloy fluctuations were performed using our multiscale drift-diffusion framework. Here, our calculation showed the alloy disorder enhanced the radiative and non-radiative Auger-Meitner recombination rates. Alloy disorder also generated percolative pathways for easier carrier injection into the active region, but with the added potential effect of carrier leakage. We then go on to investigate a simulation of a multi-QW deep UV LED where special attention is paid to the carrier injection and recombination efficiencies observed for different hole activation energies. There it was found that p-doping the electron blocking layer significantly improved the hole injection into the active region, thereby suppressing electron overflow, whereas the radiative recombination efficiency stayed relatively high and consistent between different activation energies. These findings further highlight that the limiting factor of the internal quantum efficiency for DUV-LEDs is related to the current injection efficiency. While we have not considered the LEE in our calculations, we can extrapolate the LEE values when combining our data with literature EQE data. In doing so we find that the most promising way to substantially improve the EQE is by improving the LEE for deep UV-C LEDs.

Finally a summary and an outlook for future topics of research are discussed in Chapter 7.

Chapter 2

Introduction

In the prologue, we provided a brief overview on the properties of III-N materials, their alloys, and heterostructures, which can be used to design UV light emitting devices. We have emphasised the importance of device simulation in guiding the development of efficient emitters, while also acknowledging the challenges to such modelling approaches. Before having an in-depth discussion of the electronic, optical and carrier transport properties of this material system for use in LEDs, it is essential to first understand the fundamental characteristics of their crystal structure, an aspect which will significantly influence their behaviour.

The III-N systems exhibit different properties than other III-V materials, with some of these tightly linked to the crystal structure. Therefore, we first must discuss the wurtzite crystal structure commonly adopted by III-N materials (Sec. 2.1), followed by a discussion on how this structure shapes the electronic properties (Sec. 2.2). Given the importance for UV emitters and our aim to study III-N-based LEDs, a brief overview of the main concepts underlying a LED structure will be provided (Sec. 2.3 and Sec. 2.4), along with a definition of LED device efficiencies (Sec. 2.5). We shall begin by exploring the wurtzite crystal structure the III-nitrides tend to adopt.

2.1 Wurtzite crystal structure

A crystalline structure consists of a 3D periodic arrangement of the atoms. The overall crystal structure can be determined and described using the basic periodic repetition of the lattice points known as the *unit cell* [47]. There are

seven crystal classes (cubic, hexagonal, tetragonal, orthorhombic, monoclinic, trigonal and triclinic) and four different 3D unit cells [47]: 1) primitive unit cell which has a lattice point at each corner and forms a minimum volume, 2) body-centred unit cell which has lattice points at each corner and one at the centre of the cell, 3) face-centred which has a lattice point at each corner and one at the centre of each face, 4) base-centred unit cell which has a lattice point at each corner and one pair of opposite faces. Combining these four types of lattices with seven possible unit cell produces 14 Bravais lattices. It is important to note that these lattice points represent equivalent positions in the crystal structure and thus can be occupied by either a single atom, a group of atoms, or a complex ion.

Translations from a lattice site that result in an indistinguishable lattice are defined by the basis vectors, $\mathbf{a}_{1,2,3}$, where every point on the lattice can be described by the direct lattice vector, $\mathbf{R}$ [48]

$$\mathbf{R} = n_1\mathbf{a}_1 + n_2\mathbf{a}_2 + n_3\mathbf{a}_3 \ , \tag{2.1}$$

where n_i are integers.

Gathering information on crystallographic planes, such as their lattice constants, can be extracted from experiments like diffraction measurements [49]. These planes are categorised by so-called Miller indices [47, 48]. The Miller indices are three integers (hkl) which are the reciprocal values of the axis intersections of a crystallographic plane with lattice vectors in the direct lattice:

$$h = \frac{1}{n_1}, \quad k = \frac{1}{n_2}, \quad l = \frac{1}{n_3} \ . \tag{2.2}$$

Often for the hexagonal wurtzite structure, four Miller indices are used, $(hkil)$, one can define three basis vectors in the $x-y$ plane ($\mathbf{a}_1$, $\mathbf{a}_2$, $\mathbf{a}_3$) and another in the z-direction ($\mathbf{a}_4$) rather than the *conventional* three. The angle between the adjacent $x-y$ plane $\mathbf{a}_i$'s is 120°, thus the sum of h, k, and i of a plane equal zero and reflects the threefold symmetry of the in-plane lattice [47].

The III-V materials can crystallise in different phases depending on the specific compound and growth conditions [47]. III-V materials such as GaAs,

preferentially adopt a zinc-blende phase [47]. In contrast, the III-N materials preferred phase is the hexagonal wurtzite crystal, which is thermodynamically more stable [12, 47, 50]. This is due to the relatively large ionicity factor of the cations (III^+) and anions (V^-) which, in order to minimise energy, align along the z-axis by the strong Coulomb attraction force and adopt a so called AB hexagonal crystal stacking phase [47].

The *ideal* wurtzite unit cell, as shown in Fig. 2.1, has two lattice constants, a (along the hexagonal side) and c (repeat distance along the z direction), with a C_{6v} symmetry [50]. The wurtzite crystal consists of two hexagonal, close packed sublattices along the c-axis, offset by $\frac{5}{8}c$. Each atom is tetrahedrally bonded to 4 other nearest-neighbours of the opposite charge i.e. an anion is bonded to 4 cations and vice versa. This interatomic distance between the anion and cation in the basic unit is described by the internal parameter u which is defined as the anion-cation bond length along the c-axis divided by the c lattice parameter [50]. For an ideal wurtzite structure the axial ratio is $\frac{c}{a} = \sqrt{\frac{8}{3}} = 1.633$ and $u = \frac{3}{8} = 0.375$ [50]. The hexagonal unit cell contains two anions and two cations with position vectors of

$$\mathbf{\Delta}_1 = (0, 0, 0) \ , \tag{2.3a}$$

$$\mathbf{\Delta}_2 = \left(\frac{a}{\sqrt{3}}, 0, \frac{c}{2}\right) \ , \tag{2.3b}$$

$$\mathbf{\Delta}_3 = \left(0, 0, \frac{3c}{8}\right) \ , \tag{2.3c}$$

$$\mathbf{\Delta}_4 = \left(\frac{a}{\sqrt{3}}, 0, \frac{7c}{8}\right) \ , \tag{2.3d}$$

with $\mathbf{\Delta}_{1,2}$ and $\mathbf{\Delta}_{3,4}$ being the cations and anions, respectively [51, 52].

The arrangement of the atoms exists at every point in the hexagonal Bravais lattice and are defined in terms of the primitive lattice vectors, where [51, 52]

$$\mathbf{a}_1 = \left(\frac{\sqrt{3}a}{2}, \frac{-a}{2}, 0\right) \ , \tag{2.4a}$$

$$\mathbf{a}_2 = (0, a, 0) \ , \tag{2.4b}$$

$$\mathbf{a}_3 = (0, 0, c). \tag{2.4c}$$

The growth direction for commercially available III-N LEDs is largely the c-direction. The III-N materials can be grown on multiple crystallographic planes, such as $(1\bar{1}00)$ plane, but current difficulties on reducing dislocation

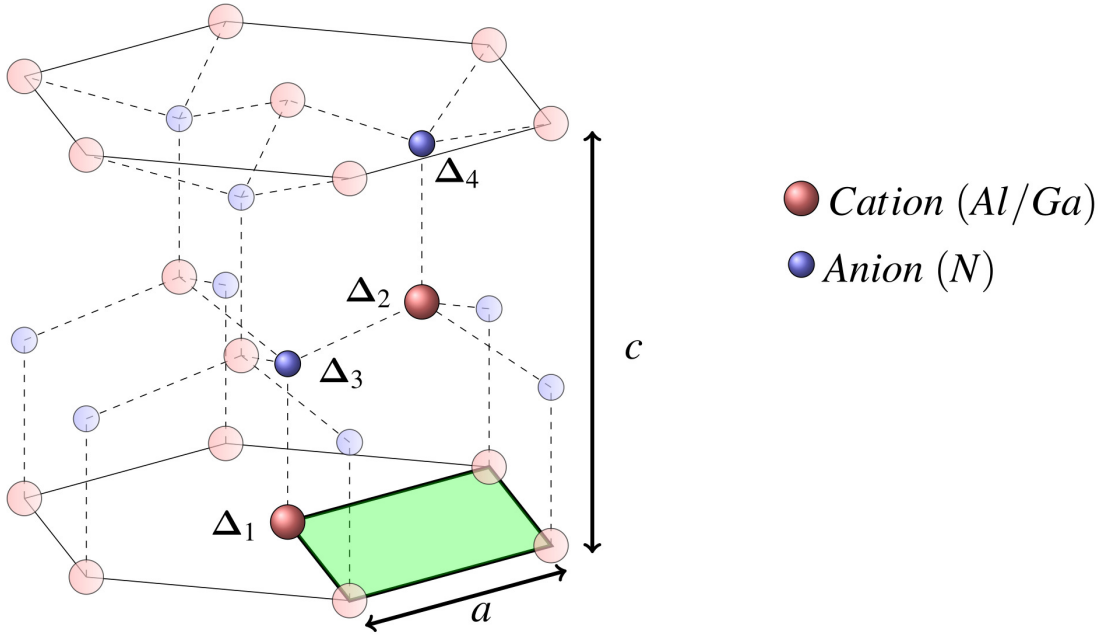


Figure 2.1: Hexagonal cell of the wurtzite crystal structure. The cations are in red and the anions are in blue. The lattice constant a (in-plane) and c (out-of-plane) are shown. The green plane highlights the hexagonal close-packed structure with the four basis atoms labelled $\mathbf{\Delta}_1$, $\mathbf{\Delta}_2$, $\mathbf{\Delta}_3$ and $\mathbf{\Delta}_4$. The faded atoms represent periodic replicas of the unit cell ions.

densities are still prominent [53]. For this thesis we are interested in wurtzite structures grown in the [0001] direction along the c-axis and thus define the c-plane as the growth plane and label this sometimes as the in-plane.

As previously mentioned, physical properties of a crystal structure can be extracted from experimental measurements, such as X-ray diffraction [49], which utilise the reciprocal lattice space to describe the spatial frequency of points in the direct lattice. Therefore, operating in reciprocal space provides fundamental insight into material properties, such as the lattice constants. The reciprocal lattice is also useful for describing the electronic properties of the III-nitride material because, like the direct lattice, the reciprocal lattice can be divided into primitive cells with primitive reciprocal lattice vectors. The primitive cell in the reciprocal lattice is referred to as the first Brillouin zone (FBZ) [54] and is depicted in Fig. 2.2 for a wurtzite system. It is particularly useful because it provides a compact and unique representation of the crystal's periodicity in reciprocal space, avoiding repetition of equivalent lattice information [47, 54]. The reciprocal lattice vector, $\mathbf{G}$, is the set of all wave vectors which describe waves with the same periodicity as the given Bravais lattice and therefore satisfy the equation [47, 54]

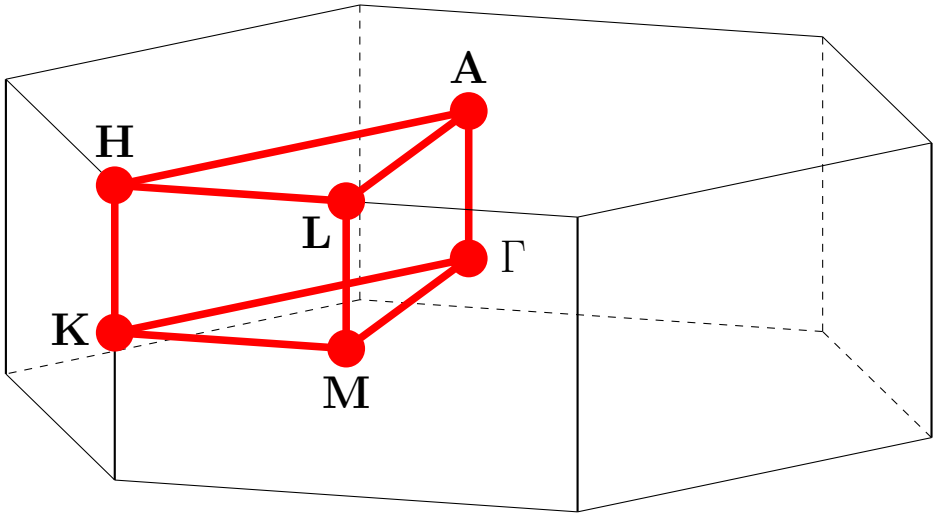


Figure 2.2: Schematic of the first Brillouin zone for a hexagonal lattice. Highlighted in red are points of high symmetry with the Γ-point indicating $\mathbf{k} = \mathbf{0}$.

$$e^{i\mathbf{G}\cdot\mathbf{R}} = 1 \quad \therefore \quad \mathbf{G}_j \cdot \mathbf{a}_j = 2\pi m_j \ , \tag{2.5}$$

where $\mathbf{R}$ is defined in eq. (2.1) and m_j are integers. The reciprocal lattice vector $\mathbf{G}$ can be expressed by the primitive reciprocal lattice vectors:

$$\mathbf{G} = m_1\mathbf{b}_1 + m_2\mathbf{b}_2 + m_3\mathbf{b}_3 \ , \tag{2.6}$$

which in 3D are determined by [47, 54]

$$\mathbf{b}_i = 2\pi \frac{\mathbf{a}_j \times \mathbf{a}_k}{\mathbf{a}_i \cdot (\mathbf{a}_j \times \mathbf{a}_k)}. \tag{2.7}$$

For wurtzite, the FBZ also adopts a hexagonal structure with the reciprocal lattice vectors being

$$\mathbf{b}_1 = \frac{4\pi}{\sqrt{3}a}(1, 0, 0) \ , \tag{2.8a}$$

$$\mathbf{b}_2 = \frac{2\pi}{a}(\frac{1}{\sqrt{3}}, 1, 0) \ , \tag{2.8b}$$

$$\mathbf{b}_3 = \frac{2\pi}{c}(0, 0, 1) \ . \tag{2.8c}$$

With this now defined, we are equipped to discuss the electronic band structure.

2.2 Electronic band structure

In order to study the electronic structure of an ideal crystal we first must solve the time-independent Schrödinger equation. This will in principle allow us to determine the energy levels and the wave functions of the electrons. Here the full time-independent Hamiltonian takes into account the kinetic energy terms for all the electrons (T_e) and nuclei (T_n) in the system which depend on the electron, m, and nuclei, M, mass. V_{e-n}, V_{e-e} and V_{n-n} are the potential energy terms which include the attractive electron-nucleus interaction, the repulsive electron-electron interaction and the repulsive nucleus-nucleus interactions [55]

$$H = \underbrace{-\frac{\hbar^2}{2m}\sum_{i=1}^{n}\nabla_i^2}_{T_e} \underbrace{-\frac{\hbar^2}{2M}\sum_{I=1}^{N}\nabla_I^2}_{T_n} \underbrace{-\sum_{i=1}^{n}\sum_{I=1}^{N}\frac{1}{4\pi\epsilon_0}\frac{Z_I e^2}{|\mathbf{r}_i-\mathbf{R}_I|}}_{V_{e-n}} + \underbrace{\frac{1}{2}\sum_{i}^{n}\sum_{j\neq i}^{n}\frac{1}{4\pi\epsilon_0}\frac{e^2}{|\mathbf{r}_i-\mathbf{r}_j|}}_{V_{e-e}} + \underbrace{\frac{1}{2}\sum_{I}^{N}\sum_{J\neq I}^{N}\frac{1}{4\pi\epsilon_0}\frac{Z_I Z_J e^2}{|\mathbf{R}_I-\mathbf{R}_J|}}_{V_{n-n}} . \tag{2.9}$$

Z_I (Z_J) is the proton number for nucleus I (J). $\mathbf{R}_I$ and $\mathbf{r}_i$ describe the positions of the nuclei and electrons, respectively. Employing the widely used Born-Oppenheimer approximation [56], we are able to decouple the kinetic energy of the nuclei from the electrons due to the fact that the mass of the nuclei is much greater than the mass of the electrons ($M >> m$). Therefore, the kinetic energy of the nuclei is negligible compared to the electrons. This reduces the Schrödinger equation to

$$H = T_e + V_{e-n} + V_{e-e} + V_{n-n} \ . \tag{2.10}$$

This equation is still very complex, particularly due to V_{e-e}, as the energy of the electrons depend on the positions of all the other electrons. To mitigate this, we utilise the single-particle approximation where we assume that the particle is moving through an effective potential generated by all other electrons and nuclei in the system [57]. This allows us to rewrite the Hamiltonian in

terms of the electron kinetic energy operator and an effective potential where the total energy of the system is the sum of the energies of the single-particle states. The interaction of the single-particle state with the other electrons is included in the effective potential term, V_{eff}, leaving us with the single-particle time-independent Schrödinger equation

$$H\psi(\mathbf{r}) = \frac{-\hbar^2}{2m}\nabla^2\psi(\mathbf{r}) + V_{\text{eff}}(\mathbf{r})\psi(\mathbf{r}) = E\psi(\mathbf{r}) \ . \tag{2.11}$$

where ψ is the single-particle wave function.

Even with this *simplified* equation, solving the Schrödinger equation over the length scale of the crystal is still too challenging due to the large number of atoms in the system, which are still in V_{eff}. However, due to the underlying symmetry of the crystal structure, and the Born-Oppenheimer approximation stating that the nuclei cannot move as fast as the electrons, one is left with an ordered array of nuclei. Meaning the effective potential above will have the same periodicity as the crystal lattice

$$V_{\text{eff}}(\mathbf{r} + \mathbf{R}) = V_{\text{eff}}(\mathbf{r}) \ . \tag{2.12}$$

Where $\mathbf{r}$ denotes the position in real space and $\mathbf{R}$ is a lattice vector, defined by eq. (2.1). With this assumption for a perfect crystalline material we utilise Bloch's theorem [48, 58] which states that the electronic wave function can be expressed as a product of a plane wave, $e^{i\mathbf{k}\cdot\mathbf{r}}$, with wave vector $\mathbf{k}$ (which is related to the crystal momentum, $\mathbf{p} = \hbar\mathbf{k}$) and a function (Bloch factor) with the same periodicity as the crystal lattice, $u_{\mathbf{k}}(\mathbf{r}) = u_{\mathbf{k}}(\mathbf{r} + \mathbf{R})$:

$$\psi_{\mathbf{k}}(\mathbf{r}) = e^{i\mathbf{k}\cdot\mathbf{r}}u_{\mathbf{k}}(\mathbf{r}) \ . \tag{2.13}$$

Here, for a given $\mathbf{k}$

$$\psi_{\mathbf{k}}(\mathbf{r}+\mathbf{R}) = e^{i\mathbf{k}\cdot(\mathbf{r}+\mathbf{R})}u_{\mathbf{k}}(\mathbf{r}+\mathbf{R}) = e^{i\mathbf{k}\cdot\mathbf{R}}(e^{i\mathbf{k}\cdot\mathbf{r}}u_{\mathbf{k}}(\mathbf{r})) \tag{2.14}$$

$$\psi_{\mathbf{k}}(\mathbf{r}+\mathbf{R}) = e^{i\mathbf{k}\cdot\mathbf{R}}\psi_{\mathbf{k}}(\mathbf{r}). \tag{2.15}$$

Thus, the electronic wave function is periodic with the periodicity of the crystal lattice up to a phase factor of $e^{i\mathbf{k}\cdot\mathbf{R}}$. From Bloch's theorem, for each $\mathbf{k}$ there is a discrete set of eigenstates and eigenvalues when solving the Schrödinger equation, eq. (2.11). To illustrate the implications of Bloch's theorem more clearly, we consider a 1D periodic lattice with a unit cell of length L, following Ref. [59]. In this case the wave function can be written as

$$\psi_k(x) = e^{ikx}u_k(x), \tag{2.16}$$

with $u_k(x) = u_k(x+L)$. We introduce the reciprocal lattice vector (in this case a 1D version), $G_m = \frac{2\pi m}{L}$ where m is an integer. When we multiply the single-particle electronic wave function by a plane wave with a periodicity of the lattice, $e^{i2\pi mx/L}$, and its complex conjugate, we find

$$\psi_k(x) = e^{ikx}e^{i\frac{2\pi mx}{L}}e^{-i\frac{2\pi mx}{L}}u_k(x) \tag{2.17}$$

$$= e^{i(k+\frac{2\pi m}{L})x}\left(e^{-i\frac{2\pi mx}{L}}u_k(x)\right). \tag{2.18}$$

Therefore, the term $e^{-iG_mx}u_k(x)$ also has the periodicity of the lattice and thus, the wave function properties, ψ_k, are the same at k and $k+G_m$. Furthermore, the energy, $E(k)$, at a given k point in reciprocal space are also equal at $k+G_m$ i.e. $E(k) = E(k+G_m)$. This allows us to restrict calculations to the interval of $[\frac{-\pi}{L}, \frac{\pi}{L}]$ which correspond to the FBZ. This is known as the reduced zone scheme [59].

For each $\mathbf{k}$ there is a discrete set of n eigenstates and corresponding eigenvalues, $E_n(\mathbf{k})$. The variations of these energy levels with $\mathbf{k}$ are closely spaced in a bulk system and form so-called energy bands. Collectively, the set of all such bands give rise to the "electronic band structure" of a material. A 3D system in reciprocal space with different atomic arrangements, depending on the crystal

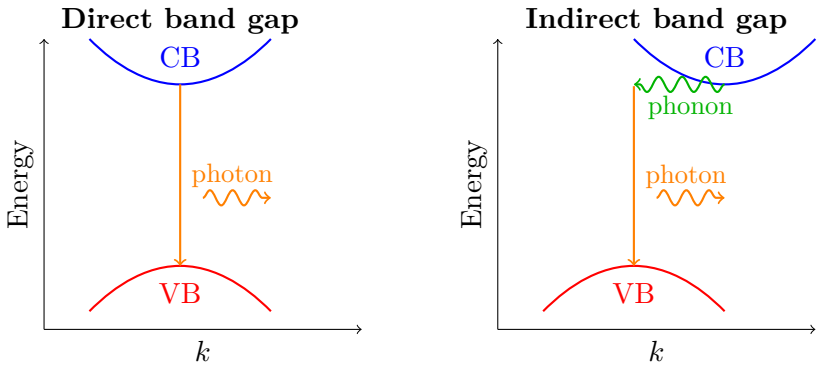


Figure 2.3: Schematic of light emission in a direct (left) and indirect (right) band gap material. In direct band gaps, a vertical transition from the conduction band (CB) and valence band (VB) emits a photon. In indirect band gaps, a phonon assists the transition to conserve momentum (k).

lattice structure, makes plotting these band structures significantly more complex. Therefore, one selects points of "high symmetry" in the FBZ to visualise the 3D band structure of a real crystal. An example of these points for a hexagonal Bravais lattice are Γ, A, L, M, H, K and is shown in Fig. 2.2 and Ref. [51].

For wurtzite III-nitrides (AlN, GaN, InN), all materials exhibit their conduction band minimum and valence band maximum at the Γ point [60] which lies at the centre of the FBZ, $\mathbf{k} = (0,0,0)$. Materials that have conduction band minimum and valence band maximum at the same point in the FBZ are called direct band gap semiconductors. Such semiconductors are ideal candidates for light emitting devices.

Since photons carry negligible momentum, vertical transitions are highly efficient for light emission. This is because in direct band gap semiconductors, the initial k_i and final k_f states are at the same **k**-point ($k_i \approx k_f$), momentum is conserved and the transition can occur readily. The excess energy released during an optical transition between the bands is emitted as a photon. In contrast, indirect band gaps require a phonon to conserve momentum, as $k_i \neq k_f$, making radiative recombination less probable [47]. A schematic illustration of light emission of a direct and indirect band gap is shown in Fig. 2.3.

While the emission wavelength is determined by the band gap energy, other factors also influence the optical transitions. In particular, the polarisation of emitted or absorbed light also plays a key role. In the case of III-N materials, this polarisation is tightly linked to the structure of the valence band at the Γ

point, where the direct band gap occurs [61, 62].

2.2.1 Degree of optical polarisation

For the wurtzite crystal, the conduction band edge at the centre of the Brillouin zone is mostly s-like, while the valence band states at $\mathbf{k} = \mathbf{0}$ are p_x, p_y, p_z-like in character. The degeneracy of the p-states is broken due to the anisotropy between the a- and c-axis introducing the crystal field splitting energy, Δ_{cf} [63]. This splits the valence bands into a non-degenerate state (p_z) and a double degenerate state (p_x, p_y) in the absence of spin-orbit coupling (SOC). The inclusion of the SOC further lifts the degeneracy of the p_x- and p_y-states leading to a three edge structure in the vicinity of the Γ point for the valence band [61, 62, 63]. In this thesis, we denote the three highest valence bands at the Γ point as A-, B-, and C-bands. While their orbital character can in general be associated to be p_z (C) and $p_{x,y}$-like (A and B) in character, the weak SOC effect in nitrides can lead to band mixing effects changing the orbital character. The energy ordering of these bands is different depending on the material: in GaN, the A- and B-bands form the valence band edge at Γ, while in AlN, the C-band is highest in energy.

Fundamental differences in the electronic band structures of AlN and GaN [61, 62, 64] stem from the magnitude and sign of the crystal field splitting energy. For GaN, values of +9 to +38 meV have been reported in the literature, while for AlN much larger and *negative* numbers, ranging from −169 meV up to −295 meV, are found [64, 65, 66, 67]. This difference in the sign of Δ_{cf} leads to a different ordering of the valence bands in GaN when compared to AlN with a schematic illustration shown in Fig. 2.4.

The topmost valence band in AlN is mainly p_z-like in character [62, 68]. This means that the band is a superposition of atomic-like p_z basis states, which are oriented along the wurtzite c-axis. As a consequence, emission processes involving the (s-like) conduction band and this p_z-like valence band result in transverse magnetic (TM) polarised light emission [16, 69, 70, 71, 72] where the light is polarised along the c-axis. Due to the opposite sign of Δ_{cf} in GaN, when compared to AlN, the topmost valence band in GaN is a linear combination of p_x- and p_y-like states. So in the case of GaN when only the top most valence band is involved in the light emission process, transverse electric (TE) polarised emission occurs where light is polarised perpendicular to the c-axis [16, 69, 70, 71, 72]. This means in (Al,Ga)N alloys the optical

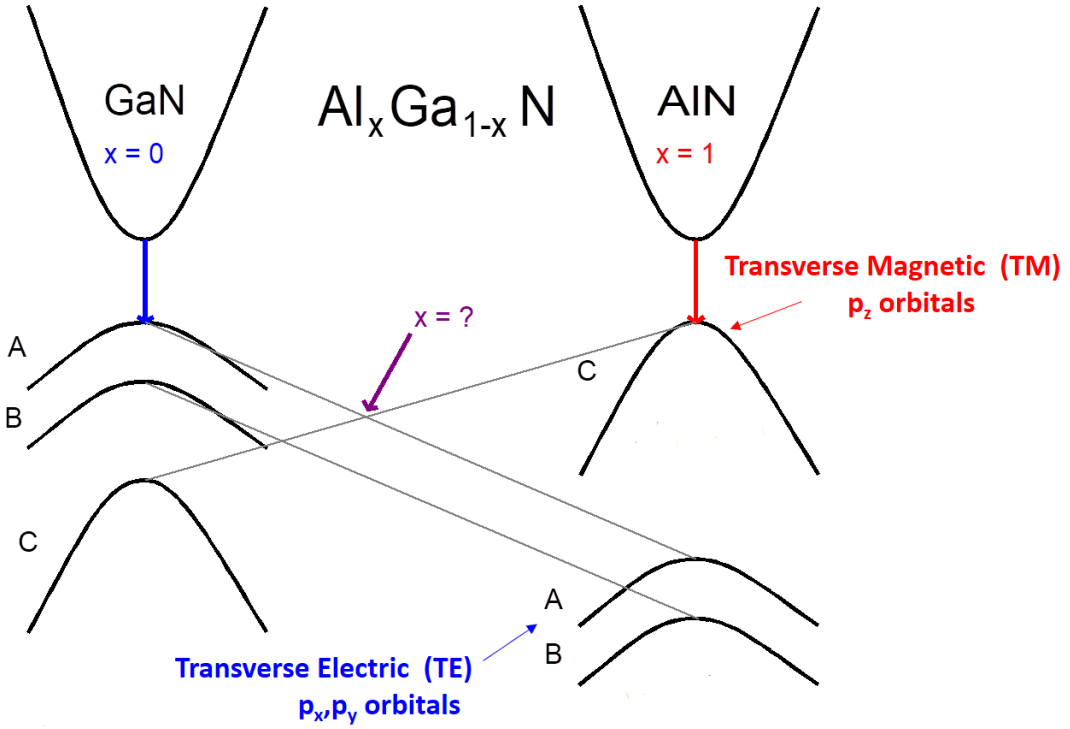


Figure 2.4: Schematic illustration of the band edges at the Γ point for GaN and AlN. The A, B and C bands denote the p_x-, p_y- and p_z-orbitals, respectively. The grey lines indicate that at a certain Al composition x in an $Al_xGa_{1-x}N$ alloy there will be a crossing of the bands.

polarisation characteristics of the emitted light will switch from, for instance, TE to TM polarised emission at a certain Al content. Since most of the conventional (Al,Ga)N LEDs are designed to be bottom or top emitting devices, TE polarisation light emission is essential for efficient light extraction [71, 72].

It should be noted that for heterostructures, such as quantum wells (QW), in addition to the crystal field splitting energy, effects such as quantum confinement and strain will significantly affect the valence band ordering and thus the degree of optical polarisation (DOP). Such an analysis will be discussed in Chapter 5. These effects indicate that by introducing heterostructures one is capable of tailoring and manipulating the electronic and optical properties for (Al,Ga)N based-light emitters.

2.3 Heterostructures

For this thesis, the heterostructure of a quantum well is of particular interest because of its wide use in operating LEDs. A QW is generally composed of two

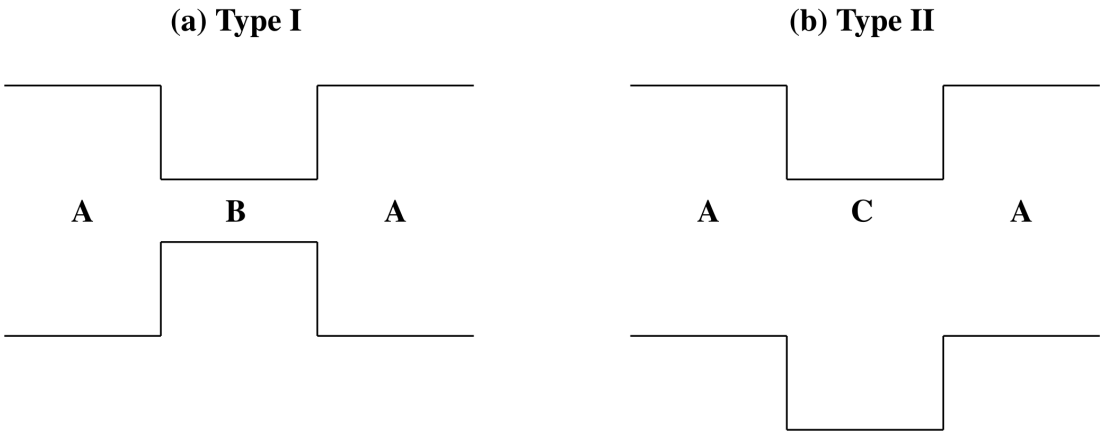


Figure 2.5: Schematic of a double heterostructure with a (a) type I band alignment where the carriers are confined in both the conduction and valence band in material **B**, and (b) a type II band offset where only one band confines carriers in the region of material **C** (in this example, the conduction band).

materials with different band gaps. These heterostructures (or double heterostructures) can be classified by their band alignment i.e. type I or type II [47]. A type I band alignment, as illustrated in Fig. 2.5 (a), shows that, in this example, material **B** which has a smaller band gap is embedded in material **A** which has a larger band gap. Thus, both the electrons and holes will be confined in material **B**. A type II heterostructure, shown in Fig 2.5 (b), confines only one type of carrier within material **C** due to its band alignment, in this example the electrons. This band alignment will depend on the materials band gap and valence band offset which can be determined experimentally or theoretically [61, 65, 73]. For an LED, a type I band alignment is the ideal alignment because the confinement in the same spatial region lead to good wave function overlap of the electrons and holes, resulting in a very high rate of radiative recombination. A schematic of this can be seen in Fig. 2.6. In a type I QW, the confinement of electrons and holes lead to discrete energy levels, and by adjusting or controlling factors, such as the QW width, one can influence the eigenenergy and thus the emission wavelength [74]. Incorporating a QW into an optoelectronic device enhances the radiative recombination efficiency, as the quantum confinement increases the overlap between the electron and hole wave functions.

Experimentally, such heterostructures and related devices are typically realised by growing, for example, (Al,Ga)N-based layers with varying Al compositions via methods such as metalorganic vapour phase epitaxy, metalorganic chemical vapour deposition or molecular beam epitaxy [18, 31, 32]. However, growing

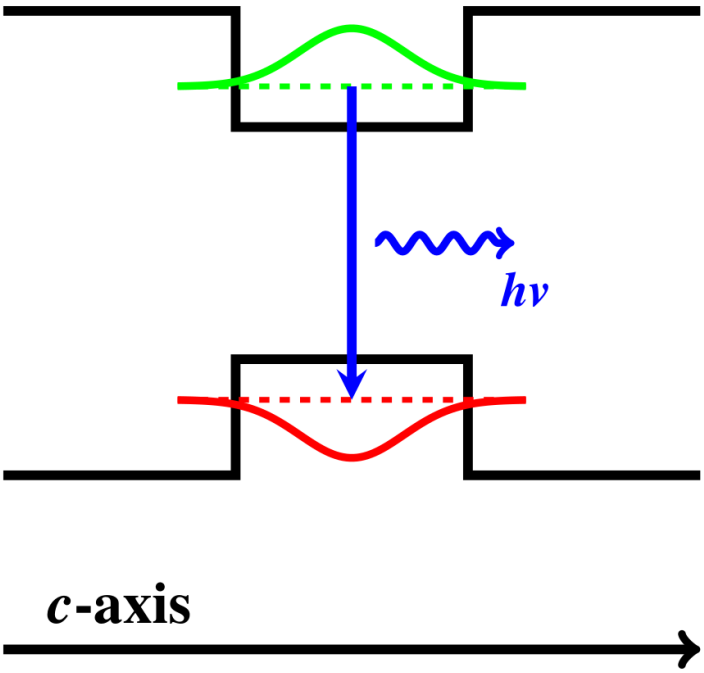


Figure 2.6: Schematic of a quantum well (QW) bandstructure. The inclusion of a QW confines the electron (green) and hole (red) wave functions within the region of lower band gap energy. This increases the wave function overlap and allows efficient photon emission (hv) of a lower energy than the barrier material. Without the QW there would be poor wave function overlap and thus inefficient recombination.

material **A** onto material **B** can lead to addition effects, such as strain in the heterostructure, as material **A** and **B** often differ not only in band gap but also by lattice constants. To minimise the elastic energy, the crystal expands/compresses along the growth direction. This strain alters the atomic bonding environment, leading to a deformation of the axial c/a ratio distorting the 'ideal' tetrahedral bond, and thus modifies the electronic structure [66, 75, 76]. In III-V materials it is shown that compressive hydrostatic strain causes the energy band gap to increase, with the conduction band energy increasing and the valence band energy lowering [77]. For GaN and AlN the a lattice constants differ by approximately 2.4% [14]. This lattice mismatch will lead to strain effects in a heterostructure, for example, an $Al_xGa_{1-x}N$ QW embedded in an $Al_yGa_{1-y}N$ barrier where $y > x$, will undergo biaxial compressive strain.

This strain can be described as a second rank tensor,

$$\varepsilon = \begin{pmatrix} \varepsilon_{xx} & \varepsilon_{xy} & \varepsilon_{xz} \\ \varepsilon_{yx} & \varepsilon_{yy} & \varepsilon_{yz} \\ \varepsilon_{zx} & \varepsilon_{zy} & \varepsilon_{zz} \end{pmatrix}, \tag{2.19}$$

where the ij^{th} component describes the relative change in position along the i-direction due to a deformation along the j-direction. It is shown in Ref. [78] that through linear elasticity theory, the strain tensor is symmetric i.e. ε_{xy}=ε_{yx}, ε_{xz}=ε_{zx} and ε_{yz}=ε_{zy}. Therefore, this is often written in Voigt notation,

$$\varepsilon = \begin{pmatrix} \varepsilon_1 & \varepsilon_2 & \varepsilon_3 & \varepsilon_4 & \varepsilon_5 & \varepsilon_6 \end{pmatrix}^T, \tag{2.20}$$

where $\varepsilon_{xx} = \varepsilon_1$, $\varepsilon_{yy} = \varepsilon_2$, $\varepsilon_{zz} = \varepsilon_3$, $2\varepsilon_{yz} = \varepsilon_4$, $2\varepsilon_{xz} = \varepsilon_5$, and $2\varepsilon_{xy} = \varepsilon_6$.

For a QW heterostructure that is strained to the barrier or substrate material, the in-plane a lattice constant is forced to match the in-plane of the barrier/substrate. Whereas the QW is allowed to relax along the c-direction minimising the elastic energy of the system [14, 79]. This is shown to be [14]

$$\varepsilon_{33} = -2\frac{C_{13}}{C_{33}}\varepsilon_{11}. \tag{2.21}$$

Here, ε_{33} is the out-of-plane strain, C_{ij} are the elastic constants of the well material and $\varepsilon_{11} = (a_B - a_W)/a_W$ is the in-plane strain given by the fractional difference between the barrier a_B and well a_W lattice constants, relative to the well. Although this description is valid for an overall macroscopic picture of a heterostructure, to resolve changes in the bond length *within* a unit cell requires an atomistic description of the strain effect. More details on this can be found in Sec. 3.2.3.1.

In addition to the effect of strain on the electronic structure, III-nitride heterostructures also exhibit strong internal polarisation fields due to the wurtzite crystal structure. As mentioned in Sec. 2.1, the cation and anions exhibit a large ionicity factor, which arises from their difference in electronegativity. This is important for crystals which contain more than one atomic species because, due to these differences in the electronegativity, each

bond will have a dipole moment associated with it. A crystal structure with a centre of symmetry does not experience this because the dipole moments cancel each other out leaving the net dipole moment per unit volume equal to zero, and thus no polarisation is observed. For the wurtzite crystal, which lacks an inversion centre along the c-axis (growth direction), there exists a permanent dipole moment per unit volume which is usually defined along the direction from the anion to the cation. This polarity stems from the different stacking sequence and stronger second nearest neighbours interactions, in comparison to the zinc-blende phase, leading to a change in the interatomic separation (embodied in the u parameter) between the first-nearest neighbours (the ionic contribution) together with a rearrangement of the electronic clouds (electronic contribution) [80]. These contributions cause a stretching of the bonds along the [0001] crystal direction in the absence of strain. These features lead to the so called spontaneous polarisation, P_{sp}, and it is a macroscopic effect [80, 81]. For a "real" GaN crystal and not an ideal structure, the c/a ratio and internal parameter u remain close to the ideal values ($c/a = 1.633$ and $u = 0.375$), with $c/a = 1.627$ and $u = 0.377$. In contrast, AlN deviates significantly more with $c/a = 1.601$ and $u = 0.382$ [50].

When this crystal is deformed by e.g. strain, the atoms are further displaced and these electronegative anions and cations give rise to an additional contribution to the internal polarisation field. This is often referred to as piezoelectric polarisation [14, 80]. Such strain-induced polarisation can occur in any non-centrosymmetric crystal undergoing strain and has more than two atomic species, but the III-N's are noticeable in that their piezoelectric coefficients are one order of magnitude larger than the typical III-V semiconductors [80]. Effects such as inhomogeneities, partial relaxation of strain, structural defects etc. may also distort the lattice more and cause the piezoelectric polarisation to be amplified even further.

When calculating the spontaneous polarisation in wurtzite III-N materials using the modern theory of polarisation via the Berry phase method, a reference structure with zero net formal polarisation is required to determine the change in spontaneous polarisation [82]. The zinc-blende structure is commonly used as the reference [82], as its [111] crystallographic direction can be formally matched to the [0001] direction of wurtzite in polarisation calculations. However, Dreyer *et al.* proposed in Ref. [82] that a hexagonal structure should be used as the correct reference frame. This is because zinc-blende exhibits a residual formal polarisation which was neglected in calculations, leading to incorrect P_{sp} values.

This error also impacted the piezoelectric coefficients (termed 'proper' in Ref. [82]). To offset this error a significant correction term is required. However, when calculating the net polarisation charge (cf. Figure 2 in Ref. [82]) it was found that the incorrect zinc-blende implementation for the spontaneous and piezoelectric polarisations essentially cancel out and result in values very close to the 'correct' hexagonal implementation for the III-nitrides, particularly for (Al,Ga)N as shown by Dryer *et al.* [82]. Therefore, the zinc-blende polarisation constants used throughout this thesis (see Table A.1 in the Appendix) is still relevant for discussion.

Following Ref. [81], in Voigt notation the first-order piezoelectric polarisation, $\mathbf{P}_{pz}$ in the i direction is given by

$$\mathbf{P}_{pz,i} = \sum_{j=1}^{6} e_{ij}\varepsilon_j \ . \tag{2.22}$$

ε_j is the strain tensor and the piezoelectric coefficients e_{ij} of the piezoelectric tensor which reads in Voigt notation [80]:

$$e = \begin{pmatrix} e_{11} & e_{12} & e_{13} & e_{14} & e_{15} & e_{16} \\ e_{21} & e_{22} & e_{23} & e_{24} & e_{25} & e_{26} \\ e_{31} & e_{32} & e_{33} & e_{34} & e_{35} & e_{36} \end{pmatrix} . \tag{2.23}$$

However, due to the symmetries of the wurtzite crystal structure, many of these components are shown to be zero or equal to each other, which is the case for $e_{31} = e_{32}$ and $e_{15} = e_{24}$ [80]. Therefore, the piezoelectric tensor for wurtzite is

$$e = \begin{pmatrix} 0 & 0 & 0 & 0 & e_{15} & 0 \\ 0 & 0 & 0 & e_{15} & 0 & 0 \\ e_{31} & e_{31} & e_{33} & 0 & 0 & 0 \end{pmatrix} \tag{2.24}$$

and one is left with only three independent piezoelectric coefficients.

The total polarisation vector field is the sum of the spontaneous and piezoelectric contributions:

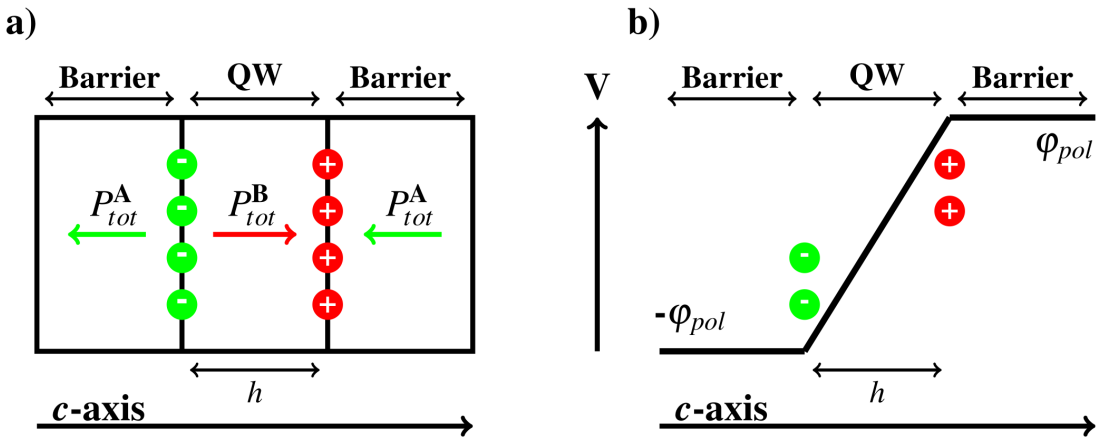


Figure 2.7: a) Quantum well (QW) (material **B**) embedded between two barriers (material **A**) inducing bound charges at the QW interfaces due to differences in the polarisation fields of material **A** and **B**. The left (right) interface has a negative (positive) sheet charge density generating a capacitor like setup. b) The potential, φ_{pol}, exhibits a capacitor-like profile which is constant outside the well and increases linearly within the well along the c-axis.

$$\mathbf{P}_{tot} = \mathbf{P}_{sp} + \mathbf{P}_{pz} \ . \tag{2.25}$$

For a bulk material, the polarisation will be constant across the entire material and will then not impact the electronic structure. Assuming there are no free charges present, the total charge density equals the bound charge, ρ_{bound}. This is given by the negative divergence of the polarisation vector field [83]

$$\rho_{bound} = -\nabla \cdot \mathbf{P} \ . \tag{2.26}$$

Thus, if there is a bulk material with no change in polarisation, then the bound charge will be zero.

However, if there is a structure with an interface between two different materials with different polarisation fields then a bound charge will be induced. The potential profile can then be found by solving Poisson's equation:

$$-\nabla \cdot (\epsilon(\mathbf{r})\nabla\varphi(\mathbf{r})) = \rho(\mathbf{r}) = -\nabla \cdot \mathbf{P}(\mathbf{r}) \ . \tag{2.27}$$

Where $\varphi(\mathbf{r})$ is the potential which depends on the position dependant dielectric

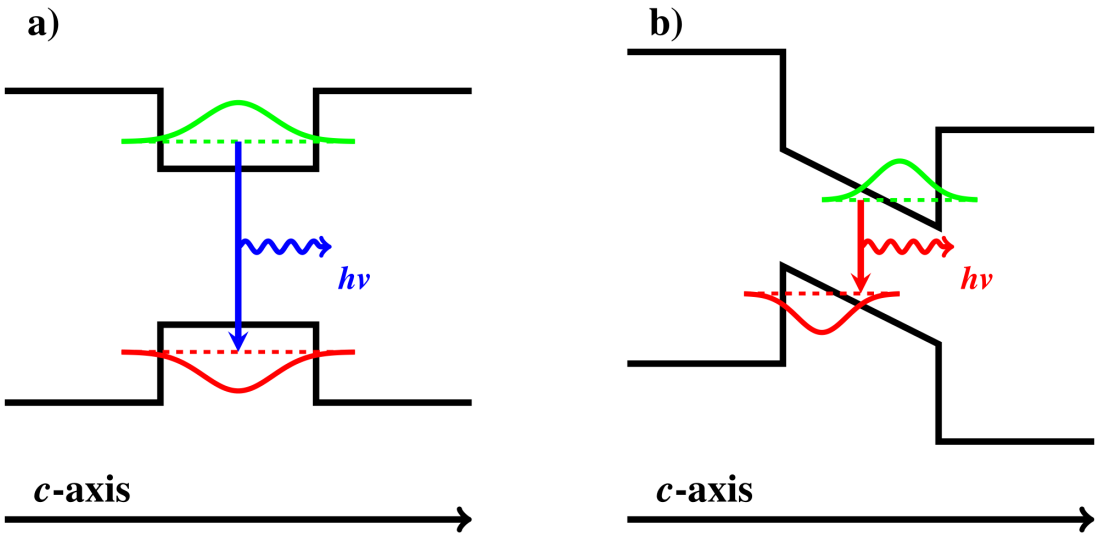


Figure 2.8: Conduction and valence band energies as a function along the c-axis (growth direction) of a quantum well. a) shows a QW with no polarisation and thus good wave function overlap of the electrons and holes leading to efficient recombination. b) shows a QW with a polarisation field and thus the built-in field shifts the electron and hole wave function to either side of the QW and reduces the band gap energy. This causes the recombination rate to reduce and the photon (hv) emitted to be redshifted.

constant, ϵ, and charge density, ρ. An example of what occurs in a QW can be seen in Fig. 2.7. As shown in Fig. 2.7 a), the bound charges on the left interface is negative and on the right it is positive. The electrostatic built-in potential across the QW is similar to the potential profile of a capacitor as shown in Fig. 2.7 b). This is called the built-in polarisation potential φ_{pol} and can be described for a QW embedded between barriers via [14]

$$\varphi_{pol}(z) = \left(\frac{P_{sp}^{W} - P_{sp}^{B} + P_{pz}^{W}}{2\epsilon_0 \epsilon_r^{W}} \right) (|z| - |z - h|). \tag{2.28}$$

Here, P_{sp}^{W} and P_{sp}^{B} is the spontaneous polarisation for the QW and barrier, respectively. P_{pz}^{W} is the piezoelectric polarisation generated by the QW strained to the barrier material, ϵ_0 is the vacuum permittivity, ϵ_r^{W} is the relative permittivity of the well, h is the QW width and z is the relative position along the c-axis.

The effect the built-in field has on the QW can be seen in Fig. 2.8. Fig. 2.8 a) shows the band edge energies of the heterostructure in the absence of the built-in field and b) displays the same in the presence of the built-in field.

Without the built-in field, the electron and hole wave functions exhibit a good spatial overlap and can thus lead to high radiative recombination rates. With the built-in field, the band edge energies are tilted leading to a triangular shaped confinement potential. Not only does this reduce the band gap energy and cause a redshifting of the emission wavelength to occur [84], it also spatially separates the electron and hole wave functions to either side of the QW. This separation is referred to as the quantum confined Stark effect (QCSE). As a result of the QCSE, the poor wave function overlap will reduce the recombination rate in the QW.

To understand how these effects, such as band bending, redshifting, reduced recombination, etc., impact the performance of LEDs, it is first necessary to outline the basic principles of LED operation.

2.4 Light Emitting Diodes

As mentioned in the prologue, LEDs are semiconductor optoelectronic devices which produce light when a bias voltage is applied. Modern LED devices are generally made up of a so-called *p*-*n* junction with a QW (or multiple QWs). To understand a *p*-*n* junction, we will first introduce the terms 'intrinsic' and 'extrinsic' semiconductors as discussed in Refs. [48, 54, 85]. An intrinsic semiconductor is where the electrons occupying the conduction band could only come from formerly occupied valence band levels. When an electron is excited into the conduction band, missing electrons in the valence bands are often called holes. Therefore, the number of conduction band electrons must equal the number of holes in the valence band in an intrinsic semiconductor. An extrinsic semiconductor is where impurities in the crystal contribute a significant fraction of electrons (holes) to the conduction (valence) band. These impurities, or dopants, provide extra sources of electrons and holes, thus making the density of electrons not necessarily equal to the density of holes. These impurities are called "donors" if they can add extra electrons to the conduction band or "acceptors" if they can add extra holes (i.e. capture electrons) to the valence band. When these impurities are introduced to a material they are often termed '*n*-type' for donors and '*p*-type' for acceptors. These electrons or holes are loosely bound to their respective impurities and therefore require, ideally, little energy in order to be excited to the conduction or valence band, respectively. This is referred to as the dopant activation energy, $E_{D/A}$, and a schematic illustrating this is shown in Fig. 2.9.

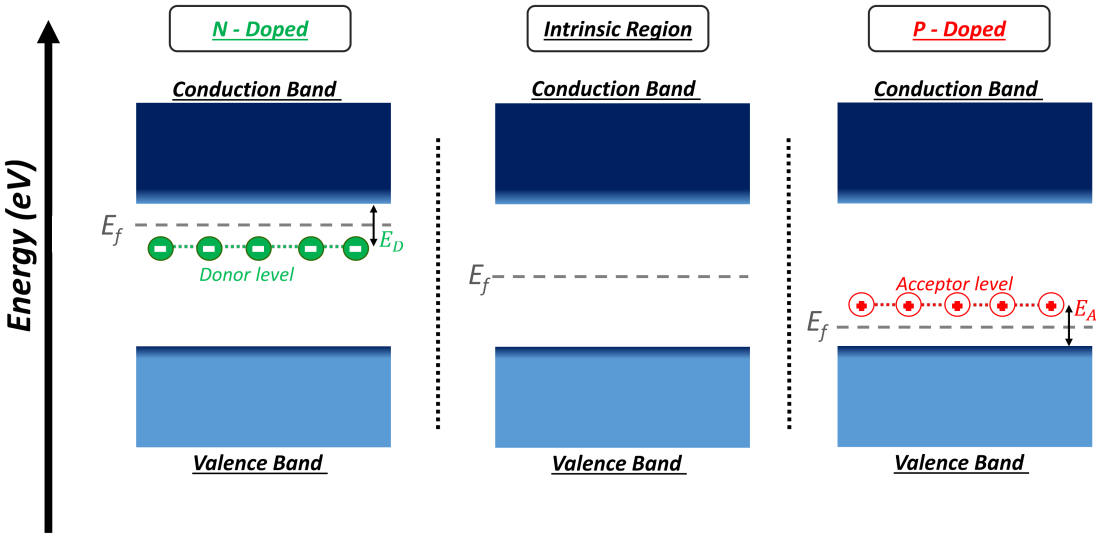


Figure 2.9: Schematic illustration of a band diagram for a n-doped, p-doped and undoped (intrinsic) material at zero temperature. The conduction and valence band energy of a semiconductor with their respective donor (green) and acceptor (red) energy levels. These energy levels sit within the band gap and ideally have a small energy level separation, E_D and E_A, between their respective bands so that it requires little energy to excite the carriers. The doping for the n-doped (p-doped) material has shifted the Fermi energy level, E_f, closer to the conduction (valence) band edge. The Fermi energy level of an intrinsic material remains in the centre of the band gap.

Electrons in a solid follow Fermi-Dirac statistics, which describe the probability $f(E)$ that a state at energy E is occupied by an electron. This probability is given by the Fermi-Dirac distribution

$$f(E) = \frac{1}{1 + e^{\frac{E - E_f}{k_B T}}} , \tag{2.29}$$

where E_f is the Fermi energy level, k_B is Boltzmann's constant, and T is the temperature. The Fermi energy level, E_f, represents the energy levels where the probability of finding an electron is 50% [48, 54, 85]. For an intrinsic semiconductor this energy level typically lies midway in the band gap at low temperature, but is close in energy to the conduction and valence band edges. Thus, providing energy in the form of heat or an applied voltage (bias) is sufficient to excite a small number of carriers into unoccupied states. Therefore, E_f is a useful tool to describe the occupation probability of a given state at a given point in a material. As shown in Fig. 2.9, by adding donor or acceptor dopants the Fermi energy level is shifted closer to the conduction or valence

band edge, respectively.

When these two doped materials are in contact to each other, e.g. by epitaxial growth, such a setup will form a p-n junction. This junction is a region where the doping profile changes abruptly creating distinct electrical properties. Here charges will flow from the region of higher Fermi level to the lower Fermi level reaching a point of equilibrium.

This is brought upon according to two factors. 1) Fick's law [48, 54, 85] which states that particles in an area of high concentration will migrate to an area of low concentration. This means in a p-n junction the n-doped electrons will diffuse across to the vacant p-doped holes and similarly the holes will diffuse across to the n-doped electrons, whereupon they will recombine. 2) In this region, the carriers have recombined and diffused away from the impurities, leaving behind positively and negatively charged ions at the interface. This generates an electric field which opposes the diffusion of the carriers and causes them to drift back to the areas of high concentration. This electric field can be calculated via Poisson's equation (eq. (2.27)).

The potential calculated keeps the Fermi energy level constant throughout the p-n system and causes the conduction band edge, CBE, and valence band edge, VBE, to bend where

$$\mathrm{CBE}(\mathbf{r}) = E_c(\mathbf{r}) - q\varphi(\mathbf{r}) \tag{2.30a}$$

$$\mathrm{VBE}(\mathbf{r}) = E_v(\mathbf{r}) - q\varphi(\mathbf{r}). \tag{2.30b}$$

Here $E_{c,v}$ is the conduction and valence band edge energy for the intrinsic material before band bending occurs, q is the elementary charge and φ is the potential. With this electric field the band energies are now at equilibrium when no external potential is applied. An illustration of this is given in the panel of Fig. 2.10.

The region where n- and p-type materials meet experience a high carrier recombination rate which in turn has a much lower density of free carriers. This is known as the depletion layer. The size of this depletion layer depends on the doping densities and may be changed by applying an external voltage, which generates an electric field across the p-n junction. When a field drives the electrons and holes further away from each other, increasing the depletion

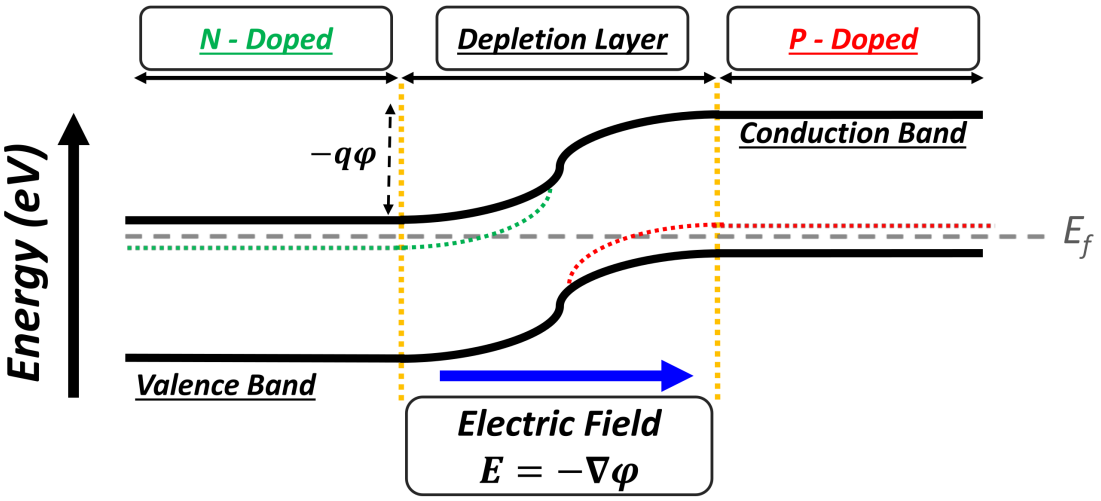


Figure 2.10: Schematic illustration of the conduction and valence band energies for a p-n junction where the built-in potential, $q\varphi$, is keeping the Fermi energy level (E_f) constant. The region where the n-doped and p-doped materials meet form the depletion layer which has a low free carrier density and the presence of an internal electric field, E. The donor impurity energies for the electrons (holes) are shown as a dashed green (red) line.

width, a reverse bias is applied. Conversely, if the applied voltage reduces the internal electric field and the electrons and holes are driven into the depletion region, reducing its width, it is called a forward bias.

For LEDs and lasers, these devices are usually operated under forward bias, allowing current to flow, which decreases this depletion width and increases carrier recombination. Additionally, as discussed in Sec. 2.3, QWs are usually incorporated into this region in order to confine the carriers into the same region of space and control the wavelength of the emitted light.

So far we have primarily discussed the distribution of carriers in a p-n junction, including the case where a QW is embedded in the depletion region. However, given that such structures are commonly used for optoelectronic devices, it is also essential to understand and describe the underlying recombination processes in such a device. The competition between radiative and non-radiative recombination plays a major role for the efficiency of LEDs. In the following section we will focus on defining these recombination mechanisms and examine their impact on device performance.

2.5 LED Efficiency & ABC model

In an optimal setting, an LED would operate with 100% efficiency. Meaning that for every electron and hole injected, a photon is generated and emitted from the device. However, this is never fully realised due to various loss mechanisms.

At low injection currents, GaN-based LEDs can emit very efficiently, making them well suited for low brightness applications. In an ideal case for an LED, increasing the current would result in an increase in the light emitted. However, at higher current densities the efficiency of the device starts to decrease above a certain threshold [86]. This current droop, often labelled as the efficiency droop, is observed across a wide wavelength spectrum for (In,Ga)N-based LEDs [87, 88] and for (Al,Ga)N-based LEDs [89, 90].

The overall performance of an LED is described by the wall plug efficiency (WPE) or power conversion efficiency (PCE) and which is defined as the ratio of the emitted output power to the total input electrical power [18]

$$\text{WPE} = \frac{P_{out}}{I \cdot V} = \eta_{EQE} \frac{\hbar\omega}{e \cdot V} \ . \tag{2.31}$$

Here P_{out} is the output power of emission, I is the drive current, V is the operating voltage, $\hbar\omega$ is the photon energy, e is the elementary charge and η_{EQE} is the external quantum efficiency (EQE). The EQE is defined as the ratio of photons emitted from the LED to the number of carriers injected into the device [18]

$$\eta_{EQE} = \frac{e \cdot P_{out}}{I \cdot \hbar\omega} \ . \tag{2.32}$$

The EQE may then be further broken up into a product of current injection efficiency (CIE), η_{inj}, radiative recombination efficiency (RRE), η_{rad}, and LEE, η_{ext}

$$\eta_{EQE} = \eta_{inj} \cdot \eta_{rad} \cdot \eta_{ext} \tag{2.33a}$$

$$= \eta_{IQE} \cdot \eta_{ext} \ . \tag{2.33b}$$

η_{ext} is defined as the fraction of photons extracted from the LED compared to the total number of photons generated. η_{rad} is the fraction of electrons and holes that recombine to emit a photon in the active region, and η_{inj} describes the ratio of carriers that reach the active region of the device versus the total current injected into the device. Here, the internal quantum efficiency (IQE), η_{IQE}, is defined as the product of the η_{rad} and η_{inj} i.e. the efficiency with which the carriers are injected into the active region of the device and successfully emit photons.

There are several methods of determining the IQE in experimental settings such as temperature and excitation power-dependant photoluminescence (PL) measurements [18]. However, one must take care when carrying out these measurements. For instance, temperature PL measurements require a low-temperature measurement which assumes that non-radiative recombination (see below) is negligible at low temperature [91, 92, 93, 94]. The excitation power-dependent method is based on fitting the integrated PL intensity dependence of the excitation power density to a rate equation model, which relies on a specific input power setup and approximates the excitation power [95]. Additionally, both methods are based on PL measurements, but under normal circumstances an LED will be operating under electrical injection. Therefore, carrying out IQE measurements under electrical injection conditions, such as electroluminescence (EL) measurements, would be preferred. However, this method still comes with difficulties such as, for example, current crowding caused by poor conductivity of high-Al containing n-doped (Al,Ga)N [96].

If we assume an ideal scenario where the η_{inj} is 100% efficient, then the IQE $= \eta_{rad}$. However, even with this assumption that an electron and hole are injected into the active region, other non-radiative recombination mechanism may occur. In such cases, the IQE is defined as the radiative recombination rate, R^{Rad}, divided by the sum of radiative and non-radiative recombination rates, $R^{non-Rad}$

$$\text{IQE} = \frac{R^{Rad}}{R^{Rad} + R^{non-Rad}} \ . \tag{2.34}$$

To describe the recombination processes quantitively, the so-called ABC model is widely employed. In the ABC model, the three main mechanisms [11, 86, 97] are prescribed as the total recombination rate per volume, which is given by

$R = R^{SRH} + R^{Rad} + R^{Aug}$. Here, the Shockley-Read-Hall (SRH) recombination is a non-radiative process where the electron and hole recombine via an intermediate state, i.e. a defect or 'trap' state that has an energy located within the band gap, without producing a photon. The SRH recombination, which is related to defect densities, is described as [98].

$$R^{SRH}(\mathbf{r}) = A(\mathbf{r})r(\mathbf{r}) \tag{2.35}$$

where $A(\mathbf{r})$ is

$$A(\mathbf{r}) = \frac{1}{\tau_p(n(\mathbf{r}) + n_i(\mathbf{r})) + \tau_n(p(\mathbf{r}) + n_i(\mathbf{r}))} \ , \tag{2.36}$$

with n (p) being the electron (hole) density, and τ_n (τ_p) the electron (hole) lifetimes. The excess carrier density, $r(\mathbf{r})$, is

$$r(\mathbf{r}) = n(\mathbf{r})p(\mathbf{r}) - n_i^2(\mathbf{r}) \tag{2.37}$$

and the intrinsic carrier density, n_i, is [98]

$$n_i^2(\mathbf{r}) = n(\mathbf{r})p(\mathbf{r})e^{(\frac{q\varphi_n - q\varphi_p}{k_B T})}. \tag{2.38}$$

Here, q is the carrier charge, $\varphi_{n,p}$ is the quasi-Fermi potential for the electrons and holes, k_B is the Boltzmann constant and T is temperature.

The radiative recombination rate, R^{Rad}, should be the dominant recombination process for a light emitting device, where the electron and hole recombine to emit a photon with energy equal to the band gap of a QW. Here,

$$R^{Rad}(\mathbf{r}) = Br(\mathbf{r}), \tag{2.39}$$

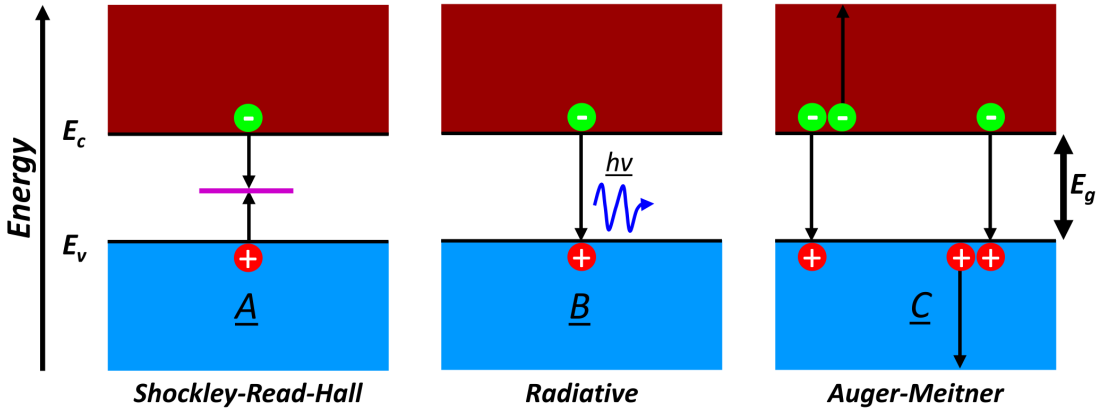


Figure 2.11: Shown are the conduction, E_c, and valence, E_v, band energy with the three recombination mechanisms of the ABC model. A) shows the Shockley-Read-Hall non-radiative recombination at a defect (trap) site. B) Radiative Recombination where the electron hole pair recombine emitting a photon. C) Auger-Meitner recombination which involves a three particle process. An electron hole pair recombine and interact with either an electron (eeh) or a hole (hhe) exciting it to higher energies.

is a two particle process with B as the radiative recombination coefficient.

Finally, Auger-Meitner recombination is a non-radiative three carrier process. Here, the electron and hole recombine and transfers its energy to a third carrier, either an electron or hole, resulting in the generation of a 'hot' carrier rather than a photon [99, 100]. The rate is [98]

$$R^{Aug}(\mathbf{r}) = (C_n n(\mathbf{r}) + C_p p(\mathbf{r}))r(\mathbf{r}) \ , \tag{2.40}$$

where C_n and C_p are the Auger-Meitner coefficients corresponding to the electron-electron-hole and electron-hole-hole process, respectively. A schematic illustration of these three recombination mechanisms [86] are shown in Fig. 2.11.

Each of these three coefficients (A, B and C) scales differently with carrier density. A scales linearly with the electron carrier density ($R_{SRH} \propto n$). B is a two particle process so it scales proportionally with the product of electron and hole densities ($R^{Rad} \propto np$). C_n and C_p are a three particle process and thus scales as ($R^{Aug} \propto n^2p + np^2$).

Thus, the ABC model captures the key mechanisms of carrier recombination processes in the active region of an optoelectronic device and is generally the main method of evaluating its efficiency [93, 101].

$$\mathrm{IQE} = \frac{Bnp}{An + Bnp + (Cnnp + Cnpp)} \tag{2.41}$$

Although the ABC model is a useful tool when it comes to modelling and determining the efficiencies of III-V devices, it needs to be treated and used with care for III-N based heterostructures and devices. Firstly, these coefficients are frequently used to fit to experimental data. Often assumptions about certain parameters are made which affect the remaining parameters. This interdependence contributes to the wide range of reported values in the literature. Moreover, variations in sample preparation and measurement conditions further compound this issue, leading to a confusing and sometimes contradictory understanding of the factors contributing to efficiency droop [86]. Thus, parameter sets from one sample may be different compared to another. On top of this, these coefficients are often assumed to not vary with temperature or carrier density [3, 102]. This is, in general, not the case however and can thus provide inaccurate predictions depending on the operating conditions. For instance, as discussed in Sec. 2.3, the built-in polarisation field induces the QCSE which reduces wave function overlap, potentially affecting the recombination coefficients. Under operating conditions at a high carrier density these internal fields will be screened by the free carriers, reducing the QCSE, improving the wave function overlap and, in turn, altering recombination rates [3, 100, 103]. This can further be exacerbated when operating a multi-QW (MQW) device, where carrier distribution across the wells may not be equal [104].

Finally, in addition to all these factors, the III-N alloys are different compared to III-V alloys in that they are prone to carrier localisation effects, as mentioned in Chapter 1. Alloy disorder can lead to spatially inhomogeneous carrier distributions, with locally high carrier densities, which in turn can significantly affect the rates of recombination. Calculations that account for alloy fluctuations have been performed to investigate these recombination rates [3, 105], which have shed light on suitable device parameters and are a valuable point of comparison with experimental data. Therefore, in the case of III-N alloys, alloy fluctuations should be taken into consideration.

2.6 Alloy disorder

As discussed above, III-N systems and alloys, such as (In,Ga)N, (Al,In)N but also (Al,Ga)N, exhibit in general very different properties when compared to other III-V materials, e.g. (In,Ga)As. For instance, experimental and theoretical studies reveal strong alloy fluctuation-induced carrier localisation effects in III-N alloys and heterostructures [29, 30, 68, 79, 106].

A significant contribution to carrier localisation in III-N alloys is the band gap difference between the binary constituents of the alloy. For (Al,Ga)N, the band gap energy for AlN is ≈ 6.16 eV whereas GaN is ≈ 3.44 eV [14]. Therefore, variations in the alloy content can lead to large fluctuations in the confining potential between the lower band gap material and the wider band gap material, in this example of (Al,Ga)N, regions with high Ga content and regions with high Al content, respectively. Further factors that can affect the energy difference are local atomistic fluctuations in the alloys strain, which in turn induce piezoelectric polarisation fields as discussed in Sec. 2.3. All these factors coupled together will modify the confining energy landscape the carriers are 'seeing' and may lead to carrier localisation, purely by alloy disorder.

A fingerprint of carrier localisation is, for instance, the so-called Stokes shift observed in the optical spectra for III-N QWs [11, 45]. This shift refers to the phenomenon where the peak emission energy occurs at a lower energy than the the peak absorption energy. In a perfectly homogeneous QW, the system can be treated as two dimensional (2D) in terms of carrier confinement, so the density of states (DOS) follows a step-like function, as shown in Fig. 2.12. In this ideal case, the absorption and emission are at the same energy and there is no Stokes shift. Carriers excited above the band edge quickly relax down to the conduction and valence band edges and recombine, emitting photons with energy approximately equal to the band gap. However, in alloys such as (Al,Ga)N, alloy disorder introduces spatial fluctuations in the band structure. This gives rise to a lower density of localised states below these ideal band edges. These localised states modify the ideal DOS by introducing an exponential tail below the band edge, leading to a smeared out absorption edge. The absorption is dominated by regions with a higher density of states, therefore the tail does not strongly affect the absorption onset. However, when carriers relax following excitation, they may fall into these Ga-rich regions which lie lower in energy than the ideal (Al,Ga)N band edge before recombining. Thus, the photon energy emitted is then redshifted relative to the absorption

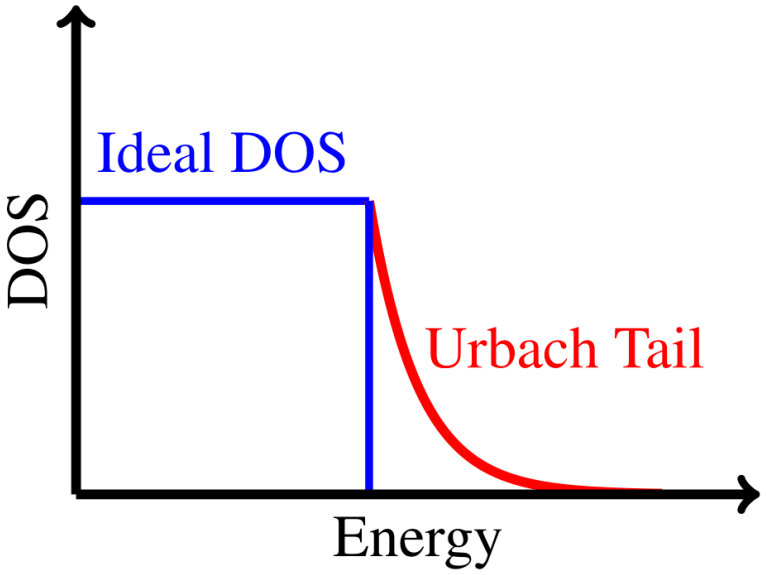


Figure 2.12: Diagram of the density of states (DOS) versus energy. In blue is the ideal step function that describes the DOS for a QW that has two degrees of freedom. The red exponential DOS describes the localised carriers generating this 'tail state'.

edge. This tail is termed the Urbach tail [11, 45] which is schematically shown in Fig. 2.12. The stronger the localisation effects in the alloy the larger this Urbach tail will be. Further experimental evidence of carrier localisation in (Al,Ga)N QWs have been observed in broad low temperature photoluminescence (PL) peaks, as well as the characteristic "S-shaped" temperature dependence of the PL peak position [31, 32, 33], both of which are indicative of carrier trapping in local potential minima arising from alloy disorder.

Experimental studies clearly indicate carrier localisation effects in III-N QWs, as the observed electronic and optical properties deviate significantly from what is observed in "conventional" QW systems. In order to accurately model and predict fundamental properties of III-N heterostructures, it is essential to include alloy disorder and the connected carrier localisation effects in theoretical studies. This is not only important for understanding the electronic and optical properties, but it is also necessary when investigating transport in LEDs. As previously mentioned in Sec. 2.5, alloy disorder can give rise to locally high carrier densities, thereby modifying the recombination rates. In addition, disorder may provide lower energy pathways for carriers to enter or leave the active region of the device, ultimately influencing the performance. However, developing a theoretical and computational framework that can capture the full impact of alloy disorder on the electronic, optical and transport properties of

(Al,Ga)N-based devices is a significant challenge to overcome. Firstly, large atomistic supercells must be generated in order to adequately capture the spatial extent of carrier localisation. Secondly, these supercells must account for both macro- and microscopic fluctuations in the strain and polarisation fields, as these effects are tightly linked to the band structure in III-N materials. Lastly, the resulting electronic structure model must then be coupled to self-consistent carrier transport calculations in order to realistically model how the alloy disorder affects carrier transport and recombination for an operating LED. In the following chapter, we shall provide an overview of the electronic structure methods and how to perform device simulations to address these challenges. We also outline a framework for incorporating these critical effects into the modelling of (Al,Ga)N-based devices.

Chapter 3

Theory

In this chapter, we introduce key concepts required to simulate the influence of alloy disorder on (Al,Ga)N-based optoelectronic devices. We begin by reviewing different approaches for describing the electronic structure, followed by methods that explicitly account for the impact of alloy disorder. Finally, we discuss widely used concepts required for device-level simulation, using the drift-diffusion model to describe carrier transport.

To simulate the effects of alloy disorder on carrier transport and recombination processes in (Al,Ga)N-based devices, it is crucial to first obtain an accurate description of the electronic structure. As discussed in Sec. 2.2, this amounts to essentially solving the time-independent Schrödinger equation. Approaches to finding the electronic structure of optoelectronic devices are usually divided into two categories, *ab initio* and semi-empirical. In *ab initio* studies, the Schrödinger equation is solved from first principles without the need for any adjustable or free parameter. By contrast, semi-empirical methods do require certain fitting of the models input parameters, either to experimentally observed data *or* first-principle calculations. Both methods have advantages and disadvantages and will be briefly introduced and discussed in this chapter.

First we will look at an extremely popular and versatile *ab initio* method known as density functional theory (DFT) in Sec. 3.1. We then turn our attention to semi-empirical approaches in Sec. 3.2, starting with the $\mathbf{k} \cdot \mathbf{p}$ method (Sec. 3.2.1) followed by modified continuum based approaches for incorporating alloy fluctuations in these methods (Sec. 3.2.2). We then describe the tight-binding method and its treatment of alloy fluctuations in Sec. 3.2.3. Finally, Sec. 3.3 discusses the drift-diffusion model and how a 3D energy

landscape can be integrated into the carrier transport framework.

3.1 Density Functional Theory

Calculating the electronic structure of materials from first principles involves solving the many-body Schrödinger equation, where all interactions between charged particles, such as electron–electron and electron–nuclei Coulomb interactions, must be considered simultaneously for a given system. For N particles, this becomes a highly complex problem due to the large number of particles and their three dimensional spatial coordinates.

A major breakthrough in addressing this challenge came with the theorem put forward by Hohenberg and Kohn [107], which forms the basis of DFT. The theorem states that the ground state energy of an interacting N electron system is a unique functional of the ground state electron charge density, $\rho(\mathbf{r})$, and that the true ground state density minimises the energy functional $E[\rho(\mathbf{r})]$. These principles are so impactful because, instead of solving for a many-body wave function that depends on $3N$ spatial coordinates, DFT reduces the problem to a function of only three spatial variables, as the charge density is a collective quantity. This greatly reduces the difficulty in solving the ground state energy of the system.

In order to calculate correctly the ground state energy of an interacting electron system, Kohn and Sham derived a set of effective single-particle equations [108]. In this interpretation, the interacting many particle system under the influence of an external potential can be mapped onto a non-interacting system with an effective potential, V_{eff}, that contains the effect from these interactions. Here, the energy functional $E[\rho(\mathbf{r})]$ can be expressed as [59, 109]

$$\begin{aligned} E[\rho(\mathbf{r})] &= T[\rho(\mathbf{r})] + V_{\text{eff}}[\rho(\mathbf{r})] \\ &= T[\rho(\mathbf{r})] + \int d^3r\, V_{\text{ext}}(\mathbf{r})\rho(\mathbf{r}) + W[\rho(\mathbf{r})] + E_{xc}[\rho(\mathbf{r})]\ . \end{aligned} \tag{3.1}$$

T is the kinetic energy functional of the non-interacting single-particle system with density, ρ, and the external potential in which the particles move is V_{ext}. W is the Hartree contribution to the Coulomb interaction energy of the electrons

$$W[\rho(\mathbf{r})] = \frac{e^2}{2}\int d^3r \int d^3r' \frac{\rho(\mathbf{r})\rho(\mathbf{r}')}{|\mathbf{r}-\mathbf{r}'|} \tag{3.2}$$

and the term $E_{xc}[\rho(\mathbf{r})]$ is the exchange-correlation functional. With this interpretation by Kohn and Sham, all the terms in eq. (3.1) correspond to a non-interacting reference system whose density matches that of the real interacting system. This means that for the true ground state energy of a given system of interacting electrons, the kinetic energy term, T, of a non-interacting system, which is not necessarily equal to the kinetic energy of the interacting system, will be described correctly assuming that the corrections are properly taken into account via the exchange-correlation functional.

There are a variety of approaches to approximate the exchange correlation functional to obtain the electronic structure of a material. The local density approximation (LDA) is one of the earliest and simplest methods. The LDA approach defines the local exchange-correlation energy functional, $E_{xc}[\rho]$, by assuming that at each point in space, the exchange-correlation energy per electron is the same as in a uniform electron gas with the same local density [110]. This approach works particularly well for materials where the electron density varies slowly such as, for example, a bulk material. However, the LDA approach does not fare well predicting the properties of materials where the electron density is not uniform overall, for example, atoms, molecules or materials that exhibit carrier localisation effects [59].

Other more complex approaches have been developed in order to take into account the non-uniform distribution of the electron density, e.g. generalized gradient approximation (GGA), which may provide more accurate results (compared to LDA) for certain material properties e.g. H-bonding [111]. However, GGA or LDA are known to underestimate the band gaps for semiconductors in general, including for the III-N alloys [81, 112].

Hybrid density functional theory offers a further improvement on GGA results where a portion of exchange from Hartree-Fock theory (HF) is included. One example is the Heyd-Scuseria-Enzerhof (HSE) screened exchange hybrid functional [113, 114] scheme which can offer an approach with a high degree of accuracy calculating the properties of III-Ns [35, 81]. The HSE hybrid functional is built from the hybrid PBE (PBE0) exchange-correlation functional [115, 116] but with the addition of splitting the exchange energy term into short range and long range components. The long range HF is ignored but

compensated with the PBE long range term i.e. 'screening' of the long range part of the Coulomb potential.

This method provides a better description of the III-N material parameters such as lattice constants and their respective band gaps, but noticeably increases the computational time in comparison to other DFT calculations [114]. Therefore, typical HSE calculations can only run systems on the order of tens to hundreds of atoms for a reasonable computational cost [35, 117]. Recent state-of-the-art calculations via a linear scaling of the DFT software have been shown to be capable of system sizes of a few thousand atoms [118, 119] but this approach still requires extensive research in order to be applied and refined for use in e.g. the III-N materials. In addition to this, as discussed in Sec. 2.6 for the III-Ns, the alloy disorder will induce carrier localisation effects. This means in order to accurately model a heterostructure such as a QW, one need to treat large supercells that take into account the atomic disorder of the barrier material and the well. Large in-plane dimensions are also required in order to fully capture potential carrier localisation effects with 'typical' localisation lengths, as seen in (In,Ga)N, of ≈ 1 nm for the holes and larger for the electrons [120]. Therefore, utilising a semi-empirical approach is often required in order to simulate structures large enough to capture the effects of alloy disorder while maintaining a reasonable computational cost.

3.2 Semi-Empirical

Semi-empirical methods are widely employed in electronic structure calculations for solids because they possess lower computational cost compared to *ab initio* methods [59, 121], allowing for the treatment of large scale systems such as heterostructures with varying alloy compositions. These semi-empirical approaches can be divided into two broad categories: 1) continuum-based models which assume a uniform repeated unit cell to describe a material and 2) atomistic frameworks which allow for parameters within the unit cell to vary. First we will discuss the $\mathbf{k} \cdot \mathbf{p}$ method, a continuum based approach which is widely employed in the literature to carry out investigations into alloy materials.

3.2.1 $\mathbf{k} \cdot \mathbf{p}$ method

In semiconductors, the energy dispersion near the band edge is often assumed to be parabolic. While this resembles the behaviour of a free electron, the carrier is

not truly free due to the periodic potential of the crystal lattice, which leads to changes in the energy dispersion and the appearance of additional bands. To account for this an effective mass for the carriers, m^*, is introduced. This effective mass modifies the simple free electron picture by incorporating effects from interactions with other bands, while still assuming a parabolic energy dispersion near the band edges. This is often referred to as the nearly free electron model and forms the basis for the effective mass approximation (EMA). In the single band EMA the energy dispersion relation $E_n(\mathbf{k})$ of the bulk bands, near the extrema of the band edge, can be approximated to be

$$E(\mathbf{k}) = \frac{\hbar^2 \mathbf{k}^2}{2m^*}. \tag{3.3}$$

Employing the single band EMA approach is usually a direct and viable method to provide initial insight into the conduction and valence states in semiconductor heterostructures near the bands edge e.g. $\mathbf{k} = \mathbf{0}$ for direct band gap III-V materials. However, the accuracy of the EMA for the electronic structure depends on several material specific factors.

For instance, if the electronic structure exhibits a non-parabolic behaviour near the band edge then the EMA becomes less accurate and may no longer provide a reliable description of the band dispersion. The dispersion near a given $\mathbf{k}$-point will depend on its interaction with all the other bands. For bands that are far away in energy this impact will be negligible, but bands that are close in energy will influence the dispersion. Furthermore, the EMA technique also neglects coupling between bands that are close in energy [63], a feature which is important when considering the complex valence band structure in (Al,Ga)N as shown in Sec. 2.2.1.

To improve the single-band EMA, one can include more bands and allow for coupling between the different bands. This approach is referred to as $\mathbf{k}\cdot\mathbf{p}$ method [59, 122], and are based on time-independent perturbation theory. This model is used to describe the electronic band structure of a semiconductor near to the k-point of interest if the exact energy levels are known in the FBZ [59]. The k-points for a given band structure may also retain certain specific properties e.g. the Γ point at $\mathbf{k} = \mathbf{0}$ will determine the optical properties for direct band gap semiconductors, as mentioned in Sec. 2.2. Following Ref. [59], we start from the Hamiltonian, H_0, of a single electron moving in a periodic

solid:

$$H_0 = -\frac{\hbar^2}{2m}\nabla^2 + V(\mathbf{r}) \ , \tag{3.4}$$

with V($\mathbf{r}$+$\mathbf{R}$) = V($\mathbf{r}$). We know from Bloch's theorem that the eigenstates, $\Psi_{n\mathbf{k}}(\mathbf{r})$, can be written as the product of a plane wave, $e^{i\mathbf{k}\cdot\mathbf{r}}$, and a periodic function, $u_{n\mathbf{k}}(\mathbf{r})$, with associated energy levels, $E_n(\mathbf{k})$. For a chosen value of $\mathbf{k}$, say $\mathbf{k}_0$, Schrödinger's equation reads

$$H_0\Psi_{n\mathbf{k}_0}(\mathbf{r}) = H_0\Big(e^{i\mathbf{k}_0\cdot\mathbf{r}}u_{n\mathbf{k}_0}(\mathbf{r})\Big) = E_n(\mathbf{k}_0)\Big(e^{i\mathbf{k}_0\cdot\mathbf{r}}u_{n\mathbf{k}_0}(\mathbf{r})\Big). \tag{3.5}$$

Assuming that the allowed energy levels $E_n(\mathbf{k}_0)$ at $\mathbf{k}_0$ are known, we now attempt to find the energy levels, $E_n(\mathbf{k})$, at a wave vector $\mathbf{k}$ close to $\mathbf{k}_0$. For this, the Schrödinger equation takes the form

$$H_0\Big(e^{i\mathbf{k}\cdot\mathbf{r}}u_{n\mathbf{k}}(\mathbf{r})\Big) = E_n(\mathbf{k})\Big(e^{i\mathbf{k}\cdot\mathbf{r}}u_{n\mathbf{k}}(\mathbf{r})\Big). \tag{3.6}$$

Since we are interested in a $\mathbf{k}$ close to $\mathbf{k}_0$, we rewrite eq. (3.6) as

$$H_0e^{i(\mathbf{k}-\mathbf{k}_0)\cdot\mathbf{r}}\Big(e^{i\mathbf{k}_0\cdot\mathbf{r}}u_{n\mathbf{k}}(\mathbf{r})\Big) = E_n(\mathbf{k})e^{i(\mathbf{k}-\mathbf{k}_0)\cdot\mathbf{r}}\Big(e^{i\mathbf{k}_0\cdot\mathbf{r}}u_{n\mathbf{k}}(\mathbf{r})\Big) \tag{3.7}$$

and multiply both sides of eq. (3.7) from the left by $e^{-i(\mathbf{k}-\mathbf{k}_0)\cdot\mathbf{r}}$. The following equation is obtained:

$$\begin{aligned}\Big[e^{-i(\mathbf{k}-\mathbf{k}_0)\cdot\mathbf{r}}H_0e^{i(\mathbf{k}-\mathbf{k}_0)\cdot\mathbf{r}}\Big]\Big(e^{i\mathbf{k}_0\cdot\mathbf{r}}u_{n\mathbf{k}}(\mathbf{r})\Big) &= \Big[e^{-i(\mathbf{k}-\mathbf{k}_0)\cdot\mathbf{r}}E_n(\mathbf{k})e^{i(\mathbf{k}-\mathbf{k}_0)\cdot\mathbf{r}}\Big]e^{i\mathbf{k}_0\cdot\mathbf{r}}u_{n\mathbf{k}}(\mathbf{r}) \ , \\ &= E_n(\mathbf{k})\Big(e^{i\mathbf{k}_0\cdot\mathbf{r}}u_{n\mathbf{k}}(\mathbf{r})\Big) \ .\end{aligned} \tag{3.8}$$

When transforming eq. (3.7) into eq. (3.8), this modified Schrödinger equation includes a Hamiltonian which is now $\mathbf{k}$-dependent. This is denoted as $H_{\mathbf{q}}$, where $\mathbf{q} = \mathbf{k} - \mathbf{k}_0$. Equation (3.8) can be written as

$$H_{\mathbf{q}}\phi_{n\mathbf{k}}(\mathbf{r}) = e^{-i\mathbf{q}\cdot\mathbf{r}}\left(-\frac{\hbar^2}{2m}\nabla^2 + V(\mathbf{r})\right)e^{i\mathbf{q}\cdot\mathbf{r}}\phi_{n\mathbf{k}}(\mathbf{r}) \tag{3.9}$$

where the Bloch wave functions is $\phi_{n\mathbf{k}}(r) = e^{i\mathbf{k}_0\cdot\mathbf{r}}u_{n\mathbf{k}}(\mathbf{r})$. With some manipulation, eq. (3.9) becomes

$$\begin{aligned} H_{\mathbf{q}}\phi_{n\mathbf{k}}(\mathbf{r}) &= \left(-\frac{\hbar^2}{2m}\nabla^2 + V(\mathbf{r}) + \frac{\hbar^2}{m}\mathbf{q}\cdot\frac{1}{i}\nabla + \frac{\hbar^2 q^2}{2m}\right)\phi_{n\mathbf{k}}(\mathbf{r}) \\ &= \left[H_0 + \frac{\hbar}{m}\mathbf{q}\cdot\mathbf{p} + \frac{\hbar^2 q^2}{2m}\right]\phi_{n\mathbf{k}}(\mathbf{r}) \end{aligned} \tag{3.10}$$

where we have replaced $\frac{\hbar}{i}\nabla$ by the momentum operator, $\mathbf{p}$. Equation (3.10) forms the foundation of the $\mathbf{k}\cdot\mathbf{p}$ method. For $\mathbf{q} = \mathbf{0}$, eq. (3.10) reduces to the standard form of Schrödinger's time-independent equation. When dealing with direct gap semiconductor one often chooses the Γ-point, $\mathbf{k}_0 = \mathbf{0}$. This reduces $\mathbf{q} = \mathbf{k}$, showing where the name $\mathbf{k}\cdot\mathbf{p}$ comes from in eq. (3.10). At the Γ-point, one generally knows or can estimate the values of all relevant zone centre energies, $E_n(\mathbf{0})$. The contribution

$$H' = \frac{\hbar}{m}\mathbf{q}\cdot\mathbf{p} + \frac{\hbar^2 q^2}{2m} \tag{3.11}$$

to the full Hamiltonian is regarded as a perturbation to the zone centre Hamiltonian, H_0. Using second-order time-independent perturbation theory [123] we can derive an expression for the variation of the energy levels $E_n(\mathbf{k})$ with wave vector $\mathbf{k}(= \mathbf{q})$ close to the Γ-point. For this example, we consider a non-degenerate band where the energy of the nth band in the neighbourhood of $\mathbf{k} = \mathbf{0}$ is given by

$$E_n(\mathbf{k}) = E_n(0) + \frac{\hbar}{m}\mathbf{k}\cdot\mathbf{p}_{nn} + \frac{\hbar^2 k^2}{2m} + \frac{\hbar^2}{m^2}\sum_{n'\neq n}\frac{|\mathbf{k}\cdot\mathbf{p}_{nn'}|^2}{E_n(0) - E_{n'}(0)}\ . \tag{3.12}$$

Here $\mathbf{p}_{nn'}$ denotes the *momentum matrix element* between the nth and the n'th zone centre states, $u_{n\mathbf{0}}(\mathbf{r})$ and $u_{n'\mathbf{0}}(\mathbf{r})$,

$$\mathbf{p}_{nn'} = \int d^3r \; u^*_{n\mathbf{0}}(\mathbf{r})\mathbf{p}u_{n'\mathbf{0}}(\mathbf{r}) = \langle u_{n\mathbf{0}}|\mathbf{p}|u_{n'\mathbf{0}}\rangle \tag{3.13}$$

with the integration taken over a unit cell of the crystal structure. The momentum matrix elements, $\mathbf{p}_{nn'}$, apply corrections near Γ for a given energy state due to the effects of other energy states. One can see from eq. (3.12) that corrections linear in $\mathbf{k}$ ($\sim \mathbf{k}\cdot\mathbf{p}_{nn}$) and quadratic in $\mathbf{k}$ are present. It has been shown that for a diamond crystal structure, the linear term is zero due to its symmetry properties [124]. For III-V semiconductors, the effects of the linear in $\mathbf{k}$ terms are generally negligible, in comparison to the quadratic term, and can then be often ignored [59]. This effect holds true for the III-nitrides [59, 125].

For this example we have assumed a single non-degenerate band. However, effects such as SOC [126, 127, 128], band degeneracies [126] and multiple interacting bands may also have to be included for a realistic description of a bulk band structure. These effects lead to more complex models, but appropriate approximations can be made. For instance, eq. (3.12) reveals that the quadratic $\mathbf{k}$ term correction is inversely proportional to $E_n(0) - E_{n'}(0)$, and thus the energy separation between the bands. The number of bands that need to be included explicitly can be reduced because the energy separation increases and as such present small corrections which can thus effectively be ignored. Work done by Löwdin [129] showed electronic bands can be divided into two categories; the A-bands which are of primary interest and are treated explicitly, and the B-bands which lie far away in energy and are treated as a perturbation; the coupling between the A- and B-bands are treated implicitly. This consideration of only a few bands taken into account explicitly greatly improves the numerical demand for these kinds of calculations.

Models that consider one conduction and three valence bands along with their coupling are known as the 8 band $\mathbf{k}\cdot\mathbf{p}$ model [130]. For wide band gap materials like AlN and GaN, simpler models such as the Kohn-Luttinger Hamiltonian are often employed. Here, the coupling between the conduction band and valence band is neglected because of the large energy separation, resulting in a 6 band $\mathbf{k}\cdot\mathbf{p}$ model which only includes the three highest valence bands [127, 131].

In addition to the effects described above, the electronic structure is also influenced by both strain and polarisation fields. For example, a GaN QW coherently grown on an AlN substrate along the wurtzite c-axis will experience

biaxial compressive strain in-plane and tensile strain along the growth direction due to the in-plane lattice mismatch. In a continuum-based model, the strain is usually treated as a macroscopic effect. Typically, strain is included via the Pikus-Bir Hamiltonian [64, 126], which introduces energy corrections to the band edge by coupling the strain tensor ϵ_{ij}, as described in Sec. 2.3, to deformation potentials [127]

$$H = H_0 + H_{strain}. \tag{3.14}$$

Here, H_0 is the unstrained Hamiltonian of the QW described above and H_{strain} is the correction due to strain effects. In the case of a single band EMA applied to a 1D wurtzite QW structure grown along the c-axis, the conduction and valence band corrections are described as [64]

$$H^{CB}_{strain} = a_{ct}(\varepsilon_{xx} + \varepsilon_{yy}) + a_{cp}(\varepsilon_{zz}) \ , \tag{3.15}$$
$$H^{VB}_{strain} = D_2(\varepsilon_{xx} + \varepsilon_{yy}) + D_1(\varepsilon_{zz}). \tag{3.16}$$

Where a_{ct} and a_{cp} are the conduction band and D_2, D_1 are the valence band deformation potentials associated with the out-of-plane and in-plane strain, respectively. Shear strain components (e.g. ϵ_{xy}) for a QW are, in an ideal case, not present as the system is constrained to the in-plane lattice and assumed to be infinite/very large in the growth plane [80]. Although this is for a single band description, general expressions for multi-band models can be found in Ref. [127].

In addition to strain, wurtzite III-N materials exhibit strong spontaneous polarisation along the [0001]-direction. Strain further induces piezoelectric fields, contributing to the total built-in field, as discussed in Sec. 2.3. As defined earlier, the change in polarisation due to a QW structure leads to a capacitor-like behaviour inducing a built-in polarisation potential expressed as

$$\varphi_{pol}(z) = \left(\frac{P^W_{sp} - P^B_{sp} + P^W_{pz}}{2\epsilon_0 \epsilon^W_r} \right) (|z| - |z - h|) \ . \tag{2.28}$$

This polarisation field, like the strain correction, modifies the band edges with a position dependant potential.

Thus, the final hamiltonian for the system that includes strain and polarisation effects is

$$H = H_0 + H_{strain} - q\varphi_{pol} \ , \tag{3.17}$$

where φ_{pol} is the correction due to the potential and q is the elementary charge.

The $\mathbf{k} \cdot \mathbf{p}$ model was originally derived for bulk homogeneous crystals, where the potential is periodic and Bloch-like wave functions are eigenstates. In heterostructures such as a QW, this periodicity is broken due to variations in the material composition and built-in fields. In such cases, including the effects of strain and polarisation, can be incorporated into the $\mathbf{k} \cdot \mathbf{p}$ framework through position dependent corrections to the band edges. However, for random alloys where the atomic distribution varies on a microscopic scale, this method of calculation becomes questionable. The alloy disorder breaks the translational invariance at the atomic level, and the potential fluctuations can no longer be captured by averaged, continuum-like corrections [121]. Nevertheless, it has been found that the $\mathbf{k} \cdot \mathbf{p}$ model is a good method for simulating semiconductor alloys such as (Al,Ga)As, even with the alloy disorder [30, 121]. The reason this holds for many III-V alloys is because the perturbations introduced by the alloy disorder are small enough that it can be effectively ignored/corrected. Therefore, these materials can be modelled via a method such as a virtual crystal approximation (VCA), where the material parameters of the alloy is constructed from a linear interpolation of the binary alloys e.g. AlAs and GaAs. However, the III-N semiconductors cannot be simulated in this way due to the large potential difference between the atoms. This results in large energy fluctuations in the alloy and potential carrier localisation effects which will be neglected in VCA calculations, and can lead to inaccurate predictions of the electronic and optical properties [30]. Therefore, although the $\mathbf{k} \cdot \mathbf{p}$ method is an extremely useful semi-empirical technique that provides accurate results at a lower computational cost for *certain* materials, its applicability to the III-Ns is limited. To properly capture the impact of alloy fluctuations on the electronic structure, a different approach is needed. This can be done either by modifying the continuum based approach to include a 3D varying potential or by a

semi-empirical atomistic approach. We will first take a look at a modified continuum-based landscape before then turning to a semi-empirical atomistic technique.

3.2.2 Modified continuum-based approaches

In order to describe a continuum-based system that retains the effect of alloy fluctuation, a 3D compositional map is often employed. One such approach is described in Refs. [42, 44, 69, 132] where the cation species (e.g. Al and Ga) are randomly distributed across the lattice sites within a given simulation cell. A fully atomistic resolution is potentially too fine for continuum-based calculations. Therefore, coarser alloy maps are typically generated, where each node represents an averaged alloy composition. This is often achieved using a Gaussian smoothing procedure to determine the local alloy content.

From this 3D map the local band energies are calculated from a VCA description. This means that the local band gap is obtained from the binary materials parameters given by [14, 133]

$$E_g(\mathrm{Al}_x\mathrm{Ga}_{1-x}\mathrm{N}) = xE_g(\mathrm{AlN}) + (1-x)E_g(\mathrm{GaN}) + bx(1-x), \tag{3.18}$$

$$\tag{3.19}$$

where E_g is the band gap energy of the (Al,Ga)N alloy, x is the Al alloy composition at a given position and b is the bowing parameter. Other material parameters such as the lattice constants, effective mass and band offsets can be similarly interpolated. Using this approach, the local strain distribution is calculated with the spatially varying lattice parameters derived from the local alloy composition. Likewise, the built-in polarisation fields which depend on both the local strain and composition are computed by solving the piezoelectric and spontaneous polarisation equations [81]. This leads to the generation of a 3D potential landscape which can then be used to solve the Schrödinger equation. However, using this approach in solving the Schrödinger equation for the III-Ns remains computationally demanding. This is primarily due to the strong potential fluctuations introduced by the alloy disorder, which require a fine spatial resolution to accurately capture the electronic structure. As a result, the simulation cell must not be too coarse, or it risks neglecting the effects of alloy fluctuations. This challenge is further

exacerbated when simulating the large device-scale structures required in practical applications [40, 132]. Here, not only does the Schrödinger equation have to be solved over an extended region, but the large eigenvalue problem must be solved self-consistently with e.g. Poisson's equations, making the computation especially demanding. One method to address this is termed the localisation landscape theory (LLT) which has been developed as a means to avoid solving the numerically intensive Schrödinger equation for a random energy landscape [44].

3.2.2.1 Localisation Landscape Theory

LLT is an alternative approach that replaces the Schrödinger equation with a 'simpler' equation, which estimates the local ground state energy and wave function within each localisation region for a single band description, without solving a large eigenvalue problem. This method can also be applied to a 3D modified continuum-based model. First introduced by Filoche and Mayboroda in 2012 [134] who were studying wave localisation in a disordered medium. In 2017 this concept was later extended to semiconductors systems where the LLT treatment was applied to (In,Ga)N-based devices, in order to investigate the impact the disordered landscape had on device performance [42, 44, 45].

Here, we illustrate the main features of LLT as described in Ref. [44, 134, 135]. With this method we are capable of predicting the spatial localisation of quantum states within a potential $V(\mathbf{r})$ by solving an associated Dirichlet boundary value problem. This problem defines the localisation landscape function $u(\mathbf{r})$, which reveals regions where the quantum states are confined. For a particle with mass m, the Hamiltonian is given by

$$H = -\frac{\hbar^2}{2m}\Delta + V \ , \tag{3.20}$$

whose eigenfunctions and eigenvalues describe the quantum states of the system. The localisation landscape $u(\mathbf{r})$ is defined as the solution of

$$Hu = -\frac{\hbar^2}{2m}\Delta u + Vu = 1, \tag{3.21}$$

subject to appropriate boundary conditions such as Dirichlet, Neumann, or

periodic [135]. For our study we assume Dirichlet boundary conditions with the potential set to 0 at the boundaries. Reference [134] shows that the subregions hosting the localised eigenfunctions are delimited by the valley lines of the graph of u. This property arises directly from a fundamental inequality that any eigenfunction ψ of the operator H with eigenvalues E satisfies

$$|\psi(\mathbf{r})| \leq Eu(\mathbf{r}), \tag{3.22}$$

provided ψ is normalised so that its maximum amplitude is 1 [44, 134]. Essentially, the small values of $u(\mathbf{r})$ along its valley lines reduce the amplitude of ψ along these lines. As a result, the low energy eigenfunctions are confined or localised within the regions bounded by these valley lines. Therefore, the localisation landscape $u(\mathbf{r})$ partitions the domain into subregions, each of which traps carriers in these localised zones.

Furthermore, the function $W \equiv \frac{1}{u(\mathbf{r})}$ can essentially be interpreted as a confining potential [135]. This can be proved by transforming the Schrödinger equation through the introduction of an auxiliary function φ such that $\psi = u\varphi$. This equation,

$$\left(-\frac{\hbar^2}{2m}\Delta + V \right)(u\varphi) = Eu\varphi, \tag{3.23}$$

gives

$$-\frac{\hbar^2}{2m}\Delta\varphi - 2\frac{\hbar^2}{2m}\frac{\nabla u}{u}\cdot\nabla\varphi + \frac{1}{u}\varphi = E\varphi \tag{3.24}$$

when accounting for the definition of u in eq. (3.21). The first order term involving $\nabla\varphi$ can be absorbed into the Laplacian by rewriting both together as a divergence of $u^2\nabla\varphi$

$$-\frac{\hbar^2}{2m}\left[\frac{1}{u^2}\nabla\cdot(u^2\nabla\varphi)\right] + W\varphi = E\varphi. \tag{3.25}$$

The auxiliary function $\varphi = \psi/u$ satisfies a Schrödinger type equation where the original potential $V(\mathbf{r})$ has been replaced with a new function $W(\mathbf{r})$

$$W(\mathbf{r}) = \frac{1}{u(\mathbf{r})} \ , \tag{3.26}$$

that now acts as an "effective confining potential" [44, 135]. The boundaries of the localisation regions defined by the valley lines of u also correspond to the crest lines of this potential W, acting as a barrier for the auxiliary function φ. Thus, the function φ and the eigenfunction ψ are now bound inside the regions of W.

A detailed proof of the effective potential W can be found in the supplementary material in Ref. [135] where the following identity is satisfied by any quantum state $|\psi\rangle$

$$\langle\psi| H |\psi\rangle = \frac{\hbar^2}{2m}\left\langle u\nabla\left(\frac{\psi}{u}\right)\middle| u\nabla\left(\frac{\psi}{u}\right)\right\rangle + \langle\psi|W|\psi\rangle. \tag{3.27}$$

LLT only requires solving a system of linear equations, something which significantly reduces the numerical demand when compared to solving the eigenvalue problem of the Schrödinger equation. This is discussed in Ref. [42] where standard self-consistent Schrödinger-Poisson calculations for transport properties in (In,Ga)N/GaN-based LEDs are compared to drift-diffusion calculations utilising LLT instead. There it was shown that the LLT framework sped up the calculations by a factor of 50 on identical systems. Therefore, utilising LLT, as an example, in conjunction with drift-diffusion calculations is an ideal scenario for the III-N devices [42, 104]. The effective landscape generated by LLT captures quantum effects, such as tunnelling [42], without having to solve the Schrödinger equation.

However, one must be careful when implementing LLT. For the Schrödinger equation, the wave function ψ is independent of the zero-point of the potential energy. This is not the case for eq. (3.21) where the choice of reference energy (i.e. the zero-point of the potential energy) can influence the effective landscape. This is demonstrated in Ref. [136] where they expand the landscape function in the basis of eigenstates of H:

$$H|u\rangle = H\sum_n \alpha_n|\psi^n\rangle = \sum_n \alpha_n E_n|\psi^n\rangle \ , \tag{3.28}$$

where the sum runs over all eigenstates $|\psi^n\rangle$ of H with corresponding eigenvalues E_n. The coefficients α_n can be determined by using the orthogonality of the eigenstates, where ψ^i is the ith eigenstate of H:

$$\langle\psi^i|H|u\rangle = \sum_n \alpha_n E_n\langle\psi^i|\psi^n\rangle = \alpha_i E_i \ . \tag{3.29}$$

Using eq. (3.21), where $H|u\rangle = 1$, this gives

$$\alpha_i = \frac{\langle\psi^i|1\rangle}{E_i} \tag{3.30}$$

so that the expansion of $|u\rangle$ can be written as

$$|u\rangle = \sum_n \frac{\langle\psi^n|1\rangle}{E_n}|\psi_n\rangle. \tag{3.31}$$

Equation (3.31) shows that the landscape u explicitly depends on the values of the eigenenergies E_n. Since each term in the above sum is weighted by $1/E_n$, the contribution from each eigenstate is sensitive to the absolute value of the eigenenergy. This means that shifting the reference energy of the Hamiltonian (i.e. redefining the zero of potential energy) alters the values of E_n and thus change the shape of the landscape u. For this thesis, we are particularly interested in the ground state energy as it represents the lowest energy with the most significant localisation. Therefore, as described in Ref. [136], we require the 0^{th} term to dominate the expansion i.e. $\alpha_j << \alpha_0$ for all $j \neq 0$. As a result the reference energy of the Hamiltonian is chosen so that the ground state energy is very close to zero. This ensures that $1/E_0$ is large and that the ground state contribution is the most significant in shaping the landscape.

Another drawback of the LLT framework is that it is designed as a single band model and has yet to be extended to a multi-band description that accounts for

band mixing effects. In the case of III-N materials such as InN and GaN, this is not particularly significant, as their valence band edge is described by a band of the same symmetry and therefore does not change in (In,Ga)N alloys. The conduction band is s-like while the valence band maximum is predominantly $p_{x,y}$-like, with p_z-like bands pushed energetically away from the valence band edge, as discussed in Sec. 2.2.1. Therefore, when modelling an (In,Ga)N alloy, a single-band LLT model can effectively capture the essential physics, as there is little need to account for strong coupling between multiple bands. However, for AlN and (Al,Ga)N alloys, the situation becomes more complex. Sec. 2.2.1 described that AlN's valence band character is predominantly p_z-like due to the negative crystal field splitting. Therefore, an (Al,Ga)N alloy will potentially have a band ordering that is a mix of $p_{x,y}$- and p_z-like character, particularly for higher containing Al contents in the deep UV range. As such, (Al,Ga)N alloys can exhibit strong band mixing effects due to quantum confinement, strain and local alloy fluctuations. These effects are best described by a multi-band approach which cannot be properly captured by a single-band LLT model. Therefore, applying LLT to these alloys is not straightforward and additional consideration is required. Further discussion on how we approach this issue will be discussed in Sec. 6.3.1.

Lastly, these models typically treat the system at a macroscopic scale and rely on averaged material properties, such as composition dependent band edges or effective masses. Such approaches do not specifically account for the individual atomic species in a disordered alloy. As a result, LLT will only capture carrier localisation effects on the nm length scale depending on the choice of the broadening of the Gaussian. It will not capture effects that may become important on the unit cell level. Therefore, to capture these microscopic effects, a more detailed atomistic model is required. This leads us to the semi-empirical tight-binding (TB) approach which offers a framework to resolve the alloy disorder, local strain, built-in fields and orbital mixing at an atomic level, while remaining computationally feasible for large nanostructures.

3.2.3 Tight-binding model

Another approach that allows us to avoid the large computational costs required for ab initio calculation is the TB model [48, 59, 122]. This approach allows us to investigate the electronic structure properties of a material while retaining an atomistic resolution.

The main assumption of the TB model is that the core electrons are tightly bound to the crystal lattice ions and therefore exhibit very little overlap with the orbitals of adjacent atoms. The wave functions of the electronic states can be described as linear combinations of these strongly localised atomic-like orbitals. Furthermore, because the atomic-like orbitals are strongly localised to the ion sites, the interaction between the orbitals and distant atoms will decay rapidly.

Varying levels of complexity can be added to the model to improve accuracy, depending on the material being investigated. This can include the incorporation of overlap matrix elements beyond nearest neighbours (e.g next-nearest neighbour) [137], increasing the number of basis states (atomic orbitals) or including SOC to refine the models prediction of the electronic structure. [123, 138, 139]. For this study into (Al,Ga)N, we employ a nearest neighbour sp^3 TB model which is based on four atomic-like orbitals: s, p_x, p_y and p_z per lattice site [140]. Although effects such as the SOC can impact the electronic structure of III-V materials in general [63], for III-Ns the SOC energy Δ_{so} is relatively small in magnitude, $\approx$ 5 - 20 meV [63, 65], having little effect on the predicted electronic structure and band gaps. Therefore, it is of secondary importance and we neglect it in our description of the electronic structure of III-N materials, which is a widely used approach [63, 123].

In the following we will discuss the construction of a TB hamiltonian for a bulk system following Ref. [63]. The localised basis states, $|\mathbf{R}_n, \alpha, \nu\rangle$, describe the atomic-like orbitals of character ν (with $\nu \in s$, p_x, p_y, p_z) located at position $\mathbf{R}_n$ within the unit cell. Each unit cell may contain anions and cations of differing species, labelled by α, and n runs over all unit cells in the lattice. Starting from the assumption that an isolated atom is located at the position $\mathbf{R}_l$, the Schrödinger equations reads:

$$H_{at}|\mathbf{R}_l, \alpha, \nu\rangle = E_{at}^{\alpha,\nu}|\mathbf{R}_l, \alpha, \nu\rangle \ , \tag{3.32}$$

where the atomic Hamiltonian is

$$H_{at} = \frac{\mathbf{p}^2}{2m} + V_{at}(\mathbf{R}_l, \alpha) \ . \tag{3.33}$$

Here, $V_{at}(\mathbf{R}_l,\alpha)$ is the atomic potential of the atom α at $\mathbf{R}_l$. The presence of the other ions in the crystal will modify the wave functions of atom α. Thus, the Hamiltonian can be written as:

$$H^{\mathrm{SP}} = H_{at}(\mathbf{R}_l, \alpha) + \underbrace{\sum_{\substack{n \neq l \\ \alpha'}} V(\mathbf{R}_n, \alpha')}_{\Delta V(R_l)} \ . \tag{3.34}$$

Here $H_{at}(\mathbf{R}_l,\alpha)$ is the Hamiltonian operator of the isolated atom α at position $\mathbf{R}_l$ and $\Delta V(\mathbf{R}_l)$ is the periodic potential due to the other ions in the lattice. This potential effectively renormalises the atomic Hamiltonian, allowing for a single-particle description within the crystal environment. The bulk single-particle wave function is therefore:

$$H^{\mathrm{SP}}|\mathbf{k}\rangle = E(\mathbf{k})|\mathbf{k}\rangle \ . \tag{3.35}$$

The eigenstates can be expressed as a linear combination of Bloch-type wave functions constructed from the atomic orbitals:

$$\begin{aligned} |\mathbf{k}\rangle &= \sum_{\alpha,\nu} c_{\alpha,\nu}(\mathbf{k}) \left(\sqrt{\frac{V_0}{V}} \sum_n e^{i\mathbf{k}\cdot(\mathbf{R}_n+\Delta_\alpha)} |\mathbf{R}_n, \alpha, \nu\rangle \right) \\ &= \sum_{\alpha,\nu} c_{\alpha,\nu}(\mathbf{k}) |\mathbf{k}, \alpha, \nu\rangle \ , \end{aligned} \tag{3.36}$$

where $c_{\alpha,\nu}(\mathbf{k})$ are the expansion coefficients, V_0, is the volume of the unit cell, V is the volume of the full system, n runs over all unit cells as before and the position of the atom α within unit cell n is given by Δ_α. It can be shown that this ansatz for $|\mathbf{k}\rangle$ satisfies Bloch's theorem [63], thus we restrict our analysis to $\mathbf{k}$ being in the FBZ.

The next step is to determine the expansion coefficients. To do so, we substitute our ansatz for $|\mathbf{k}\rangle$ given in eq. (3.36) into eq. (3.35) and multiply on the left by the bra vector $\langle \mathbf{k}, \alpha', \nu'|$. After some manipulation we find:

$$\sum_{\alpha,\nu} H^{SP}_{\alpha',\nu';\alpha,\nu}(\mathbf{k}) c_{\alpha,\nu}(\mathbf{k}) = E(\mathbf{k}) \sum_{\alpha,\nu} S_{\alpha',\nu';\alpha,\nu}(\mathbf{k}) c_{\alpha,\nu}(\mathbf{k}), \tag{3.37}$$

where the Hamiltonian matrix elements, $H^{SP}_{\alpha',\nu';\alpha,\nu}(\mathbf{k})$, and the overlap matrix elements, $S_{\alpha',\nu';\alpha,\nu}(\mathbf{k})$, are given by

$$H^{SP}_{\alpha',\nu';\alpha,\nu}(\mathbf{k}) = \frac{V_0}{V}\sum_{n,m} e^{i\mathbf{k}\cdot(\mathbf{R}_n+\Delta_\alpha-\mathbf{R}_m-\Delta'_\alpha)}\langle \mathbf{R}_m,\alpha',\nu'|H^{\mathrm{SP}}|\mathbf{R}_n,\alpha,\nu\rangle \tag{3.38}$$

and

$$S_{\alpha',\nu';\alpha,\nu}(\mathbf{k}) = \frac{V_0}{V}\sum_{n,m} e^{i\mathbf{k}\cdot(\mathbf{R}_n+\Delta_\alpha-\mathbf{R}_m-\Delta'_\alpha)}\langle \mathbf{R}_m,\alpha',\nu'|\mathbf{R}_n,\alpha,\nu\rangle. \tag{3.39}$$

Due to the general assumption of the TB model that the electrons are tightly bound to the atomic sites there should be very little wave function overlap between distant atoms. Nevertheless, the atomic-like orbitals are not generally mutually orthogonal to each other when calculating the overlap of wave functions localised on different atoms in the lattice. Thus, the conditions

$$\langle \mathbf{R}_m,\alpha',\nu'|\mathbf{R}_n,\alpha,\nu\rangle = \delta_{m,n}\delta_{\alpha',\alpha}\delta_{\nu',\nu}\ , \tag{3.40}$$

for nearest neighbour sites will not necessarily be fulfilled. However, the Löwdin transformation will convert the TB basis into an orthonormal basis while preserving the localised nature of the basis orbitals and their symmetry [141]. Proceeding now as if we have used Löwdin transformation to work with orthonormal basis states, the elements of the overlap matrix, S, become

$$S_{\alpha',\nu';\alpha,\nu} = \delta_{\mathbf{R}_m,\mathbf{R}_n}\delta_{\alpha',\alpha}\delta_{\nu',\nu}\ , \tag{3.41}$$

and eq. (3.37) reduces to

$$\sum_{\alpha,\nu} H^{SP}_{\alpha',\nu';\alpha,\nu}(\mathbf{k})c_{\alpha,\nu}(\mathbf{k}) = E(\mathbf{k})c_{\alpha',\nu'}(\mathbf{k}). \tag{3.42}$$

For an easier discussion, we consider a simplified case in which there is only one atomic species and one s-like orbital at each lattice site. Thus, the sum of over

α and ν is eliminated in our discussion here:

$$H^{\mathrm{SP}}_{\alpha,\nu;\alpha,\nu}(\mathbf{k}) = \langle \mathbf{k},\alpha,\nu|H^{\mathrm{SP}}|\mathbf{k},\alpha,\nu\rangle = E(\mathbf{k}) \tag{3.43}$$

and

$$\begin{aligned}\langle \mathbf{k},\alpha,\nu|H^{\mathrm{SP}}|\mathbf{k},\alpha,\nu\rangle &= \frac{V_0}{V}\sum_{m,n} e^{i\mathbf{k}\cdot(\mathbf{R}_n-\mathbf{R}_m)}\langle \mathbf{R}_m,\alpha,\nu|H^{\mathrm{SP}}|\mathbf{R}_n,\alpha,\nu\rangle \ , \\ &= \frac{V_0}{V}\sum_{m,n} e^{i\mathbf{k}\cdot(\mathbf{R}_n-\mathbf{R}_m)} I_{mn} \ .\end{aligned} \tag{3.44}$$

Due to the localised nature of the basis states, the integrals I_{mn} in eq. (3.44) become exponentially small for large values of $|\mathbf{R}_m$-$\mathbf{R}_n|$. Using the expression of H^{SP} in eq. (3.34), and considering now a specific atomic site, m, we can approximate the integrals, I_{mn} by

$$\begin{aligned} I_{mn} &= \delta_{n,m}\left[\langle \mathbf{R}_m,\alpha,\nu|H_{at}|\mathbf{R}_n,\alpha,\nu\rangle + \sum_{l\neq n}\langle \mathbf{R}_m,\alpha,\nu|V_{at}(\mathbf{R}_l,\alpha)|\mathbf{R}_n,\alpha,\nu\rangle\right] \\ &+ \delta_{n\pm1,m}\left[\langle \mathbf{R}_m,\alpha,\nu|V_{at}(\mathbf{R}_l,\alpha)|\mathbf{R}_n,\alpha,\nu\rangle\right] \\ &+ \delta_{n\pm2,m}\left[\langle \mathbf{R}_m,\alpha,\nu|V_{at}(\mathbf{R}_l,\alpha)|\mathbf{R}_n,\alpha,\nu\rangle\right] + ... \\ &= \delta_{n,m}\tilde{E} + \delta_{n\pm1,m}\lambda + ... \end{aligned} \tag{3.45}$$

In our nearest neighbour model, the expression is truncated after the $\delta_{n\pm1,m}$ term. $\tilde{E}$ is the on-site energy, which can be interpreted as the renormalized atomic energy level modified by the influence of neighbouring atoms in the lattice. The parameters λ, which describes off-diagonals terms in the TB Hamiltonian matrix, is called a hopping integral/matrix element. It describes the coupling between orbitals located at different atomic sites, giving the probability amplitude of an electron moving from one atomic site to another [59, 63]. The contributions to the sums in eq. (3.45) involves solving two-centre and three-centre integrals depending on $\mathbf{R}_m$, $\mathbf{R}_n$ and $\mathbf{R}_l$. A two centre integral is $\mathbf{R}_m$=$\mathbf{R}_l$≠$\mathbf{R}_n$ and a three centre integral involves $\mathbf{R}_m$≠$\mathbf{R}_l$≠$\mathbf{R}_n$. Slater and Koster proposed the two centre approximation which allows us to effectively ignore the three centre integrals as they are relatively small compared

to the two centre integrals [142]. Slater and Koster expressed the two centre integrals in terms of directional cosines between the orbitals on different lattice sites [142].

There are two main approaches for determining the TB matrix elements in eq. (3.45). The first option is first principle or *ab initio* approaches where one assumes an explicit form for the basis states and calculates the matrix elements. An example of this would be a density functional tight-binding model [143, 144]. The second option is a semi-empirical or empirical approach, in which the TB matrix elements are treated as free parameters that are fitted to band structure data, either obtained from experimental results or determined from *ab initio* calculations such as DFT.

The TB model used throughout this work employs a semi-empirical method that has been fitted to HSE hybrid functional DFT band structures of bulk AlN and GaN while also being benchmarked against experimental data for alloyed systems and heterostructures [61, 81, 133]. The specific TB parameters used for AlN and GaN are provided in Table A.2 of Appendix A.

So far we have described how the TB model can be applied to a bulk binary system. To extend this model to simulate alloys, 'relatively' simple adjustments must be made. For the cation sites (e.g. Al, Ga), the nearest neighbour environment always consists of four N anions. Therefore, assuming no strain, the on-site matrix elements and hopping parameters for cation sites can be simply assigned to the corresponding bulk binary. However, for the nitrogen anion sites, the nearest neighbour environment can contain a mixture of the cations species (Al and Ga). To account for this, we follow a common approach in which the on-site matrix elements for nitrogen is given as a weighted average of the binary values, based on the ratio of nearest neighbour atomic species [81, 145, 146, 147]. The hopping matrix elements are assigned according to the specific bonding pair, therefore no interpolation between the binaries is needed. Finally, The GaN/AlN band offset is included by shifting the GaN on-site matrix elements by the valence band offset, $\Delta E_{\mathrm{VB}} = 0.9$ eV, which lies within the reported values of 0.85-1.15 eV [117, 148].

3.2.3.1 Strain & Valence Force Field Model

As described earlier for continuum-based calculations, macroscopic strain accounts for the deformation a material experiences due to, for instance, the presence of an underlying substrate. However, in addition to the macroscopic

effect, a material will also exhibit microscopic strain due to changes in the local bond lengths and bond angles. This local deformation of the crystal lattice will in turn modify the on-site energies through variations in the local potential in the surrounding lattice. Additionally, the hopping matrix elements for the TB model, which possesses an atomistic resolution of the unit cells, must also consider the impact of these local strain effects. This requires the modification of the on-site energies and the hopping matrix elements due to variations in the bond lengths and bond angles. To do this we calculate the local strain tensors. TB models have been developed to incorporate these local strain variations, but they typically require a large number of fitting parameters [149, 150]. Similar to the strain correction applied in continuum models, strain can also be included in TB models as on-site corrections. For a sp^3 basis it has been shown that strain can be added to the TB Hamiltonian [149, 151] such that

$$H = H_0 + H_{strain} \ , \tag{3.46}$$

where H_0 is the Hamiltonian of the unstrained system and H_{strain} is a site diagonal Pikus-Bir Hamiltonian for the atomic site i such that [64, 81, 152]

$$H^i_{strain} = \begin{pmatrix} S_s & 0 & 0 & 0 \\ 0 & S_{xx} & S_{xy} & S_{xz} \\ 0 & S_{xy} & S_{yy} & S_{yz} \\ 0 & S_{xz} & S_{yz} & S_{zz} \end{pmatrix}. \tag{3.47}$$

Here

$$S_s = a_{ct}(\epsilon_{11} + \epsilon_{22}) + a_{cp}\epsilon_{33}, \tag{3.48a}$$
$$S_{xx} = (D_2 + D_4)(\varepsilon_{11} + \varepsilon_{22}) + D_5(\varepsilon_{11} - \varepsilon_{22}) + (D_1 + D_3)\varepsilon_{33}, \tag{3.48b}$$
$$S_{yy} = (D_2 + D_4)(\varepsilon_{11} + \varepsilon_{22}) - D_5(\varepsilon_{11} - \varepsilon_{22}) + (D_2 + D_3)\varepsilon_{33}, \tag{3.48c}$$
$$S_{zz} = D_2(\varepsilon_{11} + \varepsilon_{22}) + D_1\varepsilon_{33}, \tag{3.48d}$$
$$S_{xy} = 2D_5\varepsilon_{12}, \tag{3.48e}$$
$$S_{xz} = \sqrt{2}D_6\varepsilon_{13}, \tag{3.48f}$$
$$S_{yz} = \sqrt{2}D_6\varepsilon_{23}. \tag{3.48g}$$

The D_i terms are the valence band deformation potentials, obtained from HSE-DFT, while a_{cp} and a_{ct} are the conduction band deformation potentials (values listed in Table A.1 Appendix A). The ε_{ij} denote the strain tensor components. Using a weighted average based on the ratio of the nearest neighbour atomic species, the deformation potentials for the highest valence band and lowest conduction band states are included directly from the HSE-DFT calculations in the TB model. This avoids fitting of parameters and describes correctly the band edge shifts at the Γ point [81]. It should be noted that the deformation potentials are fitted in the vicinity of the Γ point [66] and thus may not reliably predict the band structure undergoing strain near the edges of the FBZ. However, since the electronic and optical properties of (Al,Ga)N are primarily governed by the band edges at the Γ point, the above employed approach will be sufficient. Furthermore, it is equivalent to how strain effects are treated in multi-band $\mathbf{k} \cdot \mathbf{p}$ models of III-N heterostructures [152]. In order to apply these strain corrections, knowledge about the local strain field is required. From an atomistic perspective, deformations in the crystal lattice give rise to local strain fluctuations due to the deviation of atoms within a given unit cell, as well as overall deformations of the unit cell in a crystal. Therefore, an atomistic model compatible with the TB model that describes how these atoms are displaced is needed in order to find the relaxed atomic positions, which minimise the elastic energy of the system.

A variety of methods have been developed to describe the potential energy of a crystal, alloy or heterostructure on a semi-empirical basis [153, 154, 155, 156]. Here, we employ a so-called valence force field (VFF) model which is widely used to obtain strain fields or relaxed atomic positions in large supercells, for instance, in heterostructure simulations on an atomistic level [157, 158]. The employed VFF model reproduces real wurtzite system attributes such as deviations from the ideal c/a ratio and the internal parameter u, while explicitly incorporating electrostatic effects [78].

In this VFF model, the interatomic interaction potential include the change in bond geometries where the energy at a given atomic site, V_i, is

$$V_i = \frac{1}{2}\sum_{j\neq i}\underbrace{\frac{1}{2}k_r(r_{ij}-r_{ij}^0)^2}_{\text{bond stretching}} + \sum_{j\neq i}\sum_{k\neq i k>j}\underbrace{\frac{1}{2}k_\theta^i r_{ij}^0 r_{ik}^0(\theta_{ijk}-\theta_{ijk}^0)^2}_{\text{bond bending}}$$
$$+\underbrace{k_{r\theta}^i(\theta_{ijk}-\theta_{ijk}^0)\left[r_{ij}^0(r_{ij}-r_{ij}^0)+r_{ik}^0(r_{ik}-r_{ik}^0)\right]}_{\text{bond-angle}} + \underbrace{k_{rr}^i(r_{ij}-r_{ij}^0)(r_{ik}-r_{ik}^0)}_{\text{bond-bond}}$$
$$+\sum_{j\neq i}{}'\underbrace{\frac{e^2}{4\pi\epsilon_0\epsilon_r}\frac{Z_i^*Z_j^*}{r_{ij}}}_{\text{Coulomb}} - \frac{1}{2}\sum_{j\neq i}\underbrace{\frac{1}{4}\alpha_M\frac{e^2}{4\pi\epsilon_0\epsilon_r}\frac{Z_i^*Z_j^*}{r_{ij}^2}(r_{ij}-r_{ij}^0)}_{\text{Coulomb screening}}. \tag{3.49}$$

In this expression k_r, k_θ^i, $k_{r\theta}^i$ and k_{rr}^i are the force constants related to changes in the bond geometry: k_r describes changes in bond length (bond stretching), k_θ^i describes changes in bond angle (bond bending), $k_{r\theta}^i$ represents the coupling between the bond length and bond angle changes (bond-angle) and k_{rr}^i is the coupling between bond lengths of different bonds (bond - bond). All these terms only consider the four nearest neighbour atoms that form the local tetrahedron around a given atom, as illustrated for wurtzite in Fig. 3.1. In the unstrained bulk system, the bond length between atomic site i and j is given by r_{ij}^0, while the angle between the bonds connecting the atomic site i to atomic sites j and k is given by θ_{ijk}^0. The bond lengths and bond angles in the strained system are given by r_{ij} and θ_{ijk}, respectively. The Coulomb term in eq. (3.49) accounts for the electrostatic potential from all atoms in the crystal lattice, not just the nearest neighbours and is denoted by $'$. Here, the elementary charge is e, the vacuum permittivity is ϵ_0 and the relative permittivity is ϵ_r, Z_i^* is the effective charge for atom i, and finally, α_M is the Madelung constant. The Coulomb screening term introduces the linear repulsive correction, which screens the linear part of the Coulomb interaction between the nearest neighbours. This ensures the correct symmetry of the elastic constant and stabilises the crystal structure [78, 158].

The force constants are determined by fitting to the elastic tensor obtained from HSE-DFT calculations which is done for the binary values and can be found in Appendix A Table A.1. The model is implemented within the molecular dynamics software package LAMMPS [159]. In this work, the potential energy of the alloyed structure is minimised using LAMMPS in order to determine the relaxed atomic positions [159]. For an alloy, such as (Al,Ga)N, the force constants are obtained by taking weighted averages of the corresponding binary

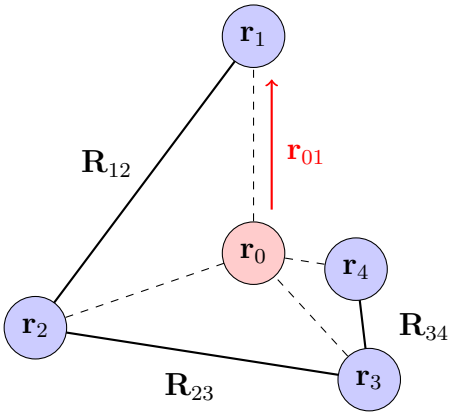


Figure 3.1: Schematic of a local tetrahedron of the cation (red) atomic site at position $\mathbf{r}_0$ bonded (dashed lines) to four nearest neighbour anions (blue). Each anion is located at vectors $\mathbf{r}_{ij}$ from atom 0. Only the vector to atom 1, $\mathbf{r}_{01}$, is shown. The local tetrahedrons edges, $\mathbf{R}_{ij}$, are shown as solid lines.

compounds force constants depending on the local environment.

The local strain tensor can be constructed using the method in Ref [81, 160]. The local strain tensor at a position $\mathbf{r}$ (e.g. $\mathbf{r}_0$ in Fig. 3.1) is given by

$$\varepsilon(\mathbf{r}) = \begin{pmatrix} R_{12,x} & R_{23,x} & R_{34,x} \\ R_{12,y} & R_{23,y} & R_{34,y} \\ R_{12,z} & R_{23,z} & R_{34,z} \end{pmatrix} \times \begin{pmatrix} R^0_{12,x} & R^0_{23,x} & R^0_{34,x} \\ R^0_{12,y} & R^0_{23,y} & R^0_{34,y} \\ R^0_{12,z} & R^0_{23,z} & R^0_{34,z} \end{pmatrix}^{-1} - \mathbf{1} \ . \tag{3.50}$$

Here, for example, $\mathbf{R}_{12} = (R_{12,x}, R_{12,y}, R_{12,z})^T$ is the edge of the local tetrahedron between atom 1 ($\mathbf{r}_1$) and atom 2 ($\mathbf{r}_2$) in Fig. 3.1. With the local strain tensor found, we can now include the effect of strain on the TB Hamiltonian described above earlier. However, these local strain effects can now lead to local piezoelectric polarisation effects. Thus, a method is needed to treat local fluctuations in the piezoelectric polarisation that arise from local fluctuations in strain.

3.2.3.2 Polarisation

To briefly summarise the discussion in Sec. 2.3, the wurtzite crystal structure of III-nitrides, such as AlN and GaN, lack an inversion of symmetry. This absence means that deformations of the crystal lattice lead to the formation of net dipole moments, known as the piezoelectric effect [81]. In addition, these materials are intrinsically polar. As a result, even in the absence of strain, the

net dipole per unit volume gives rise to spontaneous polarisation [81].

On a macroscopic level, as described in Sec. 2.3, the total polarisation can be expressed as the sum of the piezoelectric and polarisation components (eq. (2.25)). However, as similarly discussed in the case of strain, the polarisation field can also be split into macroscopic and microscopic contributions.

The relaxed atomic positions will result in local polarisation fluctuations to occur depending on the local atomic environment. By employing the VFF model to describe local fluctuations in strain for the nearest neighbour model, as outlined above, we are able to determine the associated local fluctuations in piezoelectric polarisation via the so-called local polarisation theory [81]. The central result of Ref. [81] is that the i^{th} component of the total polarisation at a given atomic site, labelled as 0 in the following, can be expressed as the sum of a macroscopic and local contribution

$$P_i = \underbrace{\sum_{j=1}^{6} e_{ij}^{(0)} \varepsilon_j}_{\text{macroscopic}} + \underbrace{P_i^{\text{SP}} - \frac{e}{V_0} Z_i^0 N_{\text{coor}}^0 \left[\mu_i - \sum_{j=1}^{3} (\delta_{ij} + \varepsilon_{ij}) \mu_{j,0} \right]}_{\text{local}} . \tag{3.51}$$

$e_{ij}^{(0)}$ are the piezoelectric coefficients obtained by a clamped-ion calculation in which the internal degrees of freedom of the atoms are not allowed to relax [161]. ε_j is the macroscopic strain in Voigt notation. The i^{th} component of the spontaneous polarisation is denoted by P_i^{SP}. The volume of the local tetrahedron (as seen in Fig. 3.1) is V_0, while Z_i^0 is the Born effective charge of atom 0 and N_{coor}^0 is the number of nearest neighbours with respect to atom 0. The bond asymmetry parameter, μ_i, is defined as a summation over the nearest-neighbour distances given by

$$\mu_i = \sum_{\alpha=1}^{N_{\text{coor}}^0} l_i^{\alpha}, \tag{3.52}$$

where

$$l_i^\alpha = \sum_{j=1}^{3} (\delta_{ij} + \varepsilon_{ij}) l_{j,0}^\alpha + t_i^\alpha - t_i^0 \ . \tag{3.53}$$

$l_{j,0}^\alpha$ denotes the j^{th} component of the vector from atom 0 to each of the nearest neighbours for the unstrained system, while ε_{ij} represents the strain tensor in Cartesian coordinates and δ_{ij} is the Kronecker delta function. The i^{th} component of the internal strain vector for atom α is t_i^α, hence t_i^0 corresponds to atom 0. Summing these vectors over all the nearest neighbours, one obtains the bond asymmetry, μ, in the local bonding environment that gives rise to piezoelectricity in the strained system. In the case for an unstrained binary wurtzite crystal, the bond asymmetry vector μ_0 has only a non-zero z component [35]. The components of μ_0 contribute to the local part of eq. (3.51) through $\mu_{j,0}$. Multiple approximations have been made in the derivation of this eq. (3.51) in Ref. [81]. 1) the spontaneous polarisation is constant throughout the crystal for binaries. However, it is defined as a local quantity in order to deal with alloys. 2) The description of the piezoelectric response to strain is truncated to first order in both the macroscopic and internal strain. 3) The off-diagonal terms of the Born effective charge tensor are zero. 4) A spherical approximation is used for the calculation of the Born effective charge of the nearest neighbours of the atom under consideration. The impact of these approximations for III-N systems have been evaluated by a comparison with DFT Berry phase calculations, demonstrating excellent agreement. Further detail can be found in Ref. [81].

Generally, polarisation can be understood as dipole moment per unit volume, and so here, P_i in eq. (3.51) can be described as the dipole density at an atomic site, $\mathbf{P}$. This value is determined for only the cation sites because each nearest neighbour is a N atom, therefore reducing the number of Born effective charges needed to just two, one for AlN and another for GaN. Using the determined polarisation vector field, we may now calculate the associated potential. In a continuum approach solving the Poisson equation is straightforward, but in an atomistic approach, the relaxed atomic positions make an irregular grid, leading to technical challenges and increased numerical cost [81]. Therefore, a point-dipole method is employed, where the potential at each atomic site is determined as the sum of contributions from all the dipoles in the lattice [81]. This method naturally discretises the strained, irregular grid determined by the

relaxed atomic positions. The local volume element for a cation is given by the volume of the tetrahedron formed by the nearest neighbours of a given atomic site. This volume, determined by the atomic positions $\mathbf{r}_j$, $j \in \{1,2,3,4\}$, is

$$V_{1234} = \frac{1}{6}\left|(\mathbf{r}_1 - \mathbf{r}_4)\cdot[(\mathbf{r}_2 - \mathbf{r}_4)\times(\mathbf{r}_3 - \mathbf{r}_4)]\right| . \tag{3.54}$$

It can be shown that V_{1234} corresponds to the volume of a tetrahedron and that the summation of the volumes of all the tetrahedra contained in the material sample would underestimate the system volume by a factor of 6. Therefore, the tetrahedra volume is

$$\tilde{V} = 6V_{1234} . \tag{3.55}$$

If we label the grid points by their positions $\mathbf{r}_i$, the dipole moment, $\mathbf{p}_i$, with the corresponding volume, $\tilde{V}$, is given by

$$\mathbf{p}_i = \mathbf{P}_i\tilde{V}. \tag{3.56}$$

The point dipole at $\mathbf{r}_\alpha$ generates a potential at position $\mathbf{r}$, $\phi_\alpha(\mathbf{r})$, which is given by the multipole expansion [162]

$$\phi_\alpha(\mathbf{r}) = \frac{1}{4\pi\epsilon_0\epsilon_r}\frac{\mathbf{p}_\alpha\cdot(\mathbf{r}-\mathbf{r}_\alpha)}{|\mathbf{r}-\mathbf{r}_\alpha|^3} . \tag{3.57}$$

Thus, at a given atomic site the total polarisation potential will be the sum of all the contributions at that point. For example, the polarisation potential, φ_{pol}, at the atomic site at position $\mathbf{r}$, will be given by

$$\varphi_{\mathrm{pol}}(\mathbf{r}) = \sum_{k\neq\alpha}\phi_k(\mathbf{r}) . \tag{3.58}$$

Incorporating the polarisation into the electronic structure within the TB framework is done by using a site-diagonal correction, as performed for the

strain corrections described above.

Finally, the total Hamiltonian is

$$H = H^{\mathrm{SP}} + H_{strain} - q\varphi_{pol} \tag{3.59}$$

The described atomistic framework allows us now to determine the TB energies and wave functions by constructing and diagonalising the full Hamiltonian, H, for disordered III-N semiconductors. The model accounts for the effects of (local) strain and built-in fields, enabling fundamental insight into carrier localisation effects exhibited by (Al,Ga)N alloys and their impact on the electronic and optical properties. With this electronic structure framework in place, we now turn our attention to the carrier transport properties in (Al,Ga)N heterostructures, and how alloy disorder and localisation effects can be incorporated in drift-diffusion (DD) simulations. To do this, we next introduce the DD model, a widely employed set of equations which describes the carrier dynamics in semiconductor devices.

3.3 Drift-Diffusion

Similar to the calculation of the electronic band structure, there are many techniques for modelling the carrier transport in semiconductors, alloys and related devices. Broadly, these methods can be grouped into three categories based on how quantum effects are treated. First, fully quantum mechanical frameworks account for the propagation of carriers in a fully quantum mechanical description and is essential for accurately describing transport in nanoscale systems [163]. A prominent example of this method is non-equilibrium Green's function [164].

A second method is a semi-classical framework which lies in between a fully quantum mechanical model and a classical description. This framework has a significantly reduced numerical demand, in comparison to quantum mechanical approaches, while still incorporating quantum derived inputs such as band structure, effective masses and Fermi-Dirac statistics into the description of transport. An example is the Boltzmann transport equation [163, 165] which can capture carrier drift, diffusion and scattering rates.

Lastly, there is a purely classical model which treats carriers as point particles that obey classical mechanics. These models neglect both the wave nature of

the electrons and the underlying electronic band structure. It forms the basis for widely used models like the DD equations [163, 165] which describe carrier transport by utilising the macroscopic quantities like electric fields, carrier densities and their mobilities. Detailed derivations can be found in Refs. [163, 165].

Many III-N systems model carrier transport through a semi-classical method using a a self-consistent 1D Schrödinger-Poisson approach coupled with DD. This technique has been widely applied to study carrier transport properties for devices with large dimensions, such as LEDs, solar cells, transistors etc. However, this method is numerically very demanding for a 3D system, even if one neglects alloy disorder. In this work, we instead develop a semi-classical quantum corrected framework building on LLT and DD to simulate carrier transport in a 3D system.

To begin we will give a description of the DD equations as a starting point, and then go on to include quantum corrections via LLT. The resulting model can thus be regarded as a semi-classical approach, balancing computational efficiency with key quantum effects.

3.3.1 Drift-Diffusion Model

The standard expression of the DD model for the *electrons* is [166]

$$\frac{\partial n}{\partial t} + \nabla \cdot \mathbf{J}_n = G - R \ , \tag{3.60}$$

$$\mathbf{J}_n = \underbrace{-D_n \nabla n}_{Diffusion} + \underbrace{\mu_n n \nabla \psi}_{Drift} \ . \tag{3.61}$$

Equation (3.60) is the continuity equation for the particle density, describing the rate of change of the electron density, n, into and out of a given volume due to the divergence of the electron current density, $\mathbf{J}_n$, equal to the difference between the generation, G, of carriers and their recombination rate, R. Here, R can be described using the ABC model, where the (total) recombination rate is the sum of all three recombination processes discussed in Sec. 2.5.

Equation (3.61) describes the electron current density which is driven by the diffusion constant, D_n, where particles in an area of high concentration diffuse to an area of lower concentration resulting in a uniform distribution, and the

drift current describing the movement of charged particles due to an electric field, ψ, governed by the mobility, μ_n. These equations are also derived for hole densities, p, giving identical equations except that the electric field exerts a force in the opposite direction.

$$\frac{\partial p}{\partial t} + \nabla \cdot \mathbf{J}_p = G - R \ , \tag{3.62}$$

$$\mathbf{J}_p = -D_p \nabla p - \mu_p p \nabla \psi \ . \tag{3.63}$$

When a system is at equilibrium the current density is zero i.e. the rate of carrier generation equals the rate of recombination and the drift current is equal to the diffusion current. The carrier mobility is related to the diffusion constant through the Einstein relation [54] meaning

$$\mu_{n,p} = \frac{q}{k_B T} D_{n,p} \ . \tag{3.64}$$

This relationship can be visualised in a p-n junction where the high density of electrons and holes on the n- and p-side, respectively, diffuse to regions of lower density. As detailed in Sec. 2.4, this diffusion of charge particles results in an internal electric field pointing in the opposite direction, opposing further diffusion and forcing the carriers to drift back to an area of high concentration, thus reaching equilibrium. As described in the above equations, both the carrier continuity and current density will depend on the electrostatic potential, ψ, related to the intrinsic field. This potential will depend on the spatial distribution of the charged electron and hole particles. Therefore, to correctly simulate devices, the Poisson equation:

$$-\nabla \cdot (\epsilon(\mathbf{r}) \nabla \psi(\mathbf{r})) = \rho(\mathbf{r}) = q\Big(p(\mathbf{r}) - N_A^-(\mathbf{r}) - n(\mathbf{r}) + N_D^+(\mathbf{r})\Big) \ , \tag{2.27}$$

needs to be coupled with eq. (3.60) and eq. (3.61)

For a bi-polar system, such as an LED structure (see Sec. 2.4), both electrons and holes contribute to the charge density ρ. The net charge density is replaced with the total free electron charge density, $\rho = q(N_D - n)$, and the excess holes

are, $\rho = q(p - N_A)$, where N_D and N_A are the donor and acceptor densities, respectively. q is the elementary charge.

To describe how the current equations are coupled with Poisson's equation, we follow Ref. [98]. In this framework, the carrier densities for the electrons and holes in a semiconductor device are described in terms of a statistical function

$$n = N_c \mathcal{F}\left(\frac{q\psi - q\varphi_n - E_c}{k_b T}\right), \tag{3.65}$$

$$p = N_v \mathcal{F}\left(\frac{q\psi - q\varphi_p - E_v}{k_b T}\right). \tag{3.66}$$

Here, k_B is the Boltzmann constant and T is the temperature. $\varphi_{n,p}$ is the quasi-Fermi potential. From Poisson's equation given above, the electrostatic potential ψ is generated from the spatial distribution of mobile charges and fixed charges. E_c and E_v is the conduction and valence band edge energies, respectively, of the undoped material i.e. the absence of any electrostatic potential. $N_{c,v}$ are the effective density of states which, for a 3D system, is defined as

$$N_{c,v} = 2\left(\frac{m^*_{n,p} k_B T}{2\pi\hbar^2}\right)^{\frac{3}{2}}. \tag{3.67}$$

Here, $m^*_{n,p}$ is the effective mass of the electron and hole. $\mathcal{F}$ is a statistical distribution function that describes the occupation of energy states in the semiconductor by defining the relationship between the density of the free carriers, the electrostatic potential and the quasi-Fermi potentials. It can be described using a Boltzmann approximation for low carrier densities where

$$\mathcal{F}(\eta) \to exp(\eta), \tag{3.68}$$

or for more general cases with Fermi-Dirac statistics where $\mathcal{F}(\eta)$ is the Fermi integral of order 1/2

$$\mathcal{F}(\eta) = \frac{2}{\sqrt{\pi}} \int_0^\infty \frac{\xi^{1/2}}{1 + exp(\xi - \eta)} \mathrm{d}\xi. \tag{3.69}$$

Using the Einstein relation, eq. (3.64), and carrier density expressions, eq. (3.65) and eq. (3.66), the current density can be rewritten using the quasi-Fermi potentials [98] as follows:

$$\mathbf{J}_n = \mu_n n \nabla \varphi_n, \tag{3.70}$$
$$\mathbf{J}_p = -\mu_p p \nabla \varphi_p. \tag{3.71}$$

So far we have discussed the carrier density and their current density. To convert this to charge current density, the flow of electrons and holes are $\mathbf{j}_n = -q\mathbf{J}_n$ and $\mathbf{j}_p = +q\mathbf{J}_p$, respectively. Thus, the charge current densities are [98]

$$\mathbf{j}_n(\mathbf{r}) = -q\mu_n(\mathbf{r}) n(\mathbf{r}) \nabla \varphi_n(\mathbf{r}) \ ,$$
$$\mathbf{j}_p(\mathbf{r}) = -q\mu_p(\mathbf{r}) p(\mathbf{r}) \nabla \varphi_p(\mathbf{r}) \ .$$

This leads to the system of equations known as the van Roosbroeck system [167]:

$$-\nabla(\varepsilon(\mathbf{r})\nabla\psi(\mathbf{r})) = q\Big(p(\mathbf{r}) - N_A^-(\mathbf{r}) - n(\mathbf{r}) + N_D^+(\mathbf{r})\Big) \ , \tag{3.72a}$$
$$q\frac{\partial n(\mathbf{r})}{\partial t} - \nabla \cdot \mathbf{j}_n(\mathbf{r}) = q\Big(G(\mathbf{r}) - R(\mathbf{r})\Big) \ , \tag{3.72b}$$
$$q\frac{\partial p(\mathbf{r})}{\partial t} + \nabla \cdot \mathbf{j}_p(\mathbf{r}) = q\Big(G(\mathbf{r}) - R(\mathbf{r})\Big) \ , \tag{3.72c}$$
$$\mathbf{j}_n(\mathbf{r}) = -q\mu_n n(\mathbf{r}) \nabla \varphi_n(\mathbf{r}) \ , \tag{3.72d}$$
$$\mathbf{j}_p(\mathbf{r}) = -q\mu_p p(\mathbf{r}) \nabla \varphi_p(\mathbf{r}) \ . \tag{3.72e}$$

These set of equations, introduced in 1950, describe the transport of electrons and holes in a self-consistent electric field using a DD approximation. Since then the van Roosbroeck system, which is often just termed the DD system, has

become the standard model to describe the current flow and recombination in semiconductor devices at a macroscopic scale. An applied bias can be introduced via the boundary conditions of the quasi-Fermi potentials.

These DD equations are solved self-consistently with the Poisson equation, eq. (2.27), because the potential will depend on the position of the charges in the system. However, in many semiconductors, particularly for the III-Ns, not all dopant atoms are necessarily ionised at a given temperature [16]. This effect, known as incomplete ionisation [85], must be taken into account to accurately model the correct carrier density. The total density of ionised dopants depend on the position of the quasi-Fermi level relative to the dopant energy level and is governed by Fermi–Dirac statistics. For example, the concentration of ionised donors, N_D^+, can be expressed as [168]

$$N_D^+ = \frac{N_D}{1 + g_D \exp\left(\frac{E_{F,n} - E_{D,i}}{k_B T}\right)} \,, \tag{3.73}$$

where N_D is the total donor concentration, g_D is the donor degeneracy factor, $E_{F,n}$ is the quasi-Fermi level for electrons in the conduction band and $E_{D,i}$ is the energy of the neutral donor impurity. $E_{D,i}$ is defined as $E_{D,i} = E_c - e\varphi_n - E_A^n$ where φ_n is the quasi-Fermi potential of the electrons, E_A^n is the donor activation energy and e is the positive elementary charge. A similar expression holds for the ionised acceptors N_A^-

$$N_A^- = \frac{N_A}{1 + g_A \exp\left(\frac{E_{A,i} - E_{F,p}}{k_B T}\right)} \,. \tag{3.74}$$

Here, N_A is the total acceptor concentration and g_A is the acceptor degeneracy factor, $E_{F,p}$ is the quasi-Fermi level for the holes in the valence band and $E_{A,i}$ is the energy of the neutral acceptor impurity. As similarly defined, $E_{A,i} = E_v - e\varphi_p + E_A^p$, where φ_p is the quasi-Fermi potential of the holes and E_A^p is the acceptor ionisation energy.

For the degeneracy factors, $g_d = 2$ because a donor level can accept one electron either spin up or spin down, while $g_A = 4$ because each acceptor impurity level can accept one hole (lose an electron) of either spin and the impurity level is doubly degenerate as a result of the two degenerate/closely spaced valence

bands at $\mathbf{k} = 0$ [85, 168]. Incomplete ionisation becomes especially important at low temperatures or when deep-level dopants are present. The latter is particularly significant for p-doping in (Al,Ga)N materials, where high acceptor activation energies significantly limit hole activation, more detail is discussed in Chapter 6. This results in lower free carrier concentrations than predicted by full ionisation assumptions, and directly affects the space charge density ρ in the Poisson equation, as well as the devices electrical behaviour.

For this thesis, we are only interested in the steady-state current, so the time derivative of the electron and hole densities is irrelevant in the set of van Roosbroeck equations in eq. (3.72). In addition, for optoelectronic devices, the generation rate describes the production of free electrons and holes in the device. However, we are focusing on electrically pumped devices. Therefore, the generation rate is assumed to be negligible, especially in comparison to the recombination rate.

3.3.2 Energy Landscape for drift-diffusion

An important ingredient for establishing 3D quantum corrected DD models is determining the band edge energies. To do so we extract the band edge energies directly from our TB model and generate an energy landscape on an atomistic mesh. The advantage of our approach is that the band edge energies are directly extracted from the TB Hamiltonian which already includes the effect of local atomistic strain and polarisation fields. This enables us to generate an energy landscape for large scale devices while maintaining an atomistic resolution.

To extract this energy landscape we assume a nearest neighbour TB Hamiltonian, H, constructed for a supercell that incorporates alloy disorder. As outlined in Sec. 3.2.3.1, the equilibrium position of all atoms in the supercell are found by minimising the elastic energy of the VFF model and the local strain and polarisation fields are calculated. Thus, for a given lattice site only the interactions between the orbitals on nearest neighbour sites of the tetrahedra is necessary. Diagonalising the Hamiltonian allows us to find the single-particle states and energies. In addition, we can construct a *local* Hamiltonian, H^{local}, and diagonalise it at each lattice site to obtain the local band edges and, thus, an energy landscape $V(\mathbf{r})$. In the case of our nearest-neighbour sp^3 TB model H^{local} is a 8 x 8 matrix where [169]

$$H^{local} = \begin{pmatrix} E^0 & H_{int}^{1-4} \\ H_{int}^{1-4\dagger} & E^{1-4} \end{pmatrix}. \tag{3.75}$$

Here, E^0 is a 4×4 matrix describing the on-site energies of s, p_x, p_y and p_z orbitals of a given lattice site. H_{int}^{1-4} is a 4×4 matrix that is simply the sum of interactions (hopping matrix elements) between orbitals at the lattice site and its four nearest neighbours. E^{1-4} is another 4×4 matrix which contains the average on-site energies for s and p-orbitals of the nearest neighbours for a lattice site. Given that these matrix elements of H^{local} are taken from the full TB Hamiltonian, the effect of local strain and built-in polarisation fields are already included into the local band edges. This allows us to circumvent the need for additional calculations of averaging elastic or piezoelectric coefficients to obtain these fields. In addition, this energy landscape stems from a multi-band sp^3 TB description which inherently captures band mixing effects. This method of extracting the energy landscape from a TB Hamiltonian is further detailed in Refs. [2, 40, 104, 169, 170].

Ref. [42] demonstrates that the spatial length scale over which potential fluctuations influence charge transport of the electrons and holes is determined by the de Broglie wavelength. As a consequence, the charge carrier wave function will "see" a wider area of the energy landscape than just the single lattice site. This wave like nature of the carriers contrasts with the classical DD framework which treats charges as point-like particles, whereas a quantum mechanical treatment characterises the carriers as a wave function. To account for this behaviour in an energy landscape that strongly fluctuates, a Gaussian averaging procedure is performed. Refs. [42, 106] apply a Gaussian averaging to the *local alloy content*, from which the composition dependant elastic and piezoelectric constants are interpolated. We apply a Gaussian average to the *local band edge profile* $E_{v,c}^{TB}$ extracted from the TB model which already includes the effects of local strain and built-in polarisation fields. Thus, this approach bypasses the need for the interpolation of the parameters. Here, we calculate the conduction and valence band energy at a given lattice site $\mathbf{r}_i$ as

$$E^{\sigma}_{c,v}(\mathbf{r}_i) = \frac{\sum_j E^{TB}_{c,v}(\mathbf{r}_j)\exp\left(\frac{(|\mathbf{r}_i-\mathbf{r}_j|)^2}{2\sigma^2}\right)}{\sum_j exp\left(-\frac{(|\mathbf{r}_i-\mathbf{r}_j|)^2}{2\sigma^2}\right)}\,, \tag{3.76}$$

where σ is the Gaussian width which acts as a smoothening parameter. After having determined the local band edges from the TB model, quantum corrections can now be applied. Many commercial software packages have the option to include quantum mechanical effects by solving the Schrödinger equation inside the active region of a device. However, as discussed earlier, this approach is quite numerically demanding even for a 1D simulation, let alone a fully realised 3D simulation for III-Ns where it is important to include random alloy fluctuations which account for carrier localisation effects. As mentioned in Sec. 3.2.2.1, solving LLT circumvents solving the large eigenvalue problem that is the Schrödinger equation. Here, LLT is performed using the confining potential energy landscape extracted from the TB Hamiltonian whereupon an effective confining potential $W(\mathbf{r})$ can be determined via eq. (3.26). This corrected landscape will have "softened" potential energies at heterostructure interfaces which will mimic quantum tunnelling processes, allowing carriers to overcome potential barriers at lower energies in comparison to energies found in "classical" calculations.

Finally, to numerically solve the partial differential equations of the van Roosbroeck system for a 3D landscape that retains alloy fluctuations, we generate a 3D atomistic mesh that adopts the wurtzite lattice crystal structure the TB model is based on. For the atomistic mesh, a finite element method (FEM) mesh is constructed via WIAS-pdelib [171] and TetGen [172] where each atom lattice site is defined as nodes in the mesh. Each node contains the band edge energy from the corresponding lattice site determined by the TB energy landscape described above. Both the Gaussian averaging and the LLT treatment are performed on this mesh that adopts the wurtzite lattice crystal structure the TB model is based on. Running device transport simulations on a fully atomistic mesh is numerically quite demanding. Therefore, we adopt a multiscale simulation approach where the atomic region of interest, such as the active region containing quantum wells and barrier materials, is constructed with an atomistic resolution to model the microscopic disorders significant impact on carrier dynamics. In contrast, regions where fluctuations on a small

length scale are less critical to the device performance are treated with a coarser device mesh, such as the n-/p-doped contact regions. The band edge energies for these regions can then be defined as established values from the literature or from the the TB model itself and placed on a coarser mesh. This is done in order to keep the computational cost lower for the intensive self-consistent 3D DD simulation. The activation energy of the n- and p-type materials may be influenced by the alloy disorder, although how to incorporate this effect remains an open question in the literature. Due to the uncertainty in this aspect, we vary the activation energy in later studies (see Chapter 6). If disorder influences the activation energy, then this variation potentially captures its impact within the scope of our simulations

To perform the DD equations for the atomistic region, a finite volume method (FVM) mesh is generated from the atomistic mesh, again using TetGen, producing a boundary-conforming Delauney-tetrahedral mesh which includes the original FEM lattice sites where the atomistic data has been interpolated onto it. To describe the contact regions i.e. the coarser mesh, a FVM is also applied. The coarser meshes are then attached to either side of the atomistic region, again via TetGen. Thus, generating a complete device such as a p-i-n junction which can now be simulated using the DD simulations with ddfermi [173]. We discretise the DD equations onto Voronoi cells via the FVM, following Ref. [98]. This method ensures local current conservation between cells, which is essential for accurately modelling charge transport, especially in devices with sharp material interfaces like (Al,Ga)N heterostructures. Compared to finite difference and FEM, the FVM offers better handling of discontinuities and current conservation across control volume boundaries [98]. Further implementation details and comparisons of other discretisation schemes are provided in Refs. [98, 174]. This multiscale atomistic-continuum framework allows for accurate modelling of alloy disorder in critical regions while maintaining computational efficiency. A more detailed description and investigation into these mesh generations and the treatment of Gaussian averaging and LLT can be found in Refs. [169, 170].

Overall, in this chapter we have presented fundamental theories to describe the electronic structure of materials, alongside a methodology to avoid solving a large scale eigenvalue problem, as well as a semi-classical transport calculation for multiscale simulation of semiconductor devices. Previous work within the Photonics Theory Group (PTG) in the Tyndall National Institute helped established a wurtzite TB framework [63], the VFF and local polarisation

theory [175]. Coupling the atomistic electronic structure theory to carrier transport models was developed in collaboration with the Weierstrass Institute in Berlin, Germany, to address carrier transport in (In,Ga)N-based heterostructures and devices [170]. In this thesis, we have extended and adapted these models to describe (Al,Ga)N-based materials, heterostructures and in particular (deep) UV LEDs. It is to note that major extensions are required to capture the characteristics of (Al,Ga)N systems accurately. For instance, connecting the degree of optical polarisation to a hybrid band effective mass model for carrier transport presents a significant model development aspect of this thesis, with particular attention on the orbital characteristics and unique valence band ordering, which is not found in (In,Ga)N/GaN systems. Furthermore, previous simulation activities in the PTG and Weierstrass consortium on (In,Ga)N *p-i-n* junctions were limited to structures that neglect specific device aspects such as electron blocking layers (EBL) or the analysis of the activation energy of dopants. In collaboration with the team at the Weierstrass Institute, the work in this thesis has focused on the implementation of, for example, an incomplete ionisation model for full, realistic deep UV LED simulations. In addition, we developed here a consistent and reliable method of comparing atomistic structures with alloy fluctuations to VCA calculations, as well as connecting regions in the simulation that are treated with an atomistic resolution to VCA regions. In the following chapters we apply the here developed advanced simulation methods to investigate the electronic and optical properties of (Al,Ga)N-based QWs before utilising the information we have gained to investigate its transport properties for an (Al,Ga)N-based DUV LED.

Chapter 4

Electronic properties of (Al,Ga)N/AlN QWs

4.1 Introduction

Alloy disorder-induced carrier localisation effects in semiconductor materials have been a topic of extensive research for several decades [176, 177]. In the field of nitride-based semiconductor heterostructures it has gained significant momentum in recent years, due to the importance of such effects for the electronic and optical properties of 'classical' (e.g. light emitting diodes (LEDs)) and non-classical light sources (e.g. entangled photon emitters) [40, 45, 106, 178, 179].

Experimental studies on (Al,Ga)N QWs give clear indications of strong carrier localisation effects in these systems, e.g. revealed by an "S-shaped" temperature dependence of the PL peak position [32] or the very large full width at half maximum PL linewidth at low temperature [33].

Despite these observations, theoretical studies focusing on the impact of alloy disorder on the electronic structure of (Al,Ga)N QW systems are sparse. Recent calculations using modified continuum-based (single-band effective mass) descriptions have targeted pure GaN wells with (Al,Ga)N barriers, thus neglecting any alloy fluctuations *inside* the well [180]. In the continuum-based studies of Rudinsky and Karpov [181] it is *assumed* that hole states are strongly localised but electron states are delocalised. It is important to note that in Ref. [181] the carrier localisation characteristics are an *input* to the model.

To address this gap, in this chapter we perform a microscopic theoretical study that investigates the impact of random alloy fluctuations on the electronic properties of (Al,Ga)N QWs, by employing an atomistic empirical TB model as outlined in Sec. 3.2.3. This approach has already been benchmarked against experimental results for *bulk* (Al,Ga)N systems showing, for instance, good agreement in the band gap energy as a function of the alloy content [133]. Equipped with this model, and to focus on alloy disorder-induced carrier localisation effects in the well, we follow the experimental work in Refs. [32, 33, 182, 183] and focus our attention on (Al,Ga)N QWs with AlN barriers, as we will further outline in Sec. 4.2. In Sec. 4.3 we discuss the results of atomistic calculations on (Al,Ga)N/AlN QWs, revealing that random alloy fluctuations lead to strong hole wave function localisation effects, independent of the studied Al contents. Our theoretical studies also give indications of *electron* localisation effects due to alloy fluctuations at higher Al-contents (e.g. $\geq 50\%$).

4.2 Model quantum well system

Equipped with the information about the theoretical model, as discussed in Sec. 3.2.3, we describe in the following the QW model structures it is applied to. Given the microscopic resolution of our framework, we use supercells (with periodic boundary conditions) that contain 81,920 atoms, corresponding to a cell with the dimension of approximately 10 nm $\times$ 9 nm $\times$ 10 nm, in our calculations of the electronic properties of c-plane $Al_xGa_{1-x}N$/AlN QW systems. In general, we start from a cell of pure AlN (so all atoms in the cell are either Al or N). In a second step, Al atoms are replaced by Ga atoms in a specified sub-region of the cell which defines the well (between specified z-coordinates of the cell). The number of Al atoms replacing Ga atoms is determined by the Al/Ga content in the well. Here, no preferential positioning or clustering is assumed, building on findings from (In,Ga)N systems [184]. A schematic illustration of the simulation cell, including random alloy fluctuations, is given in Fig. 4.1.

Since the aim of this study is to focus on the impact of alloy disorder in the well, and to disentangle this from any effects arising from the alloy fluctuations in the barrier, we have focused here on pure AlN barriers.

Once the (different) atoms are placed on this wurtzite lattice, again reflecting the targeted alloy content, the elastic (VFF) energy of the system is minimised.

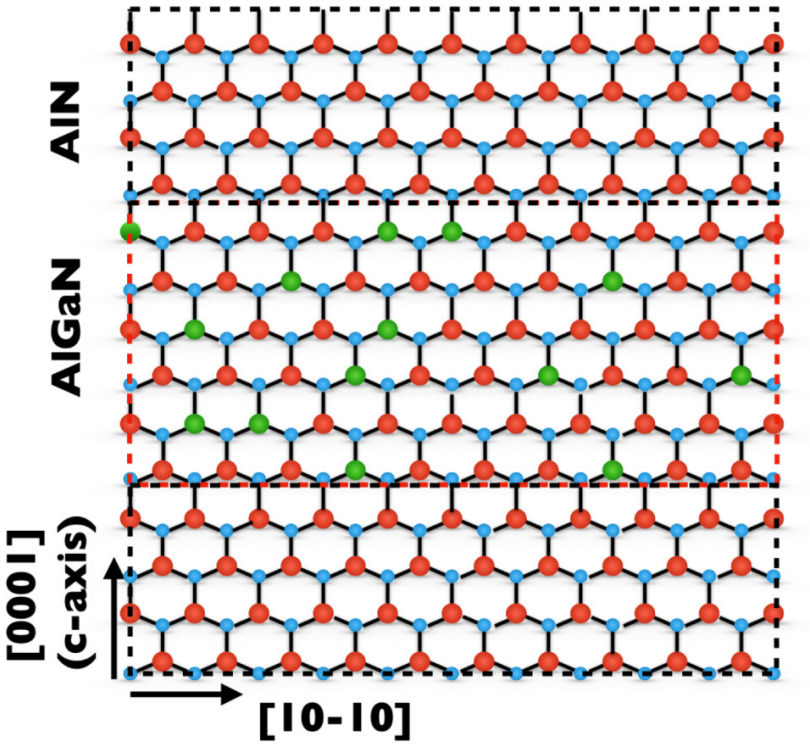


Figure 4.1: Schematic illustration of the supercell underlying the atomistic tight-binding calculations of the electronic properties of c-plane $Al_xGa_{1-x}N$/AlN quantum wells. In the region indicated by 'AlGaN', we assume a random distribution of Al (red) and Ga (green) atoms.

To do so, internal degrees of freedom for each atom are 'optimised' while the simulation cell is only allowed to expand or contract along the z-axis (c-axis), thus assuming here pseudomorphic growth on AlN. After the equilibrium structure is obtained, the underlying atom coordinates can be used for the calculation of the (local) polarisation fields and ultimately the TB model.

Below we investigate systems with Al contents of 10%, 25%, 50% and 75%. The chosen alloy contents allow us to cover the range experimentally relevant for developing emitters spanning from the UV-A all the way into the deep UV-C spectral region, even though they usually involve (Al,Ga)N barriers. We note that in the present study we always select the same number of atomic planes in which Al atoms are replaced by Ga atoms. As a consequence, after relaxing the atomic positions, and especially for different Al contents, the well width between the different calculations may be slightly different. However, overall the QW width of the different systems studied is approximately 2.9 nm. This approach allows us to focus on the impact of alloy disorder on the results rather than having well width variations as an additional parameter. However, we note that for instance, Frankerl *et al.* [32] highlighted that the well width can also

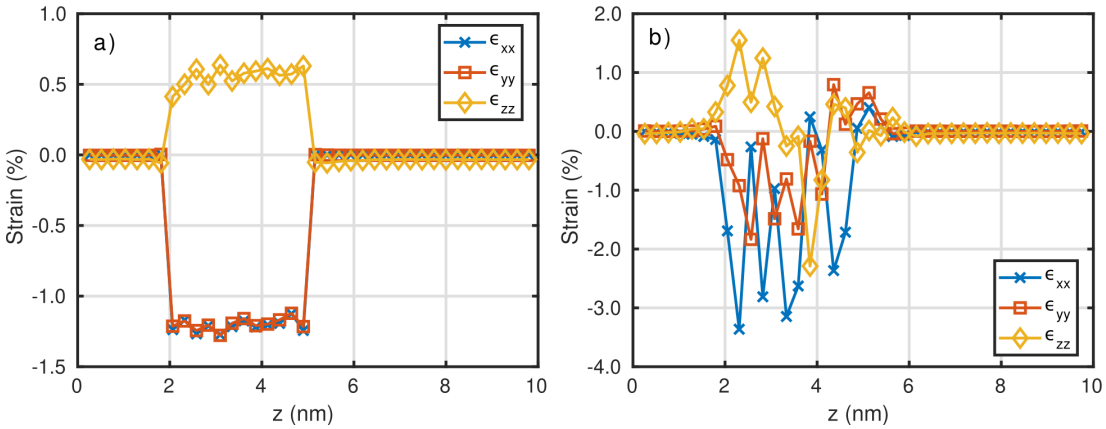


Figure 4.2: Strain tensor components ϵ_{xx}, ϵ_{yy} and ϵ_{zz} for a linescan along the z-axis (c-axis) of the simulation cell containing an $Al_{0.5}Ga_{0.5}N$/AlN quantum well. Data averaged over the simulation cell is shown in (a) while (b) shows an individual linescan.

impact carrier localisation effects. Understanding the interplay of alloy fluctuations, well width, interface roughness (well width fluctuations) and also Coulomb effects on carrier localisation effects in (Al,Ga)N QWs require further careful theoretical analysis, which can be targeted in future studies. Nevertheless, it is informative and important to understand the impact of random alloy disorder first before complicating the analysis further by considering e.g. well width fluctuations.

To characterise the structural properties of these systems, we analyse the strain profiles across the quantum wells. Using the approach discussed in Ref. [160, 185], Fig. 4.2 displays the diagonal components of the strain tensor, ϵ_{xx}, ϵ_{yy} and ϵ_{zz}, for a linescan along the c-axis of a c-plane $Al_{0.5}Ga_{0.5}N$/AlN QW. The data in Fig. 4.2 (a) are averaged over the supercell and reveal a behaviour expected from a continuum-based description of a c-plane (Al,Ga)N/AlN QW [14]: (i) there is no strain in the AlN barriers, (ii) due to the symmetry of the c-plane and the in-plane lattice mismatch between AlN and $Al_{0.5}Ga_{0.5}N$, to a first approximation $\epsilon_{xx} \approx \epsilon_{yy} \approx$ -1.2% and (iii) $\epsilon_{zz} > 0$. While Fig. 4.2 (a) shows in general a similar strain profile as can be expected from a continuum-based model, the figure reveals also differences, namely that even the averaged data show some fluctuations. This stems from the fact that the strain fluctuates locally, due to local fluctuations in Al and Ga atoms. Figure 4.2 (b) displays this clearly. Here the strain tensor components ϵ_{ii} are shown for a *single* linescan along the c-axis. In this case, ϵ_{xx} differs from ϵ_{yy} as well as ϵ_{zz}; all these components may even change sign or even exceed the

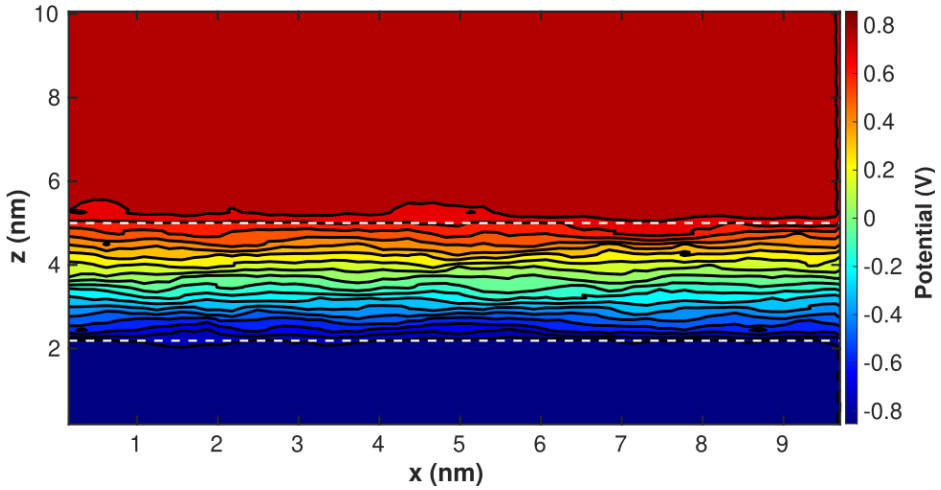


Figure 4.3: Contour plot of the polarisation potential ϕ_p arising from spontaneous and piezoelectric polarisation for an arbitrarily chosen x-z-plane in a c-plane $Al_{0.5}Ga_{0.5}N$/AlN quantum well.

lattice mismatch. Overall, several aspects are important when looking at the strain profile of an individual linescan. Firstly, since the overall energy of the system is minimised by 'optimising' the atomic positions, it is the nearest (and further away) neighbours that will determine the local strain tensor and not necessarily the atomic species at which the strain tensor is calculated. Secondly, it can be energetically more favourable to extend a bond along one direction and compress a bond (or have it even 'unstrained') along another direction. Thus, it is the full local strain tensor and not only an individual component that is reflecting the local elastic energy minimum. Therefore, it is useful to evaluate the strain averaged over the supercell, as done in Fig. 4.2 a), to gain insight into the strain in the structure in general. However, when it comes to carrier localisation effects, local strain contributions can play a significant role since they will impact the electronic structure locally. Such local strain effects are not captured in "standard" continuum-based models or a VCA of an alloy.

As already mentioned above, the overall strain profile, but also the (local) fluctuations, will give rise to (local) polarisation fields. This situation is visible in Fig. 4.3 which depicts a contourplot of the electrostatic built-in potential ϕ_p arising from spontaneous and piezoelectric polarisation in a c-plane $Al_{0.5}Ga_{0.5}N$/AlN QW. The local fluctuations in the built-in potential are reflected for instance in the situation that the contour lines within the QW are not parallel; parallel contourlines are usually expected from continuum-based calculations of polarisation fields in III-N QW structures, justifying the 1D calculations widely employed for these systems.

The analysis above already reveals that local alloy fluctuations noticeably affect strain fields and built-in potentials. Thus, these effects may significantly impact the electronic and in turn the optical properties of (Al,Ga)N QWs. To gain insight into these questions, 20 different random alloy configurations have been generated for each Al content (10%, 25%, 50% and 75%) in the well, and the influence of the alloy microstructure on the results will be discussed in more detail below.

4.3 Results

In the following section, Sec. 4.3.1, we start with some general considerations of wurtzite III-N materials and focus on differences between InN, GaN and AlN and how those differences may affect alloy-induced carrier localisation effects. In Sec. 4.3.2 we discuss the electronic structure.

4.3.1 General considerations

Before presenting our results on the electronic properties of *c*-plane (Al,Ga)N QWs, we discuss fundamental properties of AlN, GaN and InN systems first. This information will allow us to understand similarities and differences between (Al,Ga)N and (In,Ga)N-based heterostructures. In the experimental studies by Frankerl *et al.* [31] it is discussed that the atomic radius of an Al atom, in contrast to an In atom, is very similar to a Ga atom. So at first glance, replacing an Al atom with a Ga atom should perturb the local "energy landscape" to a lesser extent in an (Al,Ga)N alloy than when replacing Ga by In atoms as in an (In,Ga)N alloy. However, and in addition to this observation, several further factors are important when examining the impact of alloy disorder on the electronic structure. Firstly, even though the lattice mismatch in an (Al,Ga)N alloy is smaller in comparison to (In,Ga)N, the local strain effects seen in Fig. 4.2 (b) can still lead to noticeable fluctuations in the polarisation potential, and thus the local quantum confinement. In turn this may lead to carrier localisation effects.

Furthermore, the energy gap difference between AlN and GaN ($\Delta E_g^{\mathrm{AlN,GaN}} = E_g^{\mathrm{AlN}} - E_g^{\mathrm{GaN}} \approx 2.5$ eV) is comparable to that of GaN and InN ($\Delta E_g^{\mathrm{InN,GaN}} = E_g^{\mathrm{GaN}} - E_g^{\mathrm{InN}} \approx 2.8$) [60]; thus locally high Ga or Al contents in an (Al,Ga)N alloy may lead to significant changes in the local band gap values. Moreover, differences in the electronegativities for Al and Ga atoms (on Pauling

scale $\chi_p^{\mathrm{Al}} = 1.61$; $\chi_p^{\mathrm{Ga}} = 1.81$) are larger when comparing this to Ga and In atoms (on Pauling scale $\chi_p^{\mathrm{In}} = 1.78$) [186]. In alloys such as GaAsN, it has been shown that a contrast in electronegativity can lead to strong carrier localisation effects and band gap changes [187]. Thus taking all this together, and even though the atomic radii may not be too different between Al and Ga atoms, the above factors are indicative of strong carrier localisation effects in (Al,Ga)N.

Such an 'expectation' is further supported by the fact that in general the effective masses of the holes and the electrons in both AlN and GaN are close to, or even higher, when compared to InN [60, 64]. Similar to an (In,Ga)N QW system, strong localisation effects for holes can be expected in (Al,Ga)N wells, given the high and similar effective hole masses in both systems. However, the situation for electrons in (Al,Ga)N alloys may be different to (In,Ga)N since the conduction band effective mass in GaN and AlN is approximately at least a factor of 3 larger when compared to InN ($m_e^{\mathrm{AlN},\parallel} = 0.322$, $m_e^{\mathrm{AlN},\perp} = 0.329$; $m_e^{\mathrm{GaN},\parallel} = 0.186$, $m_e^{\mathrm{GaN},\perp} = 0.209$ and $m_e^{\mathrm{InN},\parallel} = 0.065$, $m_e^{\mathrm{InN},\perp} = 0.068$) [60, 188, 189, 190]. Based on this one may expect a stronger impact of alloy and well width fluctuations on the electron wave function in (Al,Ga)N QWs in comparison to (In,Ga)N systems. This may especially be the case for systems with 50% Al and 50% Ga contents, where smaller local regions of 'pure' GaN may be surrounded by 'pure' AlN, which can generate a local GaN/AlN quantum dot.

All this will contribute to the experimental observations that carrier localisation effects seem to be more pronounced in (Al,Ga)N/AlN wells when compared to (In,Ga)N QW systems, especially for structures close to the 50% Al and 50% Ga case, as discussed in Refs. [31, 32, 33]. However, it is important to stress that a one-to-one comparison between (Al,Ga)N and (In,Ga)N QWs is difficult, since *high quality* (In,Ga)N wells with 50% In content can basically not be realised in experiment.

4.3.2 Single-particle energies and states

We start our atomistic TB analysis of the electronic properties of *c*-plane $\mathrm{Al}_x\mathrm{Ga}_{1-x}\mathrm{N}$/AlN QWs, with Al contents ranging from 10% up to 75%, by looking at the *average* ground state energy, $E_g^{\mathrm{avg}} = \frac{1}{N}\sum_n^N E_g(n) = \frac{1}{N}\sum_n^N E_{\mathrm{GS}}^e(n) - E_{\mathrm{GS}}^h(n)$ of the $N = 20$ considered random alloy configurations per Al content. Here, $E_{\mathrm{GS}}^e(n)$ and $E_{\mathrm{GS}}^h(n)$ are the electron and hole ground state energy of a given alloy configuration n, respectively; note

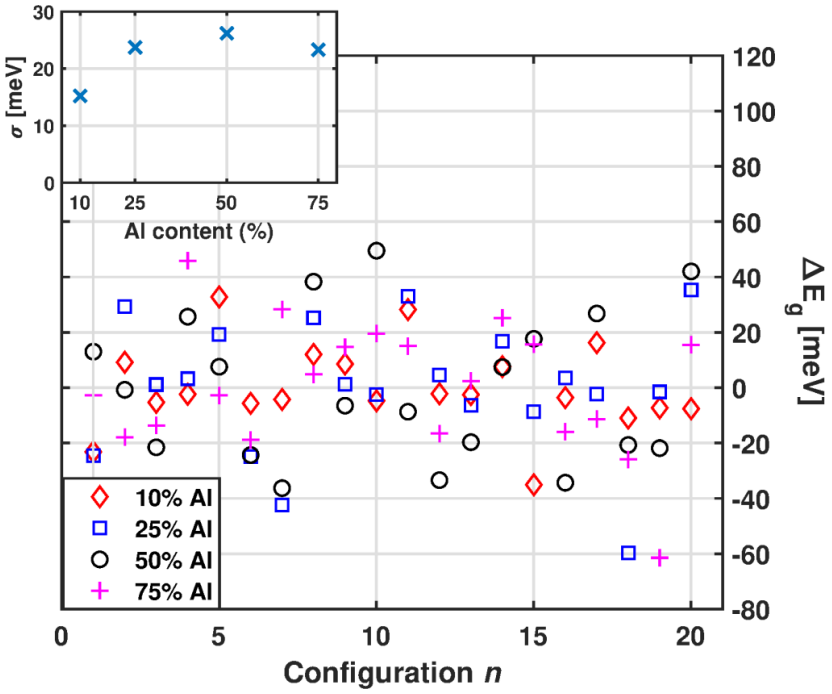


Figure 4.4: Relative ground state transition energy $\Delta E_g(n) = E_g(n) - E_g^{\text{avg}}$ in c-plane $Al_xGa_{1-x}N$/AlN QWs for different microscopic alloy configurations n; more details are given in the main text. The data are shown for Al contents of 10%, 25%, 50% and 75% in the well. The inset shows the standard deviation, σ, as a function of the Al content in the well.

that the hole ground state energy corresponds to the valence "band" edge energy in the conduction valence band picture. For E_g^{avg} we find on an absolute scale values of 2.40 ±0.015 eV, 2.89 ±0.024 eV, 3.85 ±0.026 eV and 4.97 ±0.023 eV for 10%, 25%, 50% and 75% Al in the well, respectively. Thus, our calculations reveal the expected behaviour that with increasing Al composition in the well, E_g^{avg} increases. Our values predicted for (Al,Ga)N/AlN QW systems on the high and low end of the studied Al contents are in reasonable agreement with literature experimental data when taking slight differences in well width and alloy content into account [182, 183, 191]. However, transition energies reported in Refs. [33, 192] for wells with approximately 50% Al content appear to have larger PL peak energies than the transition energy values calculated here. Differences may stem from well width fluctuations or screening of the internal built-in fields, to name only two potential sources.

We note that the experimental investigations in Refs. [33, 183, 191] all showed broad PL spectra. A similar situation has been observed in (In,Ga)N/GaN QW systems, where the broadening of the PL spectrum is usually attributed to alloy fluctuations and connected carrier localisation effects [193]. To study the impact

of alloy fluctuations on the electronic properties of *c*-plane $Al_xGa_{1-x}N$/AlN QWs within our atomistic model, we look at the *relative* ground state transition energy $\Delta E_g(n) = E_g(n) - E_g^{\text{avg}}$. Thus we are analysing by how much an individual configuration deviates from the average. The results of this analysis are displayed in Fig. 4.4 for the different alloy configurations and Al contents studied. One can infer from this figure that independent of the Al content, noticeable fluctuations in $\Delta E_g(n)$ even at low Al contents of 10% are observed. Thus this finding is consistent with the experimental observation of broad PL spectra in (Al,Ga)N/AlN QW systems [33, 183, 191]. Moreover, and in line with our general considerations above, at 25%, 50% and 75% we find several extremely large deviations from the average transition energy and thus large $\Delta E_g(n)$ values (reaching values of $\approx \pm$ 60 meV). To shed further light on this behaviour, the inset in Fig. 4.4 displays the standard deviation, σ, as a function of the Al content. While σ indeed indicates that the spread in the transition energy increases up to 50% Al content, σ slightly decreases when increasing the Al content to 75%. However, further studies with more configurations per alloy content and potentially also increasing the Al content to, e.g. 85%, are required to confirm this trend.

This leaves the question of whether these fluctuations stem mainly from variations in hole, E^h_{GS}, or electron, E^e_{GS}, ground state energies. To shed light onto this question, we proceed with a similar approach as for the transition energies and calculate the relative variation $\Delta E^\lambda_{\text{GS}} = E^\lambda_{\text{GS}}(n) - E^{\lambda,\text{avg}}_{\text{GS}}$ of the ground state energies. Here λ denotes electrons ($\lambda = e$) and holes ($\lambda = h$), respectively.

We start with the electrons. Figure 4.5 shows $\Delta E^e_{\text{GS}}(n)$ for the different random alloy configurations n. Again the data are displayed for Al contents of 10%, 25%, 50% and 75% in the well. For the Al contents below 50%, $\Delta E^e_{\text{GS}}(n)$ scatters between $\pm$10 meV. However, at higher Al content ($\geq$ 50%) noticeably larger $\Delta E^e_{\text{GS}}(n)$ values are observed. This trend is also confirmed when looking at the standard deviation, σ, as a function of the Al content in the well, as displayed as an inset in Fig. 4.5. Based on our discussion in Sec. 4.3.1, one could expect that the electron wave functions are more strongly affected by alloy fluctuations at higher Al contents, due to local confinement effects.

The data for holes are shown in Fig. 4.6. In comparison to the electrons, see Fig. 4.5, the holes exhibit much larger fluctuations in $\Delta E^h_{\text{GS}}(n)$ as a function of the alloy configuration number n. Thus, one can conclude that especially for

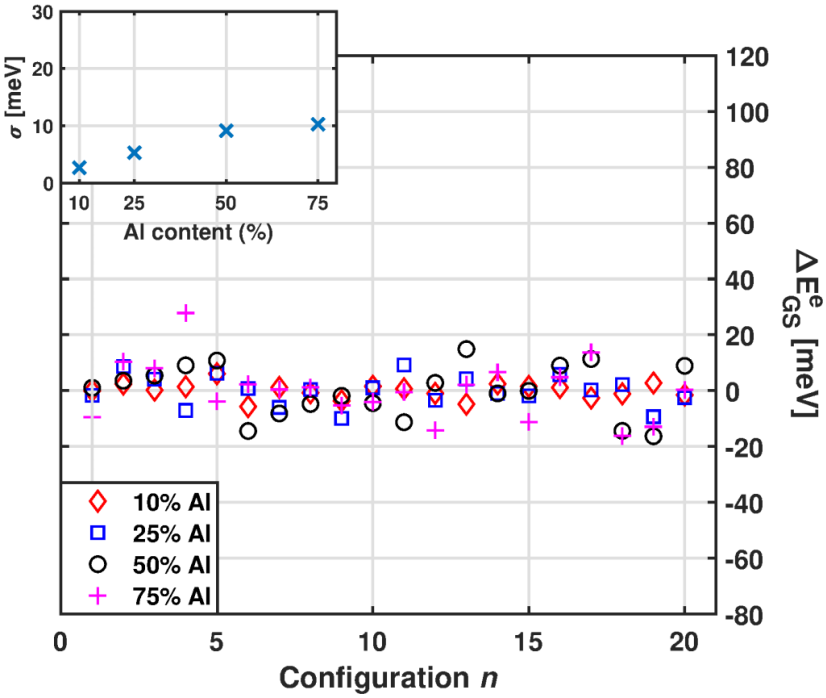


Figure 4.5: Relative *electron* ground state energy $\Delta E^{e}_{\mathrm{GS}}(n) = E^{e}_{\mathrm{GS}}(n) - E^{e,\mathrm{avg}}_{\mathrm{GS}}$ in *c*-plane $Al_xGa_{1-x}N$/AlN QWs for different microscopic configurations n; more details are given in the main text. The data are shown for Al contents of 10%, 25%, 50% and 75% in the well. The inset shows the standard deviation, σ, as a function of the Al content in the well.

lower Al contents, the spread in the transition energies arises to a large extent from variations in the hole ground state energies. Also, the slight decrease in the standard deviation for the ground state transition energy, see inset Fig. 4.4, when increasing the alloy content from 50% Al to 75% Al, is reflected in the standard deviation for the holes (see inset Fig. 4.6). This again indicates that mainly holes dictate the spread in the transition energies.

Overall, the finding that the alloy microstructure has a stronger impact on the hole ground state energy is similar to (In,Ga)N systems [194]. We attributed this here to the fact that holes have a larger effective mass than electrons (even though the electron effective mass is increased in (Al,Ga)N when compared to (In,Ga)N) and can thus be localised in smaller regions with higher Ga contents. Having discussed ground state *energies*, in a next step we focus on wave function localisation characteristics.

Fig. 4.7 displays isosurface plots of the electron (red) and hole (blue) ground state charge densities of selected alloy configurations for (a) 10%, (b) 25%, (c) 50% and (d) 75% Al contents. For 10% Al we have chosen configuration Config.

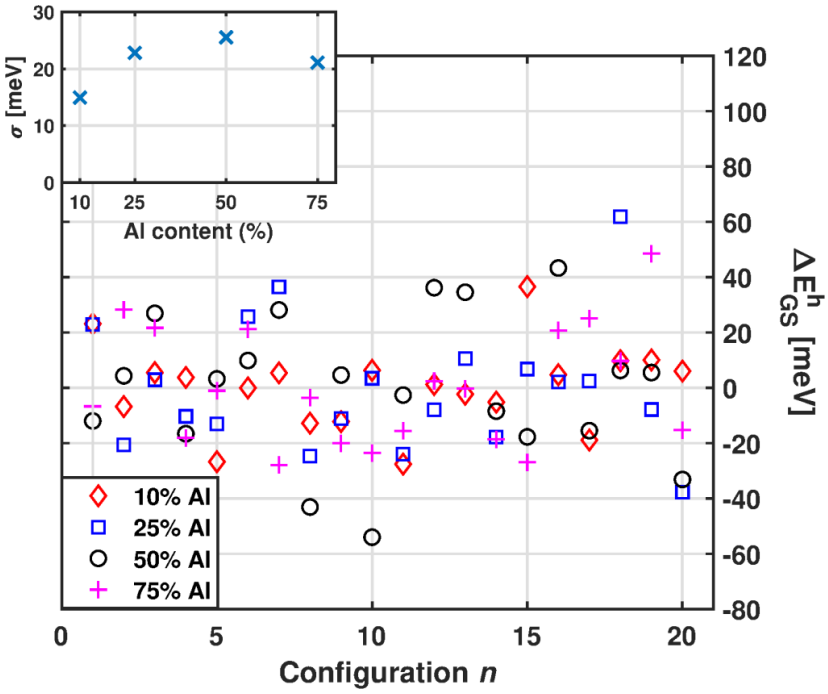


Figure 4.6: Relative *hole* ground state energy $\Delta E^h_{\mathrm{GS}}(n) = E^h_{\mathrm{GS}}(n) - E^{h,\mathrm{avg}}_{\mathrm{GS}}$ in *c*-plane $Al_xGa_{1-x}N$/AlN QWs for different microscopic configurations n; more details are given in the main text. The data are shown for Al contents of 10%, 25%, 50% and 75% in the well. The inset shows the standard deviation, σ, as a function of the Al content in the well.

5 which gives a noticeable deviation from the average ground state transition energy (see Fig. 4.4); this will give insight into how, even at lower Al contents, wave function localisation effects can play a role. For 25% Al we have chosen Config. 3, while for 50% Al Config. 2 and for 75% Al Config. 8. These configurations are close to the respective average transition energies (see Fig. 4.4) and will shed light on wave function localisation effects in an 'average' configuration. We note that Fig. 4.7 displays top-views of the charge densities, thus looking down the *c*-axis of our simulation cell; the wave functions are spatially separated along the growth direction due to the presence of the electrostatic built-in field, which is not visible in the top-view. The light and dark isosurfaces correspond to 10% and 50% of the respective maximum charge density values.

Looking at the QW system with 10% Al first, Fig. 4.7 (a), one observes hole localisation effects, whereas the electron wave function is more delocalised, thus more evenly distributed over the QW plane. We note that well width fluctuations or alloy fluctuations in the barrier material may introduce additional localisation centres for electron wave functions, as our previous study

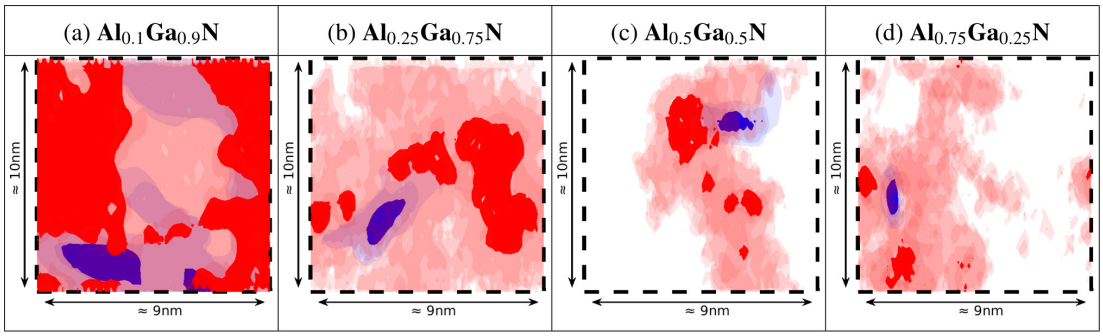


Figure 4.7: Isosurface plots of the electron (red) and hole (blue) ground state charge densities for *c*-plane (Al,Ga)N/AlN QWs with (a) 10%, (b) 25%, (c) 50% and (d) 75% Al content. The light and dark surfaces correspond to 10% and 50% of the maximum values, respectively. The charge densities are shown for a top-view (down the *c*-axis).

revealed [180]. In terms of the carrier localisation features, the here found situation is similar to (In,Ga)N/GaN systems [195], but, it is important to note that the studied $Al_{0.1}Ga_{0.9}N$/AlN well contains 90% of the low band gap material. A *high equality* (In,Ga)N/GaN QW with such as high composition of the low band gap material (InN) is experimentally very challenging and usually not available. Moving on to the QW with 25% Al, from Fig. 4.7 (b) one can infer that the hole is still strongly localised. However, the electron wave function is more noticeably affected by the alloy fluctuations in comparison to the 10% Al case (see Fig. 4.7 (a)). This effect is even more pronounced in the 50% Al case, see Fig. 4.7 (c). We note that for the 50% Al case, we have chosen a configuration close to the average transition energy. Thus the observed electron and hole localisation features are not an 'outlier' or an extreme configuration. In 11 out of the 20 configurations considered we find a very similar behaviour to the situation depicted in Fig. 4.7 (c). The remaining 9 configurations exhibit a more delocalised electron charge density similar to the situation in the QW with 25% Al as shown in Fig. 4.7 (b). Turning to the QW with 75% Al, the charge densities shown in Fig. 4.7 (d) exhibit characteristics similar to the charge density distributions in a well with 50% Al content shown in Fig. 4.7 (c): the hole state is strongly localised by the alloy fluctuations whilst the electron charge density is more evenly distributed with local 'perturbations'. As discussed above, we have chosen for the 75% Al case a configuration that in terms of its ground state transition energy lies close to the average value of all 20 configurations. However, we note also that in contrast to the holes, the standard deviation for electrons increases with increasing Al content. As such, there are also configurations in which the electron ground state energy deviates

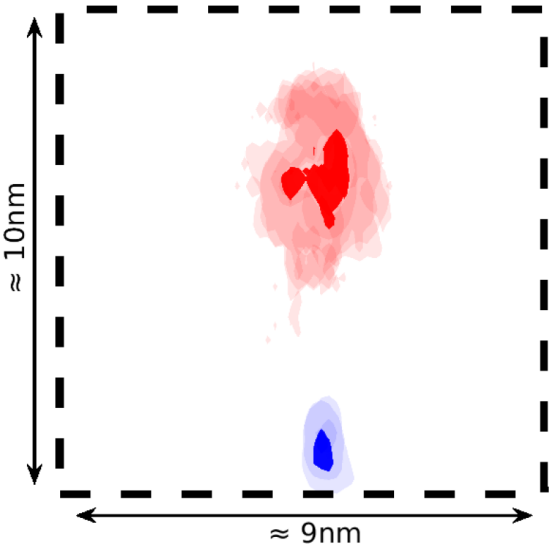


Figure 4.8: Isosurface plots of the electron (red) and hole (blue) ground state charge densities for Config. 18 of the *c*-plane $Al_{0.75}Ga_{0.25}N$ QW. The light and dark surfaces correspond to 10% and 50% of the maximum values, respectively. The charge densities are shown for a top-view (down the *c*-axis). The dashed lines are used to indicate the supercell boundaries.

noticeably from the average value (see e.g. Fig. 4.5). As an example for such a situation, we have chosen Config. 18 in the 75% Al case, allowing us to gain insight into carrier localisation effects in such a more 'extreme' configuration. Figure 4.8 displays the corresponding electron and hole charge densities. From this figure we observe that alloy fluctuations cannot only lead to strong hole localisation effects, but also electron wave functions may be more strongly localised. We observe this strong impact of the alloy fluctuations on the electron ground state charge densities in approximately 8 out of the 20 different alloy configurations. The remaining 12 configurations, in terms of their localisation characteristics, reflect more the behaviour seen in Fig. 4.7 (d). These strong localisation effects may be attributed to high Ga content regions surrounded by regions of higher Al content. Further studies, including also higher Al contents (e.g. 85%), are required to shed more light on electron localisation effects.

As already discussed in Sec. 2.3, in addition to these alloy-induced carrier localisation effects, the intrinsic electrostatic built-in field in nitride-based QWs leads to the situation that electrons and holes are spatially separated along the growth direction. Thus, the carriers localise on opposite well interfaces: the electrons at the upper interface (AlN barrier on (Al,Ga)N well) while the holes on the lower interface ((Al,Ga)N well on AlN barrier). This effect is often discussed in connection to the the QCSE [84]. Overall, this aspect is now also

important for alloy-induced carrier localisation effects: given that electrons and holes localise on opposite well interfaces, the alloy microstructure is different at these interfaces. Thus, and confirmed by Figs. 4.7 and 4.8, electron and hole wave functions do not even localise at the same *in-plane* position in the well, and may even be independently localised as observed in (In,Ga)N wells [193, 195]. Therefore, and in addition to the out-of plane spatial separation of electron and hole wave functions due to the QCSE, which is accounted for by standard continuum-based calculations, our calculations reveal that the carriers are also spatially separated in the growth plane. These effects may be even more pronounced when alloy fluctuations in (Al,Ga)N barriers are considered, since it can introduce further localisation centres [180]. Nevertheless, all these in-plane carrier localisation effects may have a detrimental impact on the radiative recombination rate.

In summary, our results show that random alloy fluctuations are already sufficient to facilitate strong carrier localisation effects. However, so far we only studied ground state properties of (Al,Ga)N/AlN QWs. For optoelectronic devices, such as LEDs, at elevated temperatures or carrier densities not only the ground states but also the energetically higher/lower lying conduction/valence states are important. Localisation characteristics in such excited states play an important role for quantities such as recombination rates (both radiative [196, 197] and non-radiative [100, 198]), but also the DOP [61]. The latter aspect is of particular importance and interest for the LEE in deep UV light emitters [16, 70, 199]. Therefore, we turn our attention in the following towards localisation effects in excited states (energetically higher/lower lying states).

For electrons we find that while ground states may exhibit localisation effects, excited states are more delocalised in nature (not shown). However, for holes the situation is different. Figure 4.9 displays isosurface plots of charge densities of the 5 energetically lowest hole states for the alloy configuration already studied in Fig. 4.7 (c) of a *c*-plane (Al,Ga)N QW with 50% Al. When looking at Fig. 4.9, it is clearly visible that not only the hole ground state is strongly localised but also the excited states. Also, we find that the charge densities may localise in spatially different regions.

Thus alloy fluctuations do not only affect ground but also the excited states. Moreover, these alloy fluctuation-induced localisation features are also expected to impact the band or orbital character mixing in these excited states. As a

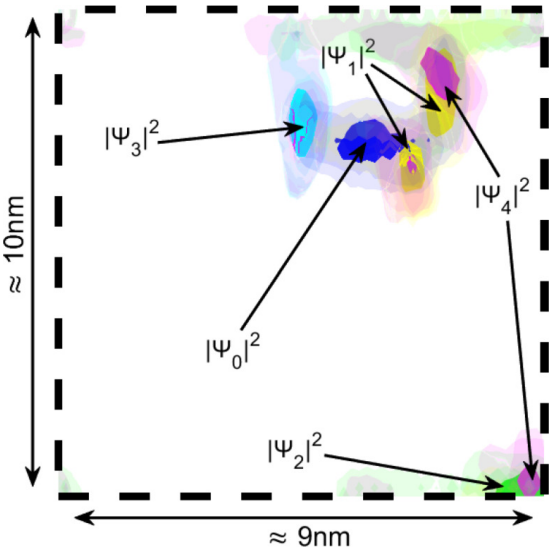


Figure 4.9: Isosurface plots of the charge densities of the five energetically lowest hole states (ψ_0^h to ψ_4^h) in a *c*-plane (Al,Ga)N/AlN quantum well with 50% Al content. The same alloy configuration as in Fig. 4.7 (c) is chosen here. The light and dark isosurfaces correspond to 10% and 50% of the respective maximum charge density values.

consequence the DOP, ρ, can also be affected by these effects. We study this question, given its importance for the LEE in (Al,Ga)N-based deep UV light emitters, in more detail in Chapter 5. In addition to its influence on the DOP, alloy disorder can also impact non-radiative processes such as Auger-Meitner recombination. A detailed analysis of this effect is presented in our recent work in Ref. [3].

4.4 Conclusion

Here, we have presented a theoretical study of the electronic properties of *c*-plane (Al,Ga)N/AlN QWs. The theoretical framework is based on an empirical atomistic TB model that accounts for (random) alloy fluctuations on a microscopic level, including connected fluctuations in strain and polarisation fields. Overall, we have not only investigated the impact of random alloy fluctuations on the results but also how the electronic properties change with Al content in the well. Here, following recent experimental studies, and to disentangle alloy fluctuation-induced carrier localisation effects from (Al,Ga)N barriers, we have studied *c*-plane (Al,Ga)N/AlN QWs. We have considered wells with Al contents of 10%, 25%, 50% and 75%, which in general cover the compositions experimentally relevant for designing light emitters operating in

the UV-A to UV-C spectral range, even though these system utilise, in general, (Al,Ga)N barriers.

Our analysis reveals that across the Al content investigated, random alloy fluctuations are already sufficient to lead to strong hole localisation effects in *c*-plane (Al,Ga)N/AlN QWs, even without the influence of e.g. well width fluctuations. For electrons the situation is slightly different. At lower Al contents, e.g. 10% Al, electron wave functions are to a first approximation delocalised across the *c*-plane. However, for higher Al contents, e.g. $> 50\%$, electrons may also start to exhibit localisation features. Such a situation is usually not seen in (In,Ga)N systems which we attribute to (i) that high-quality high In contents (e.g. $> 50\%$) are experimentally challenging to achieve and usually not available and (ii) the effective electron masses in GaN and AlN are higher when compared to InN.

These localisation effects affected both the electron and hole ground states, and in particular the higher excited hole states. This is especially important for LED devices, because it will realistically be operated at higher temperatures and carrier densities. Therefore, higher (lower) lying conduction (valence) states must also be considered when one is investigating important device characteristics such as recombination rates (see Sec. 2.5 and Ref. [3]) or optical polarisation (see Sec. 2.2.1 and Chapter 5). Also, when considering these features, it is important to note that the impact alloy disorder had on (Al,Ga)N/AlN QWs can be influenced by other external factors such as well width, alloy composition in the well *and* barrier, strain and carrier density screening. In the next chapter we aim to address these questions by first quantifying the extent of carrier localisation through the analysis of Urbach tail energies. This provides a foundation for understanding how alloy disorder affects the optical properties of (Al,Ga)N/(Al,Ga)N QW systems, with particular focus on the degree of optical polarisation.

Chapter 5

Carrier density dependant polarisation screening in (Al,Ga)N/(Al,Ga)N QWs

5.1 Introduction

(Al,Ga)N-based UV light emitters are operated at relatively high voltages due to (Al,Ga)N's large band gap, particularly in the deep UV range. These high operating voltages can lead to elevated carrier densities, which in turn screen the internal polarisation fields and alter the confinement of the wave functions. In addition to these screening effect, the difference in the valence band order between AlN and GaN, as discussed in Sec. 2.2.1, result in the degree of optical polarisation (DOP) changing with varying composition. As shown in Chapter 4, alloy fluctuations induce carrier localisation effects for both the holes and electrons. This localisation effect will break the band symmetry and can cause valence band mixing effects in (Al,Ga)N alloys. Therefore, in this chapter we investigate how these factors influence the electronic and optical properties for specific (Al,Ga)N QWs that emit TE or TM polarised light. Special attention is given to how carrier density screening impacts the optical properties.

In Sec. 5.2, we begin with an overview of the fundamental properties of the valence band structure in (Al,Ga)N alloys and how various factors influence the DOP, which is followed by a description of the heterostructures studied. The results are presented in Sec. 5.3, with the conclusion in Sec. 5.4.

5.2 Theoretical background

In the prologue, we discussed how (Al,Ga)N alloys exhibit poor external quantum efficiencies especially in the deep UV-range (<280 nm). Multiple factors contribute to the low efficiency, but the LEE is particularly low because it is tightly linked to fundamental properties of the valence band ordering of (Al,Ga)N alloys and heterostructures. In general, while in both GaN and AlN the conduction band minimum and the valence band maximum are at the Γ-point, the valence band structure of AlN is TM polarised while its GaN counterpart is TE polarised [200, 201, 202, 203, 204, 205]. As LED structures are in general surface emitting, the TM polarised light emission is detrimental for the LEE and thus the efficiency of the device [26, 69, 70, 71, 72, 199]. The Al content in the well, but also quantum confinement and strain effects affect the crossover from TE to (purely) TM polarisation in (Al,Ga)N-based LEDs. In addition to these factors, experimental and theoretical studies already give indications that alloy disorder-induced carrier localisation effects significantly impact the optical properties of (Al,Ga)N QWs [7, 32, 33, 39]. Manifesting, for instance, through broad PL linewidth or broad absorption spectra, where the latter is often described in terms of Urbach tail energies [38, 45, 197], as discussed in Sec. 2.6.

The impact of alloy disorder on the DOP, usually defined as the ratio of TE to TM polarised emission [202, 206], is largely unexplored in theoretical studies of (Al,Ga)N QWs as it presents a significant challenge for several reasons. Firstly, standard and widely available 1D multi-band $\mathbf{k} \cdot \mathbf{p}$ simulations of (Al,Ga)N QWs and heterostructures describe the alloy by averaged material parameters; local fluctuations in the alloy content are neglected [36, 37]. Secondly, modified continuum-based models, which allow for local fluctuations in alloy content in a three-dimensional simulation, have recently been employed to describe the impact of alloy disorder on the electronic and optical properties of (In,Ga)N QWs; such studies are in general based on single-band effective mass models [46, 120, 169]. These single-band models cannot intrinsically capture alloy disorder-induced valence band mixing effects, and would have to be extended to modified three-dimensional multi-band $\mathbf{k} \cdot \mathbf{p}$ models. However, studies using these more sophisticated continuum-based models are sparse for (Al,Ga)N systems. A recent study employing such an advanced treatment also relies on a combination of single-band effective mass approximation and localisation landscape theory to obtain the carrier confinement energy landscape

underlying a 3D multi-band $\mathbf{k} \cdot \mathbf{p}$ model [69].

Here, we employ our atomistic multi-band empirical TB model to gain insight into Urbach tail energies and the DOP of (Al,Ga)N-based QWs. In (Al,Ga)N heterostructures, theoretical studies on Urbach tail energies are sparse and the connected broadening of the density of states (DOS) is most often treated as a free, adjustable parameter in e.g. $\mathbf{k} \cdot \mathbf{p}$ calculations of optical gain [38, 39]. Moreover, the broadening of the DOS can also impact the DOP, an aspect usually not considered in previous theoretical studies. Given that alloy composition and quantum confinement on a macroscopic level will play an important role for the electronic structure of (Al,Ga)N wells in general, we investigate QWs with two distinctly different alloy compositions ($Al_{0.48}Ga_{0.52}N/Al_{0.63}Ga_{0.37}N$ and $Al_{0.75}Ga_{0.25}N/Al_{0.90}Ga_{0.10}N$) and of varied well widths (L_w=1.3 nm, 2.3 nm and 3.3 nm). $Al_{0.48}Ga_{0.52}N/Al_{0.63}Ga_{0.37}N$ wells often form the active region of UV-C emitters operating at the longer wavelength end of the UV-C spectrum [38, 207]. Based on experimental [207] and theoretical ($\mathbf{k} \cdot \mathbf{p}$) [38, 208, 209] literature data, these emitters are expected to mainly emit TE polarised light. On the other hand, $Al_{0.75}Ga_{0.25}N/Al_{0.90}Ga_{0.10}N$ QWs were chosen to investigate a system emitting (i) in the deep UV range and (ii) mainly TM polarised light; similar Al contents are reported in the literature for deep UV emitters both experimentally [210, 211, 212] and theoretically ($\mathbf{k} \cdot \mathbf{p}$ models) [38, 208, 209, 212]. It should be noted that we kept each system fixed at the same 15% Al composition contrast between well and barrier. Thus, our analysis should allow for a comparative investigation between emitters operating in two distinct UV-C wavelength ranges. We note that in previous studies, to keep the emission wavelengths fixed [69, 213, 214], well width and Al content are often changed simultaneously. In that case, strain and polarisation fields as well as quantum confinement change, making it difficult to disentangle the impact of all these factors on e.g. the DOP. Therefore, our studies allow for focusing on the different effects separately. Moreover, our studies also target varying carrier densities in the well, in order to gain insight into experimental relevant settings.

5.2.1 Valence Band Structure of AlN and GaN

As introduced in Sec. 2.2.1, the DOP in (Al,Ga)N alloys is tightly linked to the symmetry properties of the valence bands involved in the optical transitions between conduction and valence bands. Given the direct band gap nature of

both wurtzite GaN and AlN, the symmetry of the three valence bands energetically closest to the band edge at the Γ-point play an important role for the DOP; lower lying valence states are energetically far away from the VBE at Γ. In general, the symmetry of the energetically highest lying three valence bands can be described by p_x-, p_y- and p_z-like orbitals or respective linear combinations [127]. Crystal field splitting and spin-orbit coupling (SOC) lift the degeneracy between these bands, which are sometimes termed as A-, B- and C-valence bands [66, 206, 215]. However, the ordering of these bands depends on several factors. For instance, the crystal field splitting energy, Δ_{cr}, in AlN is of *opposite* sign to Δ_{cr} in GaN or InN. In the literature, Δ_{cr} values can vary [60, 65], but for AlN $\Delta_{\mathrm{cr}}^{\mathrm{AlN}} \approx -200$ meV whereas for GaN $\Delta_{\mathrm{cr}}^{\mathrm{GaN}} \approx 30$ meV. The sign of Δ_{cr} determines which valence band forms the VBE as the SOC energy is usually small, particularly when compared to other III-V material systems [77].

The polarisation state of the light emitted via the radiative recombination process involving the CBE and VBE is determined by the symmetry (orbital character) of the VBE state at the Γ-point. Due to the negative $\Delta_{\mathrm{cr}}^{\mathrm{AlN}}$ value in AlN, the VBE is formed by the so-called C-band which is of Γ_7 symmetry [204, 205]; this band is sometimes also called the crystal field split off hole (CH) band. Energetically below the C-band are the A- and B-bands which are mainly split by the small SOC energy in nitrides (≈ 10-20 meV) [77]. The A-band is of Γ_9 [204, 205] symmetry and often labelled as the heavy hole (HH) band; the B-band, or light hole (LH) band, has Γ_7 symmetry. In terms of the basis states forming these bands, the upper Γ_7 band exhibits mainly p_z-like character while both Γ_9 and Γ_7 are mainly p_x- and p_y-like in character [202]. For GaN, due to the positive crystal field splitting energy, the valence band order is reversed: the VBE is the A-band; B- and C-bands are energetically below the VBE [60, 204, 205, 206]. Given the difference in the orbital character/symmetry of the VBE, light emitted from AlN is TM polarised because the p_z orbitals forming the VBE are orientated along the growth direction and $\mathbf{E} \parallel \mathbf{c}$. Since the VBE in GaN is formed by p_x- and p_y-like basis states, the light emission pattern is more involved. In this case $\mathbf{E} \perp \mathbf{c}$, which leads to emission perpendicular to but also within the growth plane [27]. However, in general, the emission pattern for GaN (or low Al content systems) is denoted as TE polarised [26, 69, 200, 201, 202, 206], and regarded as emission mainly along the c-axis of the underlying wurtzite crystal, at least compared to emission of pure TM polarised light. We follow this widely used definition here. As standard UV (Al,Ga)N LEDs are top and bottom surface emitting and are

grown along the wurtzite c-axis, TE polarised light emission is desired to achieve a high LEE of the device [26, 69, 70, 202].

The above highlights that the valence band ordering in (Al,Ga)N-based QWs plays an important role when designing UV LEDs, especially in the deep UV, where high Al contents in the active region are required. However, in addition to the Al content, further factors impact the valence band ordering in $Al_xGa_{1-x}N/Al_yGa_{1-y}N$ wells. These factors include contributions from strain [69], quantum confinement and built-in polarisation fields [202].

Figure 5.1 gives a schematic illustration of how strain, confinement and built-in field affect the valence band ordering in an (Al,Ga)N system. In Fig 5.1 (a) a high Al content is assumed so that the VBE is given by the C-band (p_z-like band) and the band ordering is illustrated in the absence of strain, confinement and built-in polarisation field effects. The evolution of Δ_{cr} with Al content determines the energetic separation of the bands in a strain-free bulk (Al,Ga)N system. In our previous work [133], we found a nonlinear behaviour of Δ_{cr} with Al content, in good agreement with experimental studies [133]. The impact of in-plane biaxial compressive strain on the band structure, as for example found in a QW structure, is illustrated in Fig 5.1 (b). With respect to the unstrained case, A- and B-bands are shifted to higher energies while the C-band shifts to lower energy. Depending on strain and Al content in the well, this may already lead to a crossover of the C- and A/B-bands, but in any case a reduced energy separation between the C-band (p_z-like states) and A- and B-bands (mainly p_x- and p_y-like states) is expected. Again it should be noted that the magnitude of $\Delta_{\mathrm{cr}}(x)$ in the alloy will play an important role for the energetic separation of the bands. The reduced energetic separation between the different bands can thus lead to band mixing effects (e.g. mixing of p_x-, p_y- and p_z-like states) which affect the DOP.

Figure 5.1 (c) visualises the impact of quantum confinement along the c-axis on the band separation. This type of confinement further reduces the energetic separation of the three bands in our example. This stems from the fact that the effective hole mass of the C-band along the confinement/growth direction is lower when compared to the A- and B-bands; for instance in AlN $m_{||}^{h,C} = 0.25m_0$ and $m_{||}^{h,A} = 3.125m_0$ [60] where $m_{||}^{h}$ denotes the hole effective mass parallel to the c-axis. Therefore, to tailor the valence band ordering and thus light polarisation characteristics, one may adjust the QW width to modify and control the quantum confinement. However, this may also be achieved by

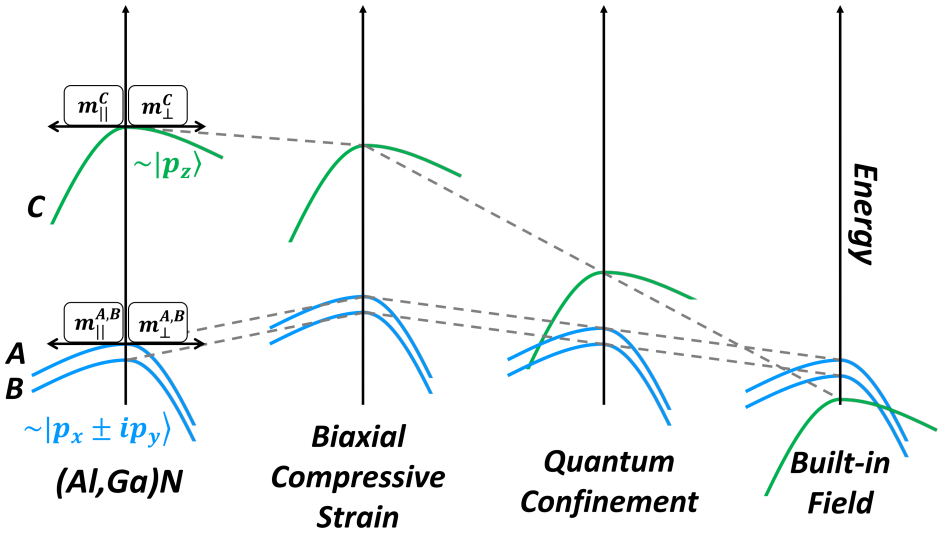


Figure 5.1: Schematic illustration of the valence band order for high aluminium content containing (Al,Ga)N systems when (a) unstrained, (b) under biaxial compressive strain, (c) in the presence of quantum confinement and (d) intrinsic built-in fields. The heavy hole, light hole and crystal field split-off bands are denoted as the A-, B- and C-bands, respectively. Note that our schematic is to highlight general trends. Quantum confinement will break the translation invariance e.g. along the wurtzite c-axis and a band structure cannot be defined along this direction. The above should however indicate how quantised energy levels that are constructed from e.g. $|p_z\rangle$-like basis states are affected by confinement effects.

changing the contrast in Al composition between well and barrier since this will modify the valence band offset.

A further factor that affects the confinement in a III-N well is the built-in polarisation field. This field spatially separates electron and hole wave functions by localising them at opposite interfaces of the well. Thus, the hole wave function may be confined to a length smaller than the well width L_w; this "additional" confinement can further influence the valence band ordering as schematically indicated in Fig. 5.1 (d). Several factors impact the strength of this field including the composition difference between QW and barriers and the overall strain in well and barrier. However, with an increasing carrier density in the QW, the polarisation field may be screened so that this polarisation field-induced confinement effect is reduced. This means that the valence band ordering in an (Al,Ga)N QW system can also be carrier density dependent.

The above is based on the assumption that in an (Al,Ga)N QW all these different contributions can be described on a macroscopic level, i.e. that local features of the alloy microstructure are of secondary importance. However, we have seen in the previous chapter that alloy disorder can give rise to carrier

localisation effects in (Al,Ga)N QWs. This can lead to, for instance, a broadening of the DOS, introducing an Urbach tail. Again, as discussed in the previous chapter, the importance of these microscopic features for the DOP are not well understood and require a three dimensional, multi-band electronic structure model to capture alloy disorder-induced valence band mixing effects in (Al,Ga)N QWs. A recent 3D $\mathbf{k} \cdot \mathbf{p}$ study [69] has focused primarily on the impact of substrate strain on the DOP, while Urbach tail energies and how the broadening of the DOS changes with Al content, well width or carrier density are not reported. Given the importance of the DOS for the DOP in (Al,Ga)N systems, we target Urbach tail energies and DOP in the framework of an atomistic multi-band electronic structure model that captures both macroscopic and microscopic contributions.

5.2.2 Model Quantum Well System, Density of States and Degree of Optical Polarisation

Overall, our aim is to study the impact of alloy disorder on the electronic and optical properties, or more specifically the DOP, of (Al,Ga)N based QWs operating in different wavelength windows. In general, the emission wavelength of such structures is mainly tailored by adjusting Al content and well width. As discussed above, both factors will impact the valence band ordering and thus the DOP. We focus on two systems in the following, targeting the upper UV-C range ($\approx$ 280 nm) and deep UV-C emitters ($\approx$ 230 nm) to gain insight into similarities, but also differences in these wavelength ranges.

The first QW system investigated is an $Al_{0.48}Ga_{0.52}N$ well with an $Al_{0.63}Ga_{0.37}N$ barrier. Such structures are often considered in the literature to realise emitters in the upper UV-C range [38, 207]. Literature data shows that the considered system exhibits TE polarised light emission [38, 207, 208, 209, 212]. To also study the impact of alloy disorder on electronic and optical properties of (Al,Ga)N-based emitters in the deep UV-C range, we investigate $Al_{0.75}Ga_{0.25}N$ QWs with $Al_{0.90}Ga_{0.10}N$ barriers. For such structures, literature results find TM polarised light emission due to the high Al content in the well [202, 208, 209, 212].

We note that while the Al content in the well and the barrier is different for the two structures, the Al content *contrast* between the barrier and the well is kept constant in our studies. Furthermore, the Al content in the underlying substrate plays a role for the strain state in the QW-barrier system and thus the

DOP [69], particularly for systems with a high Al-content in the active region [32, 33, 209]. Here, we assume that the wells and barriers are strained to a pure AlN substrate.

To study the impact of the well width, L_w, on the DOP we consider for both systems three different well widths, namely $L_w \approx 1.3$ nm, 2.3 nm and 3.3 nm. The electronic structure of the (Al,Ga)N well systems with the different well widths discussed above is modelled with our atomistic empirical TB model on supercells with dimensions of approximately $10 \times 9 \times 10$ nm^3 (81,920 atoms).

To gain insight into the DOP, it is important to note that in an 'ideal' QW structure, i.e. in the absence of carrier localisation effects, the valence subband structure also plays an important role. At elevated temperatures or carrier densities, carriers may not only populate the topmost valence band but also energetically lower lying bands, which in (Al,Ga)N wells may exhibit different orbitals and as such different light polarisation characteristics. Thus, in general an orbital resolved DOS can provide important insight into the DOP and how it changes with e.g. well width or Al content. However, in the presence of alloy disorder-induced carrier localisation effects, defining valence subbands is in general not possible since the in-plane wave vector is no longer a good quantum number. Moreover, carrier localisation effects lead to a broadening of the DOS, usually characterised by a so-called Urbach tail and a corresponding Urbach tail energy. Thus, it is useful to study changes in the Urbach tail energies for (Al,Ga)N QW systems before turning to the DOP. While we focus in the following on the Urbach tail energies, we note also that alloy disorder can lead to changes in the band structure further away from the band edges. Prominent examples where these effects become important include alloy disorder-induced carrier scattering [216] or Auger-Meitner recombination processes [103, 105].

We focus on Urbach tail energies for the valence band as (i) our previous studies showed that alloy disorder effects impact hole states more significantly than electron states and (ii) the DOP is tightly linked to the orbital character of the valence/hole states. In order to do so, we calculate the hole density of states (h-DOS) employing the atomistic empirical TB model introduced above. However, further factors need to be considered when discussing Urbach tail energies. As already mentioned above, the intrinsic electrostatic built-in field in an (Al,Ga)N QW is screened with increasing carrier density in the well. As a consequence, the electronic structure of a well is also changed and as such impacts the Urbach tails and the DOP. In order to account for the polarisation

field screening effect, a self-consistent Schrödinger-Poisson calculation is required. However, performing a self-consistent TB-Poisson calculation on our large, atomistic 3D supercell for different well widths and (Al,Ga)N QW systems as well as varying carrier densities is numerically prohibitive. Instead, we employ the method established in Ref. [103] where the screening potential at a given carrier density in the well is determined by a self-consistent 1D Schrödinger-Poisson calculation, which is then included in the full atomistic empirical TB model. Diagonalising the 'screened' empirical TB model Hamiltonian accounts for changes in the electronic structure due to built-in field screening effects, while still accounting for the impact of alloy disorder. Our recent studies on (In,Ga)N QW systems have shown that the method outlined produces results in good agreement with experiment in terms of, e.g., carrier densities at which screening of the built-in field becomes significant or the onset of the efficiency droop [103]. Therefore, we adopt this same approach here for (Al,Ga)N QW systems.

To cover carrier densities relevant to the efficiency droop in III-N LEDs ($n \approx 10^{19}$ cm^{-3}) [33, 105, 217, 218], and thus to be able to provide insight into trends in Urbach tail energy and DOP in this regime, we study carrier densities between $n = 1 \times 10^{18}$ cm^{-3} and $n = 1 \times 10^{20}$ cm^{-3}. While at typical LED operating conditions, carrier densities of the order of $n = 1 \times 10^{20}$ cm^{-3} are not found, in optical excitation studies such high carrier densities can be realised [33, 217] and are considered in theoretical studies of e.g. Auger-Meitner recombination processes. Thus, the carrier density regime beyond $n \approx 1 \times 10^{19}$ cm^{-3} is important for III-N based light emitters.

Having described how the electronic structure is obtained when accounting for carrier density screening effects, the DOS and Urbach tail energies are determined as follows. Given the finite supercell size, a sufficiently large number of (i) alloy microstructures and (ii) calculated single-particle states need to be considered to be able to resolve the Urbach tail energies and accommodate the charge carrier densities. Looking first at the number of single-particle states, the hole energies from all configurations are collated and grouped into energy bins for each (Al,Ga)N QW system and carrier density. The size of these energy bins can now be adjusted to avoid empty bins and to reduce the number of required alloy configurations explicitly calculated. However, at the same time the bin size cannot be too large, as otherwise the Urbach tail energies are 'washed out'. First, we considered how many states are sufficient to populate the highest carrier density of $n = 1 \times 10^{20}$ cm^{-3}. After this we then tested how many alloy

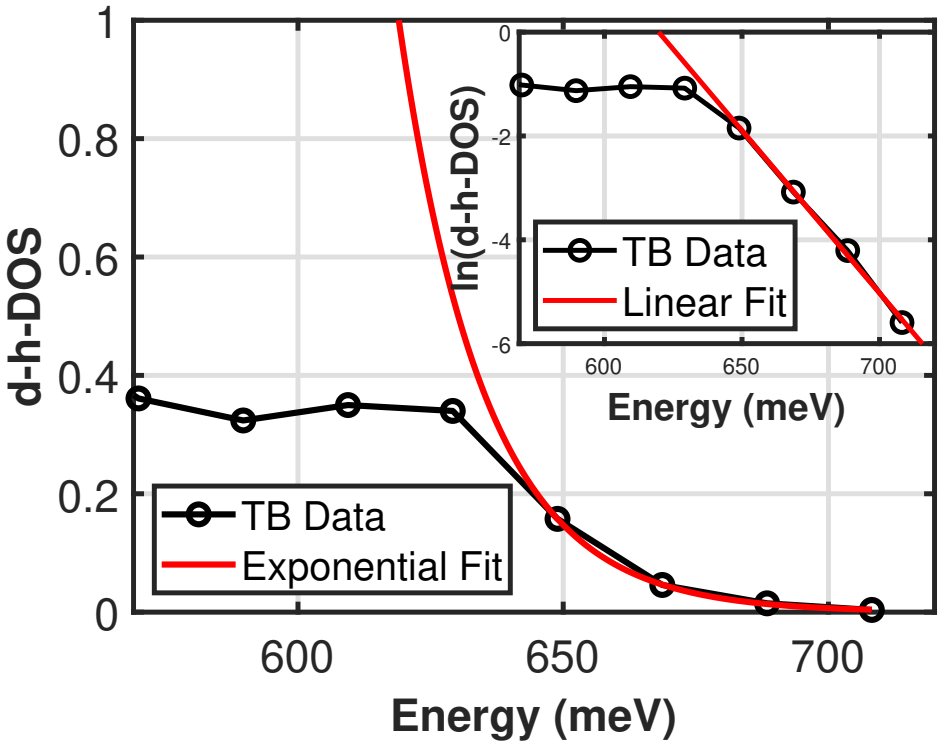


Figure 5.2: Derivative of hole density of states (d-h-DOS) calculated for the 3.3 nm $Al_{0.48}Ga_{0.52}N/Al_{0.63}Ga_{0.37}N$ quantum well at low carrier densities, i.e. in the absence of built-in field screening effects. Tight-binding (TB) data (black circles) and exponential fit to the Urbach tail (red line) are given. The inset shows the natural logarithm of the TB d-h-DOS data fitted with a linear function.

configurations were required to avoid empty bins, while studying the impact on the Urbach tail energies. We find that for the chosen supercell size, 150 alloy configurations and a 150 states per alloy configuration strike a balance between accuracy, computational effort and also to accommodate the high carrier densities discussed above. The bin sizes were adjusted for each system, since the quantum confinement and thus the electronic structure is affected by changes in the well width and carrier density dependent screening effects.

Taking the $L_w = 3.3$ nm $Al_{0.48}Ga_{0.52}N/Al_{0.63}Ga_{0.37}N$ QW as an example, Fig. 5.2 demonstrates how Urbach tail energies, E_u, for the holes are determined. In general, the VBE of unstrained AlN is used as the zero of energy. Strain and polarisation fields will shift energies with respect to the unstrained AlN VBE. Moreover, instead of looking at the h-DOS itself, we take the derivative of h-DOS (d-h-DOS) with respect to energy, ϵ, numerically. The reason for this is that the modification to the DOS due to alloy disorder, the Urbach tail, can be described by an exponential tail, $\propto \exp\left\{\left(-\frac{\epsilon}{E_u}\right)\right\}$; in the 'standard' DOS for an ideal QW (parabolic band) the h-DOS would exhibit a

piecewise constant dependence of energy. Taking the derivative of h-DOS with respect to energy ϵ one can identify the Urbach tail region in the d-h-DOS, which is again $\propto \exp\left\{\left(-\frac{\epsilon}{E_u}\right)\right\}$. Thus, this allows us to extract E_u from the empirical TB model data. Fig. 5.2 clearly shows the exponential tail in d-h-DOS. The inset figure displays the natural logarithm of the data, which reflects the expected straight line. From the slope of the line of best fit, E_u is extracted. This method is employed below to determine E_u for the considered QW systems at different carrier densities.

5.3 Results

In this section we discuss Urbach tail energies and DOP of (Al,Ga)N QW systems. Special attention is paid to the impact of (i) Al content, (ii) well width and (iii) carrier density on the results. In Sec. 5.3.1 we start with the lower Al content system, namely $Al_{0.48}Ga_{0.52}N/Al_{0.63}Ga_{0.37}N$ QWs, before turning to the higher Al content structure, $Al_{0.75}Ga_{0.25}N/Al_{0.90}Ga_{0.10}N$, in Sec. 5.3.2.

5.3.1 $Al_{0.48}Ga_{0.52}N/Al_{0.63}Ga_{0.37}N$ Quantum Well Systems

We analyse in Sec. 5.3.1.1 the Urbach tail energies of $Al_{0.48}Ga_{0.52}N/Al_{0.63}Ga_{0.37}N$ QWs of different widths. In Sec. 5.3.1.2 the DOP is studied.

5.3.1.1 Urbach Tails

Following the procedure outlined in Sec. 5.2.2, Fig. 5.3 displays the extracted Urbach tail energies, E_u, for $Al_{0.48}Ga_{0.52}N/Al_{0.63}Ga_{0.37}N$ QWs of different widths L_w as a function of carrier densities, n, in the well. In the low carrier density regime, $n = 1 \times 10^{18}$ cm^{-3}, the Urbach tail energy increases with increasing L_w. This finding indicates that with increasing well width hole localisation effects increase. Fig. 5.3 also reveals that at least for the $L_w = 2.3$ nm and $L_w = 3.3$ nm system, the Urbach tail energy E_u decreases with increasing carrier density. E_u changes by ≈ 3 meV in both systems when increasing the carrier density from $n = 1 \times 10^{18}$ cm^{-3} to $n = 1 \times 10^{20}$ cm^{-3}, which corresponds to a reduction of $\approx 20\%$ in E_u, and indicates that alloy disorder-induced carrier localisation is amplified by the built-in field. This conclusion is further supported by the data from the $L_w = 1.3$ nm system, in which the potential drop across the QW is smaller when compared to the wider well system. For the narrower well width, E_u is approximately constant and

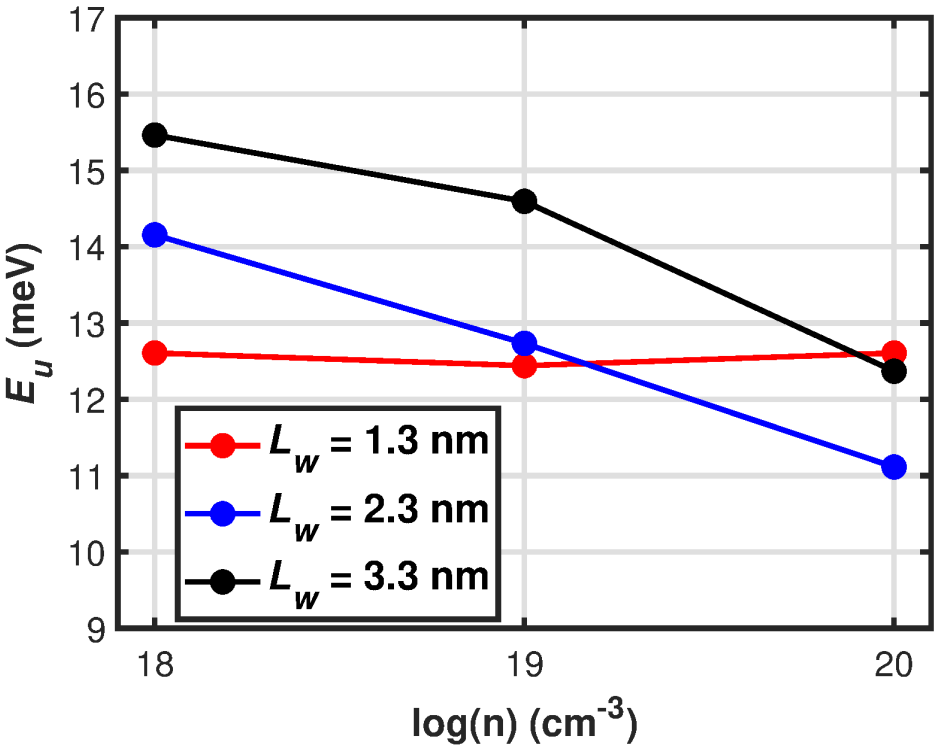


Figure 5.3: Urbach tail energy E_u for $Al_{0.48}Ga_{0.52}N/Al_{0.63}Ga_{0.37}N$ quantum wells of width $L_w = 1.3$ nm (red), $L_w = 2.3$ nm (blue) and $L_w = 3.3$ nm (black) at carrier densities of $n = 1 \times 10^{18}$ cm^{-3}, $n = 1 \times 10^{19}$ cm^{-3} and $n = 1 \times 10^{20}$ cm^{-3}.

may even slightly exceed the Urbach tail energy of the system with $L_w = 2.3$ nm and $L_w = 3.3$ nm at high carrier densities.

To gain further insight into the interplay of carrier localisation effects and built-in field, we discuss in the following the planar integrated probability density [40]

$$P_m(k) = \sum_{ij} \sum_{\alpha} |c_{ijk}^{\alpha,m}|^2 \ , \tag{5.1}$$

which builds on the empirical TB model wave function ψ_m expressed as:

$$\psi_m = \sum_{ijk} \sum_{\alpha} c_{ijk}^{\alpha,m} \phi_{ijk}^{\alpha} \ . \tag{5.2}$$

The spatial x, y and z coordinates of the $N = 81,920$ lattice sites in the supercell are labelled above by i, j and k, respectively. The sp^3 empirical TB model basis states are denoted by ϕ_{ijk}^{α} with $\alpha \in \{s, p_x, p_y, p_z\}$, and $c_{ijk}^{\alpha,m}$ being the expansion coefficient at each lattice site for the single-particle hole state m. The expansion coefficients for a given state m are obtained by diagonalising the empirical TB model Hamiltonian.

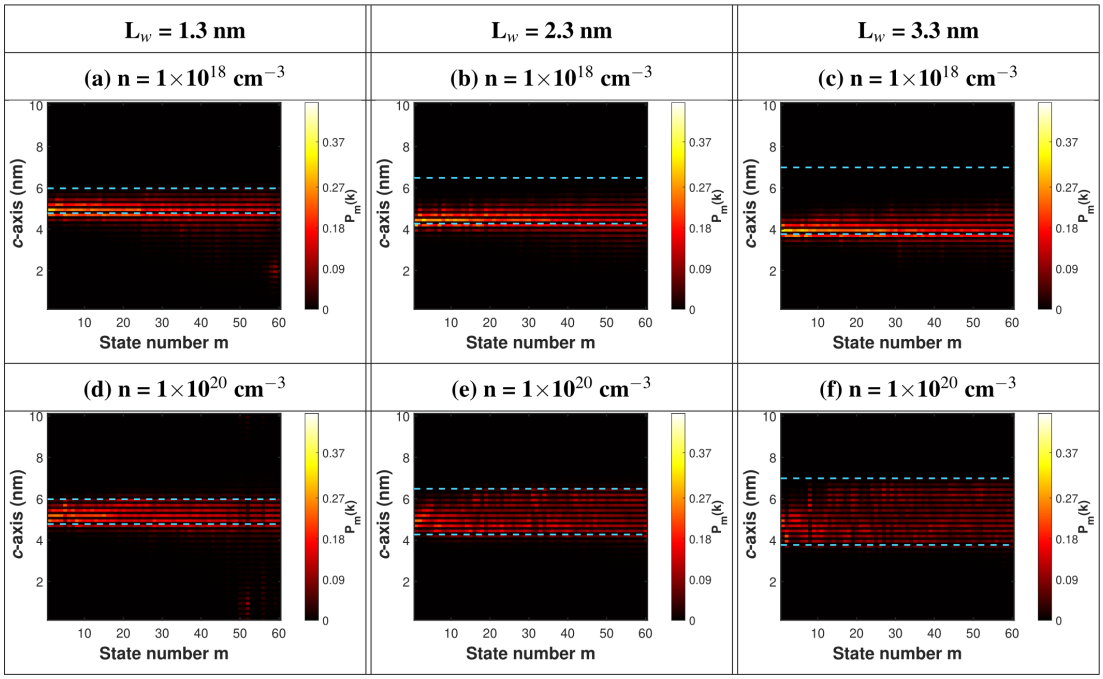


Figure 5.4: Planar integrated probability densities of holes, $P_m(k)$, for an arbitrarily chosen alloy configuration of an $Al_{0.48}Ga_{0.52}N/Al_{0.63}Ga_{0.37}N$ quantum well of width $L_w = 1.3$ nm, $L_w = 2.3$ nm and $L_w = 3.3$ nm. The data are displayed at carrier densities of $n = 1 \times 10^{18}$ cm^{-3}, (a)-(c), and $n = 1 \times 10^{20}$ cm^{-3}, (d)-(f), for 60 hole states. Index m refers to the single-particle hole state number, with $m = 1$ being the ground state, while k refers to the layer in the supercell along the wurtzite c-axis. The quantum well boundaries are indicated by the light blue dashed lines. The colourbar is kept the same between the different figures and is determined by the maximum $P_m(k)$ value found in the $L_w = 3.3$ nm $Al_{0.75}Ga_{0.25}N/Al_{0.90}Ga_{0.10}N$ quantum well system at a carrier density of $n = 1 \times 10^{18}$ cm^{-3} discussed in Sec. 5.3.2.

The quantity $P_m(k)$ gives the probability that the hole state ψ_m is found in the layer specified by k along the c-axis of the system. In Figs. 5.4 (a)-(f), $P_m(k)$ is displayed for an arbitrarily chosen configuration for the three well widths considered. The data are plotted for low ($n = 1 \times 10^{18}$ cm^{-3}) and high carrier density ($n = 1 \times 10^{20}$ cm^{-3}) values; the colour bar is kept fixed for easier comparison between the different systems and thus to gain first insight into the question of how screening of the built-in field changes carrier localisation effects in wells with different well widths and carrier densities. The maximum of the colour bar is determined by the maximum $P_m(k)$ value found in the $L_w = 3.3$ nm $Al_{0.75}Ga_{0.25}N/Al_{0.90}Ga_{0.10}N$ QW system at a carrier density of 1×10^{18} cm^3, which is discussed in Sec. 5.3.2.

In general, Fig. 5.4 (a)-(f) highlight that carrier confinement effects along the

c-axis arising from (i) the polarisation field and (ii) the well width. However, information about in-plane localisation effects is also encoded in $P_m(k)$: for a wave function that is delocalised in the c-plane and along the growth direction, $P_m(k)$ will not exhibit strong variations. Therefore, the absence of large variations in $P_m(k)$ for a given state is indicative of the absence of strong carrier localisation effects both due to built-in field and alloy disorder, in the growth plane and along the c-axis.

For the low carrier density of $n = 1 \times 10^{18}$ cm^{-3}, Fig. 5.4 (a)-(c) reveal the expected behaviour, namely that the built-in polarisation field confines the hole charge density to the lower QW barrier interface. Figure 5.4 (a)-(c) also show that the impact of the built-in polarisation field is less pronounced in the $L_w = 1.3$ nm QW system, Fig. 5.4 (a), as the potential drop is much smaller in this system when for instance compared to $L_w = 3.3$ nm. In the $L_w = 2.3$ nm, Fig. 5.4 (b), and $L_w = 3.3$ nm QWs, Fig. 5.4 (c), the hole wave functions are clearly confined to much shorter lengths along the c-axis than the quantum confinement introduced by the respective QW width. The confinement lengths here may even be below or close to 1.3 nm.

Therefore, at low carrier densities, the hole wave function for the $L_w = 2.3$ nm and $L_w = 3.3$ nm QW experiences strong confining potentials which are driven by the large potential drop present in these systems. In the $L_w = 1.3$ nm well, the quantum confinement due to the well width plays a larger role. Due to the strong confinement regime in all three cases, local fluctuations in Ga content can then lead to carrier localisation effects, given the lower band gap of GaN, when compared to AlN, and the high effective hole masses in general [7].

With increasing carrier density in the well the built-in field is screened. Figure 5.4 (d)-(f) display $P_m(k)$ now at the higher carrier density of $n = 1 \times 10^{20}$ cm^{-3}. This screening effect is of secondary importance for the $L_w = 1.3$ nm system as quantum confinement is to a large extent introduced by the well width and not the built-in potential. This is contrasted with the $L_w = 2.3$ nm and $L_w = 3.3$ nm wells, where the screening of the built-in field with increasing carrier density noticeably impacts carrier localisation. Although there are a few energy states with a high probability of being found in certain planes, overall the charge densities tend to become more delocalised along the c-axis within the QW region. As discussed above already, the absence of strong variations in $P_m(k)$ values indicates also the absence of strong in-plane carrier localisation effects. The reduction in carrier localisation effects with increasing

carrier density explains the ≈ 20% reduction in Urbach tail energies shown in Fig. 5.3 for the wider wells. Our findings thus show that alloy disorder-induced carrier localisation effects in wider (Al,Ga)N QWs are noticeably enhanced by polarisation fields. With increasing carrier density related built-in field screening, these localisation effects are strongly reduced because carrier confinement is mainly driven by the well width rather than polarisation fields. However, in narrower wells this is not the case as the potential drop is small and even in the higher carrier density regime the quantum confinement is determined to a larger extent by the narrow well width. Thus, in narrower wells, carrier localisation may still be prevalent but here driven by alloy disorder rather than the polarisation field.

5.3.1.2 Degree of Optical Polarisation

To calculate the DOP, we follow our previous work [7] and focus on the orbital character of the occupied hole/valence states as a function of carrier density for a fixed temperature of $T = 300$ K. We assume here that electron states are predominantly s-like in character, which is confirmed by our empirical TB model calculations. Thus, it is sufficient to focus on the valence band structure. To do so we define the DOP, ρ, as follows:

$$\rho = \frac{\sum_{\tilde{N}=1}^{150} \sum_{i} f(E_{i,\tilde{N}}, T)(I_x^{i,\tilde{N}} + I_y^{i,\tilde{N}} - I_z^{i,\tilde{N}})}{\sum_{\tilde{N}=1}^{150} \sum_{i} f(E_{i,\tilde{N}}, T)(I_x^{i,\tilde{N}} + I_y^{i,\tilde{N}} + I_z^{i,\tilde{N}})} \,. \tag{5.3}$$

Here $\tilde{N}$ denotes the alloy configuration, $I_\alpha^{i,\tilde{N}}$ is the p_x ($\alpha = x$), p_y ($\alpha = y$) or p_z ($\alpha = z$) orbital contribution in the ith QW state with energy $E_{i,\tilde{N}}$; $f(E_{i,\tilde{N}}, T)$ denotes the Fermi function at temperature T, where the (quasi) Fermi level is defined with respect to the band edge energies and determined by the carrier density in the system. Using eq. (5.3), we define that $\rho = 1$ corresponds to TE polarised light emission from the well at a given carrier density at $T = 300$ K, while $\rho = -1$ indicates TM polarised emission. The above approach allows us to gain first insight into the light polarisation properties. It does not provide insight into the relative strength of TM to TE polarised transition, i.e. it does not provide a full emission spectrum, which would account for the wave function overlap between different electron and hole states. This overlap will differ, for example, between localised (near band edge states) and semi-/delocalised (energetically higher/lower lying) QW states. The population of excited states

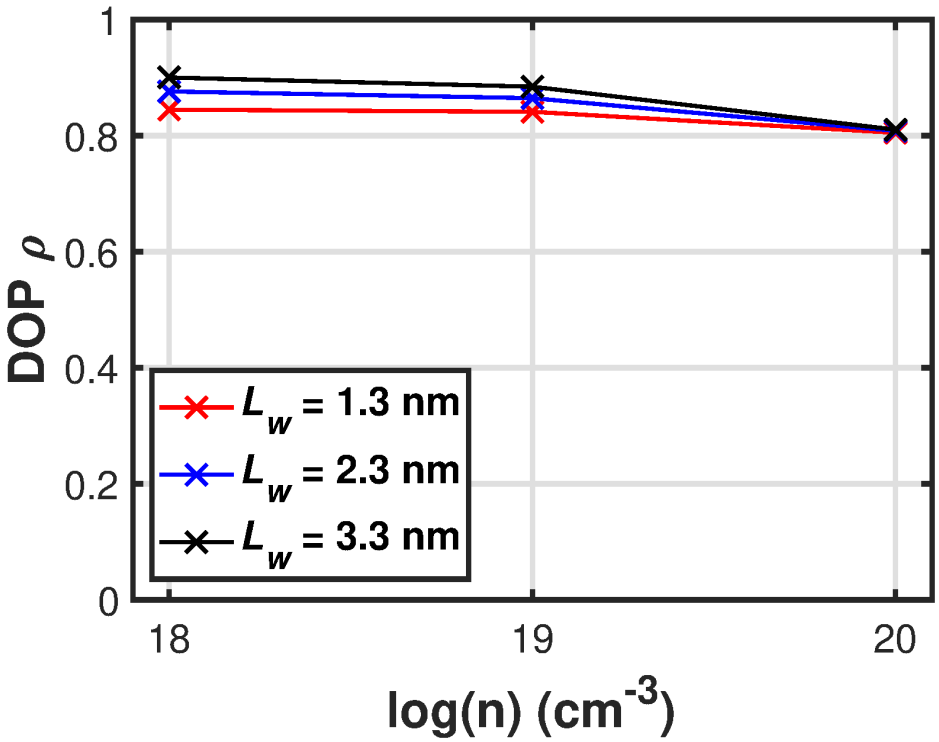


Figure 5.5: Averaged degree of optical polarisation, DOP ρ, over 150 configurations at a temperature of 300 K for $Al_{0.48}Ga_{0.52}N/Al_{0.63}Ga_{0.37}N$ quantum wells of width $L_w = 1.3$ nm (red), $L_w = 2.3$ nm (blue) and $L_w = 3.3$ nm (black) as a function of the carrier density n.

depends on carrier density and temperature. Thus, there is a competition between population probabilities of states and connected wave function overlaps. A full calculation of the emission spectrum can capture these effects but lies beyond the scope of this work. However, the framework introduced above (eq. 5.3) captures the essential requirement for generating TE- or TM-polarised light: i.e. in the absence of e.g. a p_x/p_y-like orbital character in a hole state, TE polarised light emission is absent. The definition of TE and TM polarised light emission builds on the widely used simplified description discussed in Sec. 5.2.1. Future studies may target polarisation resolved emission spectra [219], but to shed light onto how built-in polarisation fields, alloy disorder and well width affect the DOP, eq. (5.3) provides a good starting point for such an investigation.

Figure 5.5 displays the DOP for the different well widths considered, revealing that the emission of the $Al_{0.48}Ga_{0.52}N$ QW system studied is strongly TE polarised and that the well width and carrier density only slightly affect the DOP. These findings are in line with experimental and theoretical data from the literature [38, 207, 208, 209, 212]. Looking at the data displayed in Fig. 5.5 in

more detail, one observes that with increasing well width L_w the DOP slightly increases, especially when considering a low carrier density $n = 1 \times 10^{18}$ cm^{-3}. Moreover, and independent of L_w, we find that with increasing carrier density the DOP slightly decreases. We attribute these effects to changes in the electrostatic polarisation field. As discussed in the previous section, the larger potential drop in the wider wells leads to stronger wave function localisation effects at the lower QW barrier interface, cf. Fig. 5.4. Given that p_z-like basis states exhibit a lower effective mass along the c-axis, see discussion in Sec. 5.2.1, one expects that states with a large p_z-orbital contribution are pushed to lower energies and thus do not contribute significantly to the DOP. This explains why the DOP increases slightly with increasing well width. However, with increasing carrier density, the polarisation field is screened and so are carrier localisation effects, especially for wider wells. Thus, states with a higher p_z-orbital contribution may be found energetically closer to the VBE. Based on eq. (5.3), if states with higher p_z-orbital character are being populated, the DOP reduces, explaining thus the slight decrease in DOP with increasing carrier density.

Overall, our calculations show that the DOP in $Al_{0.48}Ga_{0.52}N/Al_{0.63}Ga_{0.37}N$ QWs is largely determined by macroscopic effects such as strain and polarisation field effects. As we will see in the following, this is not necessarily the case at higher Al contents in the well and barrier.

5.3.2 $Al_{0.75}Ga_{0.25}N/Al_{0.90}Ga_{0.10}N$ Quantum Well System

Having discussed Urbach tail energies and DOP for the lower Al content wells in the previous section, we turn now and investigate these quantities for the higher Al content structures with $Al_{0.75}Ga_{0.25}N/Al_{0.90}Ga_{0.10}N$. As highlighted in Sec. 5.2.2, such a system would be considered when targeting emitters in the deep UV spectral range and where competition between TE and TM polarisation is important for the LEE. We start again with Urbach tail energies, Sec. 5.3.2.1, before turning to the DOP, Sec. 5.3.2.2.

5.3.2.1 Urbach Tails

Figure 5.6 depicts the Urbach tail energies for $Al_{0.75}Ga_{0.25}N/Al_{0.90}Ga_{0.10}N$ QWs of $L_w = 1.3$ nm, $L_w = 2.3$ nm, and $L_w = 3.3$ nm, as a function of the carrier density n.

For the $L_w = 3.3$ nm QW system, E_u decreases with increasing carrier density. In contrast, E_u exhibits a much weaker carrier density dependence in the

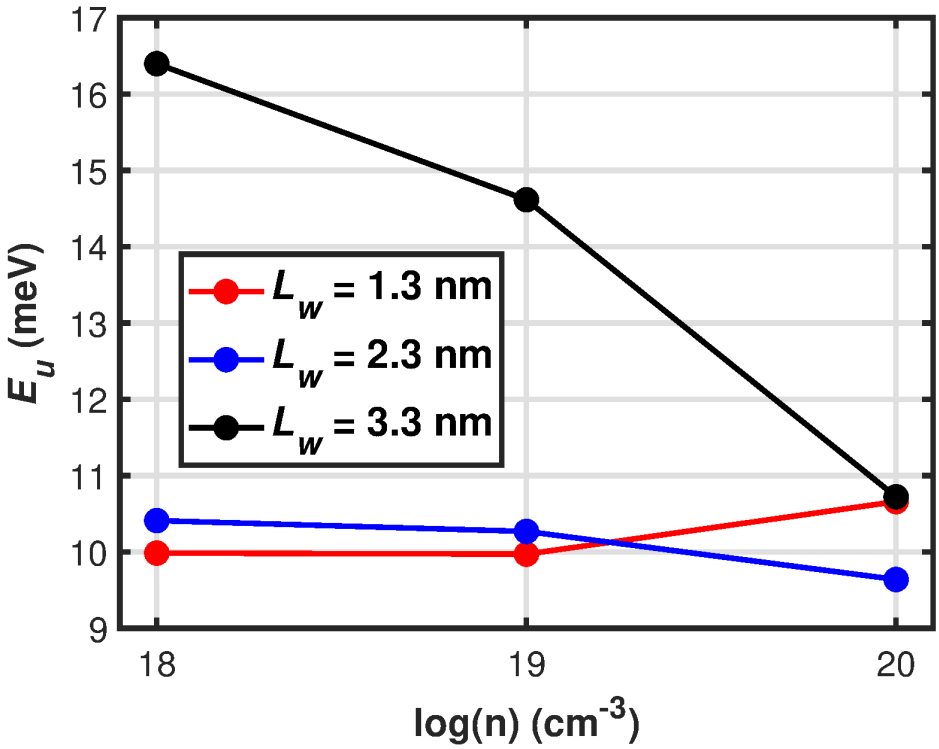


Figure 5.6: Urbach tail energies, E_u, for $Al_{0.75}Ga_{0.25}N/Al_{0.90}Ga_{0.10}N$ quantum wells of width $L_w = 1.3$ nm (red), $L_w = 2.3$ nm (blue) and $L_w = 3.3$ nm (black) at carrier densities of $n = 1\times10^{18}$ cm^{-3}, $n = 1\times10^{19}$ cm^{-3} and $n = 1\times10^{20}$ cm^{-3}.

$L_w = 1.3$ nm and $L_w = 2.3$ nm wells; also the E_u values for $L_w = 1.3$ nm and $L_w = 2.3$ nm systems are (much) smaller in magnitude when compared to the $L_w = 3.3$ nm $Al_{0.75}Ga_{0.25}N$ QW or equivalent $Al_{0.48}Ga_{0.52}N$ wells, cf. Fig. 5.3. Furthermore, Fig. 5.6 shows that the Urbach tail energies in the $L_w = 1.3$ nm and $L_w = 2.3$ nm wells behave differently with increasing n: while E_u slightly increases with increasing n for $L_w = 1.3$ nm, for $L_w = 2.3$ nm E_u slightly decreases.

To shed more light onto these findings, Fig. 5.7 depicts the planar integrated hole probability densities $P_m(k)$ for the $Al_{0.75}Ga_{0.25}N$ QWs considered. Looking at the $L_w = 3.3$ nm QW system first, we find a behaviour similar to the $Al_{0.48}Ga_{0.52}N$ wells discussed in Sec. 5.3.1. In the low carrier density regime of $n = 1\times10^{18}$ cm^{-3}, the built-in potential leads to a strong localisation of the hole wave functions at the QW barrier interface, cf. Fig 5.7 (c). When the carrier density reaches $n = 1\times10^{20}$ cm^{-3}, the built-in field is screened and carrier localisation effects are reduced, cf. Fig 5.7 (f). In the high carrier density regime, there are only a few extremely high $P_m(k)$ values, indicating thus that alloy disorder-induced carrier localisation effects are weaker in this regime.

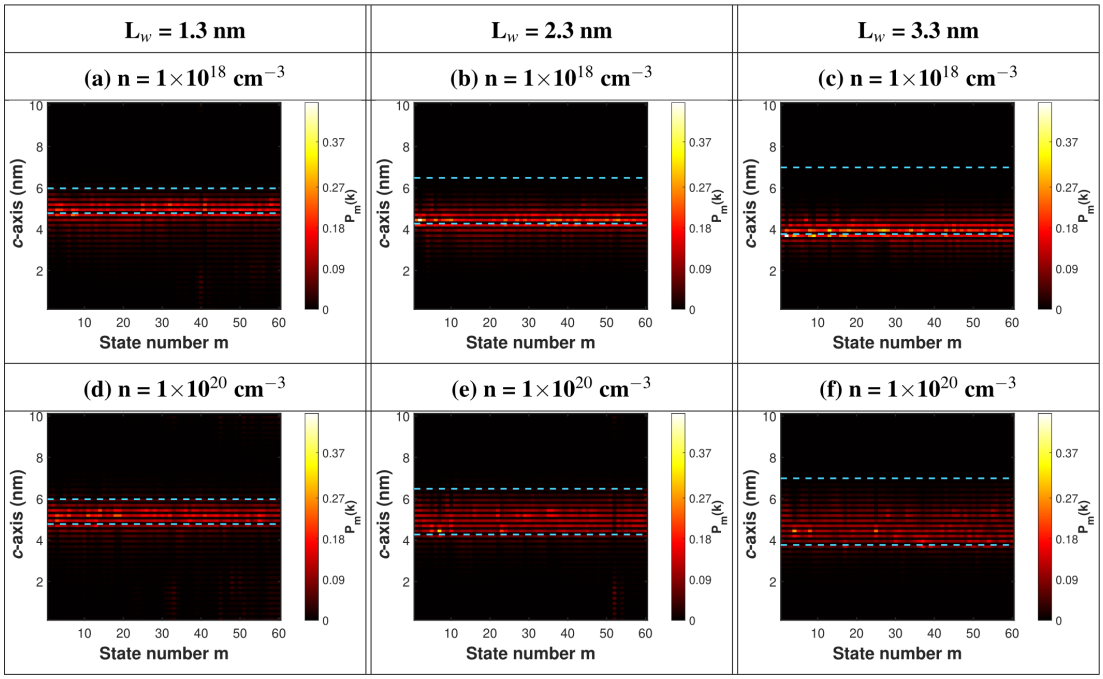


Figure 5.7: Planar integrated probability densities of holes, $P_m(k)$, for an arbitrarily chosen configuration of an $Al_{0.75}Ga_{0.25}N/Al_{0.90}Ga_{0.10}N$ quantum well of width $L_w = 1.3$ nm, $L_w = 2.3$ nm and $L_w = 3.3$ nm. The data are displayed at carrier densities of $n = 1 \times 10^{18}$ cm^{-3}, (a)-(c), and $n = 1 \times 10^{20}$ cm^{-3}, (d)-(f), for 60 states. Index m refers to the single-particle hole state number, with $m = 1$ being the ground state, while k refers to the layer in the supercell along the wurtzite c-axis. The quantum well boundaries are indicated by the light blue dashed lines. $P_m(k)$ has been plotted to the maximum $P_m(k)$ value found in the $L_w = 3.3$ nm $Al_{0.75}Ga_{0.25}N/Al_{0.90}Ga_{0.10}N$ QW system at a carrier density of $n = 1 \times 10^{18}$ cm^{-3}.

Overall, these findings explain the reduction in E_u with increasing n.

Turning to the $L_w = 1.3$ nm QW and comparing $P_m(k)$ for $n = 1 \times 10^{18}$ cm^{-3}, cf. Fig 5.7 (a), and $n = 1 \times 10^{20}$ cm^{-3}, cf. Fig 5.7 (d), one observes that carrier localisation is very different for these systems, especially for the states near the VBE, thus close to the ground state $m = 1$. While in the high carrier density regime, $n = 1 \times 10^{20}$ cm^{-3}, the hole charge densities are localised *inside* the well, for the low carrier density case, $n = 1 \times 10^{18}$ cm^{-3}, the charge density spreads more into the barrier material. This indicates a weaker carrier confinement in the $n = 1 \times 10^{18}$ cm^{-3} case when compared to $n = 1 \times 10^{20}$ cm^{-3}. This means that screening the built-in field results in improved carrier confinement for the narrow well. The stronger confinement in the well leads to a slight increase in the Urbach tail energy E_u when the carrier density increases to $n = 1 \times 10^{20}$ cm^{-3}.

The $L_w = 2.3$ nm QW system behaves similarly to the $L_w = 1.3$ nm structure in

the low carrier density regime of $n = 1 \times 10^{18}$ cm^{-3}, which means that the hole wave functions also leak into the barrier material. Thus, the Urbach tail energies at $n = 1 \times 10^{18}$ cm^{-3} for $L_w = 1.3$ nm and $L_w = 2.3$ nm are expected to be similar in magnitude, consistent with Fig. 5.6. When screening the polarisation field by increasing the carrier density in the well to $n = 1 \times 10^{20}$ cm^{-3}, cf. Fig. 5.7 (e), the hole wave functions start to localise inside the well again. However, in comparison to the $L_w = 1.3$ nm system, the potential drop is larger in the $L_w = 2.3$ nm QW system and as such screening of the built-in field becomes more important. At the highest carrier density, wave functions are now mainly confined by the well width as the potential drop is strongly reduced due to built-in field screening effects. Therefore one may expect to see a reduction in the Urbach tail energies in the $L_w = 2.3$ nm system $n = 1 \times 10^{20}$ cm^{-3} when compared to the $L_w = 1.3$ nm system, cf. Fig. 5.6, due to the hole wave function extending along a greater well width and does not sample alloy disorder of a few monolayers as in the case of the strong built-in field at low carrier densities. In general, a reduction of the Urbach tail energy can be attributed to a delocalisation of the hole wave functions. This is supported by Fig. 5.7 in the sense that (i) the wave functions spread over a larger region of the QW with increasing n and (ii) the absence of large $P_m(k)$ values on only a few layers k.

To further highlight changes in the carrier confinement and its impact of wave function localisation effects, which is more difficult to quantify from visually inspecting Figs. 5.4 and 5.7 due to the unified colour bar and given that these figures are based on one configuration only, Fig. 5.8 shows the probability of finding the hole charge density inside the QW, $|\Psi_h^{\text{avg}}|^2$, as a function of energy E_i^{avg}. Each energy state m is averaged over all 150 configurations and the energy is shifted to the average ground state energy E_1^{avg} for each QW system. Here, a higher energy means further away from the VBE. For comparison, Fig. 5.8 (a)-(c) displays $|\Psi_h^{\text{avg}}|^2$ for $Al_{0.48}Ga_{0.52}N$ wells, while Fig. 5.8 (d)-(f) depicts the data for the $Al_{0.75}Ga_{0.25}N$ wells, at carrier densities of $n = 1 \times 10^{18}$ cm^{-3} and $n = 1 \times 10^{20}$ cm^{-3}. Each energy level has been colour coded to visualise the average orbital character.

Figure 5.8 reveals that with increasing carrier density the wave function confinement inside the QW is increased due to screening of the polarisation field. However, we also note that even though the Al contrast between well and barrier is the same in $Al_{0.75}Ga_{0.25}N/Al_{0.90}Ga_{0.10}N$ and $Al_{0.48}Ga_{0.52}N/Al_{0.63}Ga_{0.37}N$ systems, the confinement is in general weaker in the high Al content system, cf. Fig. 5.8. We attribute this effect to the combination

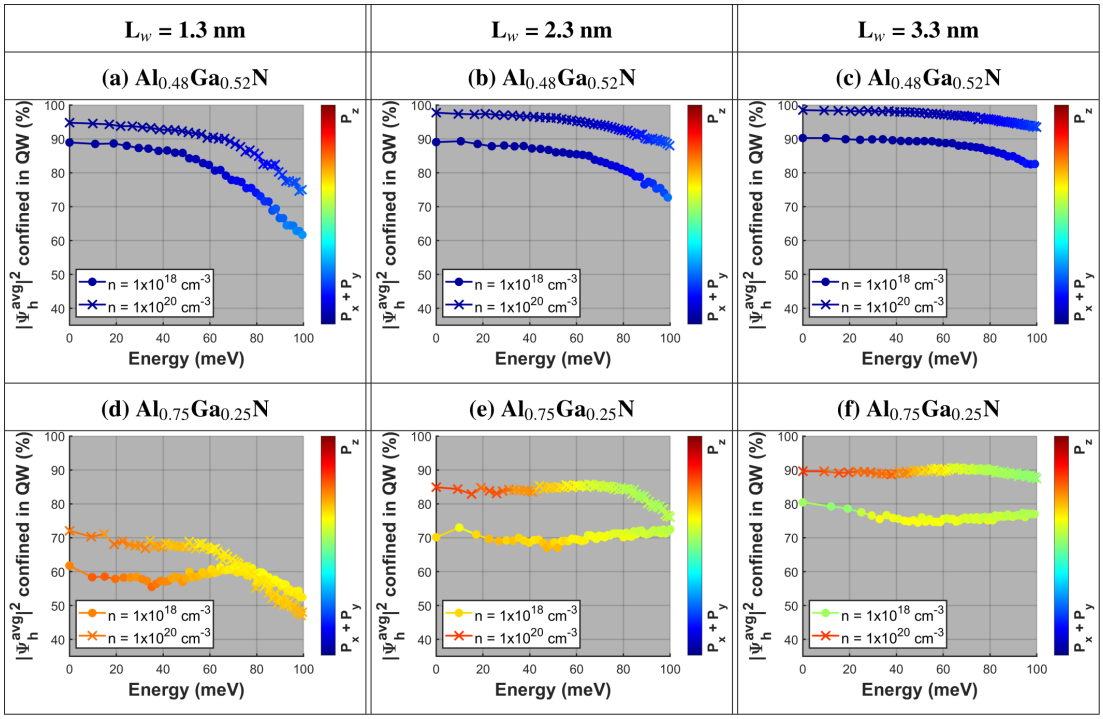


Figure 5.8: Average probability of hole charge density, $|\Psi_h^{\text{avg}}|^2$, confined inside the (Al,Ga)N quantum wells as a function of energy. The data are averaged over the 150 configurations. The average state energy is plotted with respect to the averaged ground state energy of each quantum well system. The $Al_{0.48}Ga_{0.52}N/Al_{0.63}Ga_{0.37}N$ wells are shown for (a) $L_w = 1.3$ nm, (b) $L_w = 2.3$ nm, and (c) $L_w = 3.3$ nm; the data for $Al_{0.75}Ga_{0.25}N/Al_{0.90}Ga_{0.10}N$ wells is displayed in (d)-(f). For each QW system $|\Psi_h^{avg}|^2$ is plotted for two carrier densities: $n = 1 \times 10^{18}$ cm^{-3} (circles) and $n = 1 \times 10^{20}$ cm^{-3} (crosses). The colour coding gives the averaged orbital contribution of each energy level (red: p_z; blue: $p_x + p_y$).

of two factors. Firstly, in the high Al content regime, QW states have a higher p_z orbital contribution. Secondly, p_z-like basis states/bands have a low effective mass along the wurtzite c-axis (cf. Fig. 5.1). Thus, confinement effects and changes in confinement due to carrier density screening will more strongly impact the electronic structure of the QW. Moreover, hole wave functions with a high p_z-orbital character will be leaking into the barrier. Therefore, all this contributes to reduced carrier confinement seen in Fig. 5.8. Narrow QWs with high Al contents are widely used in deep UV LEDs [208, 211]. These structures often suffer from low EQEs. Our calculations provide a possible reason for this behaviour, if the wave functions are weakly confined, recombination at defects may be more likely, due to a higher probability of the hole charge densities at a defect site, assuming a delocalised electron wave function. Thus our findings suggest that using wider wells for (Al,Ga)N-based deep UV LEDs can be

beneficial for the device performance. As expected from our discussion in Sec. 5.2.1, Fig. 5.8 also confirms that the orbital character of the hole states is sensitive to QW width and carrier density. Thus, the DOP will also be impacted by these factors. It should be noted that while Fig. 5.8 displays the average orbital character for each state, the population of the different states with carriers is not accounted for in this plot. In the following section we discuss the impact of well width and carrier density on the DOP in $Al_{0.75}Ga_{0.25}N/Al_{0.90}Ga_{0.10}N$ QWs for different carrier densities in more detail. Thus, we account for both the orbital character, as shown in Fig. 5.8, and population of the different states when evaluating the DOP.

5.3.2.2 Degree of Optical Polarisation

Before turning to the DOP in $Al_{0.75}Ga_{0.25}N/Al_{0.90}Ga_{0.10}N$ QWs we revisit briefly the $Al_{0.48}Ga_{0.52}N$ wells. The colour coding in Fig. 5.8 (a)-(c) reveals that in the $Al_{0.48}Ga_{0.52}N$ QWs the hole states in an energy range of 100 meV below the VBE are predominately p_x- and p_y-like in orbital character. Building on our definition for the DOP ρ, eq. (5.3), this confirms the earlier finding that independent of well width or carrier density, light emitted from the $Al_{0.48}Ga_{0.52}N$ QWs will be predominately TE polarised.

Turning in a second step to the $Al_{0.75}Ga_{0.25}N$ systems, Fig. 5.8 (d)-(f), one finds a more complex behaviour. Firstly, one observes that the orbital character of the states varies with energy. Independent of the well width or carrier density, states near the VBE are a mixture of p_x-, p_y- and p_z-like orbitals, in contrast to the $Al_{0.48}Ga_{0.52}N$ wells. Looking at the low carrier density of $n = 1 \times 10^{18}$ cm^{-3} results for the three different wells, Fig. 5.8 (d)-(f), indicate that with increasing well width the p_z-orbital contribution in the states energetically closest to VBE, i.e. the zero of energy, is reduced. This is indicative of an increasing DOP with increasing well width at low carrier densities. One may expect the opposite behaviour, given that the quantum confinement due to the increasing well width is reduced and that the states with predominately p_z orbital character may shift to energies energetically closer to the VBE; this expectation is based on the fact that p_z-like states exhibit a lower effective mass along the c-axis. However, with increasing well width, the potential drop across the well also increases and thus increases the carrier confinement. This is also reflected in the increase of $|\Psi_h^{\text{avg}}|^2$ with increasing well width at the fixed carrier density of $n = 1 \times 10^{18}$ cm^{-3}. Therefore, due to the lower effective mass of p_z-like states along the c-axis growth direction, stronger confinement arising from the built-in potential will

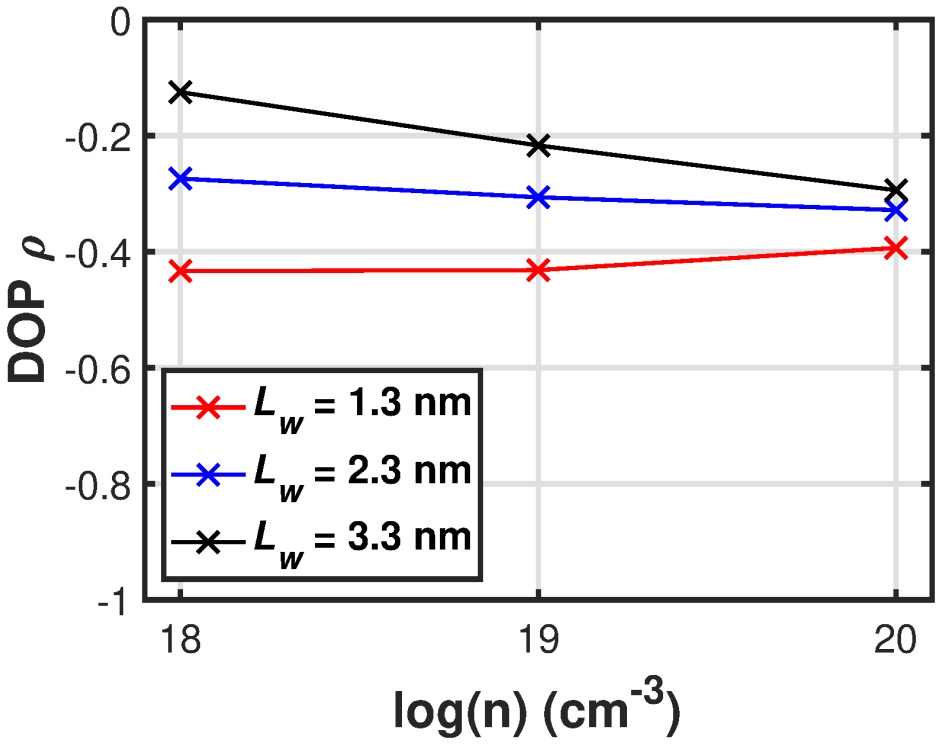


Figure 5.9: Averaged degree of optical polarisation, DOP ρ, over 150 configurations at a temperature of 300 K for $Al_{0.75}Ga_{0.25}N/Al_{0.90}Ga_{0.10}N$ quantum wells of width $L_w = 1.3$ nm (red), $L_w = 2.3$ nm (blue) and $L_w = 3.3$ nm (black) as a function of carrier density n.

shift p_z-like states energetically away from the VBE.

With increasing carrier density the built-in field is screened and the confinement effect introduced by this field is reduced. Consequently, at a high carrier density of $n = 1 \times 10^{20}$ cm^{-3}, the p_z orbital character near the VBE increases with increasing well width L_w as Fig. 5.8 (d)-(f) reveals. Thus, at high carrier densities, the DOP is expected to decrease with increasing well width L_w.

Equipped with this insight, we use eq. (5.3) to study the DOP in the $Al_{0.75}Ga_{0.25}N/Al_{0.90}Ga_{0.10}N$ QWs as a function of carrier density at a fixed temperature of $T = 300$ K. The calculated DOP values are shown in Fig. 5.9. The data indicate that the emission is indeed noticeably TM polarised for this high Al content system, which is in contrast to the $Al_{0.48}Ga_{0.52}N/Al_{0.63}Ga_{0.37}N$ wells investigated in Sec. 5.3.1, but in line with similar experimental observations in the literature [212].

Looking at the DOP as a function of carrier density n for a fixed well width, Fig. 5.9 shows that for the narrow well width of $L_w = 1.3$ nm the DOP increases with increasing carrier density. We attribute this to the effect that at low

carrier densities the hole wave functions are much weaker bound in the $L_w = 1.3$ nm QW system when compared to the high carrier density regime, which is supported by the data in Fig 5.8. In the wider wells, $L_w = 2.3$ nm and $L_w = 3.3$ nm, the DOP decreases with increasing carrier density. The observed behaviour stems from changes in the confining potential discussed above, originating from the screening of the built-in field with increasing carrier density. Also, given that these screening effects are more pronounced in the wider well, the DOP changes with increasing carrier density n more strongly in the $L_w = 3.3$ nm system when compared to $L_w = 2.3$ nm. However, even at high carrier densities of $n = 1 \times 10^{20}$ cm^{-3} a slightly larger DOP is observed in the $L_w = 3.3$ nm system when compared to $L_w = 2.3$ nm and especially $L_w = 1.3$ nm. At lower carrier densities this difference is even larger, and favours the wider wells even more for a higher DOP value.

While narrow wells, e.g. $L_w = 1$ nm or $L_w = 1.5$ nm, are often employed in deep UV light sources [208, 211], our analysis indicates that wider wells can be beneficial for these emitters for several reasons. Firstly, as shown above, in the higher Al content regime, carrier confinement in narrow wells can be poor. While this may be an advantage for carrier transport in multi-QW (MQW) systems, these systems can also be prone to defect-related recombination processes. Secondly, wider wells are promising candidates in order to lower the steady-state carrier density inside the well, which may lead to a reduction in, for instance, Auger-Meitner related recombination processes [220]. Based on our DOP calculations, wider wells with lower carrier densities will also lead to a higher DOP value when compared to the same carrier density in a narrower well. However, it should also be noted that, in general, it is expected that the radiative recombination rate is reduced in wider wells compared to narrower wells due to the quantum confined Stark effect. In addition to this, growing wider wells can also lead to material science specific challenges including strain relaxation and the formation of extended defects [221]. The latter aspect will also affect radiative recombination efficiencies [222]. However, recent experimental investigations have focused on well widths that are much larger than the here studied range, targeting thus high quality wide well system for UV LEDs [202, 213]. Further studies are now required to analyse the competition between radiative, non-radiative recombination and the DOP in deep UV light emitters, utilising wider wells.

5.4 Conclusion

In this part of the thesis, we have analysed the DOP in (Al,Ga)N QWs operating in the UV-C spectral range by means of the atomistic multi-band electronic structure model introduced in Sec. 3.2.3 in Chapter 3. Thus, the model accounts for alloy disorder-induced band mixing effects which are neglected in widely available continuum based simulation frameworks. In our study special attention has been paid on the impact of (i) Al content, (ii) carrier density and (iii) well width on Urbach tail energies and the DOP.

We have considered two (Al,Ga)N based QW well systems which differ in the Al content in the well and barrier. However, for consistent comparison, the Al contrast between well and barrier is kept constant in our investigations. The considered QW systems, $Al_{0.48}Ga_{0.52}N/Al_{0.63}Ga_{0.37}N$ and $Al_{0.75}Ga_{0.25}N/Al_{0.90}Ga_{0.10}N$ wells, are representative for structures found in the literature to achieve light emission in the deep UV-C spectral range, $Al_{0.75}Ga_{0.25}N/Al_{0.90}Ga_{0.10}N$, and the longer wavelengths end of the UV-C window, $Al_{0.48}Ga_{0.52}N/Al_{0.63}Ga_{0.37}N$. Even though the contrast in Al content is kept constant between these two systems, our calculations show that carrier confinement, especially for narrower wells, e.g. $L_w = 1.3$ nm, is much weaker in the high Al content system. This effect may be beneficial for carrier transport in deep UV light emitters with high Al content, however, it can lead also to the situation that these emitters are more prone to defect related recombination since the wave functions can significantly spread into the barrier material.

In terms of the DOP, our calculations show that in general wider wells lead to a higher DOP value. In the lower Al content system, $Al_{0.48}Ga_{0.52}N/Al_{0.63}Ga_{0.37}N$ wells, this observation is of secondary importance as the light is predominately TE polarised, which can enable a high LEE. This finding of predominantly TE polarised emission is independent of the well widths and carrier densities studied. The situation is more complicated in the higher Al content $Al_{0.75}Ga_{0.25}N/Al_{0.90}Ga_{0.10}N$ QW system. In general, with increasing well width the DOP increases, so that emission is tending towards TE polarisation. We observe in our study that this effect is more pronounced at lower carrier densities, e.g. $n = 1 \times 10^{18}$ cm^{-3}. However, even at high carrier densities of $n = 1 \times 10^{20}$ cm^{-3}, an $Al_{0.75}Ga_{0.25}N/Al_{0.90}Ga_{0.10}N$ QW of width $L_w = 3.3$ nm still exhibits a slightly higher DOP when compared to the same system with a width of $L_w = 1.3$ nm.

Overall, for (Al,Ga)N-based light emitters operating in the deep UV spectral range our calculations indicate that, in terms of carrier confinement and light polarisation characteristics, wider wells are advantageous. However, it should also be noted that there are several challenges in using wider wells for UV light emitters. This includes, for example, difficulties in growing high quality, low defect density wide QW systems. Moreover, the wider well width can also lead to a reduction in the radiative recombination rate. These factors can offset the benefits of wider wells in terms of stronger carrier confinement in the well and an increased DOP. Therefore, future studies may target a detailed analysis of balancing these competing factors as a function of the well width in deep UV light emitters to improve their efficiencies.

Having investigated the impact alloy fluctuations have on the electronic and optical properties of (Al,Ga)N QWs, we now turn our attention to the impact alloy fluctuations have on the carrier transport and recombination in deep UV LEDs.

Chapter 6

Carrier transport and recombination in (Al,Ga)N-based UV light emitters

6.1 Introduction

In order to model a realistic LED structure, multiple factors have to be taken into account. This includes considering that the active region of the device consists of a MQW system, that an electron blocking layer (EBL) is typically incorporated and that the doping profile is described appropriately. The previous chapters have shown that alloy disorder in (Al,Ga)N QWs has a significant impact on their electronic structure. This presents a significant challenge for an accurate theoretical and numerical description of the optoelectronic properties of the full LED, since a 3D treatment of, for instance, an (Al,Ga)N QW, is required ideally on an atomistic level. Numerical challenges are further amplified when these large 3D supercells require self-consistent calculations of the coupled DD and Schrödinger-Poisson equations. Significant progress has been made to address these questions [45, 106, 170] but, in comparison to (In,Ga)N, understanding the fundamental impact of alloy fluctuations on carrier transport and recombination properties in (Al,Ga)N-based QW systems is sparse. This stems from the fact that fundamental properties of (Al,Ga)N are very different from (In,Ga)N. This includes, for instance, composition dependent valence band ordering in (Al,Ga)N, which is absent in (In,Ga)N. As such methods developed for modelling (In,Ga)N cannot be easily transferred to (Al,Ga)N LED simulations.

As a first step we aim to establish fundamental insight into how alloy disorder affects carrier transport, localisation and recombination processes in a simplified set up. To do this, we will look at a 3D carrier transport calculation for a deep UV single (Al,Ga)N QW. Here we target an $Al_{0.7}Ga_{0.3}N/Al_{0.8}Ga_{0.2}N$ QW embedded in p- and n-doped regions, thus a system relevant for deep UV (Al,Ga)N-based LEDs. We employ our quantum corrected DD simulation framework to compare the results of VCA calculations to the results from an atomistic simulation which accounts for alloy disorder. To target recombination processes, this framework is coupled with the widely used ABC model [86], as discussed in detail in Sec. 2.5. Our results indicate that alloy fluctuations can promote carrier transport through the intrinsic barriers by opening up low energy percolation paths in the (Al,Ga)N alloy. These pathways appear to improve the carrier injection into the QW region – a feature that is neglected in 'conventional' calculations utilising a VCA. Moreover, while we find that alloy disorder and carrier localisation effects enhance radiative recombination, we observe also that non-radiative Auger-Meitner recombination processes are strongly increased. The resulting increase in high energy carriers via non-radiative Auger-Meitner recombination may also lead to a degradation of the material as indicated in experimental studies [223]. As a consequence, our results suggest that alloy disorder can have a detrimental effect on the device efficiency. To reduce Auger-Meitner related processes, increasing the well width or employing MQW active regions to reduce the carrier density could be a way to improve quantum efficiencies in UV emitters, as the above discussed percolation paths may be exploited to distribute the carriers more evenly between MQWs.

To explore this further, we study a full LED where the active region consists of a multi-QW system that includes alloy disorder. We incorporate an EBL and account for the effect of incomplete ionisation in the doped layers. Special attention is given to the role of the acceptor activation energy on the carrier distribution across the MQWs and its impact on the internal quantum efficiency (IQE), as determined by the current injection efficiency (CIE) and radiative recombination efficiency (RRE) (see Sec. 2.5).

Our results show that p-doping the EBL significantly improves the CIE. It was found that the electron density across the QWs remained relatively uniform, but the hole distribution was notably asymmetric, with the QWs closest to the p-side exhibiting the lowest hole density. This asymmetric feature was noticeably enhanced with alloy disorder. It was found that carrier localisation

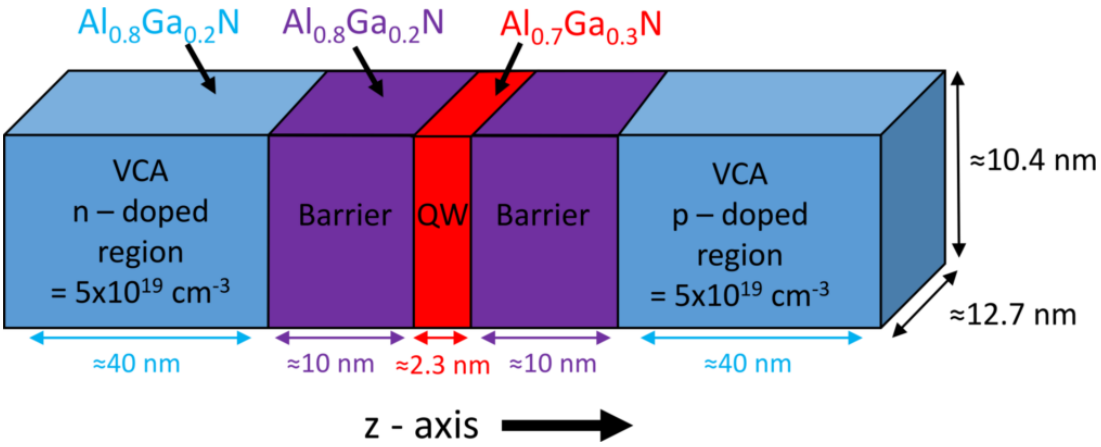


Figure 6.1: Schematic illustration of the (Al,Ga)N-based *p-i-n* system underlying the single quantum well simulations. The intrinsic barriers plus quantum well region is denoted as the "atomistic" mesh in the main text, while the *n*- and *p*-regions are described by a sparser device mesh.

due to alloy fluctuations increases the local recombination rates, hindering efficient redistribution of holes when compared to a VCA. It was also found that the alloy fluctuations in the barrier material preceding the EBL had a significant effect promoting electron leakage.

6.2 Single (Al,Ga)N QW

The quantum corrected multiscale simulation framework described in detail in chapter 3 is here applied to a *p-i-n* system where the intrinsic (*i*) region contains a 2.3 nm wide $Al_{0.7}Ga_{0.3}N$ QW embedded into approximately 10 nm wide intrinsic $Al_{0.8}Ga_{0.2}N$ barriers, following the UV-C device design in Ref. [38]. The atomistic mesh region describing the active region of the device has the dimensions of roughly $17.4 \times 15.1 \times 22.2$ nm^3, corresponding to $\approx$ 560,000 atoms, and is coupled with a sparser device mesh by adding 40 nm of *n*- and *p*-doped regions, respectively. The doping density is 5×10^{19} cm^{-3} following the set-up described in Ref. [69]. A schematic illustration of the structure is given in Fig. 6.1. To connect the conduction band and valence band edges between the atomistic and the sparser mesh, we use a blend of Gaussian softening and LLT to avoid discontinuities at such an interface. Details on the Gaussian softening and the effect of LLT on the energy landscape can be found in chapter 3 and Ref. [170]. To test the impact of the in-plane dimensions of the simulation cell and thus also the influence of the alloy microstructure on the results, the calculations have been repeated for different cell sizes (not shown). These

different calculations revealed in general the same trends as reported below, so that the above detailed simulation set up gives a representative picture of the impact of alloy disorder on the carrier transport in the discussed device.

For this alloy composition, the DOP appears potentially to be a mix of TE and TM polarisation [7, 71, 208, 209], as discussed in the previous chapter. In principle, a detailed study of band mixing and how this affects effective masses is required and we will return to this in Sec. 6.3.1. However, the aim of this section is to understand the impact of alloy disorder on the carrier transport and recombination mechanisms. Therefore, we assume that the effective mass is mainly determined by the A-band, and carry out a a linear interpolation between the GaN and AlN band.

6.2.1 Results

To investigate the impact alloy fluctuations have on the carrier transport and the recombination process we proceed as follows: Our starting point is a fully atomistic description, meaning that alloy fluctuations in both the intrinsic (Al,Ga)N QW and (Al,Ga)N barriers are accounted for (cf. Fig. 6.1). To study the impact of alloy disorder on the carrier injection, we investigate a second set-up in which alloy fluctuations in the (Al,Ga)N QW are treated on an atomistic level, however the intrinsic (Al,Ga)N barriers are described in a VCA. Finally, we employ a VCA description of the entire QW plus barrier system. This last setting is basically equivalent to one-dimensional carrier transport simulations widely employed in commercially available software packages. In order to establish a comparable VCA description of the targeted system, without introducing additional free parameters (e.g. alloy dependence and/or bowing parameters of material parameters), the atomistic energy landscape is averaged over the corresponding areas e.g. well or barrier. To achieve this averaging procedure, the QW was treated initially with Dirichlet boundary conditions so that, except from alloy fluctuation-induced variations, the conduction and valence band edges are flat. A VCA description of the barriers is then straightforward and achieved by averaging the atomistic energy landscape over the entire barrier volume. However, the QW VCA description is slightly more complicated as piezoelectric and spontaneous polarisation-induced built-in fields across the QW cause the band edges to bend. Thus, a volume average over the QW region is not possible. In this case, the atomistic energy landscape is averaged across each c-plane along the growth direction (c-axis).

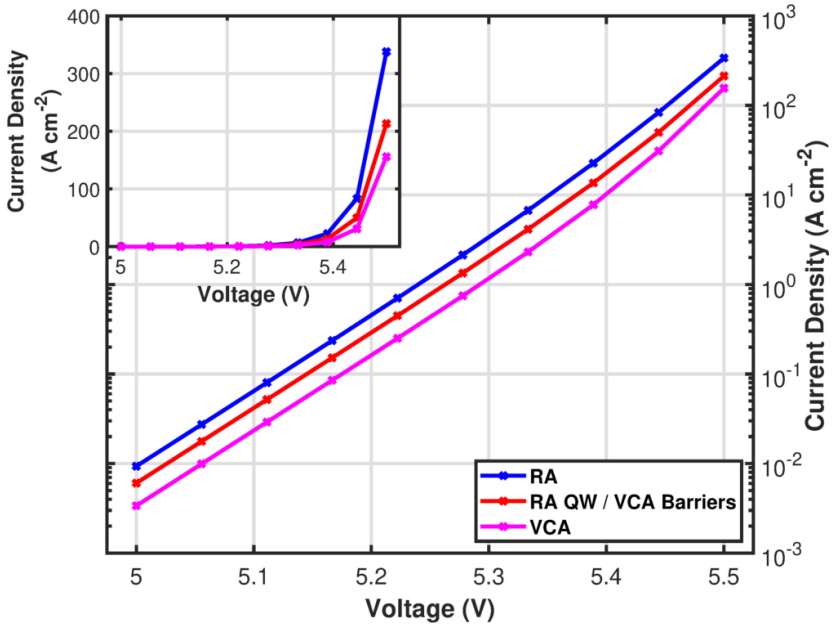


Figure 6.2: Current-voltage curves, on a log-scale, for an $Al_{0.7}Ga_{0.3}N/Al_{0.8}Ga_{0.2}N$ quantum well embedded in a *p-n* junction. The data are shown for simulations that (i) account for random alloy (RA) fluctuations in the well and barriers (blue), (ii) account for RA fluctuations in the well but treat the barrier in a virtual crystal approximation (VCA) (red), and (iii) use a VCA in the entire *p-i-n* structure (pink). The inset shows the I-V curves on a linear scale.

While this can lead to slight fluctuations in the energy landscape, the approach chosen here is better suited to compare the different calculations, since it avoids constructing a VCA that requires specific information on how to average e.g. material and TB parameters with composition, or to perform a separate VCA built-in field calculation.

Building on these different simulation set-ups, Fig. 6.2 displays the calculated current-voltage (I-V) curves of the above described (Al,Ga)N *p-i-n* structure using (i) the fully atomistic approach (RA), (ii) accounting for alloy fluctuations in the well but not the barrier (RA QW/VCA Barriers) and (iii) a VCA of the entire system. One can infer from this figure that the fully atomistic treatment gives independent of the applied voltage the highest current density, while the full VCA description of the system (well and barriers) results in the lowest density. Figure 6.2 also reveals that the current density, especially at lower bias values, is increased when accounting for alloy fluctuations in the barrier; this can be seen from the comparison of the I-V curves for the fully atomistic and 'partial' VCA (RA QW, VCA Barriers) treatment. Thus, our results indicate that alloy fluctuations are beneficial for the carrier injection into the QW region.

We note also that the I-V curves (on semi-log plot) shown in Fig. 6.2 exhibit a close to linear behaviour over the bias range considered. From the slope of an I-V curve in a semi-log plot, further information about physical processes that dominate the behaviour of an LED can be obtained. This is often done in terms of the so-called ideality factor, η [224, 225], which is derived from the diode equation and is given by:

$$\eta = \frac{q}{k_B T} \frac{\partial V}{\partial \ln(I)} \ , \tag{6.1}$$

which on a log-scale is

$$\eta = \frac{q}{2.303 k_B T} \frac{1}{m} \ , \tag{6.2}$$

where m is the slope extracted from Fig. 6.2. The ideality factor is discussed in 3 different regimes: $\eta = 1$ indicates current is dominated by diffusion of carriers, $\eta = 2$ indicates that current is dominated by carrier recombination processes and $\eta > 2$ suggests traps, leakage and/or series resistance effects (non-ideal effects). The slopes of the I-V curves (RA, RA QWs / VCA Barriers, VCA) in Fig 6.2 have an ideality factor of $\eta \approx 1.8$, which indicates that recombination is dominating the device structure considered. This result is consistent with the simplified nature of the studied LED structure, which lacks for example multiple QWs or an EBL. Moreover, it contains a high and even free carrier density (complete ionisation of dopants), and perfectly ohmic contacts are assumed. All of this is expected to lead to minimal series resistance effects. When considering MQWs or EBLs, the slope of the I-V curve is only piecewise constant, with varying ideality factors [226] as we will see and discuss in Sec. 6.3. For the aim of this section, namely to shed light on the impact of alloy disorder on carrier transport, the considered simplified LED structure is sufficient.

To visualise the impact of alloy fluctuations on the carrier transport and recombination further, Fig. 6.3 depicts an isosurface plot of the current density in the intrinsic (Al,Ga)N QW and barrier regions, cf. Fig. 6.1, at a fixed bias point of 5.5 V obtained from the fully atomistic description of the system. One can infer that alloy fluctuation-induced band edge energy fluctuations lead to regions of higher and lower current densities. Thus, the fluctuations in the band

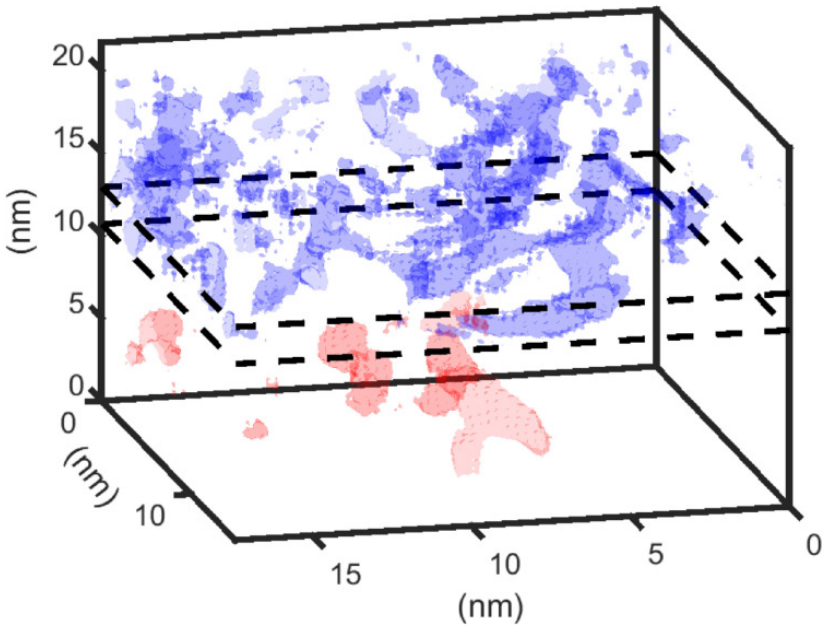


Figure 6.3: 3D isosurface plot of the current density in the intrinsic (Al,Ga)N quantum well and barrier regions at a bias of 5.5 V, using the fully atomistic description, described in the main text. The current density for the holes (blue) and electrons (red) are plotted at 700 A cm^{-2}, reflecting locally high current densities due to alloy fluctuations; dashed black lines indicate well boundaries.

edge energies enable percolation paths into the active region; such pathways are absent in a VCA description of the system. We note that this percolation path effect has also been observed in (In,Ga)N QWs and (Al,Ga)N barriers [46, 227, 228, 229]. We further note that both electron and hole transport are affected by these percolation paths. However, due to the lower effective electron mass, the electron charge density is more smeared out, and compared to the holes, fewer regions reach the isosurface value at which the current density is plotted in Fig. 6.3. As a consequence of these percolation paths, one expects higher carrier densities in the active region in comparison to a simulation that neglects alloy disorder. Also, as we will see below, the percolation paths can lead to an increased hole density in the intrinsic barrier on the n-side of the studied system. Such a situation may be beneficial for inter-well transport in (Al,Ga)N multi-QW systems as recently reported in (In,Ga)N-based LEDs [230].

To study the impact of alloy fluctuations on the carrier transport and recombination in (Al,Ga)N-based LED structures in further detail, Fig. 6.4 depicts electron and hole carrier densities above the turn-on voltage of the device, at a bias of 5.5 V. Figure 6.4 (a) displays the *averaged* carrier density,

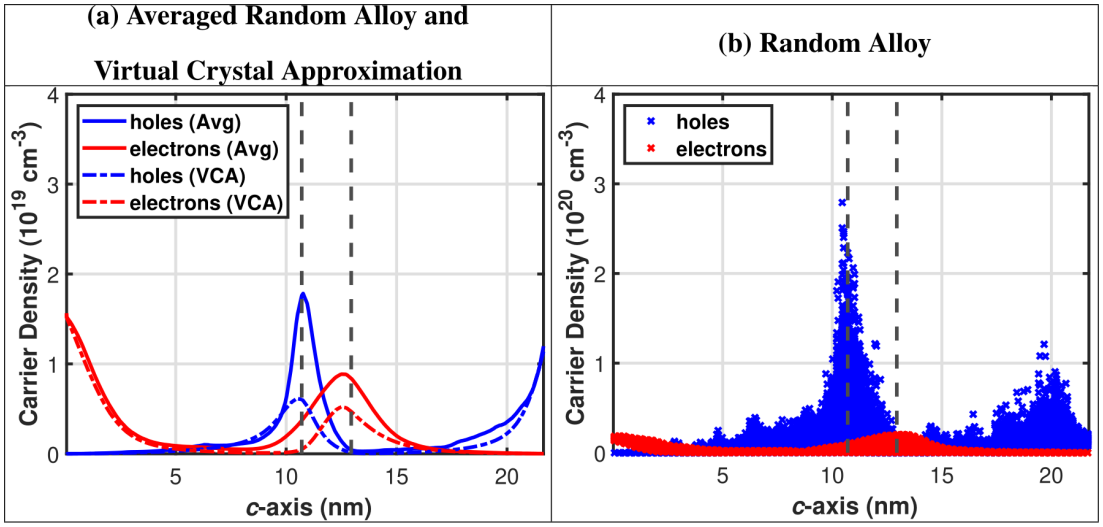


Figure 6.4: Electron (red) and hole (blue) density along the c-axis of a $Al_{0.7}Ga_{0.3}N/Al_{0.8}Ga_{0.2}N$ quantum well embedded in a p-i-n junction at a bias of 5.5 V; data are shown for the intrinsic regions of the device. (a) Averaged carrier distribution of the fully atomistic calculation over each c-plane along the c-axis (solid lines), and the carrier distribution for the virtual crystal approximation (dashed lines); (b) Scatter plot of the carrier distribution in the fully atomistic calculation. The vertical dashed black lines indicate well boundaries. Note (b) is an order of magnitude larger than (a) on the y-axis.

over each c-plane, for the random alloy system along the c-axis (growth direction) together with the VCA data which neglects alloy disorder. When comparing the averaged random alloy data with the VCA results, it becomes clear that *on average* both electron and hole carrier densities are increased in the well when taking alloy fluctuations into account. Figure 6.4 (a) indicates that the *average* hole charge density does not leak as much into the intrinsic (Al,Ga)N barrier material on the n-side of system (region below 10.7 nm), when compared to the hole density profile in VCA; one may attribute this to alloy-induced hole localisation effects which are not accounted for by the VCA description. The *average* electron density extends further into the (Al,Ga)N barrier region on the p-side (region above 13 nm) when compared to the VCA data; we relate this to the effect that alloy disorder and quantum corrections effectively reduce the quantum confinement between well and barrier and that the electrons are less strongly affected by alloy-induced carrier localisation effects as already seen in (In,Ga)N-based systems [170]. However, it must be noted that the random alloy data in Fig. 6.4 (a) are averaged over each c-plane. Thus, while on average the hole density may be smaller in e.g. the intrinsic barrier of the n-region when compared to VCA, local alloy regions may have

high hole densities. To shed light onto this behaviour, Fig. 6.4 (b) displays a scatter plot of the carrier densities along the c-axis in the intrinsic (Al,Ga)N regions. The symbols give the carrier density at each lattice site within the respective c-planes. Figure 6.4 (b) reveals strong fluctuations in the *local* densities which may be an order of magnitude higher than the *average* densities displayed in Fig. 6.4 (a). The *local* hole carrier density is also noticeably higher when compared to the electrons. In general, due to the higher effective mass, carrier localisation for holes is more pronounced when compared to electrons [7]. Therefore, we conclude that percolative pathways, can promote easier transport of the carriers through the barriers. Thus, holes may transport to the n-side of the system more easily when compared to predictions from a VCA model. This aspect is of interest when designing MQW-based (Al,Ga)N LEDs, since it can help with a more equal distribution of holes between the wells. Such an effect is important for optimising recombination processes, and we will explore this further in the following sections.

Equipped with this information we turn our attention now to the recombination process in the system. To do so we employ the widely used ABC model. In the following we mainly focus our attention on the radiative and Auger-Meitner (non-radiative) processes; with increased current densities radiative and non-radiative Auger-Meitner processes become dominant over Shockley-Read-Hall (SRH) recombination as these contributions scale with carrier density n as $\propto n^2$ (radiative) and $\propto n^3$ (Auger-Meitner) compared to $\propto n$ (SRH).

We note that defect related non-radiative processes, such as SRH and trap assisted tunnelling (TAT) processes can also affect the device performance of UV-C (Al,Ga)N-based LEDs significantly. While we take SRH into account, TAT processes have not been considered here but could be accounted for as a SRH-like process with different capture rates as detailed in Ref. [231]. Turning to radiative and Auger-Meitner (non-radiative) recombination rates, Fig. 6.5 depicts these rates calculated (i) including random alloy fluctuations and thus carrier localisation effects and (ii) using VCA for the entire system, consequently excluding alloy disorder. Figure 6.5 displays the random alloy (RA) data averaged over each c-plane. We stress that the recombination rates are calculated using the *local* carrier density data, thus accounting for the effect that locally one may encounter both high electron and hole densities. The required radiative (B) and Auger-Meitner (C_{nnp} and C_{npp}) recombination coefficients are taken from Ref. [69]. We note that building on this often used

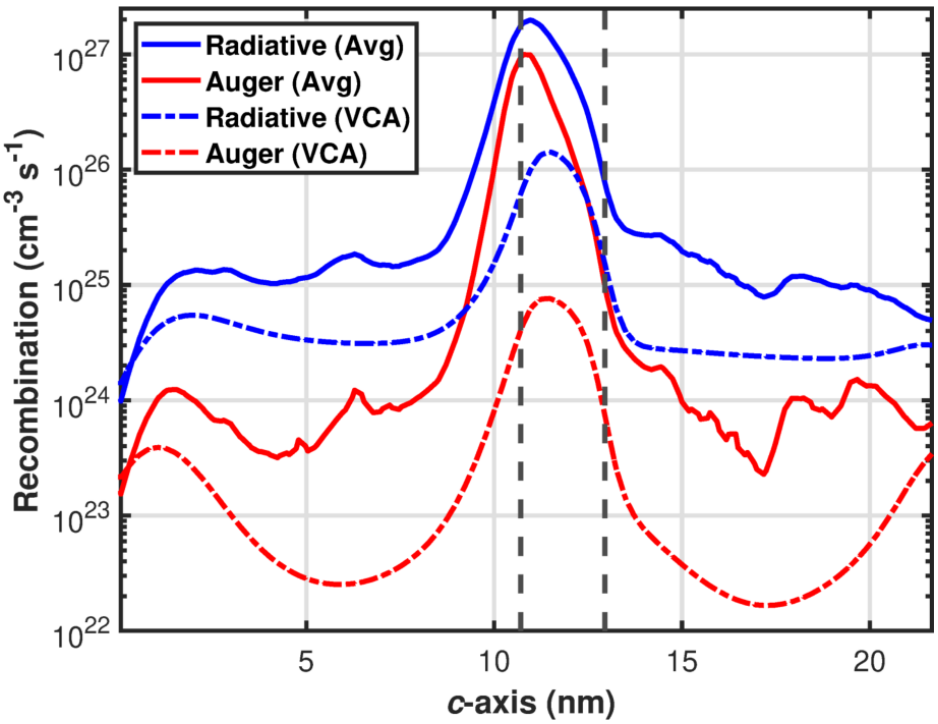


Figure 6.5: Radiative and Auger-Meitner non-radiative recombination rates along the c-axis of the $Al_{0.7}Ga_{0.3}N/Al_{0.8}Ga_{0.2}N$ p-i-n system at a bias of 5.5 V; the data are shown for the intrinsic regions of the device. Solid lines: results from the atomistic calculations taking alloy fluctuations into account (averaged over each c-plane). Dashed lines: data obtained from a virtual crystal approximation of the same system; vertical dashed black lines indicate well boundaries.

carrier density dependent recombination model, the wave function character of electrons and holes is not taken into account. While the symmetry of the wave functions can affect radiative and non-radiative recombination rates, analysing the spatial overlap of electron and hole charge density provides first insight into the impact of alloy disorder on the recombination rates. Comparing the atomistic calculation with the VCA data it becomes clear that both radiative and non-radiative contributions are enhanced by alloy disorder since this can improve the carrier injection but also induce carrier localisation in the wells. But, upon further inspection, Fig. 6.5 reveals that the non-radiative rate increases more strongly when compared to the radiative. In the VCA the ratio of radiative to non-radiative peak values is $r^{\mathrm{VCA}} \approx 19$ while in the atomistic simulation it is $r^{\mathrm{RA}} \approx 2$ at a bias of 5.5 V. In general, and using the ABC model [86] as a starting point, the radiative recombination contributes with Bn^2 while the Auger-Meitner non-radiative rate with Cn^3, where n is the carrier density. Thus, when alloy disorder increases the carrier density in local regions of the well, the Auger-Meitner rate is expected to increase more quickly than

the radiative rate. Moreover, the Auger-Meitner rate is a three-particle process and has basically two contributions, namely an electron-electron-hole and a hole-hole-electron process. [99] Given that alloy-induced carrier localisation effects are significant for holes, locally the hole-hole wave function overlap is (strongly) increased. In turn this can result in increased Auger-Meitner rates [3, 100]. Taking all this together, alloy disorder and related carrier localisation effects are expected to lead to a significant increase of the non-radiative Auger-Meitner effect and thus have a detrimental effect on the performance of (deep) UV LEDs; a similar effect has been seen (In,Ga)N-base LEDs [46]. Moreover, strong Auger-Meitner non-radiative recombination may also lead to material degradation effects in deep UV LEDs, as recently indicated in experiments [223, 231].

In this section we have carried out a detailed analysis of the impact of alloy disorder on the carrier transport and recombination processes in (Al,Ga)N heterostructures embedded in a *p-i-n* junction. We have seen that alloy fluctuations can help to promote the carriers through the barrier material, a feature which may prove useful for inter-well transport, while also enhancing recombination rates. Building on this understanding of carrier transport in (Al,Ga)N-based systems and the importance of alloy disorder, we now turn to a more comprehensive analysis that includes key aspects of a full LED device, such as MQWs, EBLs, doping profiles, and the impact of the dopant activation energy.

6.3 (Al,Ga)N-based MQW DUV LED

With the general theoretical framework established above, we now target a description of a realistic (Al,Ga)N-based DUV LED. Having gained insight into the impact of alloy disorder, we focus on additional aspects of a full LED structure that will influence carrier transport and ultimately recombination. This includes features such as, multiple QWs in the active region of the device, an EBL and incomplete ionisation of the carriers. Furthermore, we make here refinements to our model to account for the effects of valence band mixing by introducing a hybrid effective mass.

For this study we extend our DD model to target a "conventional" 235 nm DUV LED design similar to Ref. [90]. Our structure contains a 10 nm n-$Al_{0.85}Ga_{0.15}N$ contact layer, followed by a 10 nm $Al_{0.85}Ga_{0.15}N$ barrier, a 5 layer MQW system consisting of 7 nm $Al_{0.85}Ga_{0.15}N$ barriers with 2.3 nm $Al_{0.75}Ga_{0.25}N$ QWs, which is then followed by a 21 nm $Al_{0.85}Ga_{0.15}N$ barrier, a 15 nm AlN EBL, a 10 nm p-$Al_{0.85}Ga_{0.15}N$ hole injection layer (HIL) and capped with an 11 nm p-GaN contact layer. The p-doped GaN layer has a 1 nm region at the interface from $Al_{0.85}Ga_{0.15}N$ to GaN where the band edges are linearly graded. The atomistic region (AR) defines the area of interest for our investigation of the importance of alloy disorder on the carrier distribution and recombination processes in the active region of the device. The active region includes the 5 QWs and 7 nm barriers, and also the 21 nm $Al_{0.85}Ga_{0.15}N$ barrier. The doped regions (n-$Al_{0.85}Ga_{0.15}N$, EBL, p-$Al_{0.85}Ga_{0.15}N$ and p-GaN) were mapped onto a sparse device mesh using a VCA description, with band energies calculated from our TB model, as similarly described in Sec. 6.2.1, and connected to our fully AR. This approach not only reduces computational cost but also allows us to follow the widely used continuum based description of an incomplete ionisation model. The aspect of doping alloy disorder is largely unexplored in the literature and potentially adds to the uncertainty reported for the large variations in the activation energy in (Al,Ga)N alloys, with studies in the future required to address this issue.

It is commonly observed that Mg-doped (Al,Ga)N layers exhibit low levels of activation, resulting in limited free hole concentrations [16]. GaN has measured activation energies (E_A) of $\approx$ 120 - 200 meV [16, 69], with free hole densities of the order of 10^{17} cm^{-3} for p-GaN [16], while AlN has been reported to have much higher $E_A \approx 500$ meV [16]. However, studies have found significantly lower E_A for high Al-containing p-(Al,Ga)N films where Ref. [232] suggests an

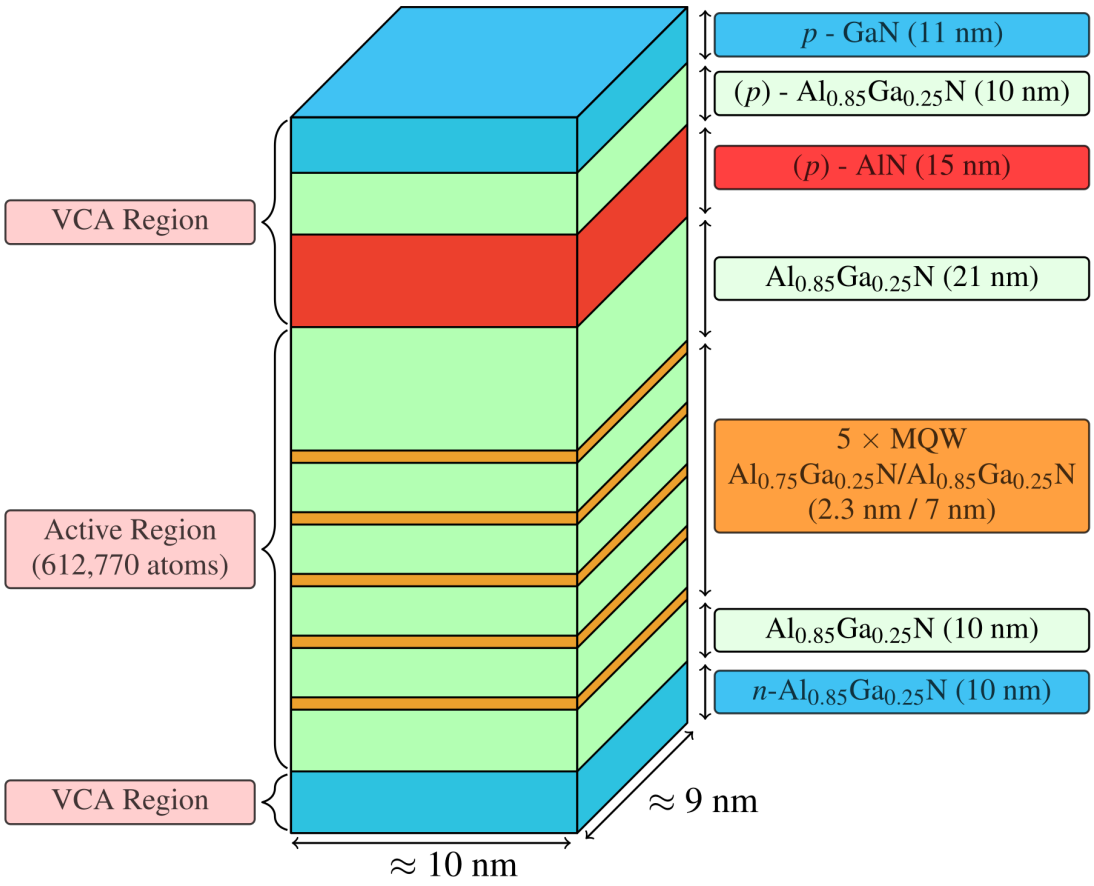


Figure 6.6: Schematic of the deep UV LED investigated. The VCA regions are composed of the n-doped $Al_{0.85}Ga_{0.15}N$ contact layer, p-doped GaN contact layer, the (p)-$Al_{0.85}Ga_{0.15}N$ and (p)-AlN electron blocking layer (EBL). Between the EBL and n-$Al_{0.85}Ga_{0.15}N$ contact layer is the active region that accounts for alloy disorder. The $Al_{0.75}Ga_{0.25}N$ QWs are shown in orange, the $Al_{0.85}Ga_{0.15}N$ barriers are in green, the EBL is in red and and the contact layers are in blue. The bracketed (p) layers indicate the regions of varied activation energy and doping densities.

E_A of < 72 meV for bulk p-$Al_{0.7}Ga_{0.3}N$ films grown on sapphire substrates. Additionally, it has been shown that for Mg-doped GaN, with increasing doping density, there is a corresponding decrease in activation energies [233]. This reduction is due to the increasing acceptor concentration generating an acceptor level distribution i.e. a broad band rather than a discrete energy level promoting the free hole density.

Furthermore, it has also been widely reported that p-doping the EBL improves the device performance by means of preventing electron overflow [234, 235, 236, 237]. This improvement arises because p-doping the EBL raises the conduction band of the EBL to higher energies, preventing

electron leakage, and lowers the hole Fermi energy level allowing for easier hole injection [237, 238, 239]. For UV-C LEDs, the EBL requires typical thickness of $\approx$ 20 nm and an Al composition greater than 75% [236]. However, as stated previously, current activation energies for Mg-doped AlN, which is required for a DUV LED, is a significant challenge for generating free holes. In addition, challenges such as Mg passively moving from the EBL to the active region can result in defect formation and performance degradation over time, contributing to the poor lifetimes (Al,Ga)N DUV LEDs experience [240, 241].

Here we pay special attention to the impact on p-doping and activation energies for the EBL and HIL, examining how they influence the current injection efficiency (CIE), radiative recombination efficiency (RRE), internal quantum efficiency (IQE) and carrier redistribution across the MQW.

The simulation cell for the LED considered has dimensions of roughly 10.0 $\times$ 8.6 $\times$ 106.4 nm^{-3}, The total mesh has 679,620 nodes with the AR corresponding to $\approx$ 612,770 atoms. A schematic illustration of the device design is shown in Fig. 6.6. Both contact regions have the same doping density of 10^{19} cm^{-3}. Only the p-$Al_{0.85}Ga_{0.15}N$ and p-EBL region have the E_A varied, while the contact regions are kept a fixed value. Due to the wide range of reported activation energies, it is important to understand their influence on device performance. Therefore, we examine two E_A for the p-doped material, 180 meV which is close to reported values for GaN [16, 69] and 450 meV which is obtained via a linear interpolation of GaN and AlN for $Al_{0.85}Ga_{0.15}N$, as shown in Ref. [16]. We also investigate the impact of an undoped EBL and HIL has on the device performance. Six systems (SYS) were examined in total as shown in Table 6.1.

Table 6.1: Investigated systems (SYS) with varying activation energies E_A for the electron blocking layer (EBL) (p-AlN) and hole injection layer (HIL) (p-$Al_{0.85}Ga_{0.15}N$). N/A denotes no p-doping in this region.

	(p) - **AlN** (meV)	(p)-**$Al_{0.85}Ga_{0.15}N$** (meV)
SYS 1	$E_A^{\mathrm{EBL}} = 180$	$E_A^{\mathrm{HIL}} = 180$
SYS 2	$E_A^{\mathrm{EBL}} = 450$	$E_A^{\mathrm{HIL}} = 180$
SYS 3	$E_A^{\mathrm{EBL}} = 450$	$E_A^{\mathrm{HIL}} = 450$
SYS 4	$E_A^{\mathrm{EBL}} = N/A$	$E_A^{\mathrm{HIL}} = 180$
SYS 5	$E_A^{\mathrm{EBL}} = N/A$	$E_A^{\mathrm{HIL}} = 450$
SYS 6	$E_A^{\mathrm{EBL}} = N/A$	$E_A^{\mathrm{HIL}} = N/A$

6.3.1 Theoretical framework

When modelling an (Al,Ga)N alloy, simply using a linear interpolation of the effective mass between the binary GaN and AlN values, derived from *ab initio* methods or experimental calculations, may not be sufficient. This is particularly true for a heterostructure, as we have seen in Chapter 5, where the negative crystal field splitting energy in (Al,Ga)N plus band mixing effects can lead to a reordering of the valence bands. With the *A*-, *B*- and *C*-bands switching between the top most band edge depending on composition and other factors. To address this, multi-band models can be used to account for coupling between the different bands. However, the alloy disorders impact on the local strain and polarisation fields adds another layer of complexity by breaking the band symmetry, resulting in mixed orbital characteristics. Generating a 3D supercell in which a multi-band model is solved self-consistently with DD equations is possible, but is numerically very expensive.

In our initial discussion of carrier transport and recombination in (Al,Ga)N systems (Sec. 6.2), we applied a single band model within the LLT framework, assuming that only the *A*-band was involved in the hole transport. To address the limitation of using a single effective mass, we develop a hybrid band effective mass approach [2]. In this method, a single effective band is constructed by using the orbital character obtained from TB calculations. The orbital character acts as a measure of band mixing which is captured by the DOP, allowing contributions from both the band edge and remote valence bands to be considered. This yields a hybrid effective mass which can be used in LLT to generate a single band that represents the average orbital character of the alloy.

In general, Ref. [2] presents a comparison of the electronic structure obtained from a hybrid single band model against the results from the atomistic TB calculations of the systems investigated in Chapter 5 ($Al_{0.48}Ga_{0.52}N/Al_{0.63}Ga_{0.37}N$ and $Al_{0.75}Ga_{0.25}N/Al_{0.90}Ga_{0.10}N$). It was found that applying a shift in the QW band edges for the EMA resulted in good agreement between the TB results. This lends trust that the hybrid band model is suitable for DD simulations.

Building on the methodology outlined in Ref. [2], we go on to construct a hybrid single band model to investigate our DUV LED. For our calculation of the system, $Al_{0.75}Ga_{0.25}N/Al_{0.85}Ga_{0.15}N$, we have taken the DOP values for the 2.3 nm QW of $Al_{0.75}Ga_{0.25}N/Al_{0.90}Ga_{0.10}N$ presented in Sec. 5.3.2.2, at a carrier density of 1×10^{19} cm^{-3}, with ρ = -0.306. Given the similarity between the two

structures, this DOP value is considered a reasonable approximation for the current system.

From the DOP value, we can determine the probability of TE, P_{TE}, and TM, P_{TM}, emission.

$$P_{TE} = \frac{1+\rho}{2} \ , \tag{6.3}$$

$$P_{TM} = \frac{1-\rho}{2} = 1 - P_{TE} \ . \tag{6.4}$$

Using the expressions given in eq. (6.3) and eq. (6.4), we find that the contribution of $p_x + p_y$ orbitals is 0.347 and the p_z contribution is 0.653, respectively. From these values we proceed as follows to construct a hybrid effective mass for the holes.

To calculate the hole effective mass we use the Luttinger-like effective mass parameters A from Ref. [60], which are shown in Table A.1 in Appendix A. The masses are calculated far from the Γ-point for each band, following the classification from Chuang and Chang [127], because the hole states are highly confined and thus contributions from larger k-values farther from the centre of the Brillouin zone will become significant.

The effective masses for the holes in $Al_xGa_{1-x}N$ are calculated via a weighted harmonic mean of the binary masses:

$$\left(\frac{1}{m_K^{alloy}}\right) = \left(\frac{x}{m_K^{AlN}}\right) + \left(\frac{1-x}{m_K^{GaN}}\right) \ , \tag{6.5}$$

where K denotes which band is being evaluated (A-, B- or C-band). A harmonic mean is used instead of a linear one, since the kinetic energy depends on the inverse of the effective mass [2]. For the holes, we account for band mixing by constructing a hybrid mass using P_{TE} and P_{TM} determined from the DOP in eq. (6.3) and (6.4):

$$\left(\frac{1}{m_{Hybrid}^{alloy}}\right) = \left(\frac{P_{TE}}{m_A^{alloy}}\right) + \left(\frac{P_{TM}}{m_C^{alloy}}\right) \ . \tag{6.6}$$

The B-band may also contribute to the TE emission. However, with this said, the B-band is predominantly p_x- and p_y-like in character (with some p_z),

especially when (i) the SOC is small and (ii) the crystal field splitting energy is large, as is the case for AlN. From this perspective the B-band may be considered symmetry-wise similar to the A-band. To capture the change in DOP, which can be attributed to changes in the valence band ordering, and thus the symmetry of the involved bands, we focus only on the A- and C-valence bands when constructing the hybrid effective mass [127]. For electrons, the effective mass is calculated using the same procedure as described for the holes (eq. (6.5)). However, no correction for band mixing is required since the conduction band for both AlN and GaN is s-like in character, and thus not subject to orbital mixing effects.

With the hybrid effective mass now well defined, we proceed to simulate the full device framework. A TB supercell of the active region of the device (as labelled in Sec. 6.3) is generated. Following the same procedure outlined in Sec. 6.2, we extract the 3D energy landscape at each lattice site within the TB supercell. We apply quantum corrections to the energy landscape by solving LLT, with the hybrid effective mass, which generates an effective confining potential to be used in the DD calculations [45, 104]. The DD calculations employ the van Roosbroeck system of equations [167] as described in Sec. 3.3.1. The effective mass for the density of states is taken as the geometric mean of the in-plane (x, y), and out-of-plane (z) hybrid masses determined above:

$$m^{\lambda} = \left(m_{z}^{\lambda} m_{x,y}^{\lambda} m_{x,y}^{\lambda}\right)^{1/3} , \tag{6.7}$$

where $\lambda \in \{n, p\}$ with n denoting the electrons and p the holes. The parameters used for the effective mass are shown in Appendix A Table A.1, while the device parameters (e.g. mobilities and ABC coefficients) can be found in Appendix B Table B.1.

6.4 Results

In Sec. 6.4.1, we investigate how varying the activation energies of the EBL and HIL affects device efficiency. We then go on to evaluate the impact of alloy fluctuations on a deep UV MQW LED by taking a comparison with a VCA, in Sec. 6.4.2.

6.4.1 Doping and activation energy

As discussed in Sec. 2.5, and described by eq. (2.33a) and eq. (2.33b), the IQE (η_{IQE}) is the product of the CIE (η_{CIE}) and RRE (η_{RRE}). We define the CIE as the fraction of carriers that are successfully injected and recombine (radiatively or non-radiatively) in the five QWs. Following the expression in Ref. [37], the CIE is given by:

$$\eta_{CIE} = J_{QW}/J \ , \tag{6.8}$$

where J is the total current density through the device (A cm^{-2}), which includes both the current contributing to recombination as well as any leakage current that reaches the opposite contacts without recombining. J_{QW} represents the current density that is successfully injected into the QWs and undergoes recombination. J_{QW} is obtained by integrating the total recombination rate within the QW regions only.

The RRE is defined as the fraction of carriers injected into the QW that recombine radiatively:

$$\eta_{RRE} = J_{rad}/J_{QW} \ , \tag{6.9}$$

where J_{rad} is the *radiative* current density inside the QWs. Thus, the IQE can be expressed as

$$\eta_{IQE} = \eta_{CIE} \times \eta_{RRE} \ , \tag{6.10}$$

$$= J_{rad}/J \ . \tag{6.11}$$

First, we will evaluate the IQE of the six systems (SYS 1-6, see Table 6.1), which differ in their activation energies/doping regions. Figure 6.7 shows the IQE for each system. Immediately, it is clear that SYS 4-6 with no p-doping in the EBL have very low IQEs ($\approx 6\%$), regardless of the doping level or activation energy in the HIL layer. In contrast, SYS 1 ($E_A^{\mathrm{EBL}} = 180$ meV; $E_A^{\mathrm{HIL}} = 180$ meV) shows the highest peak IQE ($\approx 60\%$), whereas SYS 2 ($E_A^{\mathrm{EBL}} = 450$ meV;

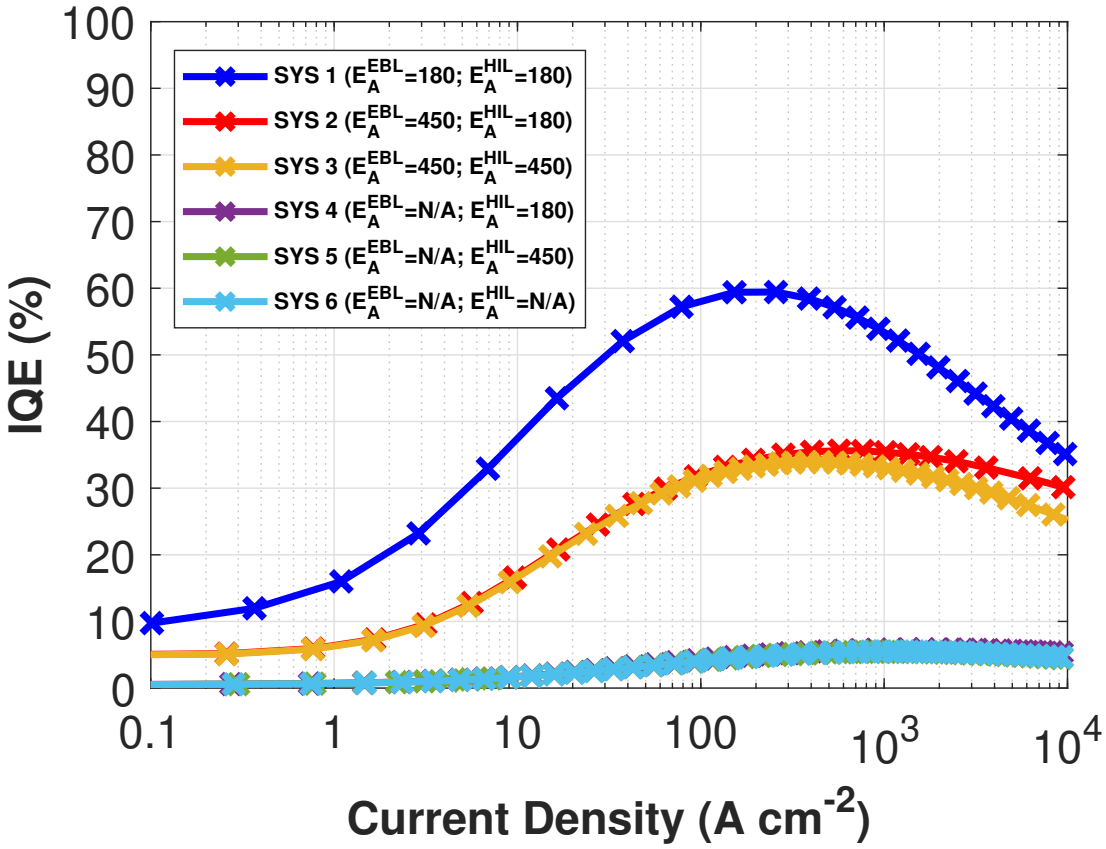


Figure 6.7: Internal quantum efficiency (IQE) as a function of current density for the six systems with different doping profiles and activation energies as shown in Table 6.1. The activation energies E_A^{α} are given in meV, with α denoting the electron blocking layer (EBL) and hole injection layer (HIL).

$E_A^{\mathrm{HIL}} = 180$ meV) and SYS 3 ($E_A^{\mathrm{EBL}} = 450$ meV; $E_A^{\mathrm{HIL}} = 450$ meV) both exhibit peak IQEs of ≈ 35 %. Although, SYS 2 and SYS 3 show similar peak IQEs, SYS 2 exhibits a *slightly* delayed droop at higher current density compared to SYS 3.

Having discussed the IQE, we can now analyse the contributing factors. Figure 6.8 (a) and (b) show the CIE and RRE, respectively. Figure 6.8 (a) reveals that varying the E_A^{EBL} greatly changes the CIE. When $E_A^{\mathrm{EBL}} = 180$ meV (SYS 1), the CIE is greater than 90%, whereas $E_A^{\mathrm{EBL}} = 450$ meV (SYS 2 & 3) reduces the CIE to ≈ 50%. Systems without EBL doping (SYS 4-6) exhibit a very low CIE of ≈ 8%. This demonstrates that p-doping the EBL, even if the activation energy is high as found for SYS 3 ($E_A^{\mathrm{EBL}} = 450$ meV; $E_A^{\mathrm{HIL}} = 450$ meV) bend the valence band and ease hole injection into the active region. When looking at Fig. 6.8 (a), for SYS 1 ($E_A^{\mathrm{EBL}} = 180$ meV; $E_A^{\mathrm{HIL}} = 180$ meV) the onset of CIE droop occurs at the lowest current density of $\approx$ 10 - 100 A cm^{-2}. SYS 2 ($E_A^{\mathrm{EBL}} = 450$ meV; $E_A^{\mathrm{HIL}} = 180$ meV) and 3 ($E_A^{\mathrm{EBL}} = 450$ meV; $E_A^{\mathrm{HIL}} = 450$ meV) essentially exhibit

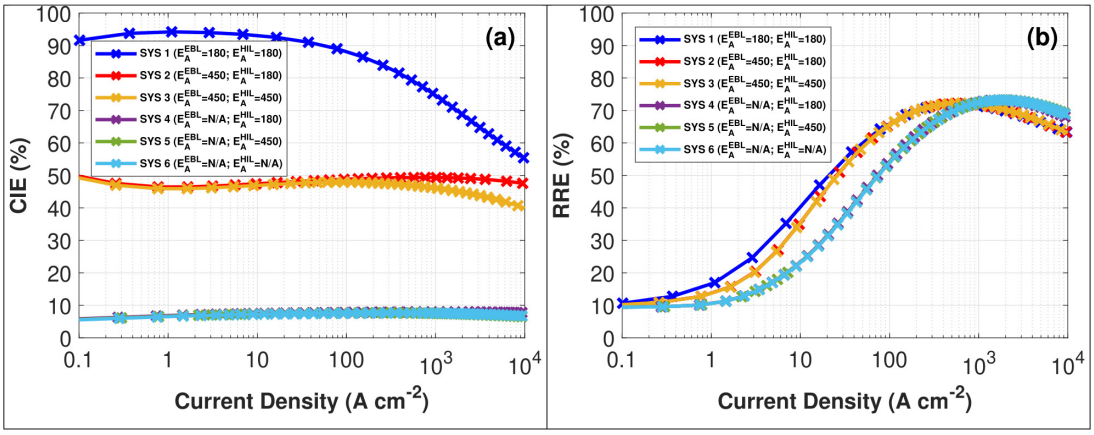


Figure 6.8: (a) Current injection efficiency (CIE) and (b) radiative recombination efficiency (RRE) as a function of current density for the six systems with different doping profiles and activation energies as summarised in Table 6.1. The activation energies E_A^α are given in meV, with α denoting the electron blocking layer (EBL) and hole injection layer (HIL).

a flat CIE, with a *slight* droop at higher current density, > 100 A cm^{-2}, clearly visible for SYS 3. This difference in the CIE droop is also reflected in the IQE, indicating that the lower E_A in the HIL (SYS 2) helps maintain hole injection at higher current densities.

When we now turn our attention to Fig. (6.8) (b), we see that each system behaves similarly in terms of the RRE, peaking at $\approx 70\%$. The major difference is that for the systems with no doping in the EBL (SYS 4-6), the peak RRE occurs at higher current densities. This means in order to get a high RRE inside the active region, systems with absent doping densities in the EBL will require a higher bias in order to successfully inject a sufficient number of carriers to radiatively recombine inside the QWs.

Overall, in this study we have performed a broad range of calculations to better understand the carrier injection and recombination processes for a deep UV MQW LED. Varying the E_A and doping density for the EBL and HIL showed that the RRE remained relatively stable across systems, while the CIE shows a strong dependence on the EBL activation energy. Ultimately, suggesting that the CIE is the determining factor for the IQE, rather than the RRE. Therefore, for high IQE device performance, improving the CIE by doping the EBL is ideally required.

To understand the impact of alloy disorder on the CIE and RRE, we next carry out a VCA calculation, following the approach outlined in Sec. 6.2.1. We focus

on SYS 3 ($E_A^{\mathrm{EBL}} = 450$ meV; $E_A^{\mathrm{HIL}} = 450$ meV) where both the p-doped EBL and HIL layer have activation energies representative of the upper range of reported values for high Al-containing (Al,Ga)N materials, in order to gain further insight into the carrier distribution for this LED system.

6.4.2 Impact of alloy disorder

Before discussing the results, we first note that the carrier distribution observed in (In,Ga)N-based devices have shown that the highest hole density typically occurs in the QW closest to the p-side [104, 242]. However, multiple studies have shown higher densities of holes on the n-side QW for high-Al containing multi-QW UV LEDs [239, 243, 244, 245], suggesting other mechanisms may be responsible for this behaviour. We discuss below the potential factors that can explain this.

For example, (In,Ga)N has difficulty with p-type doping, but (Al,Ga)N suffers from an even more severe p-type doping problem [245]. This is because, in general, with increasing band gap energy the ionisation energy for the donors and, in particular the acceptors, increases [245]. This results in fewer ionised acceptors, which in turn leads to differences in the band structure. In addition, the effective mass of both the electrons and the holes in (Al,Ga)N is much higher [7, 60] in comparison to (In,Ga)N, which impacts the carrier drift mobility [245]. These characteristics have been reported to lead to an imbalanced carrier concentration in the active region and an asymmetry in carrier transport promoting electron leakage [245, 246, 247].

Recent reports for DUV (Al,Ga)N QWs [248, 249] show devices that are capable of emitting light 20 wells or more away from the p-doped region, indicating distant hole transport across a MQW. However, Refs. [248, 249] simulations show that the hole density is highest by the p-side (with the exception of the closest p-side QW) and reduces towards the n-side. Multiple factors can be contributing to this observed effect. For example, it has been shown in Ref. [239] that the n-side QW will have the most radiative recombination for a UV LED with a p-doped barrier between the EBL and p-contact, similar to the structure discussed in our work here. However, a UV LED with a p-graded region of higher Al from the EBL to lower Al at the p-contact will have dominant emission from the QWs closest to the p-side. They attributed this to the reduced barrier height for the holes due to the graded regions induced polarisation fields generating a higher density of free hole carriers [238, 239].

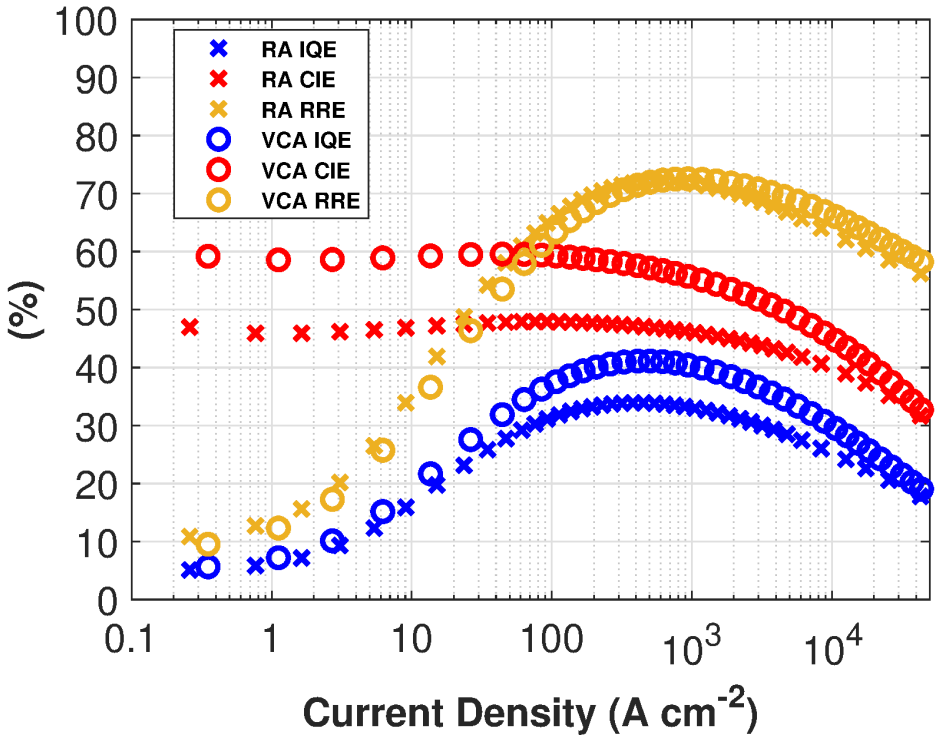


Figure 6.9: Internal quantum efficiency (IQE, blue), current injection efficiency (CIE, yellow) and radiative recombination efficiency (RRE, red) as a function of current density of the random alloy (RA, cross) and virtual crystal approximation (VCA, circle) for SYS 3 ($E_A^{\mathrm{EBL}} = 450$ meV; $E_A^{\mathrm{HIL}} = 450$ meV).

For the (Al,Ga)N LEDs with emission of over 20 QWs, both Ref. [248] and Ref. [249] incorporated either a graded region or a *p*-doped superlattice structure to increase hole injection, respectively. Both features will affect the Fermi level and band structure ultimately altering the carrier transport. Our calculations based on Ref. [90] have not considered such grading. Future calculations are required to carefully investigate the impact of these device designs when designing an (Al,Ga)N-based LED.

With that said we now turn to Fig. 6.9, which shows a comparison of the random alloy (RA) system (crosses) and VCA description (circles) for the IQE, CIE and RRE. One can observe that the RRE between the RA and the VCA appear to be near identical. However, the CIE for the VCA system is $\approx 10\%$ higher than the RA. As a result, this causes the peak IQE for the RA system to be lower by approximately 5%. This discrepancy may be explained by differences in carrier distribution in the active region.

To investigate this question, Fig. 6.10 (a) and (b) displays the conduction (valence) band edge profiles, CBE (VBE), and the conduction (valence)

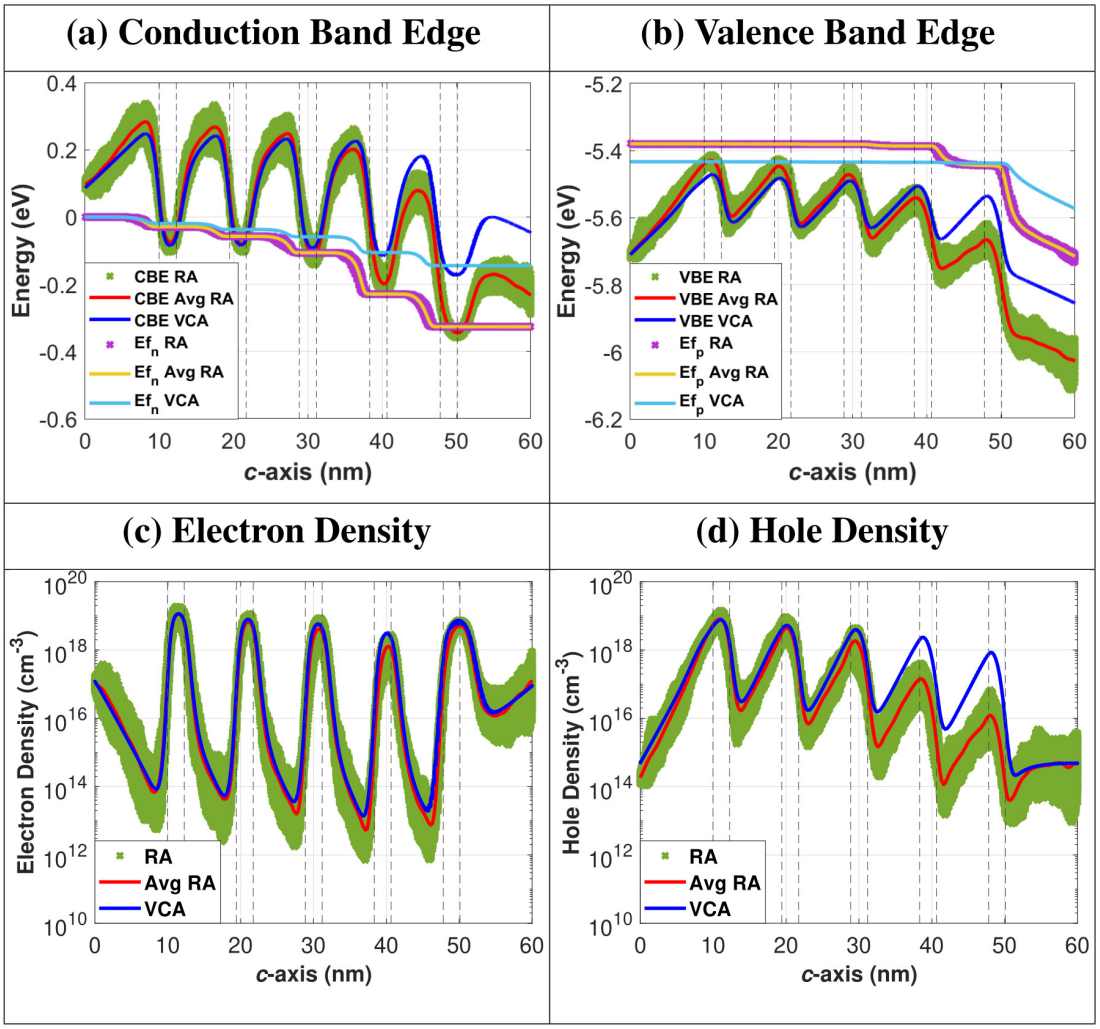


Figure 6.10: The conduction/valence band edge energies (CBE/VBE) and conduction/valence quasi-fermi levels (Ef_n/Ef_p) are shown in (a) and (b), respectively. The energies are plotted along the c-axis of the deep UV LED studied here [SYS 3 (E_A^{EBL} = 450 meV; E_A^{HIL} = 450 meV)] for both the random alloy (RA, green) and virtual crystal approximation (VCA, blue) at a current density of 135 A cm^{-2}. The RA data has also been averaged (Avg RA, red) over each plane along the wurtzite c-axis as described in Sec. 6.2.1 for Fig. 6.4. The electron and hole carrier densities (log scale) are shown in (c) and (d), respectively. All data are plotted from the end of the n-contact (0 nm) to 10 nm after the last QW (60 nm).

quasi-fermi levels, Ef_n (Ef_p), energies. Shown is (i) the RA, (ii) the RA data averaged over each plane along the wurtzite c-axis and (iii) the VCA result for the deep UV LED with an activation energy of 450 meV for the p-doped EBL and HIL (SYS 3). The data are plotted over 60 nm from the end of the n-contact region to 10 nm after the last QW at a current densities of $\approx$ 135 A cm^{-2}. In the following we denote QW1 as the QW that lies closest to

the n-side while QW5 is nearest to the EBL and p-side.

Figure 6.10 (a) reveals that Ef_n lies inside the conduction band of the QWs even though the RA system exhibits a more pronounced step-like distribution compared to the VCA. This indicates that the electron density for both the RA and VCA across all the QWs should be relatively evenly distributed across all the QWs. A different situation is observed for the valence band. Figure 6.10 (b) shows that Ef_p lies closest to the VBE of QW1 but further away for QW5, particularly for the RA. This finding suggest an uneven hole distribution.

With this said, we now turn to Fig. 6.10 (c) and (d) which has the electron and hole density for the same current density as the band edges plotted above. We find that the electron density for the RA and VCA systems across all QWs (with the slight exception of QW4) are essentially of similar magnitude. In contrast, the hole density for the RA system exhibits a very different profile in comparison to the VCA, as already indicated by our band edge analysis. In both systems the holes "travelled" to the n-side of the MQW. Although QW1 (closest to the n-contact), QW2 and QW3 have similar densities, QW4 and QW5 (closest to the p-contact) have much lower hole densities, with QW5 being significantly lower in the RA than in the VCA system.

These results suggest that the RA system has a poorer carrier confinement for QW5 and QW4 in comparison to the VCA. The reduced hole density in the p-side QWs will have a lower radiative recombination rate in e.g. QW4 and QW5. As previously discussed in Sec. 6.2, we have seen that due to the alloy disorder, radiative and Auger-Meitner recombination are enhanced in QW1 when accounting for RA fluctuations, which further affects the carrier distribution across the QWs. More discussion on the band edge energies may be found in Appendix. C.

To investigate the effect of recombination processes on the carrier distribution, we performed a calculation where we account for RA fluctuations in the barrier material, but treat the QWs in VCA. Figure 6.11 presents the average hole density for three cases: the RA system, the VCA system and a "mixed" system where QWs follow a VCA description while the barriers retain the random alloy fluctuations. The spike in carrier density for VCA QWs data outside the wells stems from a sudden transition of a VCA description to an atomistic one. The results show that the hole density distribution in the VCA QW system more closely resembled that of the full VCA, although QW5 exhibits almost one order of magnitude lower hole density when compared to the full VCA system. This

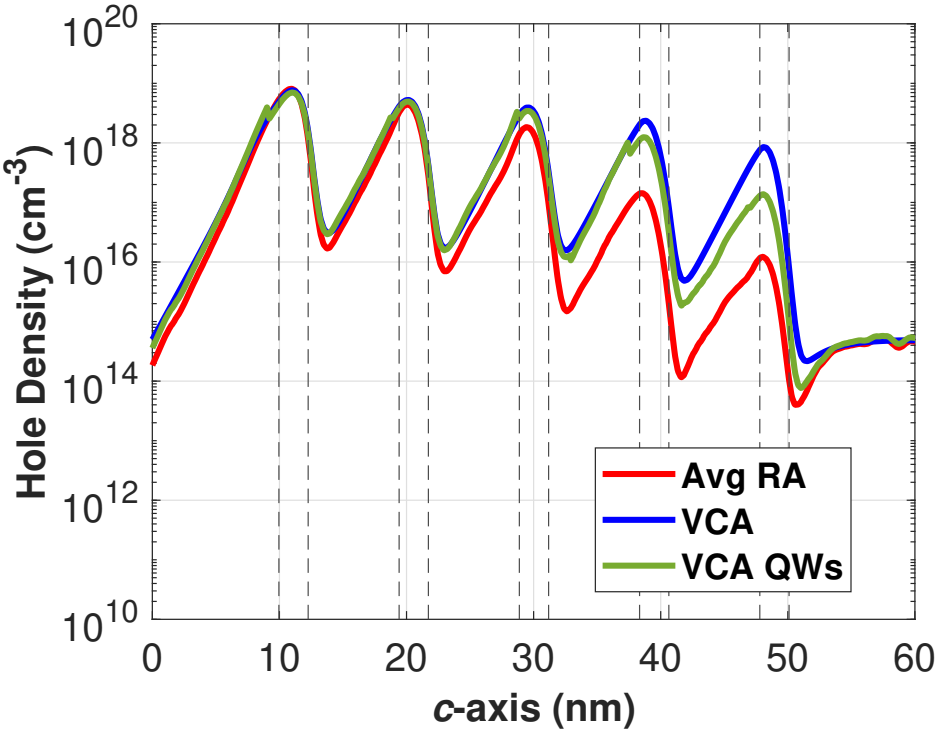


Figure 6.11: Hole density (log plot) along the c-axis of the deep UV LED [SYS 3 (E_A^{EBL} = 450 meV; E_A^{HIL} = 450 meV)]. The random alloy (RA, red) structure, the virtual crystal approximation (VCA, blue) and the random alloy structure with QWs described in VCA (VCA QWs, green) are plotted at a current density of 135 A cm^{-2}. The data is taken from the end of the n-contact (0 nm) to 10 nm after the last QW (60 nm). The random alloy and the random alloy structure with VCA QWs have been averaged over each plane along the c-axis

could be due to the alloy fluctuations in the barriers promoting hole transport out of QW5. Overall, these findings suggest that the VCA description of the QWs lead the holes to redistribute across the wells in a more similar fashion to the VCA structure. This indicates that alloy fluctuations in the QWs rather than the barrier are important in describing the recombination mechanisms and carrier distribution inside the active region, at least for the barrier regions considered in the present study. However, the influence of alloy fluctuations in the barrier may become more important for narrower barrier widths.

We have observed that alloy fluctuations in the barriers between the QWs for the system studied are of secondary importance for the hole distribution, which is instead primarily governed by the recombination processes within the QWs. Now we wish to explain why the CIE for RA is lower than the VCA as shown in Fig. 6.9. Figure 6.12 plots the percentage of *electron* leakage that reaches the p-contact, J^e_{leak}, which is defined as, Electron Leakage = J^e_{leak}/J. We find that the main limiting factor for the CIE is the electron leakage (cf. Fig. 6.12), while

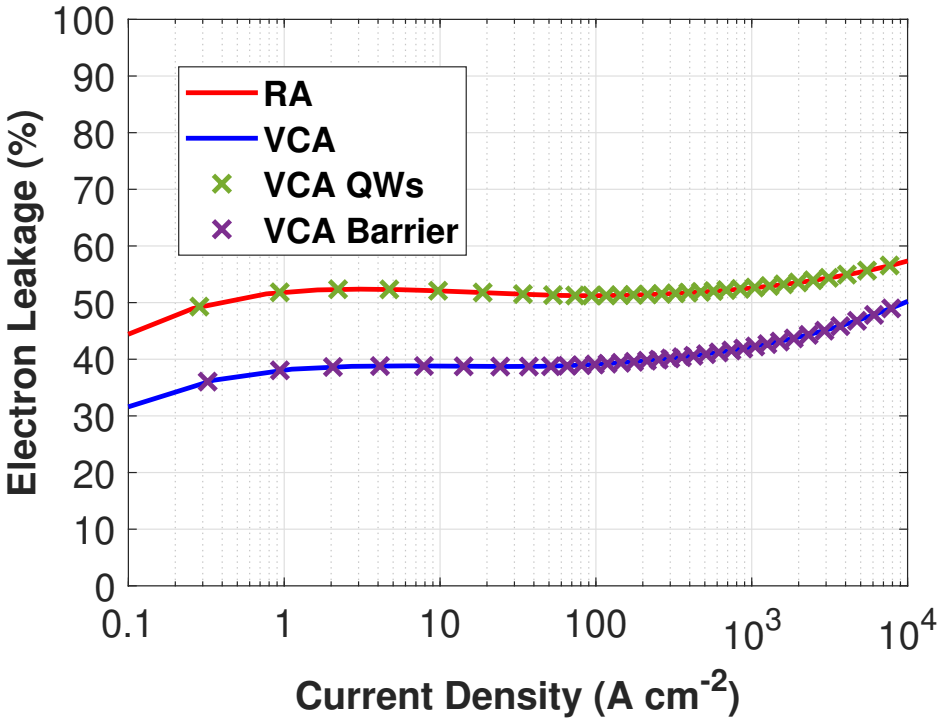


Figure 6.12: Electron leakage as a function of the current density for SYS 3 ($E_A^{\mathrm{EBL}} = 450$ meV; $E_A^{\mathrm{HIL}} = 450$ meV). Plotted is the random alloy (RA) results as a red line, the virtual crystal approximation (VCA) as a blue line, the RA with VCA QWs (VCA QWs) with green crosses and the RA structure with a VCA barrier before the EBL (VCA Barrier) as purple crosses.

the hole leakage remained negligible for the RA and VCA systems (not shown). The $\approx 10\%$ lower CIE in the RA structure compared to the VCA at current densities greater than 1 A cm^{-2}, as shown in Fig. 6.9, directly corresponded to a $\approx 10\%$ increase in the electron leakage. Note that above 1 A cm^{-2}, in Fig. 6.9, the recombination is dominated by the QWs, but below 1 A cm^{-2} there is a higher rate of non-radiative defect recombination *outside* the QW regions which are not included in the plotted CIE.

To understand what is driving this enhanced leakage in the RA system, we performed additional calculations on different structures: one with VCA described QWs but alloy fluctuations considered in the barrier regions (green), and secondly for a system where alloy disorder is retained in the full active region except for the 21 nm barrier region between the EBL and QW5 which is modelled within VCA (purple). Figure 6.12 reveals that the alloy fluctuations within the QWs do not affect the electron leakage. In contrast, the disorder in the barrier region before the EBL does have a strong effect. This is attributed to the alloy fluctuations opening up percolative pathways that enhance the

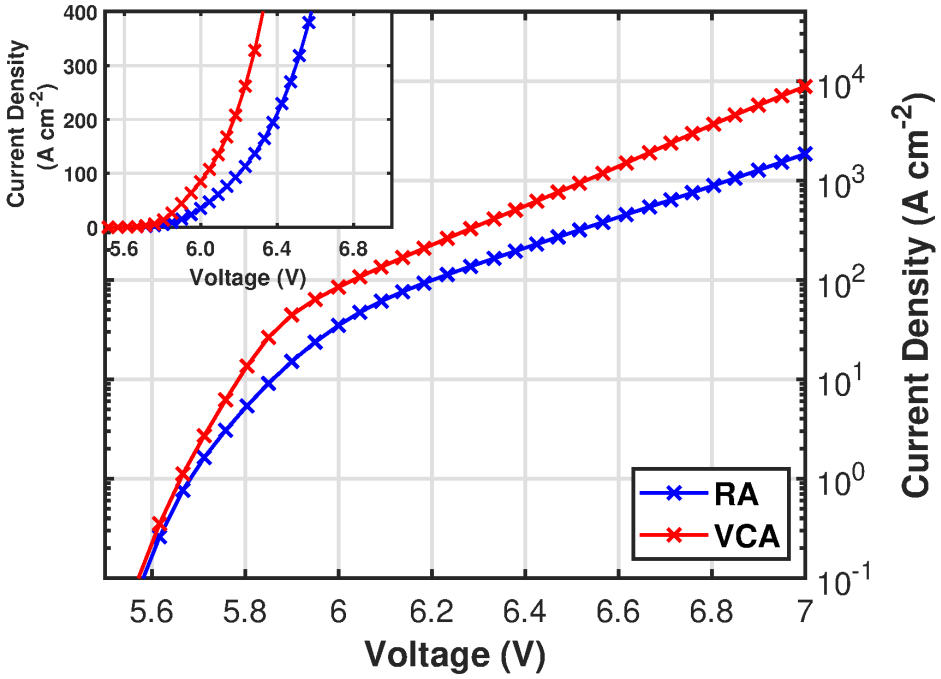


Figure 6.13: Current-voltage curves, on a log-scale, for SYS 3 (E_A^{EBL} = 450 meV; E_A^{HIL} = 450 meV) of both the random alloy (RA, blue) and virtual crystal approximation (VCA, red). The inset shows the I-V curves on a linear scale displayed up to 400 A cm^{-2}.

electron transport out of the active region.

Finally, we now turn to Fig. 6.13 which shows the I-V characteristics of SYS 3 ($E_A^{\mathrm{EBL}} = 450$ meV; $E_A^{\mathrm{HIL}} = 450$ meV) for both the full RA and VCA systems. The semi-log plot displays two distinct close to linear regions, indicating a change in the ideality factor, in contrast to the simplified LED structure studied in Sec 6.2, see Fig. 6.2.

The ideality factor for the lower voltage region is extracted between 5.4 V to 5.7 V, as between 5.7 V to 6.0 V the I-V deviates from a linear behaviour. In the linear regime we extract an ideality of $\eta \approx 1.5$. Over this voltage range, the VCA gives approximately the same ideality factor. This indicates that the device behaviour in this voltage range is determined by diffusion and recombination mechanics. In the high voltage regime, i.e., from 6.3 V to 7 V we find $\eta \approx 10$ and 8 for the RA and VCA, respectively. These values are far outside the normal ideality factor range for a simple diode, but are commonly reported for nitride based MQW LED devices [225]. Several factors have been identified and suggested in the literature to explain this behaviour, ranging from polarisation induced band profiles in MQWs and carrier leakage [250].

In addition, it is worth noting that the VCA system has a higher current density when compared to the RA, in contrast to Sec. 6.2. This implies that carrier injection for the VCA system is easier than the RA for the specific LED design considered in this section, which unlike in Sec. 6.2, contains multiple QWs and an EBL. This finding is explained by (i) an improved/enhanced hole injection and (ii) a reduction in electron leakage in the VCA when compared with the RA description of the LED structure.

Overall, when evaluating the IQE for this full LED system emitting at 235 nm, featuring a high activation energy ($E_A = 450$ meV) which lies closer to reported values of pure AlN, we find peak CIE and RRE values of approximately 50% and 70%, respectively. These peak efficiencies are not far from those reported for LEDs emitting at 260 nm [37, 251]. However, they do seem to be optimistic for a 235 nm LED, where reported IQEs are typically lower. For instance, Ref [252] and Ref [253] report IQE values of $\approx 10.5\%$ and $\approx 13\%$, respectively. However, Ref. [254] determined a rough estimate of $\approx 30\%$ for a 234 nm UV LED. It is important to note that each of these reported devices differ in the device structure, which can strongly influence the carrier injection and recombination dynamics. For instance, Ref. [252] and Ref. [253] use a 6 nm undoped AlN EBL and a 2 nm undoped AlN EBL, respectively. Our results suggest that not p-doping the EBL may impede the hole injection. In addition, these devices also incorporate a superlattice HIL [252] or an 80 nm (Al,Ga)N graded HIL [253], further complicating a direct comparison with our results.

Modifications to the device design, such as introducing a p-graded region, could help to improve the CIE. However, an increased hole density in the QWs potentially enhances the Auger-Meitner recombination. This may lead to hot carriers which generate further defects [223, 231], such as by methods suggested in Refs. [223, 234] where it is reported hot carriers break H-containing defects in the p-side potentially generating point defects near and around the active region.

Another critical factor influencing the IQE is the defect density. Threading dislocation densities (TDD) have been found to act as non-radiative recombination centres which can also induce point defects. These defects may create parasitic recombination pathways, contribute to subband gap absorption in AlN, and compensate for intentional dopants [253, 255]. Experimental studies have demonstrated that reducing the TDD from 6×10^9 cm^{-2} to 2×10^8 cm^{-2} resulted in a significant increase of the IQE from 10% to 60% for $Al_{0.73}Ga_{0.27}N$/AlN MQWs [252]. Moreover, Ref. [256] claims that point defects

are the dominant factor limiting the IQE in DUV LEDs due to their high non-radiative recombination rates. Furthermore, these point defects can lead to absorption below the band gap of AlN, greatly reducing the LEE [252, 257]. Thus, it is important to account for these effects in modelling. We do this by accounting for non-radiative recombination via the SRH process. However, instead of using a constant A parameter, we employ a more microscopic description by using non-radiative lifetimes (see Table B.1), as detailed in Sec. 2.5, eq. (2.36). While this is a first step in the direction of understanding the impact of defects on the device performance, further studies with even more sophisticated approaches are required [231].

Finally, the hole mobility used in the intrinsic region of our simulation was $\mu_h = 10$ cm^2 V^{-1} s^{-1}, based on Ref. [69]. Work by Römer *et al.* [210] on a deep UV multicolour QW structure fitted hole mobilities to experimental data, where they used $\mu_h = 0.2$ cm^2 V^{-1} s^{-1} for the (Al,Ga)N barriers and $\mu_h = 1$ cm^2 V^{-1} s^{-1} for the EBL. Their results showed that μ_h in the EBL strongly affected the CIE, which varied from $\approx 5\%$ to $\approx 75\%$ when changing μ_h from 0.1 cm^2 V^{-1} s^{-1} to ≈ 5 cm^2 V^{-1} s^{-1}. In contrast, variations in the barrier mobility were found to be of secondary importance, with minimal effect on the CIE but a noticeable influence on carrier distribution within the active region.

While the internal transport properties and recombination dynamics play a central role determining the IQE, the EQE of the DUV LED remains primarily limited by the low LEE. Reported EQE values are typically low at around $\approx$ 0.5% [16]. As the EQE is defined as a product of the IQE and the LEE (see Sec. 2.5). Based on our simulation for SYS 3 ($E_A^{\mathrm{EBL}} = 450$ meV; $E_A^{\mathrm{HIL}} = 450$ meV) with a peak IQE of $\approx 35\%$, the LEE would have to be roughly $\approx 1.5\%$. This value is not too dissimilar to values reported in the literature [258] for 239 - 222 nm UV LEDs. Experiments where DUV LEDs have been designed to optimise the LEE experienced noticeable jumps in the EQE with reported values of 4% [259] and even 10% [260]. Thus, while improving the IQE by enhancing the injection and recombination remains important, our findings suggest that the main limiting mechanism for the DUV device performance is most likely attributed to the LEE. Nevertheless, achieving high efficiency UV LEDs still demands careful consideration of the device structure, particularly for the EBL and p-doped region, to ensure effective hole injection and balanced carrier distribution across the QWs.

6.5 Conclusion

In this chapter, we have carried out multiscale simulations of the carrier transport and recombination processes in deep UV (Al,Ga)N based devices.

First, we presented a detailed analysis of the impact of alloy fluctuations on carrier transport and recombination processes in an $Al_{0.7}Ga_{0.3}N/Al_{0.8}Ga_{0.2}N$ single quantum well system embedded in a *p*-*n* junction. Our results show that alloy disorder can lead to improved carrier injection into the active region through percolative pathways. Also, these pathways can give rise to higher hole densities in the intrinsic region near the *n*-side of a device, an aspect of potential interest for tailoring inter-well transport in (Al,Ga)N-based multi-quantum well systems. However, this comes with the potential drawback in terms of promoting carrier leakage. In general, these percolation effects are not captured by standard VCA models employed in many commercially available carrier transport simulation packages. Moreover, we find that while on average the carrier densities could be of similar magnitudes inside the QW when comparing VCA and RA results, locally there can be a significant increase in the carrier density due to alloy-induced carrier localisation effects. In comparison to virtual crystal simulations, both radiative and non-radiative Auger-Meitner recombination processes are increased in the RA framework.

Moreover, the high energy of such Auger-Meitner generated carriers may lead to a degradation of the material and thus an enhancement of Shockley-Read Hall recombination. Overall, our results indicate that alloy disorder opens up percolative pathways improving carrier transport, but the enhanced Auger-Meitner effect can have a detrimental effect on the efficiency of the device. While we have focused here on relatively high Al contents in the well and barrier, the above drawn conclusions are also expected to hold for systems with lower Al contents, given that our atomistic studies in Chapter 4 reveal that even at only 10% Al in (Al,Ga)N, hole localisation effects are observed.

Second, we extended the electronic structure model to include the effect of orbital mixing by using a hybrid band approach. Furthermore, the calculations also includes incomplete ionisation which is essential for a realistic study of the hole injection efficiency for a deep UV MQW (Al,Ga)N LED. This model was used to investigate the influence of the acceptor activation energy. To gain detailed insight into the fundamental processes that affect the IQE, we analysed the MQW carrier distribution, recombination mechanisms, and overall IQE.

These investigations were performed using both a RA and VCA description to explore the role of alloy disorder on the results. Our calculations reveal, that when using a experimentally motivated LED design, the doping of the EBL is essential for successfully injecting holes into the MQW device. We found that lowering the activation energy for the holes does improve hole injection, but overall doping the EBL even when the activation energy is high (450 meV) still significantly improves the CIE of the device. When compared to a VCA description, our results show that alloy fluctuations within the active region strongly influences the carrier distribution. We also found that for both the RA and VCA, there was an asymmetric distribution of the holes, with a higher carrier density in the QW near the n-side. In the RA system, alloy fluctuations localised the carriers and enhanced the recombination rates, while also preventing the holes to redistribute across the QWs as compared to the VCA. It was also observed that the alloy fluctuations in the barrier after the last QW and before the EBL had a strong influence on the electron leakage. These findings highlight that for future investigations, improving the CIE while achieving balanced carrier distribution across the MQW would be of interest for improving the device performance. Furthermore, evaluating the effectiveness of suppressing electron leakage by methods such as p-doping and careful device design via e.g. superlattices warrants further evaluation. However, even if these factors are successfully controlled, additional non-radiative processes such as defect formations and Auger-Meitner recombination may emerge as limiting mechanisms, especially at high carrier densities within the QWs.

Based on our results, further improvement to the EQE of DUV LED devices therefore suggests that the most pressing issue to enhance the device performance is by improving the LEE. Key strategies of this can be done by either suppressing TM polarisation or by replacing the GaN contact layer with an (Al,Ga)N contact layer to reduce UV light absorption. However, implementing these approaches are not trivial and are still undergoing extensive research in order to overcome these challenges.

Chapter 7

Conclusion and outlook

7.1 Conclusion

In this thesis, special attention was focused on the impact alloy fluctuations have on the electronic, optical and carrier transport properties for (Al,Ga)N-based UV emitting heterostructures and devices, which are ideal for use in UV light emitting device applications. Experimental observations on (Al,Ga)N heterostructures exhibit clear characteristics of carrier localisation, including broad photoluminescence spectra, S-shaped temperature dependence of the peak PL position, and a Stokes shift.

All calculations utilised an atomistic semi-empirical sp^3 nearest neighbour tight binding model which takes into account the local variations in strain and polarisation fields, arising from alloy fluctuations. This method allowed us to gain insight into the impact these local fluctuations may have on (Al,Ga)N-based device properties. A multiscale framework was then constructed to connect this tight binding approach with a quantum corrected drift-diffusion model in order to simulate UV LEDs.

As a first step, calculations were performed to investigate the fundamental electronic properties of (Al,Ga)N quantum wells with a fixed well width and varying Al composition in the well. The Al composition varied from the UV-A spectrum, requiring low Al content, down into the deep UV-C spectral range at high Al content. The barriers were kept as pure AlN to disentangle potential alloy fluctuation-induced carrier localisation effects inside the well from effects introduced by alloy disorder in the barriers. It was observed that random alloy fluctuations, even at low Al contents of 10%, were sufficient to cause carrier

localisation effects. With significant localisation effects observed for both ground and excited holes states, while at high Al contents the electrons may also exhibit localisation characteristics. These findings supported experimental observations for carrier localisation characteristics, such as broad PL spectra at low temperature. Moreover, these results highlight the necessity of including alloy fluctuations when accurately modelling the properties of (Al,Ga)N-based devices.

With this atomistic tight binding model for (Al,Ga)N alloys and heterostructures established, investigation into the impact of the structural properties of the quantum well, such as well widths, on the electronic and optical properties were targeted. Here, carrier localisation effects were measured via the calculation of Urbach tail energies and special attention was focused on the impact alloy fluctuations have on the optical properties for these quantum wells. Two (Al,Ga)N quantum well systems which exhibit TE and TM polarised emission were investigated. Each system had varied quantum well widths and carrier densities which influenced the electric field the QWs exhibited. It was observed that with increasing QW width, the Urbach tail energy and thus carrier localisation effects increased. This was attributed to the potential drop across the QW increasing and enhancing the QCSE. The stronger QCSE for the wider wells confined the hole wave function to similar/smaller lengths when compared to the narrower wells. This resulted in the hole wave function localising in GaN-rich regions which were lower in energy. With increasing carrier density, the built-in field was screened and the hole wave function was able to extend along the full length for the wider QWs. This resulted in the wider wells experiencing a noticeable reduction in Urbach tail energy. A feature not observed in the narrow QWs because the QW width essentially kept the hole wave function fixed to the QW width, and thus the Urbach tail energy remained relatively constant.

Furthermore, it was found that for the QW system that predominantly emits TE polarised light, the hole wave function was confined inside the QW and that alloy fluctuations did not seem to affect the light polarisation characteristics. However, the QW system that predominantly emits TM polarised light exhibited different features. First, it was observed that the hole wave function extended further into the barrier material, a feature more noticeable for the narrow QWs. With increasing carrier density screening and thus screening of the built-in field, the hole wave function became more confined inside the QW, thus improving the hole confinement. Second, for these QWs emitting TM polarised

light, band mixing effects due to alloy-induced carrier localisation effects introduced p_x- and p_y-like states closer to the valence band edge reducing the TM polarisation observed. This was most noticeable for the wider QWs at low carrier densities due to the larger carrier localisation characteristics exhibited. At higher carrier densities, the localisation effects reduced and as a result the DOP decreased indicating more TM polarised light emission. This suggests when one is only considering improving the TE polarization in (Al,Ga)N-based light emitting devices, a wider QW may be the preferential option.

With the electronic and optical properties described for (Al,Ga)N QWs, we then turned our attention to carrier transport and recombination properties of an (Al,Ga)N-based DUV LED. To do this we developed a multiscale simulation framework that couples an atomistic tight-binding model to a semi-classical transport model. Here, the atomistic energy landscape is extracted from the tight-binding Hamiltonian. Quantum correction were included via LLT. In our initial study we investigated the impact of alloy disorder on the carrier transport and recombination process for a single deep UV (Al,Ga)N QW. To do so a set of calculations were performed where a comparison was done for a system with alloy fluctuations, with alloy fluctuations only in the QW, and a VCA description that neglected alloy fluctuations. It was observed that alloy fluctuations helped to promote carrier transport into and out of the QW via lower energy pathways. Alloy fluctuation also resulted in local regions with carrier densities an order of magnitude higher than average, which caused an increase of radiative recombination and a noticeable increase in the Auger-Meitner recombination, in comparison to the VCA description. Overall, this suggested that alloy fluctuations may promote carrier transport through a device, but may also be detrimental with respect to Auger-Meitner recombination which has been linked to device degradation due to defect formation from hot carriers. With this framework established, a full description for a deep UV LED was targeted. The effect of multiple QWs and an EBL, band mixing effects influence on the effective mass, and an incomplete ionisation model for the n- and p-doped regions were all included. Special attention was given to the impact varying the activation energy and doping density (doping vs undoped) for different p-doped regions has on the CIE, RRE and IQE for the device studied. It was observed that with varying activation energies, the RRE remained consistent but the CIE was the limiting factor. For this LED device design, doping the EBL is necessary for sufficient CIE via hole injection into the active region. In order to disentangle the impact alloy

disorder has on the device performance, a comparison to a VCA structure was also evaluated. Here it was observed that the random alloy system had a reduced CIE due to an increase in electron leakage. This was linked to the alloy disorder of the final barrier before the EBL. Furthermore, it was found that the disorder promoted the holes to the furthest QW, resulting in a more uneven hole distribution across the MQWs in comparison to the VCA model. With the QW closest to the n-side having the highest hole density and the QW closest to the p-side the lowest. This uneven carrier distribution was further exacerbated due to the enhance recombination from the alloy disorder preventing the holes to redistribute across the MQW active region. Thus, it was found that the limiting mechanism for the IQE of a deep UV MQW LED is the CIE. Careful design of the device structure can help to limit the carrier leakage and improve the hole injection, but p-doping the EBL and accurately understanding the acceptor activation energy in (Al,Ga)N alloys remains crucial, as it directly impacts hole concentration and thus the CIE. However, using literature results for the EQE, we conclude that further work on optimising the LEE is required.

Overall, our results show that for accurate modelling, alloy fluctuations are an important feature to include in order to understand the fundamental properties of (Al,Ga)N-based materials, heterostructures and devices. By explicitly including alloy disorder in our atomistic tight binding calculations we were able to reproduce carrier localisation effects, a feature observed experimentally in (Al,Ga)N-based systems. Furthermore, we have demonstrated that alloy disorder not only influences the electronic structure, but also impacts the optical emission properties, carrier transport and distribution, and overall recombination rates.

7.2 Outlook

This theoretical framework has provided useful insight into the underlying properties for (Al,Ga)N-based systems. However, several questions and features remain open. Insight into the role of Coulomb interactions between the electrons and holes have been neglected in these studies. While at high carrier densities, the free carriers may screen the Coulomb interaction and weaken the exciton formation, the impact excitonic effects have on the strong internal electric fields the III-N alloys possess, radiative recombination efficiency or carrier transport, remains an open question. While these effects have been explored in (In,Ga)N-based structures [261, 262] and work has been done for

GaN/(Al,Ga)N QWs [180], the broader implications in (Al,Ga)N-based heterostructures remain to be fully resolved.

For the determination of the DOP in Chapter 5, we have calculated the DOP by evaluating the orbital characteristic for each energy level and weighted each energy level with the probability of occupation via the Fermi function depending on the carrier density. Although this gives us a first insight into the DOP expected for the (Al,Ga)N QWs, in reality it does not give us insight into the strength of TE to TM polarised transition. To gain a more comprehensive understanding, future studies that calculate the full emission spectra will offer a more complete picture of the optical properties for (Al,Ga)N-based devices.

Similar to the calculation of the DOP, when simulating the recombination mechanisms of the (Al,Ga)N LEDs, the ABC model was employed. Although this model is widespread and extremely useful, it does neglect wave function overlap and allowed transitions between energy states. Here, the ABC model only takes into consideration the carrier densities and the recombination coefficients used are pre-determined and fixed. However, recombination rates are carrier density dependent which should be reflected in carrier density dependent recombination coefficients. For example, as discussed in Chapter 6, Auger-Meitner recombination can generate hot carriers which have been reported to form defects. For our simulation we model the impact of defects via the widely used SRH A coefficient. This value remains fixed, however, if these hot carriers generate more defects, then our A term underestimates this impact and should increase over time.

In addition to this, we have simulated n- and p-doped (Al,Ga)N barrier materials using a VCA description. However, the effect alloy fluctuations have on the activation energies for doped (Al,Ga)N alloys remains an open question. These local compositional fluctuations could influence the ionisation energy of dopants, particularly for p-type doping, which is already known to be challenging in high-Al-content materials. A deeper understanding of how alloy disorder affects the dopant activation energies may help to explain the discrepancies in the reported activation energies for p-doped (Al,Ga)N alloys, as described in Sec. 6.3.

Finally, in order to apply quantum correction to the band edges for the MQW DUV LED, LLT was employed. LLT in its current form does not account for band mixing and therefore, cannot fully capture the effects of alloy disorder across multiple valence bands. To address this, a hybrid effective mass model

was developed in order to utilise the single band LLT approach while accounting for valence band mixing effects. This hybrid band model was previously benchmarked against electronic structure TB calculations and showed very good agreement, supporting it validity for our work. However, there is no guarantee this method will accurately capture all the fine details related to alloy disorder-induced band mixing effects or the influence of higher lying states. As such, fully capturing the role of alloy fluctuations and interband interactions in carrier transport calculations is still an unresolved question. Therefore, a comparison between the hybrid effective mass model and an LLT treatment that accounts for multiple bands is an open area of research.

Overall, this thesis has provided new insight into the role of alloy fluctuations on the electronic and optical properties for (Al,Ga)N-based heterostructures by utilising an empirical tight-binding model. Connecting this atomistic model to a multiscale quantum corrected drift-diffusion model has shed light on the impact alloy disorder has on carrier transport and recombination for deep UV LEDs. Further development of this simulation framework opens up future potential for guiding and better understanding (Al,Ga)N-based UV heterstructures and devices.

Appendix A

Material parameters used for AlN and GaN

Table A.1: Material parameters used in this study for AlN and GaN calculations. a and c denote the in-plane and out-of plane lattice constants, respectively. Elastic constants and first-order piezoelectric constants are denoted as C_{ij} and e_{ij}. The spontaneous polarisation is given as P_{sp} and the dielectric constant is expressed ϵ_r. The effective electron mass parallel ($||$) and perpendicular ($\perp$) to the c-plane is given as m_e^x, while the Luttinger-like hole effective masses are shown as A_i. The conduction and valence band deformations are expressed as a_c and D_i, respectively. k_r, k_θ, $k_{r\theta}$ and k_{rr} are the force constants for bond stretching, bond bending, bond-angle and bond-bond terms, respectively. Finally the valence band offset for GaN/AlN is ΔE_{VB}.

Symbol	**GaN**	**AlN**
a (Å)	3.189 [35]	3.112 [35]
c (Å)	5.185 [35]	4.982 [35]
C_{11} (GPa)	368.6 [35]	410.2 [35]
C_{12} (GPa)	131.6 [35]	142.4 [35]
C_{13} (GPa)	95.7 [35]	110.1 [35]
C_{33} (GPa)	406.2 [35]	385 [35]
C_{44} (GPa)	101.7 [35]	122.9 [35]
e_{15} (C/m^2)	-0.32 [81]	-0.39 [81]
e_{31} (C/m^2)	-0.44 [81]	-0.63 [81]
e_{33} (C/m^2)	1.46 [81]	0.74 [81]
P_{sp} (C/m^2)	-0.040 [81]	-0.091 [81]
ϵ_r	9.6 [14]	8.5 [14]

(*table continues*)

Table A.1: (continued)

Symbol	**GaN**	**AlN**
$m_e^{\parallel}/m_0$	0.186 [60]	0.322 [60]
$m_e^{\perp}/m_0$	0.209 [60]	0.329 [60]
$A_1(\hbar^2/2m_0)$	-5.947 [60]	-3.991 [60]
$A_2(\hbar^2/2m_0)$	-0.528 [60]	-0.311 [60]
$A_3(\hbar^2/2m_0)$	5.414 [60]	3.671 [60]
$A_4(\hbar^2/2m_0)$	-2.512 [60]	-1.147 [60]
$A_5(\hbar^2/2m_0)$	-2.510 [60]	-1.329 [60]
$A_6(\hbar^2/2m_0)$	-3.202 [60]	-1.952 [60]
a_c (eV)	-4.08 [127]	-7.2
$a_c - D_1$ (eV)	-5.81 [263]	-4.21 [66]
$a_c - D_2$ (eV)	-8.92 [263]	-12.07 [66]
D_3 (eV)	5.47 [263]	9.22 [66]
D_4 (eV)	-2.98 [263]	-3.74 [66]
D_5 (eV)	-2.82 [263]	-3.30 [66]
D_6 (eV)	-5.5 [65]	-4.49 [66]
k_r (eV Å^{-2})	18.13	21.00
k_θ (eV rad^{-2})	2.75	2.00
$k_{r\theta}$ (eV Å^{-1} rad^{-1})	0.499	1.050
k_{rr} (eV Å^{-2})	0.090	0.174
ΔE_{VB} (eV)	0.90 [117]	-

Table A.2: Tight-binding parameters in eV for the nearest neighbours of wurtzite AlN and GaN.

	GaN [eV]	**AlN [eV]**
$E(s,a)$	-10.6158	-10.2006
$E(p,a)$	0.8183	0.6637
$E(p_z,a)$	0.7926	0.9237
$E(s,c)$	0.9122	2.0607
$E(p,c)$	6.6788	11.0763
$V(s,s)$	-5.9749	-8.1144
$V(x,x)$	2.3381	3.1986
$V(x,y)$	5.4697	5.6325
$V(s_a,p_c)$	4.0909	3.0442
$V(p_a,s_c)$	8.6655	10.3111

Appendix B

Multi-QW deep UV LED device parameters

Table B.1: Drift-diffusion parameters used for different regions in the simulation cell. † values are taken from Ref. [16] and the ⋄ parameters are from Ref. [69]. □ symbolises the radiative, B, and Auger-Meitner coefficients, C_{nnp} & C_{npp}, which are taken from Ref. [105].

	***n*-doped**	**Undoped**	***p*-doped**
Doping† (cm^{-3})	10^{19}	10^{10}	10^{19}
$\mu_e^{\diamond}$ (cm^2 V^{-1} s^{-1})	21.9	100	5
$\mu_h^{\diamond}$ (cm^2 V^{-1} s^{-1})	2	10	5
Activation energy† (meV)	75	-	Variable
$\tau_{n,p}^{\diamond}$ (ns)	10	10	10
$B^{\square}$ (cm^3 s^{-1})	2.0×10^{-11}	2.0×10^{-11}	2.0×10^{-11}
$C_{nnp}^{\square}$ (cm^6 s^{-1})	6.0×10^{-32}	6.0×10^{-32}	6.0×10^{-32}
$C_{npp}^{\square}$ (cm^6 s^{-1})	2.0×10^{-31}	2.0×10^{-31}	2.0×10^{-31}

Appendix C

Multi-QW deep UV LED band edge profiles

Figure C.1 shows the conduction and valence band edge energies obtained from the RA (a,c) and VCA calculations (b,d) for the deep UV LED SYS 3 ($E_A^{\mathrm{EBL}} = 450$ meV; $E_A^{\mathrm{HIL}} = 450$ meV) at a current density of 135 A cm^{-2} as discussed in Sec. 6.4.2.

In comparing the conduction band profiles of the RA (Fig C.1 (a)) and the VCA (Fig C.1 (b)), one can see step-like shifts in the electron quasi-Fermi level, $\mathrm{Ef_n}$, for the RA, particularly at QW4 and QW5, while in the VCA case this effect is much less pronounced. Due to the high mobility and low effective mass of the electrons, they are able to transverse and populate all the QWs, which have been shown in Fig. 6.10 (c).

The valence band profiles for the RA (Fig C.1 (c)) and the VCA (Fig C.1 (d)) show that the barrier region after QW5 and before the EBL has a sloped quasi-Fermi level, $\mathrm{Ef_p}$, indicating hole transport toward the active region. However, there is a pronounced shift in the $\mathrm{Ef_p}$ at QW5 for the RA system, suggesting that the holes are being driven through QW5 rather than being captured.

In comparison to the electrons, the holes have a lower mobility and larger effective mass. However, under an applied bias and due to the strong polarisation fields for the III-nitride (Al,Ga)N, it is favourable for the holes to be driven to deeper QWs. As a result, QW1-QW3 exhibit significantly higher hole densities, as already discussed and shown in Sec. 6.4.2 Fig. 6.10 (d) for the RA. When compared to the VCA system, the alloy fluctuations affect the hole

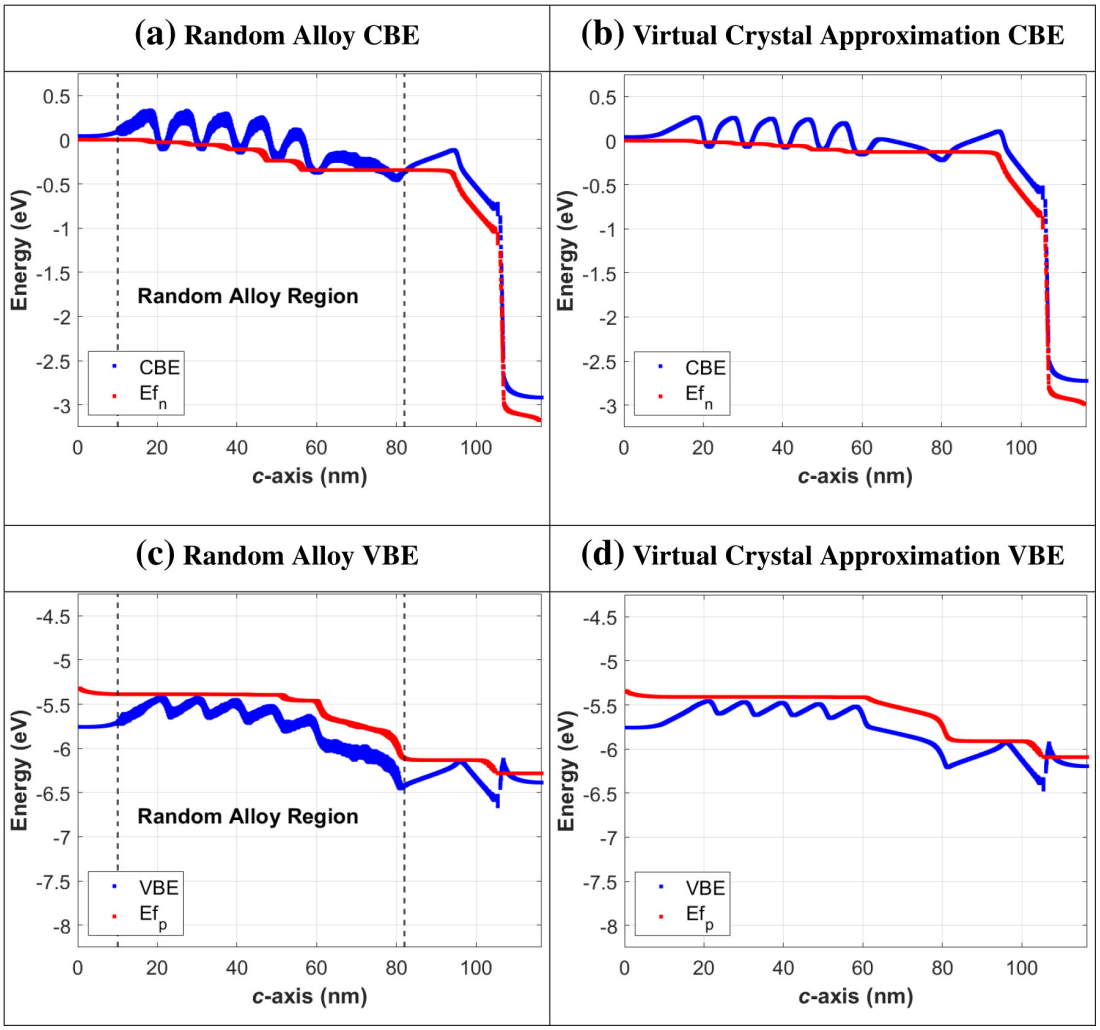


Figure C.1: Table of band edge energies for the deep UV LED SYS 3 (E_A^{EBL} = 450 meV; E_A^{HIL} = 450 meV) investigated in chapter 6 Sec. 6.4.2. The conduction (CBE) and valence band edge energies (VBE) are plotted for the random alloy (a,c) and virtual crystal approximation systems (b,d) at a current density of $\approx$ 135 A cm^{-2}. The conduction (valence) band is in blue and the electron (hole) Fermi level, Ef$_n$ (Ef$_p$), is in red. The black dashed lines define the boundaries for the random alloy in (a) and (c).

distribution across the MQW system.

References

[1] R. Finn, M. O'Donovan, T. Koprucki, and S. Schulz. Impact of carrier-density screening on Urbach-tail energies and optical polarization in (Al,Ga)N quantum well systems. *Physical Review Applied*, 24(4):044084, 2025.

[2] M. O'Donovan, R. Finn, P. Farrell, T. Streckenbach, J. Moatti, S. Schulz, and T. Koprucki. Developing a hybrid single band carrier transport model for (Al, Ga)N heterostructures. *Journal of Computational Electronics*, 24(4):1–19, 2025.

[3] J. M. McMahon, R. Finn, and S. Schulz. Theoretical study of the temperature dependence of Auger-Meitner recombination in (Al,Ga)N quantum wells. *Journal of Physics: Condensed Matter*, 37(9):095501, 2024.

[4] R. Finn, M. O'Donovan, P. Farrell, J. Moatti, T. Streckenbach, T. Koprucki, and S. Schulz. Theoretical study of the impact of alloy disorder on carrier transport and recombination processes in deep UV (Al, Ga)N light emitters. *Applied Physics Letters*, 122(24), 2023.

[5] M. O'Donovan, R. Finn, S. Schulz, and T. Koprucki. Atomistic study of Urbach tail energies in (Al,Ga)N quantum well systems. In *2023 International Conference on Numerical Simulation of Optoelectronic Devices (NUSOD)*, pages 79–80. IEEE, 2023.

[6] R. Finn, M. O'Donovan, P. Farrell, T. Streckenbach, J. Moatti, T. Koprucki, and S. Schulz. Theoretical investigation of carrier transport and recombination processes for deep UV (Al,Ga)N light emitters. In *2023 International Conference on Numerical Simulation of Optoelectronic Devices (NUSOD)*, pages 83–84. IEEE, 2023.

[7] R. Finn and S. Schulz. Impact of random alloy fluctuations on the

electronic and optical properties of (Al,Ga)N quantum wells: Insights from tight-binding calculations. *J. Chem. Phys.*, 157:244705, 2022.

[8] R. Finn and S. Schulz. Impact of random alloy fluctuations on the electronic and optical properties of c-plane $Al_xGa_{1-x}N$ quantum wells. In *2022 International Conference on Numerical Simulation of Optoelectronic Devices (NUSOD)*, pages 135–136. IEEE, 2022.

[9] H. Amano, N. Sawaki, I. Akasaki, and Y. Toyoda. Metalorganic vapor phase epitaxial growth of a high quality GaN film using an AlN buffer layer. *Applied Physics Letters*, 48(5):353–355, 1986.

[10] M. Kneissl, T.-Y. Seong, J. Han, and H. Amano. The emergence and prospects of deep-ultraviolet light-emitting diode technologies. *nature photonics*, 13(4):233–244, 2019.

[11] C. Weisbuch. On the search for efficient solid state light emitters: Past, present, future. *ECS Journal of Solid State Science and Technology*, 9(1):016022, 2019.

[12] J. Li, J. Wang, X. Yi, Z. Liu, T. Wei, J. Yan, and B. Xue. *III-Nitrides Light Emitting Diodes: Technology and Applications*, volume 306. Springer, 2020.

[13] Press release of the The Royal Swedish Academy of Sciences. Available at: `https://www.nobelprize.org/prizes/physics/2014/press-release/`. Accessed: January 09, 2025.

[14] M. A. Caro, S. Schulz, S. B. Healy, and E. O'Reilly. Built-in field control in alloyed *c*-plane III-N quantum dots and wells. *J. Appl. Phys.*, 109:084110, 2011.

[15] Yole Développement. UV LEDs and UV Lamps – Market and Technology Trends 2021. `https://www.yolegroup.com/product/report/uv-leds-and-uv-lamps--market-and-technology-trends-2021/`, 2021.

[16] H. Amano, R. Collazo, C. De Santi, S. Einfeldt, M. Funato, J. Glaab, S. Hagedorn, A. Hirano, H. Hirayama, R. Ishii, Y. Kashima, Y. Kawakami, R. Kirste, M. Kneissl, R. Martin, F. Mehnke, M. Meneghini, A. Ougazzaden, P. J. Parbrook, S. Rajan, P. Reddy, F. Römer, J. Ruschel, B. Sarkar, F. Scholz, L. J. Schowalter, P. Shields, Z. Sitar, L. Sulmoni, T. Wang, T. Wernicke, M. Weyers, B. Witzigmann,

Y.-R. Wu, T. Wunderer, and Y. Zhang. The 2020 UV emitter roadmap. *J. Phys. D: Appl. Phys*, 53:503001, 2020.

[17] Y. Muramoto, N. Kimura, and S. Nouda. Development and future of ultraviolet light-emitting diodes: UV-LED will replace the UV lamp. *Semiconductor Science and Technology*, 29(8):084004, 2014.

[18] M. Kneissl and J. Rass. *III-nitride ultraviolet emitters: Technology and applications*, volume 227. Springer, 2015.

[19] J. A. Parrish. Phototherapy and photochemotherapy of skin diseases. *Journal of Investigative Dermatology*, 77(1):167–171, 1981.

[20] P. E. Hockberger. A History of Ultraviolet Photobiology for Humans, Animals and Microorganisms. *Photochemistry and photobiology*, 76(6):561–579, 2002.

[21] S. Vilhunen, H. Särkkä, and M. Sillanpää. Ultraviolet light-emitting diodes in water disinfection. *Environmental Science and Pollution Research*, 16:439–442, 2009.

[22] M. A. Würtele, T. Kolbe, M. Lipsz, A. Külberg, M. Weyers, M. Kneissl, and M. Jekel. Application of GaN-based ultraviolet-C light emitting diodes–UV LEDs–for water disinfection. *Water research*, 45(3):1481–1489, 2011.

[23] J. Mellqvist and A. Rosen. DOAS for flue gas monitoring—I. Temperature effects in the UV/visible absorption spectra of NO, NO2, SO2 and NH3. *Journal of Quantitative Spectroscopy and Radiative Transfer*, 56(2):187–208, 1996.

[24] J. Hodgkinson and R. P. Tatam. Optical gas sensing: a review. *Measurement science and technology*, 24(1):012004, 2012.

[25] P. J. Hargis Jr, T. J. Sobering, G. C. Tisone, J. S. Wagner, S. A. Young, and R. J. Radloff. Ultraviolet fluorescence identification of protein, DNA, and bacteria. In *Optical Instrumentation for Gas Emissions Monitoring and Atmospheric Measurements*, volume 2366, pages 147–153. SPIE, 1995.

[26] J. Rass and N. Lobo-Ploch. Optical polarization and light extraction from UV LEDs. *III-Nitride Ultraviolet Emitters: Technology and Applications*, pages 137–170, 2016.

[27] M. V. Durnev and S. Y. Karpov. Polarization phenomena in light

emission from c-plane Al(In)GaN heterostructures. *physica status solidi (b)*, 250(1):180–186, 2013.

[28] J. Li, K.-B. Nam, M. L. Nakarmi, J.-Y. Lin, HX. Jiang, P. Carrier, and S.-H. Wei. Band structure and fundamental optical transitions in wurtzite AlN. *Applied Physics Letters*, 83(25):5163–5165, 2003.

[29] S. F. Chichibu, A. Uedono, T. Onuma, B. A. Haskell, A. Chakraborty, T. Koyama, P. T. Fini, S. Keller, S. P. DenBaars, J. S. Speck, U. K. Mishra, S. Nakamura, S. Yamaguchi, S. Kamiyama, H. Amano, I. Akasaki, J. Han, and T. Sota. Origin of defect-insensitive emission probability in In-containing (Al,In,Ga)N alloy semiconductors. *Nature Mater.*, 5:810, 2006.

[30] C. Weisbuch, S. Nakamura, Y.-R. Wu, and J. S. Speck. Disorder effects in nitride semiconductors: impact on fundamental and device properties. *Nanophotonics*, 10(1):3–21, 2020.

[31] C. Frankerl, F. Nippert, A. Gomez-Iglesias, M. P. Hoffmann, C. Brandl, H.-J. Lugauer, R. Zeisel, A. Hoffmann, and M. J. Davies. Origin of carrier localization in AlGaN-based quantum well structures and implications for efficiency droop. *Appl. Phys. Lett.*, 117:102107, 2020.

[32] C. Frankerl, F. Nippert, M. P. Hoffmann, H. Wang, C. Brandl, H.-J. Lugauer, R. Zeisel, A. Hoffmann, and M. J. Davies. Strongly localized carriers in Al-rich AlGaN/AlN single quantum wells grown on sapphire substrates. *J. Appl. Phys.*, 127:095701, 2020.

[33] C. Frankerl, F. Nippert, M. P. Hoffmann, C. Brandl, H.-J. Lugauer, R. Zeisel, A. Hoffmann, and M. J. Davies. Carrier dynamics in Al-rich AlGaN/AlN quantum well structures governed by carrier localization. *Phys. Stat. Sol. (b)*, 257:2000242, 2020.

[34] C. Broderick, E. P. O'Reilly, and S. Schulz. Perspective: Theory and simulation of highly mismatched semiconductor alloys using the tight-binding method. *J. Appl. Phys.*, 135:100902, 2024.

[35] M. A. Caro, S. Schulz, and E. P. O'Reilly. Hybrid functional study of the elastic and structural properties of wurtzite and zinc-blende group-III nitrides. *Phys. Rev. B*, 86:014117, 2012.

[36] B. Janjua, H. Sun, C. Zhao, D. H. Anjum, D. Priante, A. A. Alhamoud, F. Wu, X. Li, A. M. Albadri, A. Y. Alyamani, M. M. El-Desouki, T. K.

Ng, and B. S. Ooi. Droop-free $Al_{1-x}Ga_{1-x}N/Al_yGa_{1-y}N$ quantum-disks-in-nanowires ultraviolet led emitting at 337 nm on metal/silicon substrates. *Optics Express*, 25(2):1381–1390, 2017.

[37] G. Hofmann, A. Muhin, N. Susilo, F. Römer, T. Wernicke, M. Kneissl, and B. Witzigmann. Simulation of carrier injection efficiency in AlGaN-based UV-light-emitting diodes. *IEEE Photonics Journal*, 16:4, 2024.

[38] F. Römer, M. Guttmann, T. Wernicke, M. Kneissl, and B. Witzigmann. Effect of inhomogeneous broadening in ultraviolet III-nitride light-emitting diodes. *Materials*, 14(24):7890, 2021.

[39] S. Kölle, F. Römer, G. Cardinali, A. Schulz, N. Susilo, D. H. Vidal, T. Wernicke, M. Kneissl, and B. Witzigmann. Optical Gain in AlGaN Quantum Wells: Impact of Higher Energy States. *IEEE Photonics Journal*, 16:1–5, 2024.

[40] M. O'Donovan, M. Luisier, E. P. O'Reilly, and S. Schulz. Impact of random alloy fluctuations on inter-well transport in InGaN/GaN multi-quantum well systems: an atomistic non-equilibrium Green's function study. *J. Phys.: Condens. Matter*, 33:045302, 2021.

[41] D. N. Nath, Z. C. Yang, C.-Y. Lee, P. S. Park, Y.-R. Wu, and S. Rajan. Unipolar vertical transport in GaN/AlGaN/GaN heterostructures. *Applied Physics Letters*, 103(2), 2013.

[42] C.-K. Li, M. Piccardo, L.-S. Lu, S. Mayboroda, L. Martinelli, J. Peretti, J. S. Speck, C. Weisbuch, M. Filoche, and Y.-R. Wu. Localization landscape theory of disorder in semiconductors. iii. application to carrier transport and recombination in light emitting diodes. *Phys. Rev. B*, 95(14):144206, 2017.

[43] H.-T. Shen, C. Weisbuch, J. S. Speck, and Y.-R. Wu. Three-dimensional modeling of minority-carrier lateral diffusion length including random alloy fluctuations in (In,Ga)N and (Al,Ga)N single quantum wells. *Physical Review Applied*, 16(2):024054, 2021.

[44] M. Filoche, M. Piccardo, Y-R. Wu, C-K. Li, C. Weisbuch, and S. Mayboroda. Localization landscape theory of disorder in semiconductors. I. Theory and modeling. *Physical Review B*, 95:144204, 2017.

[45] M. Piccardo, C.-K. Li, Y.-R. Wu, J. S. Speck, B. Bonef, R. M. Farrell,

M. Filoche, L. Martinelli, J. Peretti, and C. Weisbuch. Localization landscape theory of disorder in semiconductors. II. Urbach tails of disordered quantum well layers. *Phys. Rev. B*, 95:144205, 2017.

[46] T.-J. Yang, R. Shivaraman, J. S. Speck, and Y.-R. Wu. The influence of random indium alloy fluctuations in indium gallium nitride quantum wells on the device behaviour. *J. Appl. Phys.*, 116:113104, 2014.

[47] K.-Y. Cheng. *III–V Compound Semiconductors and Devices*. Springer, 2020.

[48] C. Kittel. *Introduction to solid state physics*. John Wiley & Sons, 2005.

[49] M. Ueno, M. Yoshida, A. Onodera, O. Shimomura, and K. Takemura. Stability of the wurtzite-type structure under high pressure: GaN and InN. *Physical Review B*, 49(1):14, 1994.

[50] H. Morkoc. Handbook of Nitride Semiconductors and Devices, Vol. 1 Wiley, 2008.

[51] A. Kobayashi, O. F. Sankey, S. M. Volz, and J. D. Dow. Semiempirical tight-binding band structures of wurtzite semiconductors: AlN, CdS, CdSe, ZnS, and ZnO. *Physical Review B*, 28(2):935, 1983.

[52] T. Yao and S.-K. Hong. *Oxide and nitride semiconductors: Processing, properties, and applications*, volume 12. Springer Science & Business Media, 2009.

[53] M. Monavarian, A. Rashidi, and D. Feezell. A Decade of Nonpolar and Semipolar III-Nitrides: A Review of Successes and Challenges. *physica status solidi (a)*, 216(1):1800628, 2019.

[54] N. W. Ashcroft and D. N. Mermin. *Solid state physics*. BROOKS/COLE, 1976.

[55] P. Phillips. *Advanced solid state physics*. Cambridge University Press, 2012.

[56] M. Born and R. Oppenheimer. Zur quantentheorie der molekeln. *Physical Review B*, 389(20):457, 1927.

[57] S. M. Girvin and K. Yang. *Modern condensed matter physics*. Cambridge University Press, 2019.

[58] F. Bloch. Über die quantenmechanik der elektronen in kristallgittern. *Zeitschrift für physik*, 52(7):555–600, 1929.

[59] S. Schulz and E. P. O'Reilly. Electronic band structure. In *Handbook of Optoelectronic Device Modeling and Simulation*, pages 3–34. CRC Press, 2017.

[60] P. Rinke, M. Winkelnkemper, A. Qteish, D. Bimberg, J. Neugebauer, and M. Scheffler. Consistent set of band parameters for the group-III nitrides AlN, GaN, and InN. *Phys. Rev. B*, 77:075202, 2008.

[61] S. Schulz, M. A. Caro, L.-T. Tan, P. J. Parbrook, R. W. Martin, and E. P. O'Reilly. Composition-dependent band gap and band-edge bowing in AlInN: A combined theoretical and experimental study. *Appl. Phys. Express*, 6:121001, 2013.

[62] E. Sakalauskas, B. Reuters, L. R. Khoshroo, H. Kalisch, M. Heuken, A. Vescan, M. Röppischer, C. Cobet, G. Gobsch, and R. Goldhahn. Dielectric function and optical properties of quaternary AlInGaN alloys. *J. Appl. Phys.*, 110:013102, 2011.

[63] S. Schulz. *Electronic and Optical Properties of Quantum Dots: A Tight-Binding Approach*. Phd thesis, Dem Fachbereich für Physik und Elektrotechnik der Universität Bremen, May 2007.

[64] S. Schulz and T. J. Badcock and M. A. Moram and P. Dawson and M. J. Kappers and C. J. Humphreys and E. P. O'Reilly. Electronic and optical properties of nonpolar a-plane GaN quantum wells. *Phys. Rev. B*, 82:125318, 2010.

[65] I. Vurgaftman and J. R. Meyer. Band parameters for nitrogen-containing semiconductors. *J. Appl. Phys.*, 94:3675, 2003.

[66] Q. Yan, P. Rinke, M. Winkelnkemper, A. Qteish, D. Bimberg, M. Scheffler, and C. G. Van de Walle. Band parameters and strain effects in ZnO and group-III nitrides. *Semiconductor science and technology*, 26(1):014037, 2010.

[67] J.-M. Wagner and F. Bechstedt. Properties of strained wurtzite GaN and AlN: Ab initio studies. *Physical Review B*, 66(11):115202, 2002.

[68] S. Schulz, M. A. Caro, and E. P. O'Reilly. Impact of cation-based

localized electronic states on the conduction and valence band structure of $Al_{1-x}In_xN$ alloys. *Appl. Phys. Lett.*, 104:172102, 2014.

[69] H.-T Shen, Y.-C Chang, and Y.-R Wu. Analysis of Light-Emission Polarization Ratio in Deep-Ultraviolet Light-Emitting Diodes by Considering Random Alloy Fluctuations with the 3D k.p Method. *Phys. Status Solidi*, 16:2100498, 2022.

[70] M. Kneissl, T. Kolbe, C. Chua, V. Kueller, N. Lobo, J. Stellmach, A. Knauer, H. Rodiguez, S. Einfeldt, Z. Yang, N. M. Johnson, and M. Weyers. Advances in group III-nitride-based deep UV light-emitting diode technology. *Semicond. Sci. Technol.*, 26:014036, 2011.

[71] J. E. Northrup, C. L. Chua, Z. Yang, T. Wunderer, M. Kneissl, N. M. Johnson, and T. Kolbe. Effect of strain and barrier composition on the polarization of light emission from AlGaN/AlN quantum wells. *Applied Physics Letters*, 100(2), 2012.

[72] H.Y Ryu. Large enhancement of light extraction efficiency in AlGaN-based nanorod ultraviolet light-emitting diode structures. *Nanoscale Research Letters*, 9:58, 2014.

[73] P. Reddy, I. Bryan, Z. Bryan, J. Tweedie, S. Washiyama, R. Kirste, S. Mita, R. Collazo, and Z. Sitar. Charge neutrality levels, barrier heights, and band offsets at polar AlGaN. *Applied Physics Letters*, 107(9), 2015.

[74] A. Bonfiglio, M. Lomascolo, G. Traetta, R. Cingolani, A. Di Carlo, F. Della Sala, P. Lugli, A. Botchkarev, and H. Morkoc. Well-width dependence of the ground level emission of GaN/AlGaN quantum wells. *Journal of Applied Physics*, 87(5):2289–2292, 2000.

[75] Q. Yan, P. Rinke, A. Janotti, M. Scheffler, and C. G. Van de Walle. Effects of strain on the band structure of group-III nitrides. *Physical Review B*, 90(12):125118, 2014.

[76] C. E. Dreyer, A. Janotti, and C. G. Van de Walle. Effects of strain on the electron effective mass in GaN and AlN. *Applied Physics Letters*, 102(14), 2013.

[77] I. Vurgaftman, J. R. Meyer, and L. R. Ram-Mohan. Band parameters for III–V compound semiconductors and their alloys. *J. Appl. Phys.*, 89(11):5815–5875, 2001.

[78] D. S. P. Tanner. *A study of elastic and electronic properties of III-nitride semiconductors*. Phd thesis, University College Cork, 2017.

[79] S. Schulz, M. A. Caro, C. Coughlan, and E. P. O'Reilly. Atomistic anaylsis of the impact of alloy and well width fluctuations on the electronic and optical properties of InGaN/GaN quantum wells. *Phys. Rev. B*, 91:035439, 2015.

[80] M. A. Migliorato, J. Pal, X. Huang, W. Hu, M. Willatzen, and Y. Gu. Polarization in III-N semiconductors. In *Handbook of Optoelectronic Device Modeling and Simulation*, pages 219–250. CRC Press, 2017.

[81] M. A. Caro, S. Schulz, and E. P. O'Reilly. Theory of local electric polarization and its relation to internal strain: impact on the polarization potential and electronic properties of group-III nitrides. *Phys. Rev. B*, 88:214103, 2013.

[82] C. E. Dreyer, A. Janotti, C. G. Van de Walle, and D. Vanderbilt. Correct implementation of polarization constants in wurtzite materials and impact on III-nitrides. *Physical Review X*, 6(2):021038, 2016.

[83] D. J. Griffiths. Introduction to electrodynamics fourth edition. 2021.

[84] C. X. Ren. Polarisation fields in III-nitrides: effects and control. *Materials Science and Technology*, 32:418–433, 2016.

[85] S. M. Sze, Y. Li, and K. K. Ng. *Physics of semiconductor devices*. John wiley & sons, 2006.

[86] J. Piprek. Efficiency droop in nitride-based light-emitting diodes. *Phys. Status Solidi A*, 207:No. 10, 2217–2225, 2010.

[87] W. S. Zuo, Y. X. Niu, L. Yang, X. Z. Chi, J. J. Liu, and X. H. Zhang. Inserting a AlN electron blocking layer for InGaN/GaN blue light-emitting diodes. In *Materials Science Forum*, volume 1014, pages 126–130. Trans Tech Publ, 2020.

[88] Y. Yang, X. A. Cao, and C. Yan. Investigation of the nonthermal mechanism of efficiency rolloff in InGaN light-emitting diodes. *IEEE Transactions on Electron Devices*, 55(7):1771–1775, 2008.

[89] W. Sun, M. Shatalov, J. Deng, X. Hu, J. Yang, A. Lunev, Y. Bilenko, M. Shur, and R. Gaska. Efficiency droop in 245–247 nm AlGaN

light-emitting diodes with continuous wave 2 mW output power. *Applied Physics Letters*, 96(6), 2010.

[90] H. Hirayama, S. Fujikawa, N. Noguchi, J. Norimatsu, T. Takano, K. Tsubaki, and N. Kamata. 222-282 nm AlGaN and InAlGaN-based deep-UV LEDs fabricated on high-quality AlN on sapphire. *physica status solidi (a)*, 206(6):1176–1182, 2009.

[91] M. Shatalov, J. Yang, W. Sun, R. Kennedy, R. Gaska, K. Liu, M. Shur, and G. Tamulaitis. Efficiency of light emission in high aluminum content AlGaN quantum wells. *Journal of Applied Physics*, 105(7), 2009.

[92] R. G. Banal, M. Funato, and Y. Kawakami. Extremely high internal quantum efficiencies from AlGaN/AlN quantum wells emitting in the deep ultraviolet spectral region. *Applied Physics Letters*, 99(1), 2011.

[93] F. Nippert, M. Tollabi Mazraehno, M. J. Davies, M. P. Hoffmann, H.-J. Lugauer, T. Kure, M. Kneissl, A. Hoffmann, and M.R. Wagner. Auger recombination in AlGaN quantum wells for UV light-emitting diodes. *Appl. Phys. Lett*, 113(7):071107, 2018.

[94] J. Mickevičius, G. Tamulaitis, M. Shur, M. Shatalov, J. Yang, and R. Gaska. Internal quantum efficiency in AlGaN with strong carrier localization. *Applied Physics Letters*, 101(21), 2012.

[95] Z. Bryan, I. Bryan, J. Xie, S. Mita, Z. Sitar, and R. Collazo. High internal quantum efficiency in AlGaN multiple quantum wells grown on bulk AlN substrates. *Applied Physics Letters*, 106(14), 2015.

[96] M. L. Nakarmi, K. H. Kim, K. Zhu, J. Y. Lin, and H. X. Jiang. Transport properties of highly conductive n-type Al-rich $Al_xGa_{1-x}N$ ($x \geq 0.7$). *Applied Physics Letters*, 85(17):3769–3771, 2004.

[97] J. Piprek. Efficiency models for GaN-based light-emitting diodes: Status and challenges. *Materials*, 13(22):5174, 2020.

[98] P. Farrell, N. Rotunda, D. H. Doan, M. Kantner, J. Fuhrmann, and T. Koprucki. Mathematical Methods: Drift-Diffusion Models. In J. Piprek, editor, *Handbook of Optoelectronic Device Modeling and Simulation*, volume 2, chapter 50, page 733.771. CRC Press, 2017.

[99] E. Kioupakis, D. Steiauf, P. Rinke, K. T. Delaney, and C. G. Van

de Walle. First-principles calculations of indirect Auger recombination in nitride semiconductors. *Phys. Rev. B*, 92:035207, 2015.

[100] J. M. McMahon, E. Kioupakis, and S. Schulz. Atomistic analysis of Auger recombination in *c*-plane (In,Ga)N/GaN quantum wells: Temperature-dependent competition between radiative and nonradiative recombination. *Phys. Rev. B*, 105:195307, 2022.

[101] Ž. Podlipskas, R. Aleksiejūnas, A. Kadys, J. Mickevičius, J. Jurkevičius, G. Tamulaitis, M. Shur, M. Shatalov, J. Yang, and R. Gaska. Dependence of radiative and nonradiative recombination on carrier density and Al content in thick AlGaN epilayers. *Journal of Physics D: Applied Physics*, 49(14):145110, 2016.

[102] C. Weisbuch, M. Piccardo, L. Martinelli, J. Iveland, J. Peretti, and J. S. Speck. The efficiency challenge of nitride light-emitting diodes for lighting. *physica status solidi (a)*, 212(5):899–913, 2015.

[103] J. M. McMahon, E. Kioupakis, and S. Schulz. Carrier density dependant Auger recombination in c-plane (In,Ga)N/GaN quantum wells: insights from atomistic calculations. *J. Phys. D: Appl Phys.*, 57:125102, 2024.

[104] M. O'Donovan, P. Farrell, J. Moatti, T. Streckenbach, T. Koprucki, and S. Schulz. Impact of random alloy fluctuations on the carrier distribution in multicolor (In,Ga)N/GaN quantum well systems. *Physical Review Applied*, 21(2):024052, 2024.

[105] N. Pant, K. Bushick, A. McAllister, W. Lee, C. G. Van de Walle, and E. Kioupakis. Carrier confinement and alloy disorder exacerbate Auger–Meitner recombination in AlGaN ultraviolet light-emitting diodes. *Applied Physics Letters*, 125(2), 2024.

[106] A. Di Vito, A. Pecchia, A. Di Carlo, and M. Auf der Maur. Simulating random alloy effects in III-nitride light emitting diodes. *Journal of Applied Physics*, 128(4), 2020.

[107] P. Hohenberg and W. Kohn. Inhomogeneous Electron Gas. *Phys. Rev.*, 136:B864–B871, 1964.

[108] W. Kohn and L. J. Sham. Self-Consistent Equations Including Exchange and Correlation Effects. *Phys. Rev.*, 140:A1133, 1965.

[109] E. Lipparini. *Modern many-particle physics: atomic gases, nanostructures and quantum liquids*. World Scientific, 2008.

[110] D. S. Sholl and J. A. Steckel. *Density Functional Theory*. John Wiley Sons, Inc., Hoboken, New Jersey, 2009.

[111] T. J. Giese and D. M. York. Density-functional expansion methods: Evaluation of LDA, GGA, and meta-GGA functionals and different integral approximations. *The Journal of chemical physics*, 133(24), 2010.

[112] C. Stampfl and C. G. Van de Walle. Density-functional calculations for III-V nitrides using the local-density approximation and the generalized gradient approximation. *Physical Review B*, 59(8):5521, 1999.

[113] Jochen Heyd, Gustavo E Scuseria, and Matthias Ernzerhof. Hybrid functionals based on a screened Coulomb potential. *The Journal of chemical physics*, 118(18):8207–8215, 2003.

[114] Jochen Heyd and Gustavo E Scuseria. Efficient hybrid density functional calculations in solids: Assessment of the Heyd–Scuseria–Ernzerhof screened Coulomb hybrid functional. *The Journal of chemical physics*, 121(3):1187–1192, 2004.

[115] Matthias Ernzerhof and Gustavo E Scuseria. Assessment of the Perdew–Burke–Ernzerhof exchange-correlation functional. *The Journal of chemical physics*, 110(11):5029–5036, 1999.

[116] Carlo Adamo and Vincenzo Barone. Toward reliable density functional methods without adjustable parameters: The PBE0 model. *The Journal of chemical physics*, 110(13):6158–6170, 1999.

[117] P. G. Moses, M. Miao, Q. Yan, and C. G. Van de Walle. Hybrid functional investigations of band gaps and band alignments for AlN, GaN, InN, and InGaN. *J. Chem. Phys.*, 134(8), 2011.

[118] A. Nakata, J. S. Baker, S. Y. Mujahed, J. T. L. Poulton, S. Arapan, J. Lin, Z. Raza, S. Yadav, L. Truflandier, T. Miyazaki, and D. R. Bowler. Large scale and linear scaling DFT with the CONQUEST code. *The Journal of chemical physics*, 152(16), 2020.

[119] S. Kokott, F. Merz, Y. Yao, C. Carbogno, M. Rossi, V. Havu, M. Rampp, M. Scheffler, and V. Blum. Efficient all-electron hybrid density functionals

for atomistic simulations beyond 10 000 atoms. *The Journal of Chemical Physics*, 161(2), 2024.

[120] D Watson-Parris, MJ Godfrey, P Dawson, RA Oliver, MJ Galtrey, MJ Kappers, and CJ Humphreys. Carrier localization mechanisms in $In_xGa_{1-x}N$/GaN quantum wells. *Physical Review B—Condensed Matter and Materials Physics*, 83(11):115321, 2011.

[121] P. Harrison and A. Valavanis. *Quantum wells, wires and dots: theoretical and computational physics of semiconductor nanostructures*. John Wiley & Sons, 2016.

[122] D. W. Snoke. *Solid state physics: Essential concepts*. Cambridge University Press, 2020.

[123] E. O'Reilly. *Quantum theory of solids*. Taylor & Francis, Taylor & Francis Group, 2002.

[124] E. O. Kane. Physics of III-V compounds. *Semiconductors and Semimetals*, 1:75, 1966.

[125] D.J. Dugdale, S. Brand, and R. A. Abram. Direct calculation of k·p parameters for wurtzite AlN, GaN, and InN. *Physical Review B*, 61(19):12933, 2000.

[126] S. L. Chuang, N. Peyghambarian, and S. Koch. Physics of optoelectronic devices, 1996.

[127] S. L. Chuang and C. S. Chang. k·p method for strained wurtzite semiconductors. *Phys. Rev. B*, 54(4):2491, 1996.

[128] H. Haug and S. W. Koch. *Quantum theory of the optical and electronic properties of semiconductors*. world scientific, 2009.

[129] P. Löwdin. A note on the quantum-mechanical perturbation theory. *The Journal of Chemical Physics*, 19(11):1396–1401, 1951.

[130] C. R. Pidgeon and R. N. Brown. Interband magneto-absorption and Faraday rotation in InSb. *Physical Review*, 146(2):575, 1966.

[131] E. O. Kane. Energy band structure in p-type germanium and silicon. *Journal of Physics and Chemistry of Solids*, 1(1-2):82–99, 1956.

[132] T.-Y. Tsai, K. S. Qwah, J.-P. Banon, M. Filoche, C. Weisbuch, Y.-R. Wu, and J. S. Speck. Carrier localization in III-nitride versus conventional

III-V semiconductors: A study on the effects of alloy disorder using landscape theory and the Schrödinger equation. *Physical Review Applied*, 20(4):044069, 2023.

[133] C. Coughlan, S. Schulz, M. A. Caro, and E. P. O'Reilly. Band gap bowing and optical polarization switching in $Al_{1-x}Ga_xN$ alloys. *Phys. Status Solidi B*, 252:879, 2015.

[134] M. Filoche and S. Mayboroda. Universal mechanism for Anderson and weak localization. *Proceedings of the National Academy of Sciences*, 109(37):14761–14766, 2012.

[135] D. N. Arnold, G. David, D. Jerison, S. Mayboroda, and M. Filoche. Effective Confining Potential of Quantum States in Disordered Media. *Physical Review Letters*, 116:056602, 2016.

[136] D. Chaudhuri, J. C. Kelleher, M. R. O'Brien, E. P. O'Reilly, and S. Schulz. Electronic structure of semiconductor nanostructures: A modified localization landscape theory. *Physical Review B*, 101:035430, 2020.

[137] T. Yang, S. Nakajima, and S. Sakai. Electronic structures of wurtzite GaN, InN and their alloy $Ga_{1-x}In_xN$ calculated by the tight-binding method. *Japanese journal of applied physics*, 34(11R):5912, 1995.

[138] T. B. Boykin. Improved fits of the effective masses at Γ in the spin-orbit, second-nearest-neighbor sp 3 s* model: Results from analytic expressions. *Physical Review B*, 56(15):9613, 1997.

[139] M. Luisier, A. Schenk, W. Fichtner, and G. Klimeck. Atomistic simulation of nanowires in the sp 3 d 5 s* tight-binding formalism: From boundary conditions to strain calculations. *Physical Review B—Condensed Matter and Materials Physics*, 74(20):205323, 2006.

[140] S. Schulz, S. Schumacher, and G. Czycholl. Tight-binding model for semiconductor quantum dots with a wurtzite crystal structure: From one-particle properties to coulomb correlations and optical spectra. *Physical Review B—Condensed Matter and Materials Physics*, 73(24):245327, 2006.

[141] P-O. Löwdin. On the non-orthogonality problem connected with the use of atomic wave functions in the theory of molecules and crystals. *The Journal of Chemical Physics*, 18(3):365–375, 1950.

[142] J.C. Slater and G.F. Koster. Simplified LCAO method for the periodic potential problem. *Physical review*, 94(6):1498, 1954.

[143] W.M.C Foulkes and R. Haydock. Tight-binding models and density-functional theory. *Physical review B*, 39(17):12520, 1989.

[144] G. Seifert. Tight-binding density functional theory: an approximate kohn-sham dft scheme. *The Journal of Physical Chemistry A*, 111(26):5609–5613, 2007.

[145] E. P. O'Reilly, A. Lindsay, S. Tomic, and M. Kamal-Saadi. Tight-binding and $k \cdot p$ models for the electronic structure of Ga(In)NAs and related alloys. *Semicond. Sci. Technol.*, 17:870, 2002.

[146] Z. Q. Li and W. Pots. Electronic density of states of semiconductor alloys from lattice-mismatched isovalent binary constituents. *Phys. Rev. B*, 46:2109, 1992.

[147] T. B. Boykin, N. Kharache, G. Klimeck, and M. Korkusinski. Approximate bandstructures of semiconductor alloys from tight-binding supercell calculations. *J. Phys.: Condens. Matter*, 19:036203, 2007.

[148] W. Mönch. Empirical tight-binding calculation of the branch-point energy of the continuum of interface-induced gap states. *J. Appl. Phys.*, 80(9):5076–5082, 1996.

[149] T.B Boykin, G Klimeck, R. C. Bowen, and F. Oyafuso. Diagonal parameter shifts due to nearest-neighbor displacements in empirical tight-binding theory. *Physical Review B*, 66(12):125207, 2002.

[150] Y-M. Niquet, D. Rideau, C. Tavernier, H. Jaouen, and X. Blase. Onsite matrix elements of the tight-binding hamiltonian of a strained crystal: Application to silicon, germanium, and their alloys. *Physical Review B—Condensed Matter and Materials Physics*, 79(24):245201, 2009.

[151] J.-M. Jancu, R. Scholz, F. Beltram, and F. Bassani. Empirical spds* tight-binding calculation for cubic semiconductors: General method and material parameters. *Physical Review B*, 57(11):6493, 1998.

[152] M. Winkelnkemper, A. Schliwa, and D. Bimberg. Interrelation of structural and electronic properties in $In_xGa_{1-x}N$/GaN quantum dots using an eigh-band k.p model. *Phys. Rev. B*, 74:155322, 2006.

[153] F.H. Stillinger and T.A. Weber. Computer simulation of local order in condensed phases of silicon. *Physical review B*, 31(8):5262, 1985.

[154] J. E. Jones. On the determination of molecular fields.—I. From the variation of the viscosity of a gas with temperature. *Proceedings of the Royal Society of London. Series A, Containing Papers of a Mathematical and Physical Character*, 106(738):441–462, 1924.

[155] M. J. P. Musgrave and J. A. Pople. A general valence force field for diamond. *Proceedings of the Royal Society of London. Series A. Mathematical and Physical Sciences*, 268(1335):474–484, 1962.

[156] P. N. Keating. Effect of invariance requirements on the elastic strain energy of crystals with application to the diamond structure. *Physical Review*, 145(2):637, 1966.

[157] M. R. Martin. Relation between elastic tensors of wurtzite and zinc-blende structure materials. *Physical Review B*, 6(12):4546, 1972.

[158] R. M. Martin. Elastic properties of ZnS structure semiconductors. *Physical Review B*, 1(10):4005, 1970.

[159] A. P. Thompson, H. M. Aktulga, R. Berger, D. S. Bolintineanu, W. M. Brown, P. S. Crozier, P. J. In't Veld, A. Kohlmeyer, S. G. Moore, T. D. Nguyen, et al. LAMMPS-a flexible simulation tool for particle-based materials modeling at the atomic, meso, and continuum scales. *Computer Physics Communications*, 271:108171, 2022.

[160] C. Pryor, J. Kim, L. Wang, A. Williamson, and A. Zunger. Comparison of two methods for describing the strain profiles in quantum dots. *J. Appl. Phys.*, 83:2548, 1998.

[161] F. Bernardini, V. Fiorentini, and D. Vanderbilt. Spontaneous polarization and piezoelectric constants of III-V nitrides. *Phys. Rev. B*, 56:R10024(R), 1997.

[162] J. D. Jackson. *Classical electrodynamics*. John Wiley & Sons, 1999.

[163] F. Bertazzi, M. Goano, G. Ghione, A. Tibaldi, P. Debernardi, and E. Bellotti. Electron transport. In *Handbook of Optoelectronic Device Modeling and Simulation*, pages 35–80. CRC Press, 2017.

[164] S. Datta. Nanoscale device modeling: the Green's function method. *Superlattices and microstructures*, 28(4):253–278, 2000.

[165] M. Lundstrom. Fundamentals of carrier transport, 2nd edn. *Measurement Science and Technology*, 13(2):230–230, 2002.

[166] M. Auf Der Maur. A multiscale simulation environment for electronic and optoelectronic devices. *Ph. D. dissertation*, 2008.

[167] W. Van Roosbroeck. Theory of the flow of electrons and holes in germanium and other semiconductors. *The Bell System Technical Journal*, 29(4):560–607, 1950.

[168] Stefan Birner. Modeling of semiconductor nanostructures and semiconductor-electrolyte interfaces. 2011.

[169] D. Chaudhuri, M. O'Donovan, T. Streckenbach, O. Marquardt, P. Farrell, S. K. Patra, T. Koprucki, and S. Schulz. Multiscale simulations of the electronic structure of III-nitride quantum wells with varied indium content: Connecting atomistic and continuum-based models. *J. Appl. Phys.*, 129:073104, 2021.

[170] M. O'Donovan, D. Chaudhuri, T. Streckenbach, P. Farrell, S. Schulz, and T. Koprucki. From atomistic tight-binding theory to macroscale drift-diffusion: Multiscale modeling and numerical simulation of uni-polar charge transport in (In,Ga)N devices with random fluctuations. *J. Appl. Phys.*, 130:065702, 2021.

[171] J. Fuhrmann, T. Streckenbach, et al. pdelib: A finite volume and finite element toolbox for pdes. [software]. `http://pdelib.org`, 2019. Version: 2.4.20190405, Weierstrass Institute (WIAS).

[172] S. Hang. TetGen, a Delaunay-based quality tetrahedral mesh generator. *ACM Trans. Math. Softw*, 41(2):11, 2015.

[173] D. H. Doan, P. Farrell, J. Fuhrmann, M. Kantner, T. Koprucki, and N. Rotundo. ddfermi – a drift-diffusion simulation tool. ddfermi – a drift-diffusion simulation tool, Weierstrass Institute (WIAS), doi: `http://doi.org/10.20347/WIAS.SOFTWARE.DDFERMI`, 2020.

[174] C. Cancès, C. Chainais-Hillairet, J. Fuhrmann, and B. Gaudeul. A numerical-analysis-focused comparison of several finite volume schemes for a unipolar degenerate drift-diffusion model. *IMA Journal of Numerical Analysis*, 41(1):271–314, 2021.

[175] M. A. Caro Bayo. *Theory of elasticity and electric polarization effects in the group-III nitrides*. Phd thesis, University College Cork, 2013.

[176] T. Brandes and S. Kettemann. *Anderson Localization and Its Ramifications*. Springer, 2003.

[177] D. J. Thouless. Anderson's theory of localized states. . *Phys. C: Solid State Phys.*, 3:1559, 1970.

[178] S. K. Patra and S. Schulz. Exploring the potential of c-plane indium gallium nitride quantum dots for twin-photon emission. *Nano Lett.*, 20:234, 2020.

[179] S. K. Patra and S. Schulz. Indium gallium nitride quantum dots: consequence of random alloy fluctuations for polarization entangled photon emission. *Mater. Quantum. Technol.*, 1:015001, 2021.

[180] A. A. Roble, S. K. Patra, F. Massabuau, M. Frentrup, M. A. Leontiadou, P. Dawson, M. J. Kappers, R. A. Oliver, D. M. Graham, and S. Schulz. Impact of alloy fluctuations and coulomb effects on the electronic and optical properties of *c*-plane GaN/AlGaN quantum wells. *Scientific Reports*, 9:18862, 2019.

[181] M. E. Rudinsky and S. Yu. Karpov. Radiative and auger recombination constants and internal quantum efficiency of (0001) AlGaN deep-UV light-emitting diode structures. *Phys. Status Solidi A*, 217:1900878, 2020.

[182] C. Adelmann, E. Sarigiannidou, and D. Jalabert. Growth and optical properties of GaN/AlN quantum wells. *Appl. Phys. Lett.*, 82:4154, 2003.

[183] S. Ichikawa, Y. Iwata, M. Funato, S. Nagata, and Y. Kawakami. High quality semipolar (1-102) AlGaN/AlN quantum wells with remarkably enhanced optical transition probabilities. *Appl. Phys. Lett.*, 104:252102, 2014.

[184] L. Rigutti, B. Bonef, J. Speck, F.Tang, and R. A. Oliver. Atom probe tomography of nitride semiconductors. *Scripta Materialia*, 148:75, 2018.

[185] T. P. Sheerin, D. S. P. Tanner, and S. Schulz. Atomistic analysis of piezoelectric potential fluctuations in zinc-blende InGaN/GaN quantum wells: A stillinger-weber potential based analysis. *Phys. Rev. B*, 103:165201, 2021.

[186] L. Pauling. *The Nature of the Chemical Bond*. Cornell University Press: Ithaca, New York, 3rd edition, 1960.

[187] E. P. O'Reilly, A Lindsay, and S. Fahy. Theory of the electronic structure of dilute nitride alloys: beyond the band-anti-crossing model. *J. Phys.: Condens. Matter*, 16:S3257, 2004.

[188] C. Persson, A. Ferreira da Silva, R. Ahuja, and B. Johansson. Effective electronic masses in wurtzite and zinc-blende GaN and AlN. *Journal of Crystal Growth*, 231:397–406, 2001.

[189] M. Suzuki and T. Uenoyama. First-principles calculations of effective-mass parameters of A1N and GaN. *Phys. Rev. B*, 52:11, 1995.

[190] K. Kim, W. Lambrecht, and B. Segall. Effective masses and valence-band splittings in GaN and AlN. *Phys. Rev. B*, 56:12, 1997.

[191] T. M. Al tahtamouni, J.Y. Lin, and H. X. Jiang. Optical polarization in c-plane Al-rich AlN/$Al_xGa_{1-x}N$ single quantum wells. *Appl. Phys. Lett.*, 101:042103, 2012.

[192] C. Frankerl. *Optical Properties and Carrier Recombination Mechanisms in AlGaN-based Quantum Well Structures and Epitaxial Layers*. Ph.D. thesis, Mathematik und Naturwissenschaften der Technischen Universität Berlin zur Erlangung des akademischen Grades, 2021.

[193] P. Dawson, S. Schulz, R. A. Oliver, M. J. Kappers, and C. J. Humphreys. The nature of carrier localisation in polar and nonpolar InGaN/GaN quantum wells. *J. Appl. Phys.*, 119:181505, 2016.

[194] D. S. P. Tanner, M. A. Caro, E. P. O'Reilly, and S. Schulz. Random alloy fluctuations and structural inhomogeneities in c-plane $In_xGa_{1-x}N$ quantum wells: theory of ground and excited electron and hole states. *RSC Adv.*, 6:64513–64530, 2016.

[195] D. S. P. Tanner, J. M. McMahon, and S. Schulz. Interface roughness, carrier localization, and wave function overlap in c-plane (In,Ga)N/GaN quantum wells: interplay of well width, alloy microstructure, structural inhomogeneities, and Coulomb effects. *Phys. Rev. Appl.*, 10:034027, 2018.

[196] F. Nippert, S. Yu. Karpov, G. Callsen, B. Galler, T. Kure, C. Nenstiel, M. R. Wagner, M. Straßburg, H.-J. Lugauer, and A. Hoffmann. Temperature-dependent recombination coefficients in InGaN

light-emitting diodes: Hole localization, Auger processes, and the green gap. *Appl. Phys. Lett.*, 109:161103, 2016.

[197] J. M. McMahon, D. S. P. Tanner, E. Kioupakis, and S. Schulz. Atomistic analysis of radiative recombination rate, Stokes shift, and density of states in *c*-plane InGaN/GaN quantum wells. *Appl. Phys. Lett.*, 116:181104, 2020.

[198] C. M. Jones, C.-H. Teng, Q. Yan, P.-C. Ku, and E. Kioupakis. Impact of carrier localization on recombination in InGaN quantum wells and the efficiency of nitride light-emitting diodes: Insights from theory and numerical simulations. *Appl. Phys. Lett.*, 111:113501, 2017.

[199] H. Ryu, I. Choi, H. Choi, and J. Shim. Investigation of light Extraction Efficiency in AlGaN Deep-Ultraviolet Light-Emitting Diodes. *Appl. Phys. Express*, 6:062101, 2013.

[200] R. Goldhahn, C. Buchheim, P. Schley, A.T. Winzer, and H. Wenzel. Optical constants of bulk nitrides. *Nitride Semiconductor Devices: Principles and Simulation*, pages 95–115, 2007.

[201] E. Sakalauskas, H. Behmenburg, C. Hums, P. Schley, G. Rossbach, C. Giesen, M. Heuken, H. Kalisch, R.H. Jansen, J. Bläsing, et al. Dielectric function and optical properties of Al-rich AlInN alloys pseudomorphically grown on GaN. *J. Phys. D: Appl. Phys.*, 43(36):365102, 2010.

[202] R. G. Banal and M. Funato and Y. Kawakami. Optical anisotropy in [0001]-oriented $Al_xGa_{1-x}N$/AlN quantum wells (x>0.69). *Phys. Rev. B*, 79:121308(R), 2009.

[203] S-H. Wei and A. Zunger. Valence band splittings and band offsets of AlN, GaN, and InN. *Appl. Phys. Lett.*, 69:2719–2721, 1996.

[204] J. Pastrňák and L. Roskovcova. Optical absorption edge of AlN single crystals. *physica status solidi (b)*, 26(2):591–597, 1968.

[205] J. L. Birman. Some selection rules for band-band transitions in wurtzite structure. *Physical Review*, 114(6):1490, 1959.

[206] K. B. Nam, J. Li, M. L. Nakarmi, J. Y. Lin, and H. X. Jiang. Unique optical properties of AlGaN alloys and related ultraviolet emitters. *Appl. Phys. Lett*, 84:5264, 2004.

[207] N. Susilo, E. Ziffer, S. Hagedorn, L. Cancellara, C. Netzel, N. Lobo Ploch, S. Wu, J. Rass, S. Walde, L. Sulmoni, M. Guttmann, T. Wernicke, M. Albrecht, M. Weyers, and M. Kneissl. Improved performance of UVC-LEDs by combination of high-temperature annealing and epitaxially laterally overgrown AlN/sapphire. *Photon. Res.*, 8:589–594, 2020.

[208] C. Reich, M. Guttmann, M. Feneberg, T. Wernicke, F. Mehnke, C. Kuhn, J. Rass, M. Lapeyrade, S. Einfeldt, A. Knauer, et al. Strongly transverse-electric-polarized emission from deep ultraviolet AlGaN quantum well light emitting diodes. *Appl. Phys. Lett.*, 107(14), 2015.

[209] M. Guttmann, F. Mehnke, B. Belde, F. Wolf, C. Reich, L. Sulmoni, T. Wernicke, and M. Kneissl. Optical light polarization and light extraction efficiency of AlGaN-based LEDs emitting between 264 and 220 nm. *Japanese Journal of Applied Physics*, 58(SC):SCCB20, 2019.

[210] F. Römer, G. Hofmann, J. Höpfner, M. Schilling, A. Muhin, T. Wernicke, M. Kneissl, and B. Witzigmann. Carrier transport in a deep ultraviolet mixed quantum well light emitting diode. *IEEE Photonics Journal*, 16(1):1–6, 2024.

[211] J. Höpfner, F. Kühl, M. Schilling, A. Muhin, M. Guttmann, G. Hofmann, F. Römer, T. Wernicke, B. Witzigmann, and M. Kneissl. Unraveling carrier distribution in far-UVC LEDs by temperature-dependent electroluminescence measurements. *Applied Physics Letters*, 125(7), 2024.

[212] A. Ibanez, M. Leroux, N. Nikitskiy, W. Desrat, M. Moret, P. Valvin, G. Cassabois, J. Brault, B. Gil, F. Chugenji, K. Taiga, M. Ajmal Khan, and H. Hirayama. The Influence of Alloy Disorder Effects on the Anisotropy of Emission Diagrams in (Al,Ga)N Quantum Wells Embedded into AlN Barriers. *Phys. Status Solidi B*, page 2400215, 2024.

[213] G. Cardinali, S. Kölle, A. Schulz, N. Susilo, D. Hauer Vidal, M. Guttmann, M. A. Blonski, F. Römer, B. Witzigmann, F. Nippert, M. R. Wagner, T. Wernicke, and M. Kneissl. Gain Characteristics of Optically Pumped UVC Lasers with Wide AlGaN Single-Quantum-Well Active Regions. *physica status solidi (a)*, 221(21):2400067, 2024.

[214] H. Hirayama, S. Fujikawa, N. Noguchi, J. Norimatsu, T. Takano, K. Tsubaki, and N. Kamata. 222–282 nm AlGaN and InAlGaN-based

deep-UV LEDs fabricated on high-quality AlN on sapphire. *physica status solidi (a)*, 206(6):1176–1182, 2009.

[215] M. Winkelnkemper, A. Schliwa, and D. Bimberg. Interrelation of structural and electronic properties of InGaN/GaN quantum dots using an eight-band k.p model. *Phys. Rev. B*, 74:155322, 2006.

[216] N. Pant, Z. Deng, and E. Kioupakis. High electron mobility of $Al_xGa_{1-x}N$ evaluated by unfolding the DFT band structure. *Applied Physics Letters*, 117(24), 2020.

[217] R. M. Barrett, J. M. McMahon, R. Ahumada-Lazo, J. A. Alanis, P. Parkinson, S. Schulz, M. J. Kappers, R. A. Oliver, and D. Binks. Disentangling the impact of point defect density and carrier localization-enhanced auger recombination on efficiency droop in (In,Ga)N/GaN quantum wells. *ACS photonics*, 10(8):2632–2640, 2023.

[218] E. Kioupakis, P. Rinke, K. T. Delaney, and C. G. Van de Walle. Indirect Auger recombination as a cause of efficiency droop in nitride light-emitting diodes. *Applied Physics Letters*, 98(16), 2011.

[219] S. Schulz, D. P. Tanner, E. P. O'Reilly, M. A. Caro, T. L. Martin, P. A. J. Bagot, M. P. Moody, F. Tang, J. T. Griffiths, F. Oehler, M. J. Kappers, R. A. Oliver, C. J. Humphreys, D. Sutherland, M. J. Davies, and P. Dawson. Structural, electronic, and optical properties of m-plane InGaN/GaN quantum wells: Insights from experiment and atomistic theory. *Phys. Rev. B*, 92:235419, 2015.

[220] G. Muziol, H. Turski, M. Siekacz, K. Szkudlarek, L. Janicki, M. Baranowski, S. Zolud, R. Kudrawiec, T. Suski, and Czeslaw Skierbiszewski. Beyond Quantum Efficiency Limitations Originating from the Piezoelectric Polarization in Light-Emitting Devices. *ACS Photonics*, 6:1963–1971, 2019.

[221] C. Liu, J. Liu, Y. Huang, X. Sun, Q. Sun, M. Feng, Q. Xu, Y. Shen, and H. Yang. Toward high-performance AlGaN-based UV-B LEDs: engineering of the strain relaxation process. *Crystal Growth & Design*, 24(9):3672–3680, 2024.

[222] Y. Lin, Y. Zhang, Z. Liu, L. Su, J. Zhang, T. Wei, and Z. Chen. Interplay of point defects, extended defects, and carrier localization in the efficiency droop of InGaN quantum wells light-emitting diodes investigated using

spatially resolved electroluminescence and photoluminescence. *Journal of Applied Physics*, 115(2), 2014.

[223] J. Glaab, J. Ruschel, N. Lobo Ploch, H. K. Cho, F. Mehnke, L. Sulmoni, M. Guttmann, T. Wernicke, M. Weyers, S. Einfeldt, and M. Kneissl. Impact of operation parameters on the degradation of 233 nm AlGaN-based far-UVC LEDs. *Journal of Applied Physics*, 131(1), 2022.

[224] J. Park, C. Yu, S. Min, J.-I. Shim, and D.-S. Shin. Extracting the inherent ideality factor of a diode from electrical current–voltage characteristics. *Electronics Letters*, 59(23):e13046, 2023.

[225] F. Römer and B. Witzigmann. Signature of the ideality factor in III-nitride multi quantum well light emitting diodes. *Optical and Quantum Electronics*, 50(11):425, 2018.

[226] H. Masui. Diode ideality factor in modern light-emitting diodes. *Semiconductor science and technology*, 26(7):075011, 2011.

[227] C.-K. Wu, C.-K. Li, and Y.-R. Wu. Percolation transport study in nitride based LED by considering the random alloy fluctuation. *J. Comp. Elec.*, 14:416–424, 2015.

[228] A. A. Browne, M. N. Fireman, B. Mazumder, L. Y. Kuritzky, Y.-R. Wu, and J. S. Speck. Vertical transport through AlGaN barriers in heterostructures grown by ammonia molecular beam epitaxy and metalorganic chemical vapor deposition. *Semicond. Sci. Technol.*, 32:025010, 2017.

[229] K. S. Qwah, M. Monavarian, G. Lheureux, J. Wang, Y.-R. Wu, and J. S. Speck. Theoretical and experimental investigations of vertical hole transport through unipolar AlGaN structures: Impacts of random alloy disorder. *Appl. Phys. Lett.*, 117:022107, 2020.

[230] C. Lynsky, G. Lheureux, B. Bonef, K. S. Qwah, R. C. White, S. P. DenBaars, S. Nakamura, Y-R. Wu, C. Weisbuch, and J. S. Speck. Improved Vertical Carrier Transport for Green III-Nitride LEDs Using (In,Ga)N Alloy Quantum Barriers. *Phys. Rev. Applied*, 17:054048, 2022.

[231] N. Roccato, F. Piva, C. De Santi, M. Buffolo, M. Fregolent, M. Pilati, N. Susilo, D. Hauer Vidal, A. Muhin, L. Sulmoni, T. Wernicke, M. Kneissl, G. Meneghesso, E. Zanoni, and M. Meneghini. Modeling the electrical

degradation of AlGaN-based UV-C LEDs by combined deep-level optical spectroscopy and TCAD simulations. *Appl. Phys. Lett.*, 122:161105, 2023.

[232] T. Kinoshita, T. Obata, H. Yanagi, and S.-I. Inoue. High p-type conduction in high-Al content Mg-doped AlGaN. *Applied Physics Letters*, 102(1), 2013.

[233] St. Brochen, J. Brault, S. Chenot, A. Dussaigne, M. Leroux, and B. Damilano. Dependence of the Mg-related acceptor ionization energy with the acceptor concentration in p-type GaN layers grown by molecular beam epitaxy. *Applied Physics Letters*, 103(3), 2013.

[234] F. Piva, M. Grigoletto, R. Brescancin, C. De Santi, M. Buffolo, J. Ruschel, J. Glaab, D. Hauer Vidal, M. Guttmann, J. Rass, S. Einfeldt, N. Susilo, T. Wernicke, M. Kneissl, G. Meneghesso, E. Zanoni, and M. Meneghini. Impact of Mg-doping on the performance and degradation of AlGaN-based UV-C LEDs. *Applied Physics Letters*, 122(15), 2023.

[235] T. Kolbe, A. Knauer, J. Rass, H. K. Cho, S. Hagedorn, S. Einfeldt, M. Kneissl, and M. Weyers. Effect of electron blocking layer doping and composition on the performance of 310 nm light emitting diodes. *Materials*, 10(12):1396, 2017.

[236] T. Kolbe, F. Mehnke, M. Guttmann, C. Kuhn, J. Rass, T. Wernicke, and M. Kneissl. Improved injection efficiency in 290 nm light emitting diodes with Al (Ga) N electron blocking heterostructure. *Applied Physics Letters*, 103(3), 2013.

[237] F. Mehnke, C. Kuhn, J. Stellmach, T. Kolbe, N. Lobo-Ploch, J. Rass, M.-A. Rothe, C. Reich, N. Ledentsov, M. Pristovsek, T. Wernicke, and M. Kneissl. Effect of heterostructure design on carrier injection and emission characteristics of 295 nm light emitting diodes. *Journal of Applied Physics*, 117(19), 2015.

[238] P. Milner, V. Z. Zubialevich, S. M. Singh, P. Pampili, B. Corbett, and P. J. Parbrook. Temperature-dependent investigation of polarisation doping in 330 nm ultraviolet light-emitting diodes. *Journal of Physics D: Applied Physics*, 2025.

[239] L. Gao, F. Xie, and G. Yang. Numerical study of polarization-doped AlGaN ultraviolet light-emitting diodes. *Superlattices and Microstructures*, 71:1–6, 2014.

[240] P. P. Michałowski, S. Złotnik, J. Sitek, K. Rosiński, and M. Rudziński. Oxygen-induced high diffusion rate of magnesium dopants in GaN/AlGaN based UV LED heterostructures. *Physical Chemistry Chemical Physics*, 20(20):13890–13895, 2018.

[241] K. Köhler, T. Stephan, A. Perona, J. Wiegert, M. Maier, M. Kunzer, and J. Wagner. Control of the Mg doping profile in III-N light-emitting diodes and its effect on the electroluminescence efficiency. *Journal of Applied Physics*, 97(10), 2005.

[242] D. Aurélien, M. J. Grundmann, J. F. Kaeding, N. F. Gardner, T. G. Mihopoulos, and M. R. Krames. Carrier distribution in (0001) InGaN/ GaN multiple quantum well light-emitting diodes. *Applied Physics Letters*, 92(5), 2008.

[243] L. Li, Y. Zhang, S. Xu, W. Bi, Z.-H. Zhang, and H.-C. Kuo. On the hole injection for III-nitride based deep ultraviolet light-emitting diodes. *Materials*, 10(10):1221, 2017.

[244] Y.-K. Kuo, J.-Y. Chang, F.-M. Chen, Y.-H. Shih, and H.-T. Chang. Numerical investigation on the carrier transport characteristics of AlGaN deep-UV light-emitting diodes. *IEEE Journal of Quantum Electronics*, 52(4):1–5, 2016.

[245] J.-H. Park, D.-Y. Kim, E. F. Schubert, J. Cho, and J. K. Kim. Fundamental limitations of wide-bandgap semiconductors for light-emitting diodes. *ACS Energy Letters*, 3(3):655–662, 2018.

[246] D. S. Meyaard, G.-B. Lin, Q. Shan, J. Cho, E. F. Schubert, H. Shim, M.-H. Kim, and C. Sone. Asymmetry of carrier transport leading to efficiency droop in GaInN based light-emitting diodes. *Applied Physics Letters*, 99(25), 2011.

[247] G.-B. Lin, D. Meyaard, J. Cho, E E. F. Schubert, H. Shim, and C. Sone. Analytic model for the efficiency droop in semiconductors with asymmetric carrier-transport properties based on drift-induced reduction of injection efficiency. *Applied Physics Letters*, 100(16), 2012.

[248] H. Kobayashi, K. Sato, Y. Okuaki, T. Lee, T. Morishita, H. Goto, and N. Kuze. Milliwatt-power sub-230-nm AlGaN LEDs with> 1500 h lifetime on a single-crystal AlN substrate with many quantum wells for effective carrier injection. *Applied Physics Letters*, 122(10), 2023.

[249] M. Schilling, J. Ruschel, H. K. Cho, J. Rass, J. Höpfner, T. Wernicke, S. Einfeldt, and M. Kneissl. Effect of quantum well number on the efficiency and degradation of AlGaN-based far-UVC LEDs emitting at 233 nm and 226 nm. *Semiconductor Science and Technology*, 40(4):045004, 2025.

[250] M. Binder, B. Galler, M. Furitsch, J. Off, J. Wagner, R. Zeisel, and S. Katz. Investigations on correlation between I–V characteristic and internal quantum efficiency of blue (AlGaIn) N light-emitting diodes. *Applied Physics Letters*, 103(22), 2013.

[251] A. Muhin, M. Guttmann, V. Montag, N. Susilo, E. Ziffer, L. Sulmoni, S. Hagedorn, N. Lobo-Ploch, J. Rass, L. Cancellara, et al. Radiative recombination and carrier injection efficiencies in 265 nm deep UV LEDs grown on AlN/sapphire templates with different defect densities. *Phys. Status Solidi A*, 2022:2200458, 2022.

[252] M. Schilling, C. Hartmann, M. Guttmann, U. Juda, A. Muhin, J. Höpfner, T. Wernicke, T. Straubinger, and M. Kneissl. Light Extraction and External Quantum Efficiency of 235 nm Far–Ultraviolet-C Light-Emitting Diodes on Single-Crystal AlN Substrates. *physica status solidi (a)*, 222(8):2400812, 2025.

[253] M. Schilling, N. Susilo, A. Muhin, G. Cardinali, J. Ruschel, H. K. Cho, J. Rass, J. Höpfner, T. Wernicke, S. Einfeldt, and M. Kneissl. Effect of the AlGaN Multi-Quantum Well Growth Temperature on the Efficiency of Metal-Organic Vapor-Phase Epitaxy-Grown Far-Ultraviolet-C Light-Emitting Diodes Emitting near 235 nm. *physica status solidi (a)*, 221(23):2400392, 2024.

[254] H. Hirayama, T. Yatabe, N. Noguchi, and N. Kamata. Development of 230–270 nm AlGaN-based deep-UV LEDs. *Electronics and Communications in Japan*, 93(3):24–33, 2010.

[255] B. C. Letson, J. W. Conklin, P. Wass, S. Barke, G. Mueller, M. A. J. Rasel, A. Haque, S. J. Pearton, and F. Ren. Reliability and degradation mechanisms of deep UV AlGaN LEDs. *ECS Journal of Solid State Science and Technology*, 12(6):066002, 2023.

[256] S. Ichikawa, M. Funato, and Y. Kawakami. Dominant nonradiative

recombination paths and their activation processes in $Al_xGa_{1-x}N$-related materials. *Physical Review Applied*, 10(6):064027, 2018.

[257] M. Bickermann, B. M. Epelbaum, O. Filip, P. Heimann, M. Feneberg, S. Nagata, and A. Winnacker. Deep-UV transparent bulk single-crystalline AlN substrates. *physica status solidi c*, 7(7-8):1743–1745, 2010.

[258] F. Mehnke, L. Sulmoni, M. Guttmann, T. Wernicke, and M. Kneissl. Influence of light absorption on the performance characteristics of UV LEDs with emission between 239 and 217 nm. *Applied Physics Express*, 12(1):012008, 2019.

[259] Y. Cao, Q. Lv, J. Liu, T. Yang, T. Mi, X. Wang, S. Li, and J. Liu. Influence of the thickness of p-GaN ohmic contact layer on the performance of AlGaN-based deep-ultraviolet light-emitting diodes. *Materials Science in Semiconductor Processing*, 170:107939, 2024.

[260] M. Shatalov, W. Sun, A. Lunev, X. Hu, A. Dobrinsky, Y. Bilenko, J. Yang, M. Shur, R. Gaska, C. Moe, G. Garrett, and M. Wraback. AlGaN deep-ultraviolet light-emitting diodes with external quantum efficiency above 10%. *Applied Physics Express*, 5(8):082101, 2012.

[261] D. Tanner and S. Schulz. Electronic and excitonic properties of ultrathin (In,Ga)N layers: the role of alloy and monolayer width fluctuations. *Nanoscale*, 12(39):20258–20269, 2020.

[262] A. David and C. Weisbuch. Excitons in a disordered medium: A numerical study in InGaN quantum wells. *Physical Review Research*, 4(4):043004, 2022.

[263] Q. Yan, P. Rinke, M. Scheffler, and C. G. Van de Walle. Strain effects in group-III nitrides: Deformation potentials for AlN, GaN, and InN. *Appl. Phys. Lett.*, 95:121111, 2009.